Filiform corrosion of aluminium alloys and iron.

Coleman, Andrew John

FILIFORM CORROSION OF ALUMINIUM ALLOYS AND IRON

Andrew John Coleman

Engineering Doctorate (EngD) Thesis

Academic Supervisor:
Prof. H.N. McMurray
Department of Materials Engineering
University of Wales - Swansea

Industrial Supervisors:
Dr. A. Afseth
Novelis Inc.
Dr G.M. Scamans
Innoval Technology

Department of Materials Engineering
University of Wales – Swansea

March 2007

ProQuest LLC.
789 East Eisenhower Parkway
P.O. Box 1346
Ann Arbor, MI 48106 – 1346

Summary

The initial aim of this work was to obtain an improved understanding of filiform corrosion (FFC), as it affects organic coated aluminium alloys. The first part of the thesis describes kinetic and mechanistic studies on 6000 series alloys. Two types of attack are observed, namely "surface active" and "successive pitting" FFC. "Surface active" FFC is superficial (depth *ca.* 1-2 μm) and occurs when a shear-deformed layer is present at the alloy surface. "Successive pitting" is actually a form of intergranular attack which penetrates to a greater depth (10-50 μm) and occurs only when the deformed layer is absent or has already dissolved. In Chapter 3 on the "low-copper" AA6016-T4 alloy the deformed layer is shown to be anodically activated and to react sacrificially with respect to bulk alloy. Electrochemical polarisation measurements in dilute electrolyte (aqueous NaCl) solution and scanning Kelvin probe (SKP) measurements in humid air are used to demonstrate the free corrosion potential difference which exists between the surface deformed layer and the bulk alloy exposed by layer dissolution. It is further shown that this potential difference contributes significantly to the thermodynamic driving force for "surface-active" FFC. In chapter 4 a novel corrosion-inhibited organic coating is described, consisting of phenylphosphonic acid dissolved in polyvinylbutyral. This coating is shown to profoundly inhibit FFC on "higher copper" AA6111-T4.

Chapter 5 looks specifically at identifying inhibitors which are likely to inhibit "successive pitting" FFC on "higher copper" aluminium alloys. A screening operation is carried out by determining inhibitor efficiency with respect to pitting corrosion on bare alloy surfaces immersed in aqueous chloride electrolyte. However, the 6000 series alloys, even AA6111-T4, were found to not pit spontaneously in the absence of polarisation. Therefore, a different copper containing alloy, namely AA2024-T3, which is well known for its susceptibility to pitting under free corrosion conditions, was used. It has recently been shown that copper complexing reagents can effectively stifle oxygen reduction on pure copper. Therefore, these and other complexing reagents are studied in an attempt to determine their relative effectiveness. It became a further aim to differentiate between inhibition arising from either the de-activation of Cu-rich IMPs or the prevention of copper re-plating, thus highlighting their relative importance within the overall process of stable pitting on AA2024-T3. Through this the mechanism by which they function could be determined and so the best type of inhibitors could be identified for possible incorporation into coatings.

Finally, a specially designed, optical, dual-compartment cell was developed to study the coating disbondment mechanism in FFC using *in-situ* time-lapse photography in conjunction with a reflective light microscope. This cell allowed the gas composition and pressure in the FFC tail to be controlled separately from that above the filament head. Unfortunately, it was found that insufficient optical contrast existed in the FFC filaments on AA6000 series alloy to permit ease of study. However, FFC on iron did provide sufficient contrast and a systematic study of the effect of gas composition was carried out using this material in Chapter 7. This indicated that cathodic disbondment does not contribute to coating delamination (on iron). In Chapter 8 the cell was also used to examine (electro)osmotic models for filament head pressure development. This was done, by applying incrementally increased pressure to the filament head and following changes in filament dimensions and propagation rate. The results indicated that the maximum achievable pressures are significant (> 4 bar) and suggest that a contribution to coating delamination via mechanical disbondment is feasible.

Declaration

This work has not previously been accepted in substance for any degree and is not being concurrently submitted in candidature for any degree.

Signed.. ...(candidate)

Date.....12/6/07.....

Statement 1

This thesis is the result of my own investigation, except where otherwise stated. Other sources are acknowledged by footnotes giving explicit references.

Signed.. ....(candidate)

Date.....12/6/07.....

Statement 2

I hereby give consent for my thesis, if accepted, to be available for photocopying and for inter-library loans after expiry of a bar on access approved by the University of Wales on the special recommendation of the Constituent Institution concerned. I also give my consent for the title and summary to be made available to outside organisations.

Signed.... ..(candidate)

Date.....12/6/07.....

Acknowledgements

Firstly, I would like to begin by gratefully thanking Professor Neil McMurray for his constant enthusiasm and encouragement for my research and also his endless input of ideas and hypotheses. For his patience in passing on his experimental science skills, and also for the daily discussions about work and life, I would also like to acknowledge and thank Dr. Geraint Williams.

For providing the necessary funding for my project I would also like to take this opportunity to gratefully acknowledge the Engineering and Physical Sciences Research Council and Novelis Inc. As my industrial supervisors I wish to thank Dr. Andreas Afseth and Dr. Geoff Scamans. In particular, I am very grateful to Andreas for involving me with the Novelis technical centre in Switzerland, and for the many beers he bought me during my visits!

Particular thanks must also go to my friend and a former colleague in the corrosion group, Dr. Trystan Watson. He was a constant source of amusement and discussion, as well as being a great springboard for ideas. Finally, he is also the other half of the Watson-Coleman device and our early attempts with coffee pot and sweet jar lids will always make me laugh! I would also like to thank the other members of the corrosion group both past and present for making the work environment so enjoyable. I wish you all well for the future.

Thanks to my Dad, Jo and Rich for your continued love and support through the good times and the bad as I have progressed to this stage in life. I also would like to acknowledge and thank my late mother, Maureen, for her love and dedication to myself and my brother. Finally I wish to thank with all my love my girlfriend, Elin, who has patiently supported me through the last six years.

Thanks to you all.

Andy Coleman

Chapter 1

Introduction and Literature Review

1.1 Overview of Thesis

Corrosion prevention is a constant battle faced by engineers in the design and production of materials, which ultimately will always be lost. However, it is vital that we understand the mechanisms by which corrosion occurs so that we can develop new methods for prolonging the inhibition of corrosion attack on engineering materials. This thesis focuses on primarily improving the understanding filiform corrosion (FFC) which is particularly prevalent in the automotive and aerospace industries. Novel inhibition strategies are also investigated.

Chapter 3 presents the results of an investigation into the mechanism of FFC on an automotive aluminium alloy, AA6016-T4. It is the aim of this chapter to determine how the alloy becomes susceptible to FFC when the surface is mechanically ground during automobile manufacture.

Chapter 4 follows up the work from the previous chapter and looks at some novel inhibitors for use in a pre-treatment coating so as to prevent FFC on automotive aluminium alloy, AA6111-T4. The coatings developed in this chapter, whilst initially developed with the automotive industry in mind, may also have applications in other areas such as the architectural industry.

Chapter 5 presents results on the use of copper complexing organic compounds as potential inhibitors for use in coatings with alloys susceptible to successive pitting FFC. Inhibitor efficiencies are determined under immersion conditions using freely corroding aluminium alloy AA2024-T3.

Chapter 6 shows how the unique combination of properties of one of the inhibitors used in Chapter 5 can be used to investigate the phenomenon of "cathodic corrosion" occurring on aluminium alloy AA2024-T3.

Chapter 7 presents results investigating the mechanism of FFC on iron which has been much debated over the last 50 years. A specially constructed dual compartment gas cell is used to allow the head and tail of a filiform to be exposed to different atmospheres. This is done with the intention of identifying the electrochemical and mechanical properties behind filament propagation and coating disbondment.

Chapter 8 presents further work using the dual compartment gas cell developed in Chapter 7. An attempt is made to measure the (electro)osmotic pressure that exists in a filiform head on iron and its effect on filiform propagation. This is achieved by incrementally increasing the pressure over the head of the filiform and measuring any changes in the rate of propagation.

1.2 Aluminium Alloys

In its pure form aluminium is a lightweight, silver-white, ductile and malleable metal. It is the third most abundant element, and is the most abundant metal in the Earth's crust.[1] Alumina is mainly extracted from the mineral bauxite, which contains approximately 25 percent aluminium[1] via the Bayer process[1,2] and this is then smelted using the Hall-Héroult[1,2] process to produce aluminium. Pure aluminium is an excellent thermal and electrical conductor, it is magnetically neutral, and when highly polished it reflects well beyond the visible spectrum at both shorter and longer wavelengths.[1]

In its pure state aluminium is a relatively soft metal and tends to lose strength over time.[1] Aluminium is alloyed with varying quantities of heavy metals such as copper or zinc, thus producing relatively light alloys with good mechanical properties. However, a side effect of alloying is the reduced corrosion resistance of the alloy compared to the pure metal.[1]

On contact with air the aluminium surface oxidises to form a thin, compact and strongly adherent aluminium oxide film, which then acts as a protective layer against further corrosive attack. This so called passive behaviour results in pure aluminium having a high corrosion resistance.[1] Corrosion of aluminium alloys is described in more detail later in this Chapter. The resistance to corrosion coupled with good mechanical properties make aluminium alloys highly desirable within modern industry.

1.2.1 Alloying and Tempering

Alloying of aluminium is used to alter its base metal properties. A four digit numerical designation system is used to classify the different types of alloy incorporating the product form (wrought, casting, or foundry ingots, which have no temper designation) and are covered by the American National Standards Institute

(ANSI).[3] A summary of the characteristics of some common alloys and how and where they are most commonly used is given below in Table 1.1.

Table 1.1: Summary of main alloying elements and common applications of aluminium alloys.[3]

Series	Primary alloying components	Content range (wt%)	Typical Applications
1000	None	Al>99%	Chemical and food processing industries
2000	Copper	2-6	Aircraft structural components
3000	Manganese	0.5-0.15	Architectural, cooking utensils, chemical equipment
4000	Silicon	0.8-1.7	Machined parts
5000	Magnesium	0.5-5	Automotive, storage tanks, boat hulls
6000	Magnesium and silicon	Mg: 0.2-1.5 Si: 0.2-1.5	Automotive applications, windows
7000	Zinc and Magnesium	Zn: 5-7 Mg: 1-2	High strength applications such as aerospace
8000	Silicon and Iron	Si: 0.3-1 Fe: 0.6-2	

For the 1xxx series, the last two of the four digits indicate the minimum aluminium percentage (expressed as the two digits to the right of the decimal point in the minimum aluminium percentage). The second digit other than zero (from 1 to 9) indicates special control for one or more impurities. For the series from 2xxx to 8xxx, the second digit (from 1 to 9) indicates an alloy modification of the original alloy (indicated with 0). The last two digits identify the different alloys in the group.[3]

The 1000, 3000 and 5000 series alloys have their properties adjusted by cold work, usually by cold rolling. The exact properties gained by this process depends on the degree of cold work and whether any annealing or stabilising thermal treatment follows.[3] The 2000, 4000, 6000, 7000 and 8000 series alloys are produced through solution heat treatment and age hardening. It is possible to achieve a wide range of properties due to the wide choice of alloy compositions, solution heat treatment

temperatures and times, quench rates from temperature, choice of artificial ageing treatment and degree to which the final product has been deformed. To define the treatments used a system of standard designations is used. These are based upon the letter T and are followed by a number to describe the various conditions.[3] Table 1.2 shows the definitions of these designations.

Table 1.2: Definition of heat treatment designations for aluminium and aluminium alloys[3]

Term	Description
T1	Cooled from an elevated temperature shaping process, and naturally aged to a substantially stable condition. This designation applies to products which are not cold worked after cooling from an elevated temperature shaping process, or in which the effect of cold work in flattening or straightening has no effect on mechanical properties.
T2	Cooled from an elevated temperature shaping process, cold worked and naturally aged to a substantially stable condition. This designation applies to products which are cold worked to improve strength after cooling from an elevated temperature shaping process, or in which the effect of cold work in flattening or straightening does have an effect on mechanical properties.
T3	Solution heat treated, cold worked and naturally aged to a substantially stable condition. This designation applies to products which are cold worked to improve strength after solution heat treatment, or in which the effect of cold work in flattening or straightening does have an effect on mechanical properties.
T4	Solution heat treated and naturally aged to a substantially stable condition. This designation applies to products which are not cold worked after solution heat treatment, or in which the effect of cold work in flattening or straightening does not have an effect on mechanical properties.
T5	Cooled from an elevated temperature shaping process and then artificially aged. This designation applies to products which are not cold worked after cooling from an elevated temperature shaping process, or in which the effect of cold work in flattening or straightening does not have an effect on mechanical properties.
T6	Solution heat treated and then artificially aged. This designation applies to

	products which are not cold worked after solution heat treatment, or in which the effect of cold work in flattening or straightening does not have an effect on mechanical properties.
T7	Solution heat treated and overaged/stabilised. This designation applies to products which are artificially aged after solution heat treatment to carry them beyond a point of maximum strength to provide control of some significant characteristic other than mechanical properties.

1.2.2 Automotive AA6000 Aluminium Alloys

Due to new environmental regulations[4] currently being introduced vehicle emissions must be reduced. This has led to an increase in the use of aluminium alloys for both the automotive monocoque and exterior enclosure panels so as to increase fuel efficiency by lowering vehicle weight. In terms of enclosure panels it is the aluminium sheet alloys of the 6000 series, [Al-Mg-Si-(Cu)] that are used. In the USA the higher strength alloy AA6111 is preferred, whilst in Europe the lower copper alloy AA6016 predominates. Both possess a good combination of strength and formability in the solution treated and naturally aged T4 temper (described in Table 1.2). The formed part is then subjected to a paint bake cycle (~180°C for *ca.* 30 minutes) which increases strength by precipitation. The response to the paint bake is dependent on the prior thermal and mechanical history of the sheet and a range of pre-aging treatments have been developed to enhance paint bake response. These proprietary treatments are introduced as a low temperature age immediately following the solutionising step.

During the production of rolled aluminium sheet alloys the surface of the alloy is subject to different thermomechanical processing than that of the bulk alloy and hence develops a surface layer with different microstructural and electrochemical properties to that of the bulk alloy.[5-15] The surface layer consists of a highly deformed micrograined layer which, following subsequent high temperature heat treatment, contains secondary precipitates. The thermal stability of the fine grained structure is attributed to the presence of oxide phase particle, pinning the grain boundaries and thereby preventing the recrystallisation in the surface layers.[16] The implications of the deformed surface layer regarding the susceptibility of aluminium alloys to

intergranular corrosion are discussed in Section 1.4.1 and to filiform corrosion in Section 1.4.3.4.

1.2.3 Aerospace Alloy AA2024-T3

The process known as *age hardening* or *precipitation hardening*[17] of aluminium alloys may be used to produce a fine uniform dispersion of hard precipitate particles within a softer more ductile matrix. Ideally the precipitate thus formed is *coherent*, that is to say the planes of atoms present within the precipitate are related to (or even continuous with) matrix lattice planes. This produces a widespread disruption of the matrix lattice so that the movement of crystallographic dislocations is impeded even if these merely pass close to the precipitate particle. Conversely, the planes of atoms in *incoherent* precipitates are unrelated to matrix lattice planes. The matrix lattice is therefore unperturbed and the movement of dislocations is impeded only if these impinge directly on the precipitate particle. It is the reduction in dislocation mobility which reduces susceptibility to plastic deformation and coherent precipitates therefore produce a significantly greater hardening effect than incoherent precipitates. An important age-hardening phenomenon, the generation of S-phase particles has been examined by studying the Al-Cu-Mg ternary alloy system.[17] Age hardening is brought about by a process of solution treatment, quenching and aging. A precipitation sequence shown by Reaction (1.1) occurs; ultimately producing a face centred orthorhombic S-phase with the composition Al_2CuMg. The equilibrium S-phase particles are completely incoherent with the FCC α-aluminium matrix.

$$\alpha_{ss} \rightarrow \text{GPB zones (cylinders)} \rightarrow \text{S''} \rightarrow \text{S'} \rightarrow \text{S } (Al_2CuMg) \qquad (1.1)$$

Strengthening of optimally aged Al-Cu-Mg alloys is associated with the presence of fully coherent *Guinier-Preston-Bagaryatsky* (GPB) zones (Cu/Mg clusters) which are reported to be 1-2 nm in diameter and 4 nm long.[18] Additional strengthening arises from the presence of finely dispersed metastable precipitates. In *pseudo-binary* alloys (Cu:Mg ~ 2.2:1 wt%) these are principally S′ (Al_2CuMg) particles, whereas both S′ and θ′($CuAl_2$) particles are observed in alloys with a higher Cu:Mg weight ratio. The existence of S" is still a matter of dispute; however large stresses are thought to be

associated with its coherence. With the addition of Fe, Mn and Si, further phases may exist in equilibrium with S-phase Al_2CuMg including: β-phase $FeAl_3$, $MnAl_6$, $(CuFe)Al_6$, Cu_2FeAl_7, $CuMg_4Al_6$, $(FeMn)Al_6$, $Cu_2Mn_3Al_{20}$ and Mg_2Si.[18] An approximately equal number of phases are possible which may not exist in equilibrium with s-phase Al_2CuMg – the most noteworthy of which is $Al_6(CuFeMn)$.

Second phase (intermetallic) particles in commercial 2.0 mm thick AA2024-T3 alloy sheet stock have been characterised with respect to geometry using a combination of optical and scanning electron microscopy (SEM) and with respect to chemical composition using electron microprobe analysis (EMPA).[19] The alloy sample was sectioned in short, transverse and longitudinal planes – with respect to the original rolling direction. The distribution of particles and particle types was found to be uniform throughout. Furthermore, no significant geometrical differences were detected between particle populations imaged on different orthogonal planes. Table 1.3 summarises geometrical characteristics for all three orthogonal planes, as determined by optical image analysis of particles of diameter > 0.2 μm.

Table 1.3: Geometrical characteristics of second phase particles in 2024-T3[19]

orientation	Mean diameter (μm)	Aspect ratio	Number analysed
short	4.09 ± 2.6	1.60 ± 0.4	196
transverse	3.97 ± 2.9	1.76 ± 0.5	232
longitudinal	3.77 ± 2.8	1.87 ± 0.7	224

As shown below in Table 1.4 the S-phase (Al_2CuMg) predominates. No θ-phase (Al_2Cu) was detected in the size range studied. It is interesting that $Al_6(Cu,Fe,Mn)$ was identified as the second most abundant particle type as this cannot exist in equilibrium with that majority S-phase.[19] The $(Al,Cu)_6Mn$ particles may be thought of as corresponding (roughly) to the $Cu_2Mn_3Al_{20}$ phase.[19] The S-phase particles were found to be rounded (spherical or globular) in shape, whereas particles containing Fe and/or Mn were angular (irregular) in shape.

Although this table provides detailed analysis of particles > 0.2 μm there will also be smaller particles and dispersoids, e.g. ~200 nm AlCuMn dispersoid particles and nanometre scale strengthening S-phase particles.

Table 1.4: Particle distributions by chemical type[19]

Particle type	Number %	Area %
Al_2CuMg	61.3	2.69
$Al_6(Cu,Fe,Mn)$	12.3	0.83
Al_7Cu_2Fe	5.2	0.17
$(Al,Cu)_6Mn$	4.3	0.11
indeterminate	16.9	0.37

1.3 Corrosion Principles

1.3.1 Theory of Aqueous Corrosion

In their natural or low energy state most metals exist as ores which are generally oxides. In order to separate the metal from its ore a large supply of energy must be provided. In the case of iron ore a temperature of 1600°C and a reducing agent are required in a blast furnace.

The extracted metal is in a higher energy state than when combined in its ore form and thus there is a thermodynamic tendency for the metal to return to a lower energy state. Most metals are therefore unstable in air and will recombine with components from their environment. Corrosion is essentially the formation of the oxide of the substrate metal due to an electrochemical reaction with its environment.[20,21] Although similar to the original ore the products generated by metal degradation are generally not the same but have similar energy levels.

The difference in free energy between the metal and its corrosion product is identified as ΔG_f, the Gibbs free energy of formation of a compound from its elements in their natural state under standard temperature and pressure (298 K and 1 atm pressure) and is shown in Fig. 1.1. For a spontaneous reaction to occur ΔG must be negative, *i.e.* energy must be given out. Under standard conditions most chemical compounds of metals have lower values of ΔG than the uncombined metal and hence metals have a tendency to corrode. However, ΔG only tells us that the metals have a *tendency* to corrode and nothing about the rate at which this reaction will occur. In fact, before a metal can corrode an energy barrier known as the free energy of activation, ΔG^*, must be overcome. This energy barrier is also shown in Fig. 1.1. The size of ΔG^* determines the rate of metal corrosion.

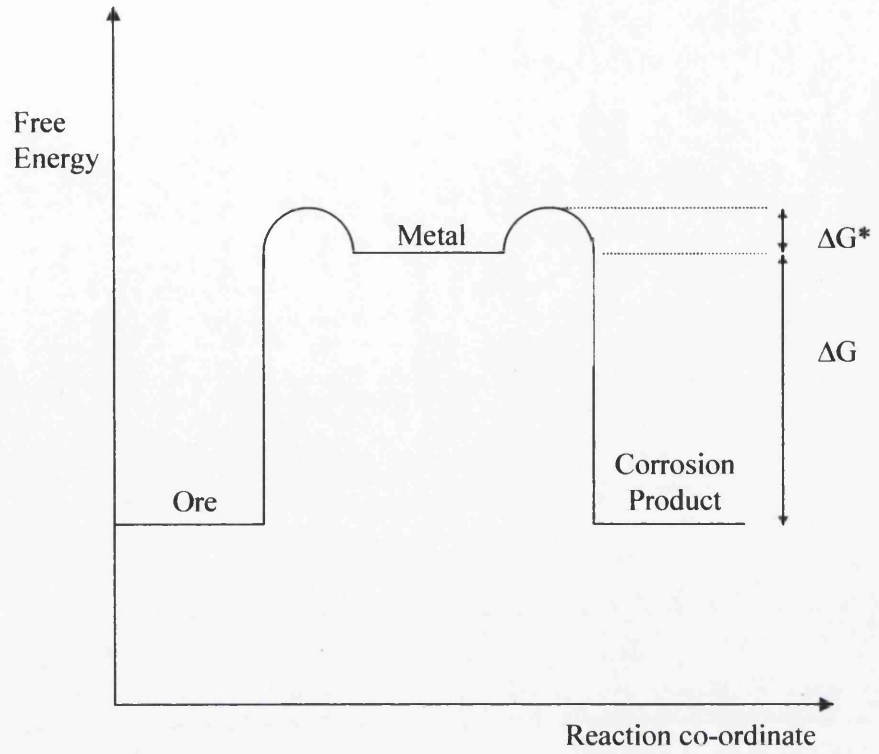

Figure 1.1: Thermodynamic energy profile for metals and their compounds.[21]

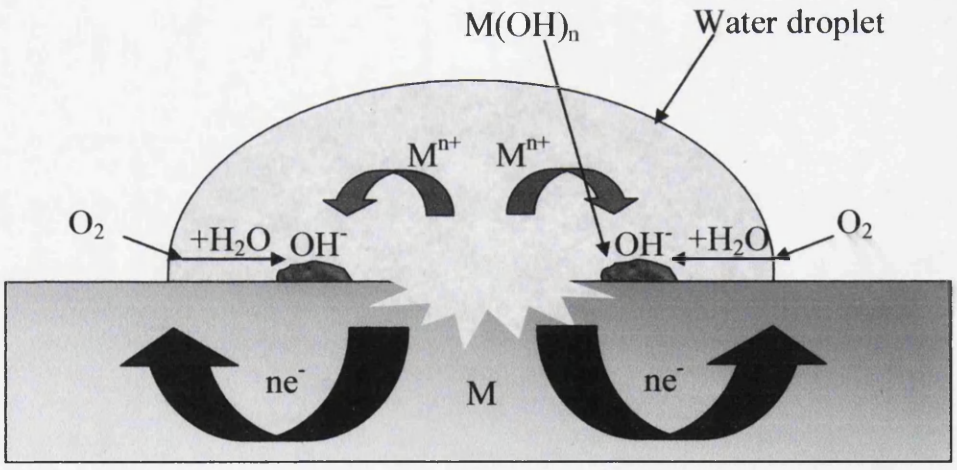

Cathodic Oxygen Reduction	Anodic metal dissolution	Cathodic Oxygen Reduction
$O_2 + 2H_2O + 4e^- \rightarrow 4OH^-$	$M \rightarrow M^{n+} + ne^-$	$O_2 + 2H_2O + 4e^- \rightarrow 4OH^-$

Figure 1.2: Schematic diagram of a typical aqueous corrosion cell.

Metals such as aluminium and iron will corrode when in an environment containing a conducting solution and air. This type of corrosion is known as aqueous or wet corrosion. A wet corrosion cell forms on the surface of the metal and requires the presence of four essential components:

i) anode (electron producing)
ii) cathode (electron consuming)
iii) electrolyte (conduction solution)
iv) conductive pathway between anode and cathode

The electrolyte or conducting solution is most commonly water or a salt solution in the environment and provides a reduced activation energy pathway between the metal and its corrosion products.

At the anode metal dissolution occurs as shown for the general case in Reaction (1.2), with the formation of metal ions and the release of electrons.

$$M_{(s)} \rightarrow M^{n+}_{(aq)} + ne^- \qquad (1.2)$$

On entering the solution the metal ions may react with other species present at the interface to form insoluble solid corrosion products. These products are often deposited on the metal surface and block further metal dissolution, resulting in passivation of the surface.

Occurring simultaneously with the anodic reaction is the cathodic reaction which complements the former by consuming the electrons produced during metal dissolution. Under low pH conditions hydrogen evolution may occur at the cathode,

$$2H^+_{(aq)} + 2e^- \rightarrow H_{2(g)} \qquad (1.3)$$

or, in aerated acidic conditions,

$$O_2 + 4H^+ + 4e^- \rightarrow 2H_2O \qquad (1.4)$$

However, more commonly under aerobic conditions at near neutral pH, the reduction of dissolved oxygen occurs by the following reaction,

$$2H_2O_{(aq)} + O_{2(g)} + 4e^- \rightarrow 4OH^-_{(aq)} \quad (1.5)$$

A schematic of a typical electrochemical cell beneath a water drop on a corroding metal surface under aerobic conditions is shown in Fig. 1.2. The anode and cathode are connected in the electrochemical cell by flow of electrons in the metal and ionic current flux in the electrolyte. The anode and cathode exist as a result of either one, or a combination of the following:

i) Local differences in metal composition.
ii) Local differences in O_2 concentration (as is the case shown in Fig. 1.2).
iii) Local differences in pH.
iv) Local differences in permeability of a passive layer e.g. oxide layer.

Anodic and cathodic sites may be seen to be spatially inseparable on the corroding surface and this is known as general corrosion. Conversely, if the anodic and cathodic sites are spatially distinct the corrosion is said to be localised. Localised corrosion is particularly damaging since anodic activity is focal in small, discrete areas resulting in intense metal dissolution. It is corrosion in its localised form that will be investigated in this thesis.

1.3.2 Redox Potentials and Corrosion Potentials

Considering a standard electrolytic cell, where the metal is surrounded by an aqueous solution containing ions of the metal, reactions will take place between the metal and ions until equilibrium between the two reactions is reached. At the interface area an electric double layer is formed. A simplified schematic of this is shown in Fig. 1.3. This layer causes the metal to have a different potential than the solution. This is known as the Galvani Potential (Φ), and the difference in Galvani potential between the metal and the solution (comparing with the Galvani potential of a reference electrode) is known as the electrode potential (E).

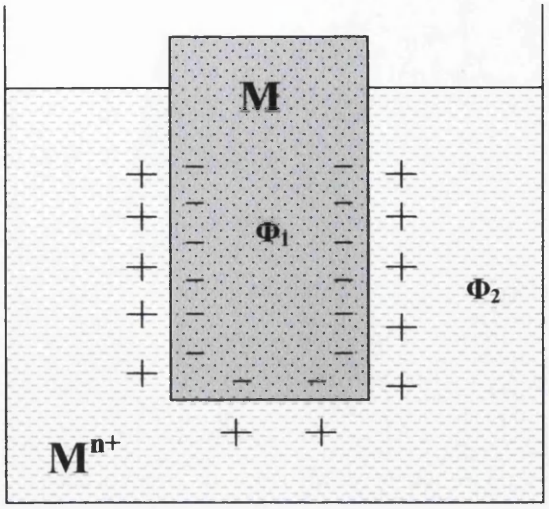

Figure 1.3: Simplified formation of the electrical double layer at a metal interface (M) in an aqueous solution of metal ions (M^{n+}).

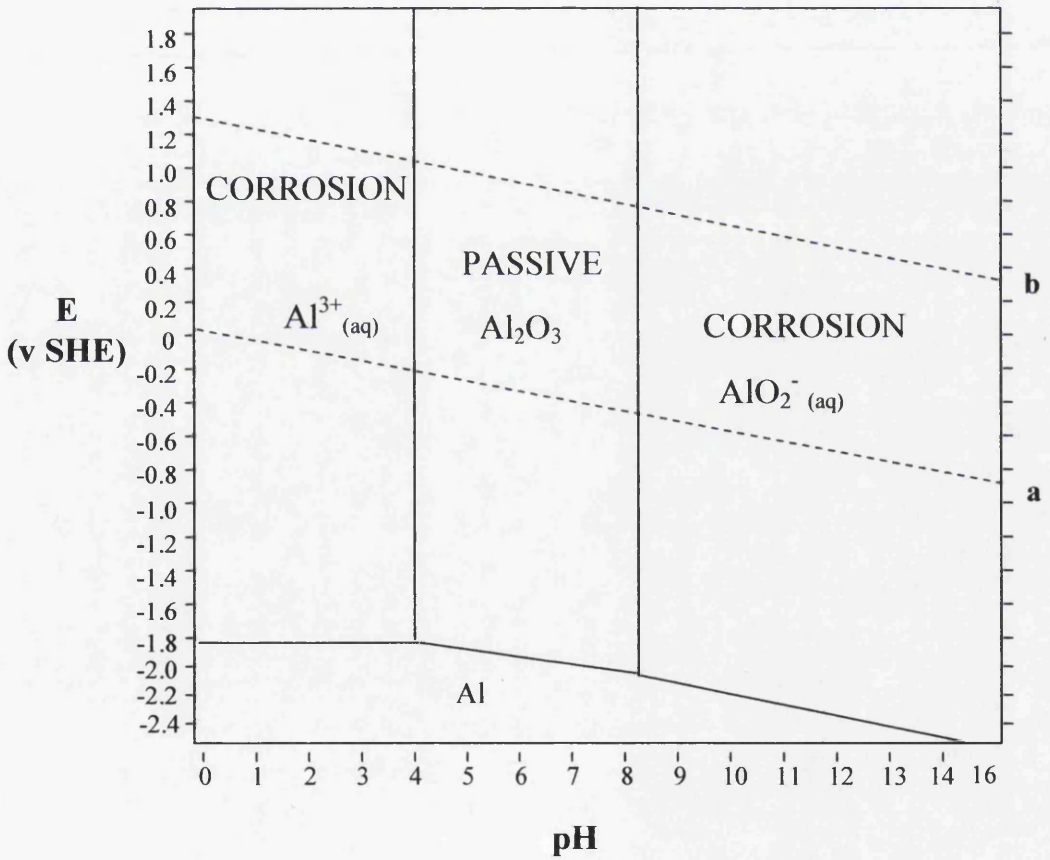

Figure 1.4: Simplified Pourbaix diagram for aluminium. Lines a and b represent respectively the equilibrium conditions of the reduction of water to gaseous hydrogen and the oxidation of water to gaseous oxygen. The area between lines a and b represents the conditions where water is thermodynamically stable under standard conditions.

A relationship then exists between this electrode potential and the activity of the metal ion, the effective metal ion concentration in the solution. It is represented by the Nernst equation,

$$E = E^{\circ} - \frac{RT}{zF} \ln \frac{[\text{products}]}{[\text{reactants}]} \qquad (1.6)$$

where E is the non-equilibrium potential generated by the reaction, [reactants] and [products] are the molar concentrations of the oxidant and reductant respectively, R is the gas constant (8.31 J mol^{-1} K^{-1}), T is temperature (Kelvin), z the number of electrons involved in the redox reaction and F is Faraday's constant (96494 C mol^{-1}).

From Equation (1.6) the standard electrode potential of all metals can be calculated and this is used to generate a table of standard reduction potentials,[20] as shown in Table 1.5. In general, when two metals are coupled together the metal with the more positive standard electrode potential (higher up in the table), is more likely to be reduced whereas the metal with the more negative electrode potential is more likely to be oxidised.

Table 1.5: Standard reduction potentials for some common metals[20]

Electrode reaction	E° (V)
$Cu^{2+} + 2e^{-} \rightarrow Cu$	0.34
$Pb^{2+} + 2e^{-} \rightarrow Pb$	-0.13
$Ni^{2+} + 2e^{-} \rightarrow Ni$	-0.25
$Fe^{2+} + 2e^{-} \rightarrow Fe$	-0.44
$Cr^{3+} + 2e^{-} \rightarrow Cr$	-0.71
$Zn^{2+} + 2e^{-} \rightarrow Zn$	-0.76
$Al^{3+} + 2e^{-} \rightarrow Al$	-1.67
$Mg^{2+} + 2e^{-} \rightarrow Mg$	-2.34

1.3.3 Corrosion Thermodynamics

A concept introduced by Marcel Pourbaix is used in electrochemical studies to identify the stability of different species under varying conditions of potential and pH and they are called Pourbaix or E/pH diagrams.[20] Pourbaix identified a *corroding* condition whereby the concentration of a corroding metals ions in solution must be $\geq 10^{-6}$ M. If the concentration of ions is less than this value then the metal is deemed to be in a condition of *immunity*. A third condition of *passivity* was also identified. This condition exists when an insoluble corrosion product forms on the metal surface preventing further contact between the metal substrate and the electrolyte, thus greatly reducing the corrosion rate. The corrosion of many metals, even in simple electrolytes, may consist of more than one reaction which is often dependent on the pH of the electrolyte. Fig. 1.4 and Fig. 1.5 show simplified Pourbaix diagrams for aluminium and iron in pure water.[22] It may be seen from Fig. 1.4 that aluminium is amphoteric, that is to say it will corrode in both acid and alkaline solutions, whilst iron is generally passive or immune above pH 8, as shown in Fig. 1.5. This property of aluminium has important implications for its corrosion resistance and will be discussed further in Section 1.4.2.

1.3.4 The Kinetics of Corrosion

While it is necessary to determine corrosion tendencies by measuring potentials, it will not be sufficient to ascertain whether a given metal or alloy will suffer corrosion under a given set of environmental conditions. This is because, even though the tendency for corrosion may be high, the rate of corrosion may be very low and thus corrosion may not be a problem. Therefore, it is also important to determine the rate of the reaction.

The anodic and cathodic reactions occurring on a surface are happening simultaneously so that the corroding metal surface can be described as a polyelectrode, *i.e.* a system wherein two or more couples, not in thermodynamic equilibrium, act simultaneously at a single electrode surface.[23-25] Furthermore, Wagner and Traud's addivity principle[26] states that the total current flowing from the polyelectrode into any external circuit will be the algebraic sum of the individual currents due to individual couples. Thus under conditions of free corrosion,

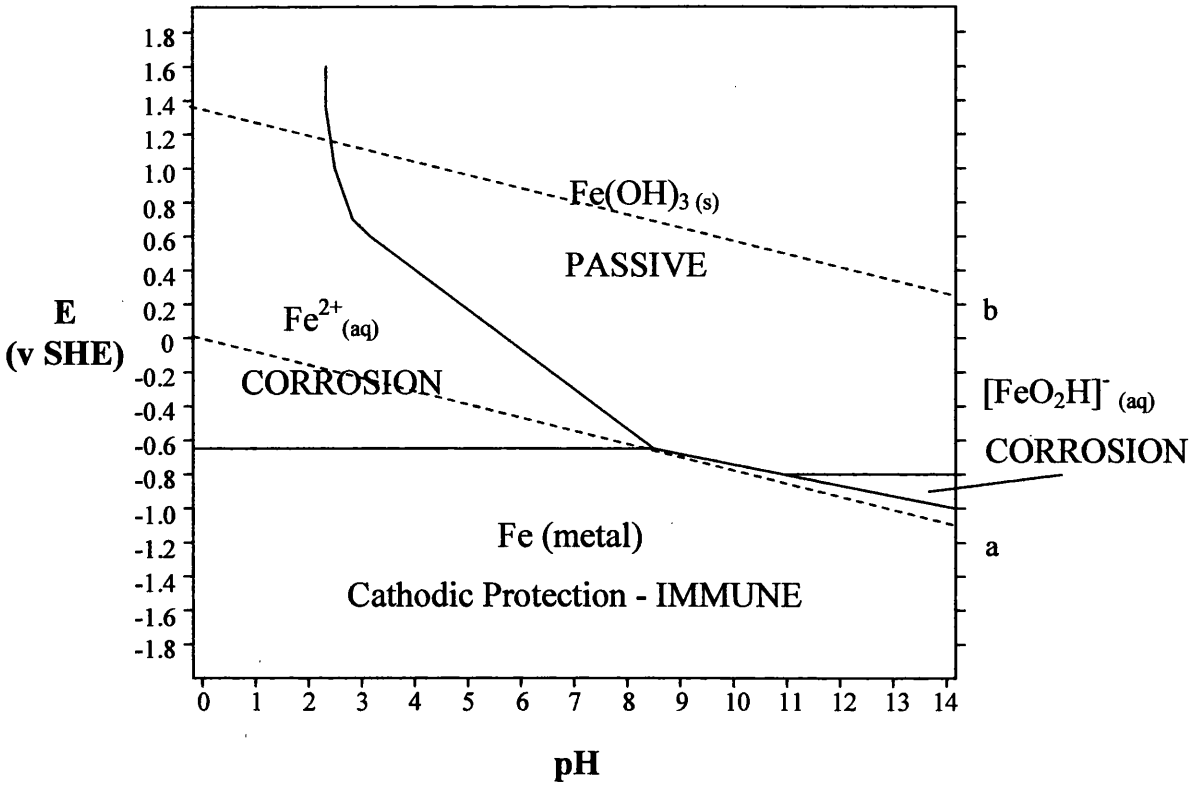

Figure 1.5: As Fig. 1.4 but for iron.

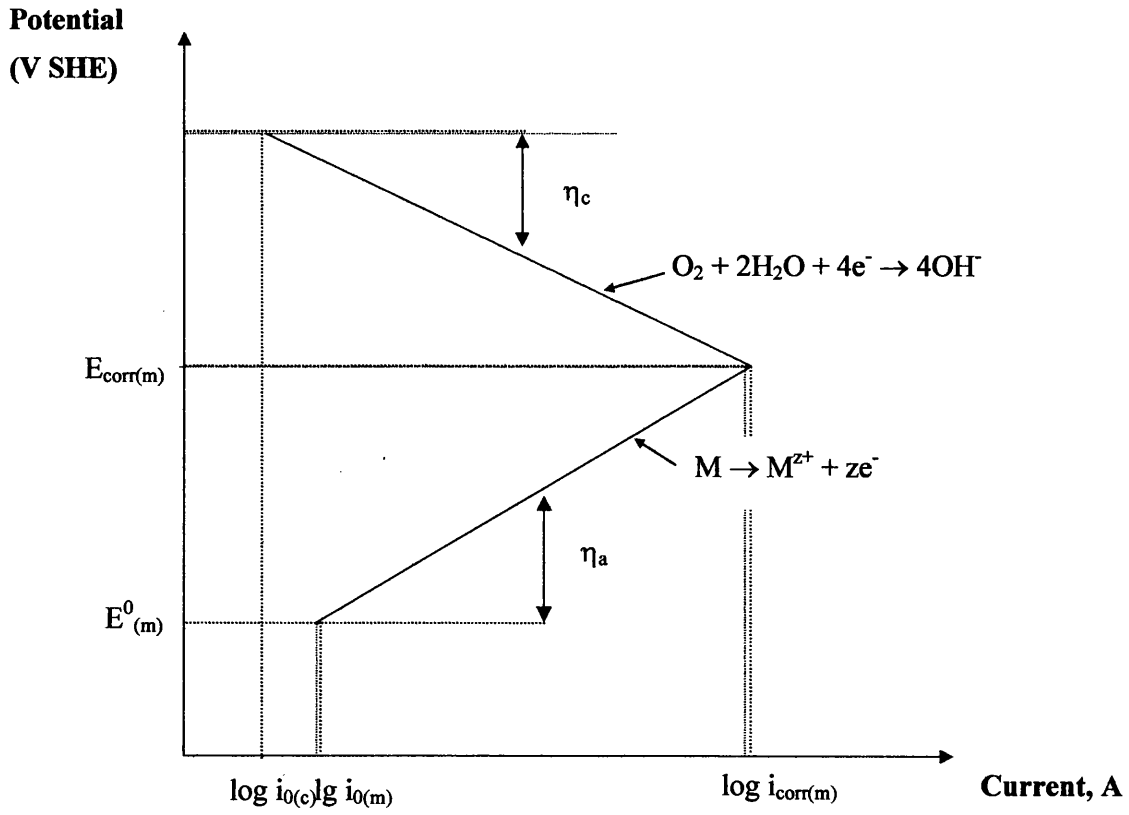

Figure 1.6: Evans diagram for a metal corroding in an aerated electrolyte.

$$\sum i_{anodic} = -\sum i_{cathodic} = i_{corr} \tag{1.7}$$

where i_{anodic} is the partial current due to any anodic processes, $i_{cathodic}$ is the partial current due to any cathodic processes and i_{corr} is the rate of corrosion expressed in terms of current. This has the important corollary that as all corrosion currents are potential dependent this restricts the corroding metal to adopting a unique potential known as the free corrosion potential, E_{corr}. At this potential the material is described as being in a steady-state condition.

The mathematical relationship between current density i, and potential E is defined by Tafel[27] as,

$$i_{anodic} \propto \exp(E) \tag{1.8}$$

and

$$-i_{cathodic} \propto \exp(E) \tag{1.9}$$

When E is plotted as a function of log i, a straight line is produced and this is identified as a Tafel plot. By combining both the anodic and cathodic processes for a corrosion reaction on one graph, a mixed potential plot called an Evans diagram is created. Fig.1.6 shows a simple theoretical Evans schematic diagram for a metal corroded in the presence of an aerated electrolyte. The anodic reaction produces excess electrons which build up at the anodic site as the metal cations enter the solution. These electrons then flow to the cathodic site. Hence, as corrosion proceeds anodic polarisation occurs whereby the anode becomes less negative and its potential is shifted upwards by an amount, η_a. Conversely, the flow of electrons to the cathode causes it to become more negative and hence its potential is shifted downwards by an amount η_c. This process is known as cathodic polarisation.

As shown in Fig. 1.6, the point of intersection of the two Tafel slopes where the anodic and cathodic current are equal, *i.e.* their sum is zero as stated in Equation (1.7) and is defined as the free corrosion current, i_{corr}. Hence, the free corrosion potential E_{corr} for the system may also be determined from an Evans diagram.

1.3.5 Polarisation Curves

A potentiodynamic polarisation curve determined experimentally is one of the most common methods of examining the corrosion behaviour of materials. The polarisation curve assesses the corrosion behaviour of metals and alloys on the one hand and the aggressiveness of the greatest variety of corrosion media on the other.

Corrosion rates are determined by applying a current to produce a polarisation curve (the degree of potential change as a function of the amount of current applied) for the metal surface whose corrosion rate is being determined. When the potential of the metal surface is polarised by the application of the current in a positive direction, it is said to be anodically polarised; a negative direction signifies that it is cathodically polarised. The degree of polarisation is a measure of how the rates of the anodic and the cathodic reactions are retarded by various environmental (concentration of metal ions, dissolved oxygen, etc. in solution) and/or surface process (adsorption, film formation, ease of release of electrons, etc.) factors. The former is called concentration polarisation, the latter activation polarisation. The variation of potential as a function of current (a polarisation curve) allows one to study the effect of concentration and activation processes on the rate at which anodic or cathodic reactions can give up or accept electrons. Hence, polarisation measurements can thereby determine the rate of the reactions that are involved in the corrosion process – the corrosion rate.

An E/ log *i* plot is normally plotted with current density data as positive and on a logarithmic scale for convenience in understanding the plot. Essentially this is done to allow the compression of a large range of current densities and also a clearer indication of when the current density changes from negative to positive, *i.e* the E_{corr} value or the condition the sample would have reached if no overpotential was applied to the sample. A typical polarisation curve for aluminium is shown in Fig. 1.7. From this plot it is also possible to determine the pitting potential. This is characterised by a sharp increase in current density in the passive region, as indicated in Fig. 1.7. Up to several hundred millivolts below this potential metastable pits may be found which are very small in size and repassivate in seconds, whilst above the pitting potential stable pits may be maintained. Pitting corrosion of aluminium alloys is discussed further, in Section 1.4.2.

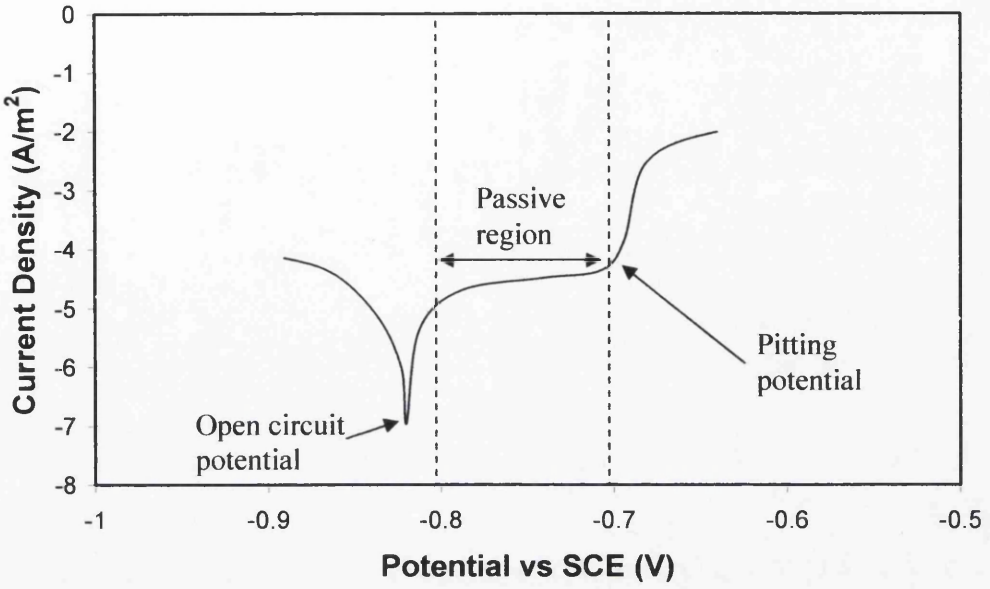

Figure 1.7: Schematic of a polarisation curve for aluminium.

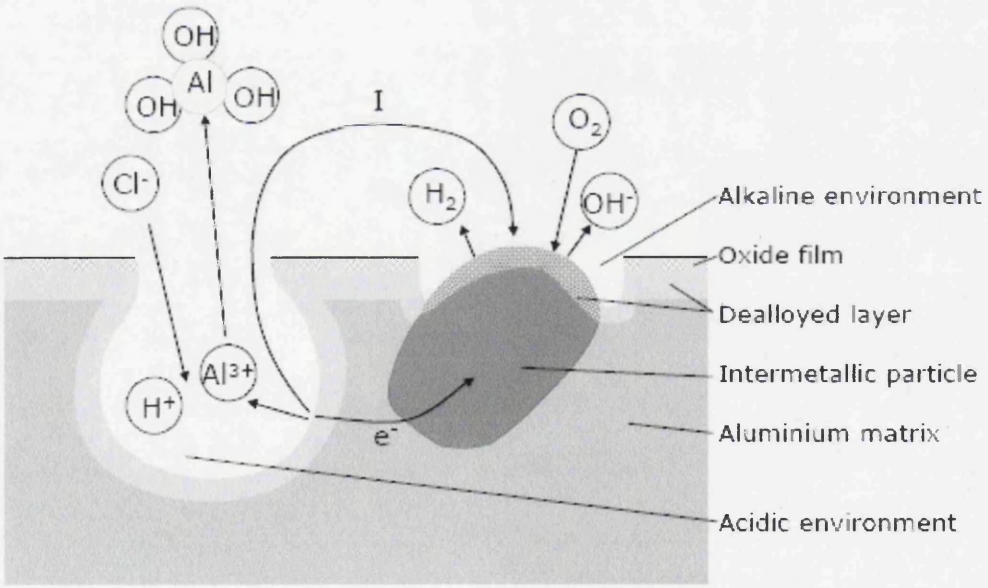

Figure 1.8: Generalised illustration of pitting corrosion on aluminium alloys.

1.4 Localised Corrosion

Localised corrosion occurs when spatially resolved anodes and cathodes exist on a metal surface (as described in Section 1.3.1). Localised corrosion phenomena associated with aluminium and iron that are studied in this research are discussed in the following sub-sections.

1.4.1 Intergranular Corrosion

Intergranular corrosion (IGC) occurs when a grain boundary is attacked because of the presence of precipitates in this region.[20] The composition of the precipitate formed at the grain boundary controls the severity and nature of the attack. In 7xxx series alloys, the $MgZn_2$ strengthening particles formed during ageing at grain boundaries are anodic relative to the surrounding matrix.[28,29] Therefore in this case and all other cases where the precipitates formed are anodic to the surrounding matrix, preferential dissolution of the precipitate will occur at the grain boundary leaving behind a porous material. When the precipitate formed is cathodic to the surrounding matrix, as in the case of $CuAl_2$ and $FeAl_3$ precipitates, the surrounding metal will be attacked. The precipitation process of strengthening particles at grain boundaries is also associated with the formation of precipitate free zones along the grain boundaries. This is due to the depletion of alloying elements from solid solution in the regions immediately adjacent to grain boundaries as a result of diffusion of solute atoms to the grain boundaries. This is particularly true during precipitation hardening and can have a deleterious effect on the corrosion resistance of the metal.[20]

The 6000 series alloys are generally relatively corrosion resistant, but precipitation can increase susceptibility to IGC. Copper content is critical, and it has been shown that IGC susceptibility can be minimised by keeping Cu below *ca.* 0.1 wt %.[30-33] However, copper content may not be the only important factor involved. A "copper-free" model alloy (composition by wt. 0.61% Mg, 0.76% Si, 0.21% Mn, 0.23% Fe and balance Al) aged at 180°C for 0.5 hours has also been shown to exhibit IGC susceptibility.[34] In AA6111 (containing 0.75 wt % Cu) aged at 180°C for between 0.5 and 11 hours, two precipitating phases, monoclinic ß″ (Mg_2Si) and hexagonal Q ($Cu_2Mg_8Si_7Al_4$), coexist.[35] In similarly aged AA6016 (containing 0.05 wt % Cu), the only precipitate is ß″.[35] Noble Q phase grain boundary (gb) precipitates are believed to behave as local cathodes and couple microgalvanically

with adjacent Cu and Si depleted zones, so increasing IGC susceptibility.[30,31,36] Conversely, the ß″ phase has been shown to exhibit E_{corr} between -1.113 V and -1.294 V *vs.* SHE as electrolyte NaCl concentration is varied between 0.01M to 0.6M.[37] Over the same electrolyte range, pure aluminium exhibits E_{corr} between -0.437 V and -0.607 V *vs.* SHE. Consequently ß″ gb precipitates galvanically coupled to the surrounding matrix are predicted to undergo preferential anodic dissolution.[33,34,37]

1.4.2 Pitting Corrosion of Alumnium Alloys

1.4.2.1 Introduction

Pitting is a form of localised corrosion that usually occurs on metals with passive oxide layers. The natural oxide layer generally protects the alloy against general corrosion attack but the layer itself tends to be incomplete. Defects in the layer will expose underlying metal creating a local decrease in resistance to corrosion. However, the existence of a defect in the natural oxide layer does not necessarily mean that a stable pit will generate at that site. For instance, scratching the surface of aluminium will damage the protective oxide layer but will not always lead to stable pitting. The generation of stable pitting has been shown to depend on potential, temperature and the concentration of halide ions, suggesting that a complex mechanism is involved. The pitting potential is determined by potentiodynamic polarisation experiments as described in Section 2.3 and may be seen as a sharp increasing current at a particular potential (pitting potential) in the passive region as described, in Section 1.3.5. During a pitting event rapid metal dissolution occurs within the pit whilst cathodic oxygen reduction occurs on the adjacent surface. The pitting process is autocatalytic, *i.e.* once started it is self sustaining. Metal cations formed in the pit attract the migration of charge balancing chloride ions. In addition the metal cations also tend to undergo hydrolysis, so reducing pH; whilst both chloride ions and low pH stimulate metallic dissolution and act to prevent repassivation. A schematic diagram of a stable pit can be seen in Fig. 1.8.[38] Whilst pitting corrosion occurs on many aluminium alloys the following literature review concentrates primarily on the Al-Cu system as this is the reason for the susceptibility of AA2024 to pitting corrosion.

1.4.2.2 Copper Redistribution – Role of Copper

In general, the susceptibility of aluminium-copper alloys to pitting corrosion increases with copper content. This effect has been attributed to the formation of galvanic cells at copper-rich intermetallic particles, matrix or Cu-depleted grain boundary zones, or by the enhanced electrocatalytic activity (for cathodic oxygen reduction) at those intermetallics or at otherwise copper-enriched regions on the alloy surface.[39-43] Furthermore, it has long been known that the electrochemical heterogeneity of AA2024-T3 makes this alloy susceptible to pitting corrosion, intergranular corrosion and stress-corrosion cracking in aqueous chloride electrolytes.[39,44,45] Galvanic relationships between discrete microstructural elements of AA2024-T3 have been inferred from a list of free corrosion potentials (E_{corr}) of aluminium alloy intermetallic phases under various environmental conditions.[46] Data of this sort has indicated that Al-Cu-Fe-Mn phases will be noble with respect to the α-aluminium matrix and will therefore tend to act as sites of cathodic oxygen reduction.[42] Conversely, the S-phase Al_2MgCu particles are predicted to be more active than the Al-matrix and these are generally regarded as being sites of preferential anodic attack.[42] It is therefore evident that the onset of corrosion in AA2024-T3 is likely to be highly localised in nature. However, this picture is further complicated by the observation that once corrosion has commenced copper becomes redistributed at the alloy surface, producing large localised changes in electrocatalytic activity with respect to cathodic oxygen reduction.

It has been shown that copper redistribution on the surface of copper-containing aluminium alloys such as AA2024-T3 occurs via dealloying processes.[19,47-50] The two principal sources of copper are the S-phase particles, which comprise *ca.* 25 atom % Cu and exhibit a surface coverage of *ca.* 2.7% (see Table 1.4), and the matrix, which contains *ca.* 0.2 – 0.5 wt % Cu in solid solution.[18] The surface oxide covering S-phase particles is not very protective and pre-existing defects or transient breakdown events may expose the underlying intermetallic to corrosive electrolyte. Following oxide breakdown Mg dissolves as $Mg^{2+}_{(aq)}$ and this process transiently inhibits particle repassivation, so allowing Al dissolution from the S-phase. The remaining Cu forms a very high surface area porous sponge, in a manner which is typical of bicontinuous dealloyed microstructures.[48] However, from the point of view

of percolation theory the 25 atom % Cu content of the S-phase is only marginally sufficient for the formation of a Cu network which will remain mechanically stable on dealloying.[49] Consequently, nanometre-scale (10-100 nm) ligaments of copper (Cu clusters) may become mechanically disconnected from the Cu sponge.[19] The resulting copper clusters may then be dispersed by the mechanical action of growing corrosion product or by convection in solution. It has been argued that under certain circumstances this non-Faradic liberation and transport of copper from and to the alloy surface may account partially or wholly for the observed copper enrichment of corroding AA2024-T3 surfaces.[48]

The open-circuit potentials typically adopted by freely corroding AA2024-T3 are almost 1 V lower than the reversible potential of copper.[48] Consequently, no anodic copper dissolution can take place so long as the remnant dealloyed copper sponge remains electrically connected to the matrix. However, copper clusters which become electrically isolated from the alloy surface may adopt a free corrosion potential characteristic of pure copper and undergo anodic dissolution to $Cu^{2+}_{(aq)}$ in aggressive electrolytes, such as those containing Cl^-. This phenomenon has been demonstrated using a rotating ring disc electrode (RRDE) approach in which Cu^{2+} ions emitted from a freely corroding AA2024-T3 disc are collected by cathodic electrodeposition on a concentrically mounted platinum or silver ring electrode. The quantity of Cu accumulated on the ring electrode over a given time period is then quantified by anodic stripping.[48,49] It is also believed that dissolved copper may become replated onto the AA2024-T3 substrate.[48] Certainly, the spontaneous electrodeposition of copper onto aluminium surfaces from Cu^{2+} containing electrolytes, with a consequent acceleration of corrosion through enhanced rates of cathodic oxygen reduction, is a well established phenomenon. The electrodeposition of copper on the oxide covered surface of the aluminium matrix may at first seem surprising, but it would appear that regions of this surface are at least transiently bare. Furthermore, the oxide layer is undoubtedly defective and exhibits semi-conducting properties.[51]

1.4.2.3 Cathodic Corrosion and Matrix dealloying

It is evident that cathodic oxygen reduction, whether it occurs on intact intermetallic particles, copper-rich dealloyed intermetallics, detached and re-deposited

copper clusters or replated copper, will give rise to local alkalization.[49,52-54] Moreover, it is well known that alkalization of this sort, whether it occurs as a result of oxygen reduction or hydrogen evolution, may destroy the passivity of the aluminium matrix and promote the dissolution of Al via the following reaction,[53,55-58]

$$Al_{(s)} + 4OH^-_{(aq)} \rightarrow \left[Al(OH)_4\right]^-_{(aq)} + 3e^- \qquad (1.10)$$

This matrix dealloying process may give rise to significant levels of copper exposure in AA2024-T3, the matrix of which is believed to contain 0.2 – 0.5% Cu in solid solution,[56] and result in the agglomeration of solid solution Cu into Cu particles which may serve as cathodic sites to support still more oxygen reduction. Additionally, dissolution of aluminium will bring new precipitate S-phase particles to the surface, which can activate anodically and subsequently turn into oxygen reduction cathodes. This process is known by the descriptive term *"cathodic corrosion"* because it occurs more rapidly with the passage of cathodic current than under simple electrolyte immersion. However, it should be understood that the dissolution of Al via Reaction (1.10) is still a process of anodic oxidation and that only the *net current* (*i.e.* anodic current component minus cathodic current component) is cathodic.

Cathodic oxygen reduction usually occurs via one, or both, of two basic reaction mechanisms. The first is a direct $4e^-$ pathway in which O_2 becomes completely reduced to hydroxyl ions (OH^-) as shown by Reaction (1.5). The second is shown below by Reaction (1.11) and is a $2e^-$ reduction pathway through which O_2 is reduced to a mixture of H_2O_2 and OH^-.

$$O_2 + 2H_2O + 2e^- \rightarrow H_2O_2 + 2OH^- \qquad (1.11)$$

Which of these two reaction pathways predominates depends on the composition of the metal substrate and the presence, or absence, of any surface oxide film.[59]

Rotating disc electrode (RDE) studies of cathodic oxygen reduction were carried out on both real AA2024-T3 and a photolithographically produced "synthetic alloy" consisting of 1.8 μm Cu discs in a square array with 9.5 μm nearest-neighbour spacing on a Al 1 wt. % Cu solid-solution α–aluminium substrate.[49] The results of these were taken to demonstrate that in stagnant or weakly stirred electrolyte the

copper-rich dealloyed S-phase particles and Cu discs behave similarly as "microelectrode arrays" for cathodic oxygen reduction and that (area averaged) oxygen reduction current densities on the alloy surface may approach those seen on pure copper electrodes.

Solution pH immediately adjacent to individual S-phase particles was measured ampereometrically using the tip of a 0.25mm diameter Pt-20%Ir wire electrode.[49] It was thus shown that for AA2024-T3 freely corroding in stagnant neutral 0.1M aqueous NaCl solution pH immediately adjacent to S-phase particles tended towards a steady-state value of ~pH 9.5 within 20 min of immersion. It was further argued that the lateral spread of high pH zones depends upon the hydrodynamically determined Nernst diffusion layer thickness (δ) and the nearest-neighbour spacing (s) of S-phase particles. Thus, in highly stirred solution $\delta << s$ and the zones of increasing pH are cut off by convection so that only the matrix immediately adjacent to S-phase particles is exposed to high pH and activated to cathodic corrosion. Whereas, in poorly stirred or stagnant solutions $\delta >> s$ and the zones on increasing pH overlap so that the entire matrix surface may be exposed to high pH and so activated to cathodic corrosion. The overall conclusion reached by these authors was that for real AA2024-T3 freely corroding in 0.5M aqueous NaCl the matrix dealloying and particle dealloying/back-plating mechanisms make approximately equal contributions to observed copper redistribution. However, they also point out that copper particles, whatever their origin, may have finite lifetimes as active cathodes. A copper particle may stop functioning as a cathode either because it eventually becomes undercut by alkaline dissolution of aluminium and becomes disconnected, or from buildup of a gel-like aluminium hydroxide which blocks the cathode from access to oxygen. Similar observations and further developments on this work were made by Jakab *et al*[54] who determined that the charge-transfer oxygen reduction reaction rate increased linearly with copper coverage. However, the mass transfer controlled oxygen reduction reaction increased as a complex function of copper coverage of the inverse of the boundary layer thickness. In practical terms when considering possible inhibitor systems to use they suggest, "that where the overall corrosion rate is controlled by the cathodic reaction there is considerable merit in controlling and reducing copper coverage for both thick and thin electrolyte layers. However, in the case where potentials are extremely negative and electrolyte layers

are thick, this strategy is ineffective and the need to create a permeation barrier is suggested".

Leclere and Newman[53] have studied the kinetics of cathodic oxygen reduction on materials intended to resemble the matrix of AA2024-T3. These consisted of Al 1%wt. Cu and Al 4%wt Cu alloys in the solution annealed and quenched condition, *i.e.* in which copper should be substantially present in metastable solid solution. They found that exposing either alloy to a pH 11 aqueous solution containing NaOH for time periods between 5 mins and 1 hour resulted in aluminium dissolution and a corresponding Cu enrichment of the alloy surface. They also found that, by comparison to the untreated alloys, the Cu enriched surfaces exhibited significantly enhanced oxygen reduction currents when subject to cathodic polarisation at -0.8 V *vs.* SCE in naturally aerated 0.1M aqueous Na_2SO_4. However, in unbuffered electrolyte the net cathodic current was severely reduced by anodic current contributions arising from ongoing cathodic corrosion of aluminium. When 0.1 M borate buffer was added and adjusted to pH 7 aluminium dissolution was suppressed and net cathodic currents increased, becoming greater for greater degrees of surface Cu enrichment. From these and other findings the authors concluded that "cathodic corrosion is a finely tuned, self-regulating process that limits the net cathodic current density that can be supplied by an AlCu solid solution to a remote corrosion site." That is to say, that whilst matrix Cu enrichment is to be expected as a result of alkaline aluminium dissolution at or near cathodic regions, the anodic current contribution arising from that same aluminium dissolution would tend to consume the greater part of any additional cathodic current contribution arising from oxygen reduction on the Cu enriched surface. It is likely therefore that Cu enrichment due to cathodic corrosion of the AA2024-T3 matrix could make only a limited contribution to the maintenance of remote anodic sites such as stable corrosion pits.

1.4.2.4 The Initiation of Pitting Corrosion

It is evident from the preceding subsections that dealloying reactions affecting both second phase particles and the adjacent α-aluminium matrix will progress rapidly when AA2024-T3 is exposed to aggressive aqueous electrolytes, such as those containing chloride ions. It is also evident that the associated metal loss will be localised to a greater or lesser extent and that the resulting surface copper enrichment

will significantly depolarise cathodic oxygen reduction. All of these factors could reasonably be expected to promote the establishment of ongoing localised corrosion phenomena, such as the pitting corrosion which is so characteristic of AA2024-T3. However, a question arises as to whether the ultimate location of individual corrosion pits is random or predetermined to some extent by the alloy microstructure and particularly by the location or distribution of second phase particles. A number of studies have been carried out with the aim of elucidating this problem but most limit their investigations to the very earliest stages of pitting. Consequently the "pits" alluded to by the majority of authors are not the stable, acid-filled, pits described earlier in this introduction. They are at most very small (typically <10 μm diameter) transient pits, the great majority of which will not go on to develop into large, stable, pits.

Suter and Alkire[50] studied the influence of intermetallic particles on pit initiation in AA2024-T3 using a microelectrochemical cell in which the plane-ground tip of an electrolyte containing glass capillary (internal diameter 2 – 1000 μm) was placed on the AA2024-T3 surface using a layer of silicone rubber as a seal. Using this approach small sample areas (<100 μm diameter), including known numbers and identities of intermetallic particles, were isolated and subject to potentiodynamic polarisation. The sample surface was first cathodically polarized at -1.0 V vs. SCE for 1 min and then scanned anodically at a scan rate of 1 mV/s. Thus it was shown that pitting became initiated at potentials between ~-0.6V and ~-0.1 V *vs.* SCE in 1 M aqueous NaCl when no inclusions were present in the sample area. This was very much higher than pitting potentials measured for pure (99.999%) aluminium (~-0.75V to ~-0.6V *vs.* SCE) using the same apparatus and the authors therefore inferred that copper in solid solution acted to increase the pitting resistance of the α matrix in AA2024. However, the range of pitting potentials measured in 1M aqueous NaCl became significantly broader and lower when intermetallics were present in the sample area; ~-0.2V to 0.9V *vs.* SCE for single AlCuFeMn particles, ~-0.75V to -0.1V *vs.* SCE for single AlCuMg (S-phase) particles and ~-0.4V to -0.2V *vs.* SCE for populations containing both AlCuMg and AlCuFeMn particles.

Post-polarisation SEM investigation of sample areas containing single S-phase particles showed that pit initiation at lower potentials (in the measured range) occurred on the sample matrix immediately adjacent to the particle, whereas pit

initiation at higher potentials occurred beneath a dealloyed Cu-rich remnant. SEM images also suggested that magnesium and aluminium undergo anodic dissolution preferentially at the particle edges, producing a micro-crevice at the interface between the matrix and inclusion which then acts as a site for pit initiation. However, microcracks were sometimes observed in the adjacent matrix, possibly as a result of cathodic hydrogen evolution, which could also act as pit initiation sites. These findings would seem to suggest that the most probable site for the establishment of a stable pit on AA2024 is on the matrix immediately adjacent to an S-phase particle.

Leblanc and Frankel[42] have used atomic force microscopy (AFM) and scanning Kelvin force microscopy (SKFM) to study the initiation of pitting corrosion in AA2024-T3 exposed to chloride containing electrolytes (0.1M to 0.5M aqueous NaCl). A technique involving surface masking with a thin polymeric "ink" film and re-exposure of small selected sample areas by AFM tip scratching was used to investigate both the corrosion behaviour of inclusion populations and the interactions occurring between individual inclusions. In small area exposure (20 x 20 μm to 100 x 100 μm) experiments Al-Cu-Fe-Mg inclusions were found to be noble and immune to anodic dissolution but to behave as active cathode sites and to drive pit initiation in the surrounding area. When the exposed area contained only a single Al-Cu-Fe-Mg inclusion and some surrounding matrix accelerated dissolution of the matrix was observed, starting at the inclusion-matrix interface and quickly propagating away from the inclusion and into the matrix. When the exposed area contained mixed populations of Al-Cu-Fe-Mg and Al_2CuMg inclusions the pattern of anodic attack was found to depend on the area ratio of Al-Cu-Fe-Mg to total exposed area. Thus, for a low area fraction of Al-Cu-Fe-Mg limited matrix dissolution was observed and Al_2CuMg was preferentially attacked, but as the area fraction of Al-Cu-Fe-Mg increased the extent of matrix dissolution was observed to increase. No attack was seen on exposed areas containing no intermetallics and, typically, no attack was seen on areas containing only matrix and Al_2CuMg particles. Certain large Al_2CuMg inclusions were seen to dissolve without the presence of Al-Cu-Fe-Mg cathodes, leaving a Cu-rich remnant. However, the remnants thus formed did not become active cathodes driving anodic dissolution of the surrounding matrix. For large exposed sample areas (>1 cm^2) pits were reported to originate "at Al_2CuMg intermetallics" under open-circuit conditions. Thus, the findings of Leblanc and

Frankel seem to be consistent with those of Suter and Alkire but draw attention to the significance of Al-Cu-Fe-Mg particles as active cathodes driving pit initiation elsewhere – most probably at, or near, s-phase Al_2CuMg particles.

None of the above requires anything other that straightforward anodic attack at S-phase particles or at the S-phase – matrix interface to explain pit initiation. However, various authors have shown that the alkalinity developed at cathodic intermetallic particles on corroding aluminium alloys can dissolve the adjacent α–aluminium matrix as described above in Section 1.4.2.3, creating grooves or pit-like clusters.[19,43,48,57,60] Later on, by a process not well understood, it is claimed that these cavities may switch to an acid-pitting mechanism.[43] Some authors refer to the localised alkaline attack itself as pitting,[61] but it is self-evident that this can only ever be a transient step towards the evolution of a stable pit. The phenomenon has been treated as one of galvanic corrosion between the particle and the matrix,[19] and matrix copper depletion in the close vicinity of copper-containing inclusions has been implicated in localising the attack. However, electron microprobe analysis (EMPA) studies have shown no evidence of matrix copper depletion[19] and significant ohmic potential differences (in solution) are unlikely to exist over such small distances in highly conductive electrolytes (such as 0.1 – 0.5 M aqueous NaCl) except in cases of rapid (stable) pitting.[53] It is therefore most likely that the evolution of high localised pH and the process of cathodic corrosion discussed in preceding subsections are responsible for the observed effects.[53]

Bucheit et al.,[19] have reported two distinct pit morphologies on AA2024-T3 freely corroding 0.1M aqueous NaCl, which they refer to as *selective dissolution* and *peripheral pitting*. Both of these involve dealloying of S-phase particles with the creation of a Cu-rich remnant, as discussed previously. In selective dissolution the Cu-rich remnant breaks up and is substantially lost leaving a depression, or pit, approximately the size and shape of the original S-phase particle. In peripheral pitting the Cu-rich remnant remains substantially intact and localised (alkaline) attack occurs on the matrix immediately peripheral to that remnant. Total pit densities were reported to range between 1×10^4 mm^{-2} and 4×10^4 mm^{-2} as bulk solution pH was varied between pH 1 and pH 12, and to reach a maximum at pH 4. The density of peripheral pitting was approximately independent of pH at *ca.* $1 - 2 \times 10^4$ mm^2, whereas selective dissolution exhibited strongly peaked pH dependence, reaching a

maximum of 4 x 10^4 mm^{-2} at pH 4. It is self-evident that the reported pit-densities are very much greater than those typically encountered for populations of stable pits. Consequently, the selective dissolution and peripheral pitting phenomena must be regarded as transient events. However, the process by which individual transient pits are selected to go on developing as stable pits was not discussed.

Park *et al.*,[43] have studied the influence of Fe-rich β-phase (Al_3Fe) intermetallic inclusions on pit initiation on AA6061-T6 aluminium alloy in aerated 0.6M aqueous NaCl. The Al_3Fe particles are cathodic to the α–aluminium matrix at all times so that pit initiation by selective (anodic) dissolution of intermetallic particles is not possible for this system. However, in un-buffered solutions alkaline attack on the adjacent matrix and peripheral pitting was observed after 40 mins immersion. Furthermore, at longer immersion times the extent of dissolution became distinctly dependent on inclusion size, with larger cavities being found around larger inclusions. After 3-5 hours immersion "active" (stable) pits were found that produced hydrogen gas. Conversely, in buffered solutions peripheral pitting was not observed and anodic attack was limited to the crevice between the specimen and the epoxy mounting material.

On the basis of these findings the authors proposed a pit initiation sequence in which, initially, the matrix slowly dissolves through cathodic corrosion at the inclusion-matrix interface to produce a population of micro-crevices or "cavities". Because the size and shape of intermetallics influence the local dissolution rate in the later stages of cavity formation the cavity population will itself become heterogeneous with respect to depth and growth rate. It was further proposed that "the recesses of faster growing cavities may therefore accumulate dissolved Al^{3+} faster than it can be neutralised by the OH^- produced on the surface of the inclusions". Hydrolysis of Al^{3+} aquo-cations would therefore begin to occur in a few of the larger cavities, reducing local pH and promoting a transition to acid pitting. In order to support the increased local anodic dissolution rate, nearby inclusions would be captured as galvanic "slaves". That is to say they would continue to act as local cathodes but anodic dissolution of their peripheral matrix would cease or continue at a much diminished rate, reducing the probability of further transitions to acid pitting.

This model certainly explains how a large density of (transient) peripheral pitting events may become translated into a much smaller density of (stable) acid pits.

It also explains how in AA2024-T3 cathodic inclusions such as Al-Cu-Fe-Mn, or cathodic Cu-rich remnants produced by the dealloying of S-phase intermetallics, may promote pitting of the α–aluminium matrix. However, the question of how cavity pH can change from alkaline to acid without going through neutral, with the consequent expectation of matrix re-passivation, remains unanswered.

1.4.2.5 Pitting Corroison Inhibition

It is widely accepted that water soluble chromium (VI) oxyanions are highly effective in inhibiting localised corrosion of precipitation hardened Al alloys such as AA2024-T3.[62-66] The efficiency of inhibition derives in part from the ability of Cr(VI) oxyanions to passivate S-phase IMPs and forestall anodic dealloying processes.[62,67] In addition, it has also been demonstrated that cathodic oxygen reduction on both Cu rich IMPs and elemental deposits produced by dealloying is strongly inhibited by the presence of Cr(VI) oxyanions.[64,67,68] Other modes of action, such as the build up of a protective Al(III)/Cr(III) surface oxide[69,70] and the coulombic hindering of Cl^- adsorption by non-faradic adsorption of Cr(VI) species on the surface Al oxide[51,70-77] have also been suggested. However, it is the inhibition of electrochemical processes, especially the oxygen reduction reaction (ORR), on Cu-rich IMPs by Cr(VI) which is receiving significant current attention from researchers keen to mimic the action of Cr(VI) using environmentally benign alternatives.[77]

It has recently been shown that copper complexants such as 2,5-dimercapto-1,3,4-thiadiazolate (DMTD) effectively stifle oxygen reduction on pure copper.[77] It has also been demonstrated that the benzotriazolate anion (BTA), a well known inhibitor of copper corrosion, can inhibit localized corrosion on bare AA2024-T3 immersed in Cl^- containing solution.[78]

Work described in Chapter 5 of this thesis will examine these and other reagents which react with Cu(II) aquo-cations to try and differentiate between inhibitors that either function by the de-activation of Cu-rich IMPs or the prevention of copper re-plating, thus highlighting their relative importance within the overall process of stable pitting on copper containing aluminium alloys.

1.4.3 Filiform Corrosion

Filiform Corrosion (FFC) was first accurately described by Sharman[79] in 1944 appearing on lacquered tobacco tins. FFC is an atmospheric corrosion attack that occurs on organic coated metal substrates, producing characteristic thread-like deposits of corrosion product beneath the surface. FFC has been detected on aluminium, iron and magnesium surfaces.[80] It has recently received new interest in the aluminium industry due to its appearance in the ever widening architectural and automotive industries. Extensive reviews of FFC have already been undertaken elsewhere[81-83] and hence will not be carried out in this work. However, an attempt to describe the filiform mechanism will be made.

Although superficial in nature FFC attack is aesthetically unpleasant and therefore unacceptable in modern industry. It is of particular importance in the automotive industry where ever increasing warranties demanded by customers necessitate more corrosion resistant alloys. FFC can also lead to more serious corrosion phenomena with catastrophic consequences as in the aeronautical industry where stress corrosion cracking has occurred in filiform tails around rivet heads.[81]

FFC requires specific conditions to initiate; oxygen, aggressive ions such as chloride and typically a relative humidity of 60 - 95% must all be present. FFC usually arise from surface defects in protective films in the presence of soluble ionic species.[81]

The filiform threads can exhibit a wide variety of appearances from nodular shapes such as those on some aluminium alloys to the fine sharply defined filaments observed on organically coated steel. Fig. 1.9 shows examples of FFC on iron and aluminium alloy AA2024-T3.

1.4.3.1 Filiform Characteristics

The primary characteristics that are necessary for FFC to occur on coated aluminium and iron substrates are listed below:[5,80,82-84]

i) FFC initiates at defects/weaknesses in the applied coating

ii) Aggressive anions need to be present for FFC to initiate

a)

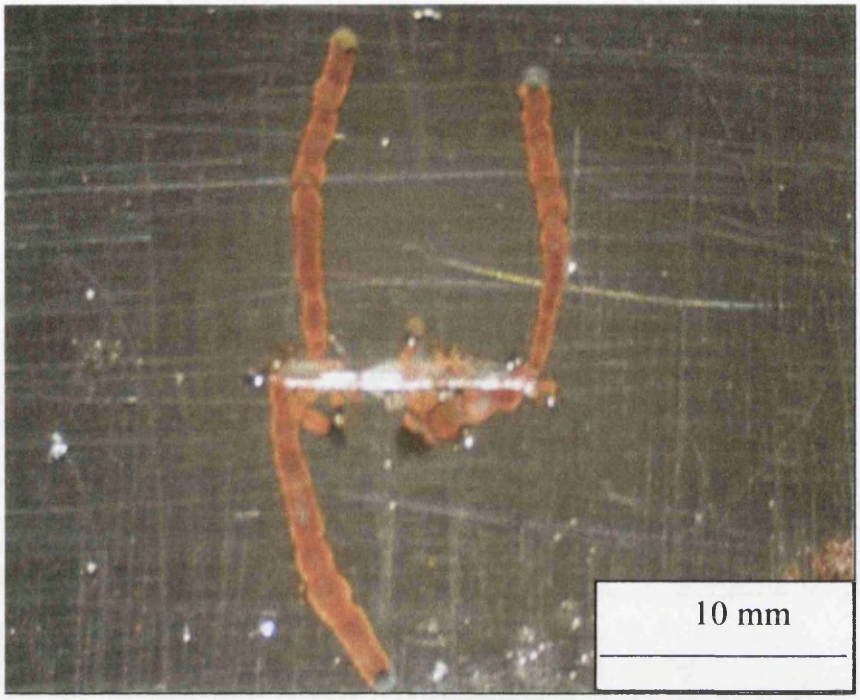

b)

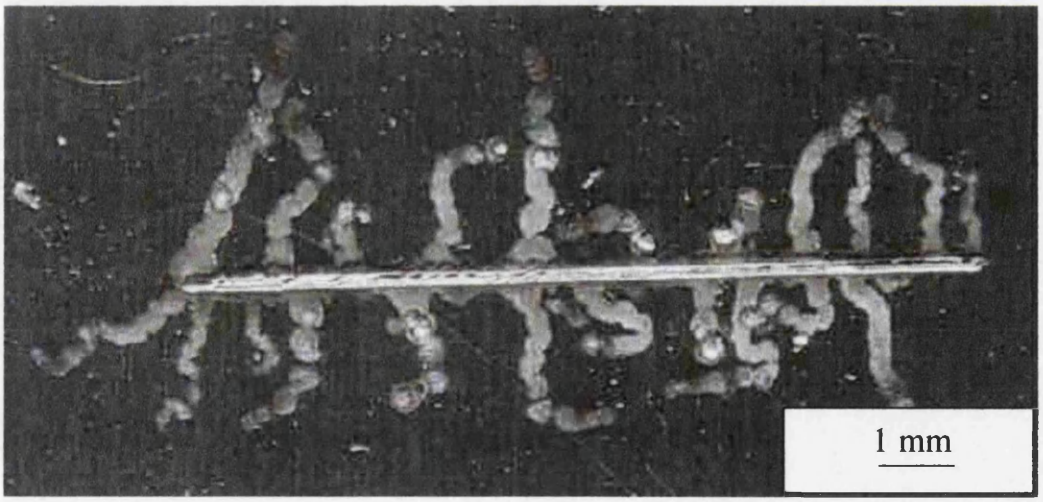

Figure 1.9: Photographic images of filiform corrosion on: a) iron and b) aluminium alloy AA2024-T3.

iii) FFC only occurs above 30% R.H. up to around 95% R.H. Above this relative humidity filaments coalesce and blistering occurs

iv) Oxygen is required for FFC to propagate

v) The filament motion is directionally stable; the tracks are relatively straight for long distances and propagate mainly in the rolling direction

vi) Tracks generally do not cross each other or break in the surface coating although this has been observed

vii) The front edge of the head contains a solution of low pH and appears to be the most anodically active area

viii) Anions of the "inoculating" salt, primarily chloride, are conserved in the head, cations are not conserved

A schematic of a filiment occurring on a coated aluminium alloy substrate is shown in Fig. 1.10. The filament essentially consists of an active head region, containing electrolyte, and a passive tail region filled with porous corrosion products. It is now generally accepted that the primary mode of water and oxygen transport takes place through the tail[82,85,86] and not by diffusion through the coating for FFC as has also been suggested.[87] Upon drying, the corrosion products found in the tail become very porous allowing the transport of O_2 and water through the medium. Ruggeri and Beck[82] calculate that the transport of O_2 through the coating would be ten times slower than that through the defect and porous tail. This directional supply of oxygen from the tail causes a differential aeration cell to be set up in the head with the majority of the cathodic reaction (oxygen reduction) occurring at the back of the head and the majority of the anodic reaction (metal dissolution) occurring at the front of the head in the relatively deaerated region.[80-83,88]

FFC only occurs in a certain range of relative humidity. For aluminium, when initiating with hydrochloric acid, filiform growth has been observed down to 30% R.H.[80] However, near 100% R.H. filiforms coalesce and blistering occurs.[80,82,89]

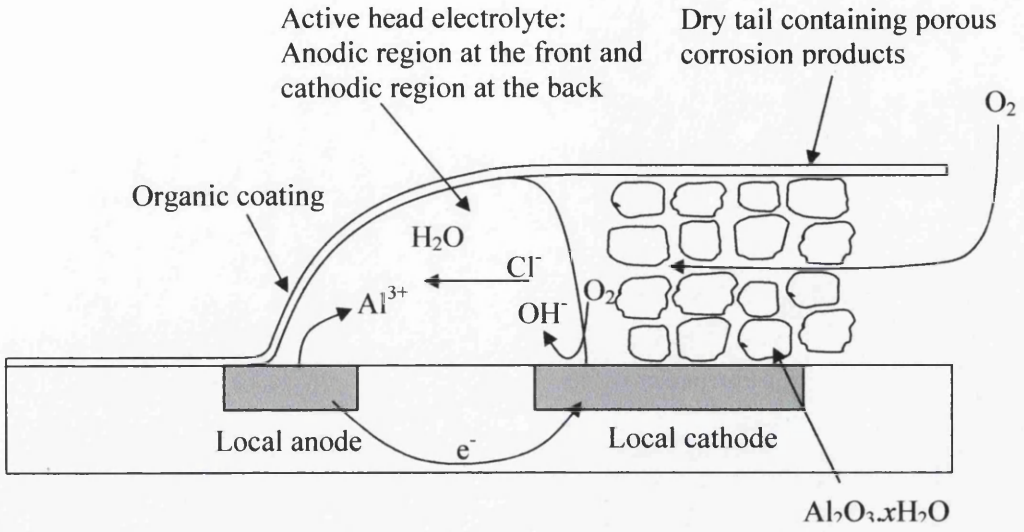

Figure 1.10: Schematic diagram of filiform corrosion occurring on a coated aluminium alloy substrate.

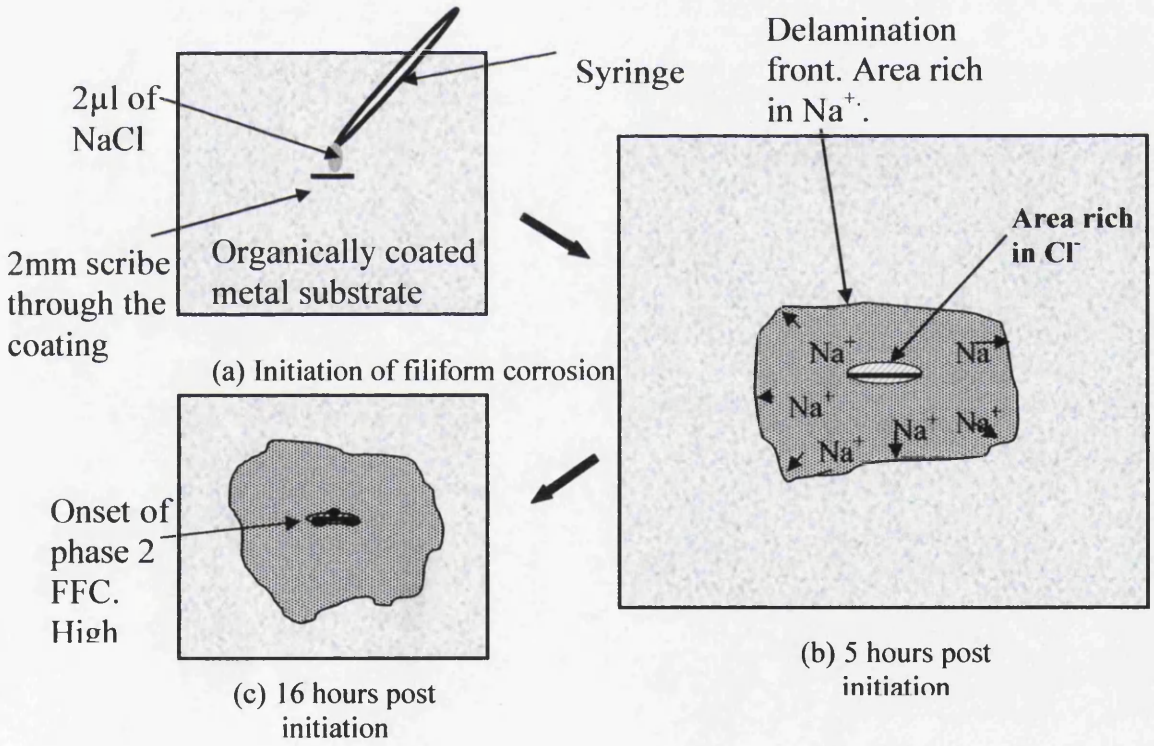

Figure 1.11: A schematic of Phase I filiform attack on occurring on organically coated iron in the presence of group (I) cations.

This section will now go on to discuss the mechanisms of FFC occurring on aluminium and iron separately, in more detail.

1.4.3.2 Filiform Initiation on Aluminium

Filiform corrosion has been shown to start at defects in the coating – for example cut edges,[80,82,90] scratches,[5,79,81-83,85,89-95] rivet heads[81,84] and other sites where the coating is discontinuous. At these points inoculating salt (primarily chloride) can accumulate and cause potential initiation sites. Leidheiser[96] and Bauista[81] state that electrolyte forms due to osmosis at the defect and the presence of a high relative humidity. If there is also the presence of a soluble salt, (either being present having penetrated the defect or because it was already on the metal surface before the coating was applied) a small liquid aggregate is formed owing to the high affinity of ions such as Na^+ and Cl^- for water. Once a large enough number of molecules have gathered for the aggregate to act as a liquid, additional water diffusing through the coating is retained due to the low water vapour pressure of concentrated electrolyte solutions.

1.4.3.3 Filiform Propagation on Aluminium

It has clearly been shown that anodic undermining (as opposed to cathodic delamination) is the method of propagation occurring on aluminium substrates. Low pH values (pH = 1) consistent with an anodic dissolution mechanism have been measured at the front of the filiform head.[80,84] Hoch[84] also mixed a sensitive pH indicator into a primer resin before its application, observing acidic areas around the leading edge of a filiform head. Therefore, at the leading edge of the filiform head chloride-induced substrate depassivation[51] and anodic dissolution and immediate hydration of aluminium occurs by Reaction (1.12)[88,97,98]

$$Al_{(s)} + 6H_2O_{(l)} \rightarrow \left[Al(H_2O)_6\right]^{3+}_{(aq)} + 3e^- \qquad (1.12)$$

As Reaction (1.12) proceeds, the coating becomes undercut, Cl^- ions migrate beneath the delaminated coating to preserve electroneutrality and water is drawn in by osmosis to produce an electrolyte droplet.[95] Once initiated, filaments tend to propagate away from the coating defect under the influence of differential aeration.[79,81,82]

Aluminium cations produced by Reaction (1.12) at the leading edge of the filament-head migrate toward the trailing edge where OH^-, produced by Reaction (1.5), induces cation hydrolysis and the eventual precipitation of water-insoluble $Al(OH)_3$.[81,82,88,99] $Al(OH)_3$ in the filament tail region slowly loses water and may incorporate carbonate ions from atmospheric CO_2.[83,88] Cl^- anions continually migrate toward the anodic leading edge with the result that all water-soluble salt and, through osmosis, liquid water becomes retained in the filament head.[81,82] Williams and McMurray[94] have shown using secondary ion mass spectrometry (SIMS) that Cl^- is substantially conserved in the filament-head electrolyte throughout the experimental period. Furthermore, similar results have been reported on AA2024-T3 using energy-dispersive analysis, with little or no Cl^- detectable in either filament tails or coating defects following FFC initiation with HCl vapor.[94]

To further support the anodic undermining mechanism Lenderink[83] showed that FFC was not slowed down by the application of strips of foil across a coated surface. These strips stopped oxygen diffusion through the coating but did not hinder filiform propagation, proving that there was not a cathodic delamination process occurring. Lenderink[83] also stated that oxygen transport through aluminium corrosion products is 10^4 times faster than through an equally thick intact coating. Further analysis of his own and others work, showed that the rate of growth of a filament is linear up to a point, but beyond this FFC growth is inhibited and gradually slows. The reason given for this is that oxygen diffusion through the tail becomes limited once the amount of corrosion product reaches a critical length. However, it could also be that the some Cl^- are becoming combined with precipitated aluminium hydroxide to form hydroxychloro-complexes.[95] Thus as the FFC tail length increases and more Cl^- ions are consumed the rate of the anodic reaction would slow and thus the rate of propagation would slow.[95] This is also supported by the work of Williams and McMurray[94] which showed that the rate of propagation of FFC occurring on AA2024 is highly dependent on Cl^- concentration in the filiform head.

1.4.3.4 Surface Active Layers and FFC on Aluminium Alloys

As discussed in Section 1.2.2 the introduction of a damaged surface layer either by thermomechanical processing or surface abrasion introduces a surface layer of around 0.5-5μm[5,12,83] on aluminium alloys, that can have significantly different

microstructural and electrochemical properties to that of the bulk alloy.[5-15,100] Furthermore, a strong correlation has been demonstrated between the presence of a deformed layer, the thermally-promoted precipitation of intermetallic phases within that layer, and FFC susceptibility.[6,7,9,12,14,15,90,101] The susceptibility of the alloys to FFC attack was increased dramatically with subsequent high temperature heat treatment.[5,8,9] The morphology of attack was reported as being different to that of previously observed FFC and consequently two types of FFC were identified on aluminium alloys. In the absence of a damaged surface layer a slower, more deeply penetrating "successive pitting"[6] mode of attack has been reported. However, when a damaged surface layer is present the attack becomes rapid and very superficial, limited only to the damaged surface layer itself. For 3000 and 5000 series alloys the increased susceptibility of the alloys to FFC when a damaged surface layer was present and heat treated was attributed to the preferential precipitation of Mn and Fe in the deformed surface layer generating a cathodically activated surface layer compared to that of the bulk alloy. However, it was identified that the problem of increased susceptibility to FFC through the introduction of a damaged surface layer by thermomechanical processing could easily be controlled by subsequent etching using an acid or alkaline cleaner to remove the damaged layer. This has also been shown to be the case with 6000 series aluminium alloys. Although the bulk alloy of AA6111 is more susceptible to successive pitting FFC than AA6016, Scamans *et al*[102] have shown that by proper application of the pre-treatment layer and coating system used in the automotive industry, susceptibility of the bulk alloy to corrosion can be stopped. However, the susceptibility of the alloy to fast FFC attack was reported to be the same as AA6016 when a damaged surface layer is introduced by abrasion.

The mechanism and kinetics of FFC occurring on 6000 series aluminium alloys, when a damaged surface layer is present, are studied in more detail in Chapter 3, whilst possible inhibitor coatings, for use as pre-treatment layers, are examined in Chapter 4.

1.4.3.5 Filiform on Iron: Phase 1 – Mechanism

The initiation and propagation of filiform corrosion (FFC) on polymer-coated iron following contact with aqueous group (I) chloride salts was investigated by Williams and McMurray.[94] They showed that a preceding phase occurs before the

characteristic threadlike filiforms occur. They used *in-situ* Scanning Kelvin Probe (SKP) [an electrochemical scanning technique described in more detail in Section 1.6.2] and *ex-situ* secondary ion mass spectrometry (SIMS) to show that prior to the onset of FFC a circular area of cathodic delamination is observed to grow radially from a penetrative defect. The SKP showed that for 50 hours following electrolyte introduction an approximately circular region of reduced potential centred on the coating defect occurred. It was suggested that this reduced potential represented a cathodic disbondment process. Under these circumstances cathodic O_2 reduction at the delamination front is coupled to anodic dissolution in the vicinity of the coating defect. Williams and McMurray[94] confirmed this hypothesis by initiating FFC with CsCl and incubating for the relevant time (enough for the radial growth). SIMS analysis then identified the delaminated zone to be abundant in Cs^+ ions. Conversely Cl^- ions were most abundant at the coating defect with minimal levels detected at the delamination front.

When an identical experiment was carried out by the same authors, using 0.005M $FeCl_2$ no indication of cathodic disbondment over a 36 hour period was observed. This suggested that iron cations (Fe^{2+} and Fe^{3+}) are incapable of carrying the ionic current of the phase 1 cathodic delamination cell. In the same experiment FFC did become initiated after *ca.* 40 hours and filaments were seen to propagate at a similar rate to those initiated with group (I) chlorides.

The polarity of the disbondment cell discussed above forces anodic activity to remain localised within the penetrative defect. Whilst the group (I) cations are becoming progressively depleted by migration underneath the cathodically delaminating coating, Cl^- anions are conserved in the defect site. Electroneutraility is maintained by Fe^{2+} cations released via anodic dissolution of the iron substrate. As the group (I) cations become exhausted and the delamination rate falls (eventually to zero), Fe^{2+} and Fe^{3+} chlorides at the defect site are now free to trigger the onset of FFC (Phase 2; as described in the next section), that is, subsequent filiform growth. A schematic summary of phase 1 is shown in Fig. 1.11.

Williams *et al*[94] also showed that when filaments eventually extend beyond the boundary of the centrally cathodically delaminated region they continue to grow at a similar rate. This implies that even when the filament head anode (discussed in the next section) is surrounded by a physically large under-film cathode, minimal current is able to pass between them. As such it has been suggested that a preceding cathodic

delamination plays no role in the mechanism of filament advance. The role of cathodic disbondment in the propagation of FFC on iron is investigated further in Chapter 7.

1.4.3.6 Filiform on Iron: Phase 2 – Mechanism

Phase 2 is the subsequent (or in the absence of group (I) metal cations, the initial) growth of the thread-like filaments characteristic of FFC. On iron a clearly defined v-shaped boundary exists between two zones of different colour along the length of a filiform. The head being blue, greenish blue or grey and the back being brown rust coloured as shown in Fig. 1.12. The pH of the head front depends on the type of substrate but usually ranges from pH 1 – 4.[84] The back of the head on steel has been measured by Slabaugh as pH 12.[80] The pH in the tail varies from 3-5 to slightly alkaline.

As with FFC occurring on aluminium, FFC on iron is thought to be initiated at a defect by osmosis[83,96] and the incorporation of a soluble salt in the newly formed electrolyte. The metal substrate is then likely to undergo some corrosion incorporating Fe^{2+} ions into the solution. The development of further electrochemical processes leads to a displacement of oxygen from the point in the small circular droplet where corrosion is occurring. The osmotic pressure postulate for filament initiation was first put forward by Leidheiser[96] and supported by Funke.[91] It had been argued that no significant pressure had been measured in the head of a filament to suggest an osmotic effect. However, Funke[91] refuted this by suggesting that pressure increments were intermittent and followed by rapid straining of the coating film. This idea will be revisited in Chapter 8.

Fig. 1.13 shows a schematic diagram of a filiform head on iron. When the oxygen concentration cell is fully developed the highly effective anode at the front of the head is thought to anodically undermine the coated surface allowing the filament to propagate. A potential gradient exists between the front of the head and the back of the head, thus anions migrate to the front and cations to the back of the head. The head contains the anions of the salt that triggers the attack but not the cations, these anions move with the head. Iron is oxidized in the head as Fe^{2+} according to Equation(1.13).

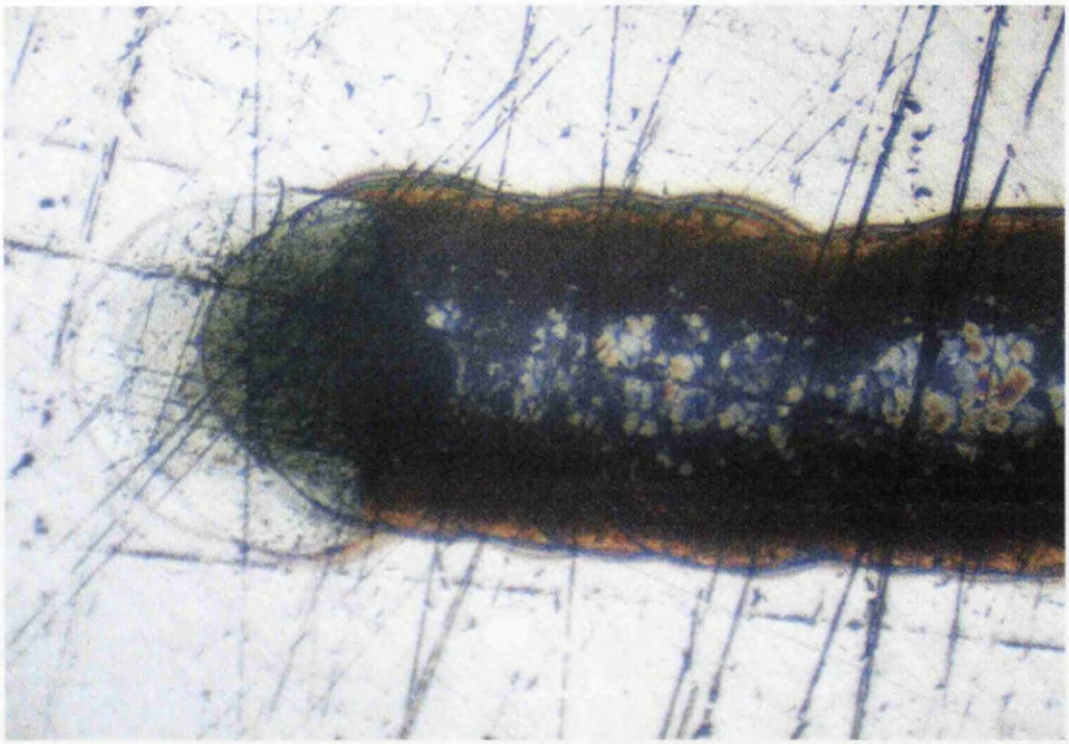

Figure 1.12: Photographic image of filiform corrosion on iron showing the filament head (on the left-hand side of the image) as the blue, greenish blue or grey area and the tail as the brown (rust) coloured area.

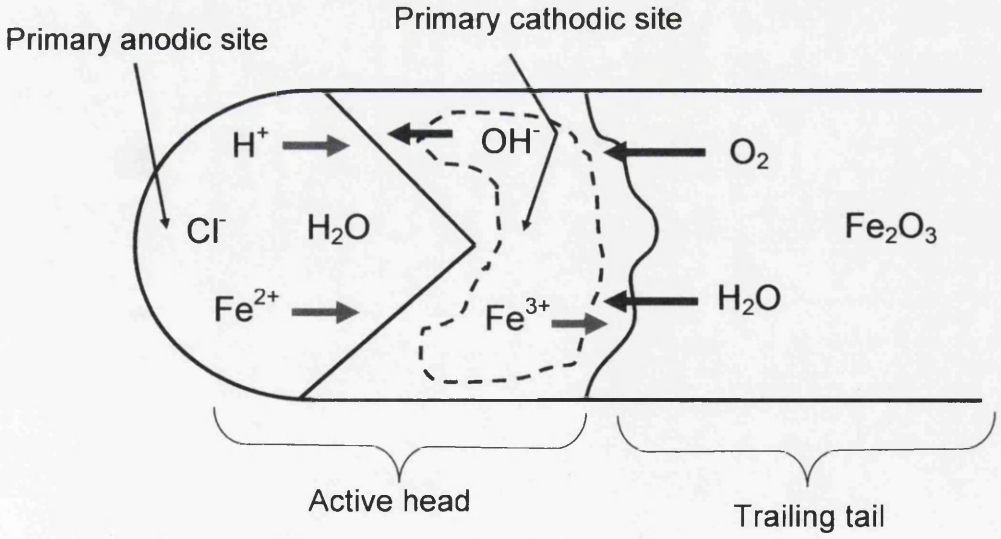

Figure 1.13: Schematic diagram of the current model for filiform corrosion on iron.

$$Fe \rightarrow Fe^{2+} + 2e^{-} \qquad (1.13)$$

The Fe^{2+} cations then migrate to the back of the head where they encounter a higher oxygen concentration due to the directional supply of O_2. Fe^{2+} is then further oxidised to Fe^{3+} by the reaction shown below,

$$4Fe^{2+} + O_2 + 2H_2O \rightarrow 4Fe^{3+} + 4OH^{-} \qquad (1.14)$$

This transition appears as a V-shaped boundary of ferrous and ferric ions and is a variably coloured interface as shown by the schematic in Fig. 1.12. A question exists as to why this boundary is V-shaped. Slabaugh[87] suggests an interesting answer, stating that the shape of the roof of the corrosion cell, shown in Fig. 1.13, as being the reason for the V-shape. Diffusion of equal quantities of atmospheric oxygen through various portions of the film which forms the roof will produce higher concentrations of O_2 in the shallow periphery region of the advancing head than at the centre, as shown in Fig. 1.14. A cross section of Fig 1.14 is shown in Fig. 1.15. Thus the conversion of Fe^{2+} to Fe^{3+} will occur faster at points (A) and (B) than at (C) in Fig. 1.14. Position C will require more time for oxidation to occur and will result in a V-shape at (D).

The hydrolysis of Fe^{3+} ions releases protons which are responsible for the acidity in the head region surrounding the anode. The Fe^{3+} then reacts with OH^{-} formed from the reduction of oxygen, as in Reaction (1.5) to form an intermediate iron hydroxide.

$$Fe^{3+} + 3OH^{-} \rightarrow Fe(OH)_3 \qquad (1.15)$$

As the filament advances the hydrated corrosion products lose water and are converted to the final inert corrosion products seen in the tail - FeOOH, by the reaction shown below.

$$Fe(OH)_3 \rightarrow FeOOH + H_2O \qquad (1.16)$$

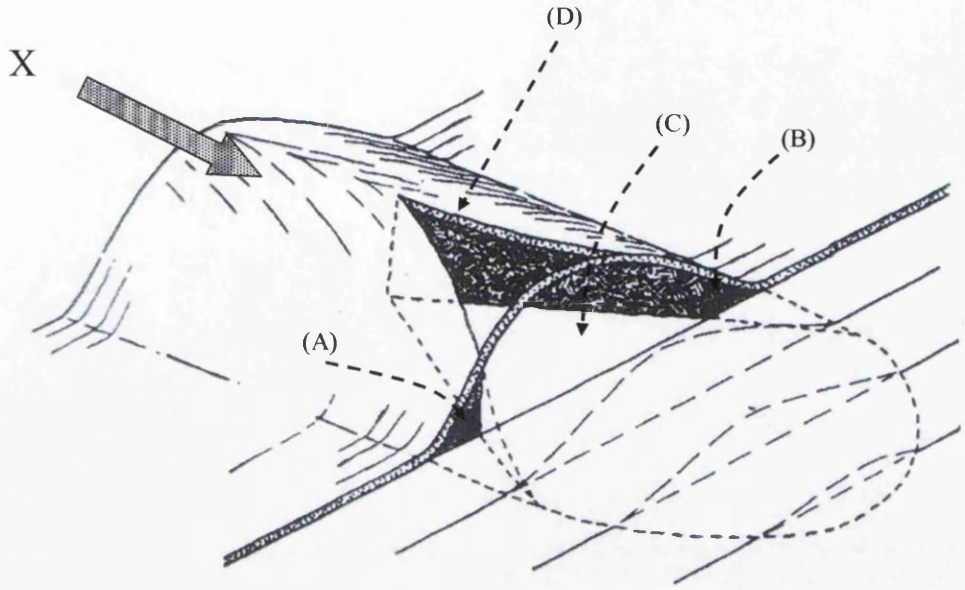

Figure 1.14: Roof of a filiform corrosion cell as proposed by Slabaugh and Grotheer.[87] Diffusion of equal quantities of atmospheric oxygen through various portions of the film mean that higher oxygen concentrations would be present in the shallow periphery regions of the head (A) and (B) than at the centre (C). This results in the V-shape boundary at position (D).

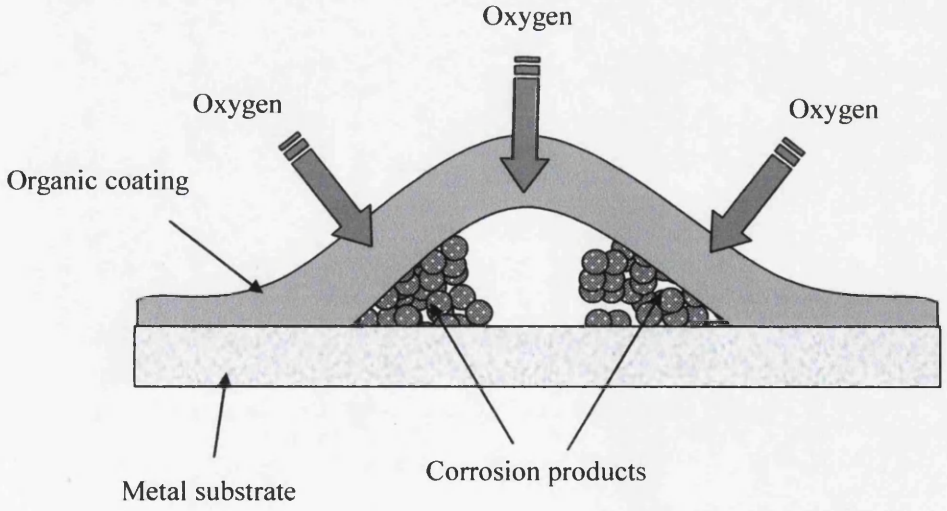

Figure 1.15: Cross-section of filiform corrosion cell as viewed along arrow X from Fig. 1.14. Oxidation of Fe^{2+} to Fe^{3+} occurs faster at the periphery region and thus more $Fe(OH)_3$ corrosion products are deposited here.[87]

1.4.3.7 Alternative Theories for Filiform Corrosion on Iron

There are some theories on the mechanisms of FFC on iron that differ from the postulate given in Section 1.4.3.6. Funke [91,103] disagrees with the anodic undermining mechanism and believes the disbondment of the organic coating is due to the activity of a preceding cathode. The external cathode appears at some distance from the head front and grows due to the concentration of hydroxyl ions under the coating until the trailing filiform head catches up. Upon converging with the head, migration of OH^- ions occurs towards the anode within the filiform head. Conversely, metal cations that were present within the head electrolyte migrate towards the preceding cathode. This results in a polarity change with the leading former cathode now becoming the leading edge of the filiform head and taking on anodic properties. The whole process is then repeated. A schematic representation of this theory is shown in Fig. 1.16. However, Ruggeri and Beck[82] disputed this hypothesis giving the following arguments in response: (i) The cathodic area is symmetric around the head. This is inconsistent with asymmetric separation between the cathodic and anodic zones in the corrosion cell. (ii) No cathodic detachment was observed experimentally in the vicinity of the filaments. Indeed it was confirmed by Koehler[104] who conducted a series of experiments on filiform and cathodic detachment where he did not observe delamination. A later investigation by Koehler does hint at a cathodic detachment which he describes as 'halo detachment' [Recently work carried out by Williams and McMurray[105] suggests the presence of cathodic delamination (as discussed in Section 1.4.3.5) but they refute claims of a small external cathode preceding the filiform head]. (iii) Assuming the cathode directs the reaction, then ionic current must flow from the anode through the coating. The size of the cathode would thus be limited by the high resistance of the protective layers. However, it could be argued that diffusion of ions from the cathodic area to the head actually occurs through a layer of water that might exist at the coating metal interface. This would allow conductivity of orders of magnitude higher than that of a wet paint film. Ruggeri and Beck[82] calculated that the thickness of the aqueous layer required would be 3.5×10^{-5} mm which clearly indicates coating disbondment, however no coating disbondment is observed preceding a filiform head. Furthermore, Hoch[84] described a cathode with a radius ten times that of the head (as shown in Fig. 1.17), which again would have too high a coating resistance for such an area to exist. Ironically 20 years after the dismissal of

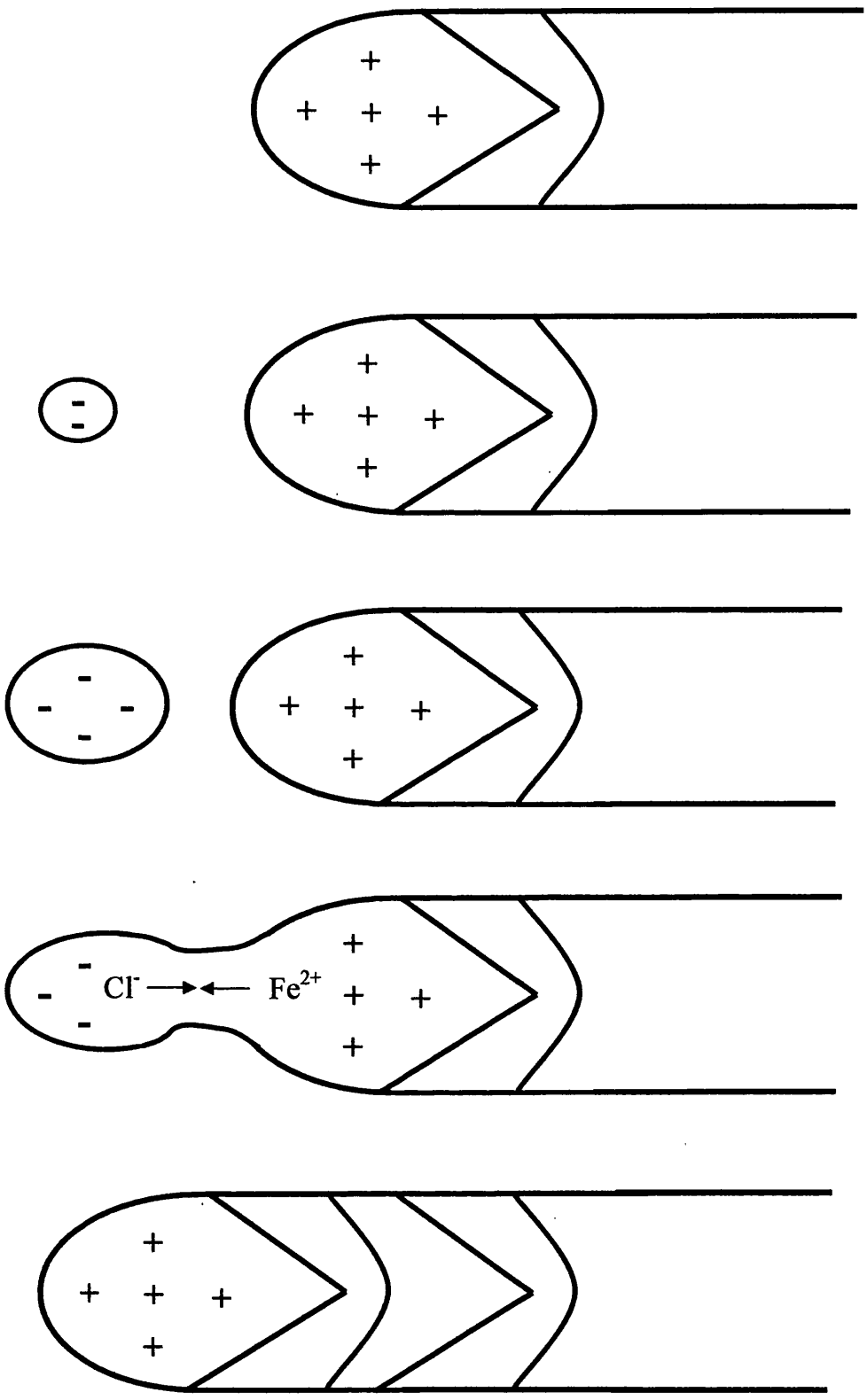

Figure 1.16: Cathodic mechanism of delamination of the protective coating in filiform corrosion as proposed by Funke.[92,103]

Hoch's radial cathode Williams and McMurray[105] used modern electrochemical techniques to confirm its presence although refuting its role as a primary cathode. They used the scanning Kelvin probe (SKP) described in Section 1.6.2 to investigate the initiation and propagation of FFC on iron following contact with aqueous group (1) chloride salts. This work is described above in Section 1.4.3.5.

1.5 Organic Coatings

Coatings have traditionally been used to protect metals from corrosion whilst at the same time provide an aesthetically improved appearance. A large number of materials have been used to achieve this but it is organic coated systems that are primarily used. A major advantage of organic coatings is that they can be used in conjunction with other corrosion prevention methods such as cathodic protection.

In Section 1.3.1 it was shown that there are four essential components that must be available for aqueous corrosion to occur. They are:

i) anode (electron producing)
ii) cathode (electron consuming)
iii) electrolyte (conduction solution)
iv) conductive pathway between anode and cathode

It is therefore essential that for a coating to prevent corrosion, it must prevent at least one of the above conditions from being met. There are a number of factors which will determine how well a coating performs in protecting the underlying metal substrate.[106]

i) Resistance to oxygen and water permeation
ii) Barrier to ion migration through the film, when wet
iii) Large electrical resistance of the coating
iv) Adhesion to the metal, especially when wet
v) Presence of any corrosion inhibitors
vi) Good resistance to attack by an alkali

Initial research into organic coatings centred on the idea that the coating should prevent oxygen and water from reaching the metal substrate. However, it was soon identified that paint films contain water for around half their life in normal conditions

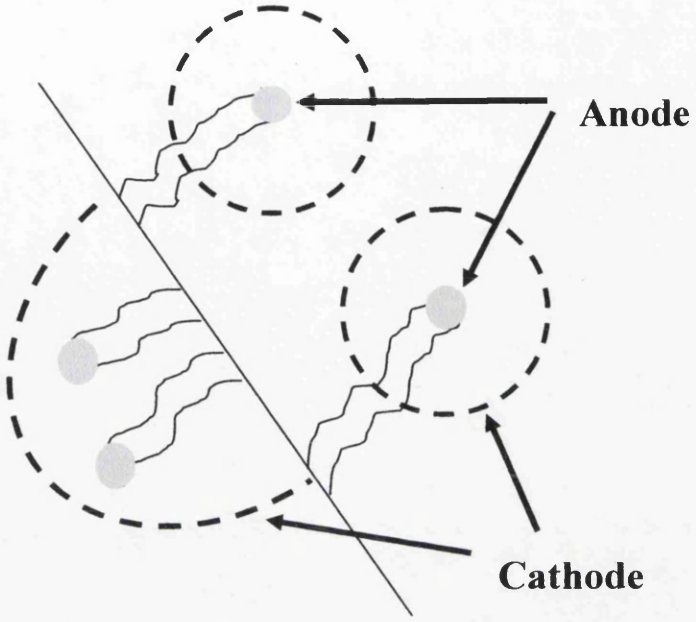

Figure 1.17: Model of the external circular cathode, situated around the anode as proposed by Hoch.[85] The cathodic area is a hundred times bigger than the anodic area.

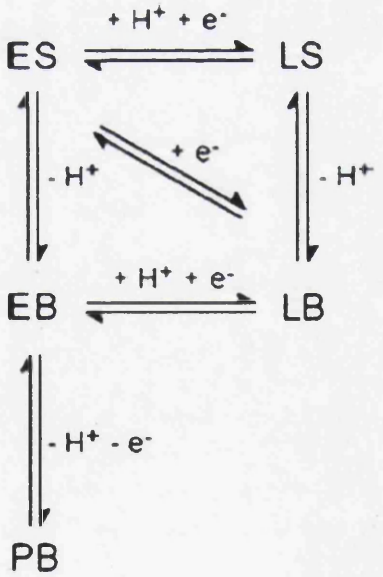

Figure 1.18: Redox and acid-base equilibria in polyaniline: ES = emeraldine salt, LS = leuco salt, EB = emeraldine base, LB = leuco base, and PB = pernigraniline base. The number of protons and electrons shown are for every two aniline residues.

and at all other times the water content was related to the relative humidity of the surrounding environment. This meant that the rate of arrival at the surface was far greater than the amount of water used up during corrosion on an unpainted metal surface. Therefore it can be concluded that water easily diffuses through paint films and that water diffusion is not a rate-determining step. More recently, Leng *et al* [107] studied the presence of water through a polymer coating and concluded that the concentration of water at the metal/polymer interface was far greater than that in the bulk polymer.

Similarly, when the rate of oxygen diffusion was measured it was found that, although slower than that observed on an uncoated metal surface, the reduction did not explain the significantly lower corrosion rates.[108,109] It was thus concluded that oxygen permeability through the paint film was not a rate-determining step.

These early studies suggested that initial ideas on the mechanism whereby a paint film inhibited corrosion by controlling water and oxygen diffusion seemed to be wrong, thus the focus of research shifted to a paints ability to resist ionic movement. A detailed study by Bacon *et al* [110] tested and clarified over 300 paint systems according to their ability to protect the substrate from corrosion by maintaining a high resistance. They used exposure tests combined with *in-situ* DC resistance measurements on panels immersed in salt solution, to try and identify a correlation between coating performance and resistance. They determined that a coating that maintained a resistance of $10^8\ \Omega\ cm^2$ was a good corrosion resistant coating and one that, when exposed, fell rapidly to $10^6\ \Omega\ cm^2$ or below was defined as poor. Coatings between these two extremes were identified as fair. Broadly speaking, the outdoor exposure results matched these designations.

1.5.1 Corrosion Inhibition

It is possible to add pigments to coatings so that the protective nature of the coating is not entirely due to its large resistance. Inhibitive pigments are substances that give inhibitive aqueous products or will react with the binder to give such products. They inhibit either the anodic or cathodic reactions when present in only small amounts in an aqueous environment, with an overall effect of reducing the corrosion rate of the metal exposed to that environment. Corrosion inhibitors are commonly incorporated as pigments into the primer layer which is applied directly to

the metal substrate. Traditionally the delivery mechanism of these anti-corrosion pigments has taken the form of sparingly soluble salts. However, more recently ion exchange pigments have begun to see wider use as a delivery method.[111,112]

1.5.1.1 Anodic Inhibitors

There are two main categories of anodic inhibitors: anodic precipitation inhibitors and oxidizing inhibitors (or cathodic depolarizers). Anodic precipitation inhibitors are anions which form insoluble salts with the metal cations generated at the anodic site. The insoluble salts then form a protective barrier film over the metal surface preventing mass transport to the anode and hence breaking the electrochemical circuit. Examples of this type of inhibitor include chromates (CrO_4^{2-}) and phosphates (PO_4^{3-}).[113]

Oxidising inhibitors have alternative cathodic reactions to oxygen reduction reaction removing electrons from the system, causing a large shift in the free corrosion potential moving the metal into a passive region. A stable insoluble oxide or hydroxide forms on the metal surface which protects against further corrosion.

1.5.1.2 Cathodic Inhibitors

Cathodic inhibitors are generally cathodic precipitation inhibitors. These are cations which form insoluble salts with the hydroxide ions generated by the oxygen reduction process and precipitate as an insoluble film on the cathodic site. The rare earth metals have been shown to be particular effective at this type of inhibition on aluminium aerospace alloys.[114,115]

1.5.2 Polyaniline Coatings

Intrinsically conducting polymers (ICPs) are electroactive, conducting polymers without the addition of a conductive (inorganic) substance and are hence sometimes referred to as "organic metals". There are a number of polymers that fall under the category of ICP and these include: polypyrrole, polythiophene, polyphenylenevinylene and polyaniline (PAni)[116] - the one used in this thesis, and the most heavily documented. PAni exists in various forms as shown in Fig. 1.18 but it is

the Emeraldine salt (ES) which is intrinsically conducting. PAni-ES is produced by protonating or "doping" Emeraldine base (EB) using Brønsted acids.

The mechanism by which PAni controls corrosion on aluminium and its alloys is contentious. However, it is generally agreed that galvanic interaction can occur between aluminium and coatings containing the oxidized and conducting PAni-ES. As a result of this interaction PAni-ES can polarise the underlying aluminium to potentials where the cathodic reactions such as oxygen reduction are greatly suppressed.

Studies have been carried out on Aluminium alloy AA2024 using both PAni-ES[117-121] and PAni-EB[120-123]. However, mixed reports have been published regarding the effectiveness of the two forms of PAni in terms of corrosion inhibition. Epstein *et al* [122] investigated PAni-EB and also a self doped sulfonated polyaniline (SPAN). A film of 20 μm was solvent cast on to AA2024 surfaces and the samples immersed in 0.1M NaCl. The coated samples both exhibited less corrosion than the bare AA2024 sample when examined by visual inspection, potentiodynamic scans and XPS. The XPS studies also revealed that there was a much reduced copper concentration in the top several hundred angstroms of the coated samples as compared to the uncoated sample when studied after 10 and 66 hours. From this they proposed a mechanism whereby PAni-EB or SPAN coatings are dissolving away the copper containing corrosion products thereby eliminating the galvanic couple between copper and aluminium and reducing the corrosion rate. However, no actual evidence is given to support this hypothesis. As there will be extensive copper replating occurring on the surface of the uncoated sample after long periods of immersion it seems entirely feasible that there would be copper enrichment at the surface. Conversely the coated samples will be protected from corrosion by the barrier properties of the coating and thus no corrosion and hence no copper replating or copper enrichment will take place at the metal/polymer interface. Thus it would be entirely expected to see reduced levels of copper upon XPS examination.

Ogurtsov *et al* [123] also report that PAni-EB has an inhibitory effect greater than that of PAni-ES on the corrosion of aluminium alloy AA3003 under immersion conditions. However, subsequent work by Williams and McMurray[120] showed that there was no interaction between a PAni-EB coating and the underlying metal substrate. Therefore the improved protection properties recorded for PAni-EB are

probably due to the enhanced barrier protection provided by the coating and not due to any interaction happening at the polymer/metal interface. From these and other studies[117] it is evident that under immersion conditions and in the absence of a topcoat the protective nature of the PAni coating is temporary. This coating failure is attributed to the reduction of PAni-ES to its non-conducting (and non-oxidising) leuco base form, as shown in Fig. 1.18.

In terms of protection against FFC it is perhaps the presence of the surface oxide film at the aluminium/PAni-ES interface, reported by several authors[117,120,124,125] that is most important. Williams and McMurray [120] show that when PAni-EB was dispersed within an organic coating there was no evidence of oxide film formation at the polymer/aluminium interface and also no ennoblement of the surface potential as recorded using a Scanning Kelvin Probe (see Section 1.6.2 for a full description of this technique). Without the presence of the oxide film no inhibition of FFC was observed. Conversely, when a PAni-ES induced oxide covered surface was re-coated using unpigmented PVB and FFC corrosion was initiated, the recorded area of delamination was an order of magnitude lower than typically observed in the absence of the oxide film. They proposed that the inhibition of FFC by PAni-ES arises principally as a result of the protective nature of the oxide film formed at the metal/polymer interface.

1.6 Scanning Electrochemical Techniques

Great advances have been made in the study kinetics and the mechanisms of corrosion in aqueous environments due to the development of scanning electrochemical techniques. The major advantage of the scanning techniques over previous electrochemical methods such as the polarisation curves described in Section 1.3.5 is their ability to spatially resolve localised corrosion. This allows quantification of the corrosion processes and information on corrosion rates. Previous techniques had tended to provide surface average information for the area exposed to testing.

The techniques basically use a microtip that is not in direct contact with the substrate under investigation to measure quantities (potential gradient, potential, current) that relate to the amount of corrosion activity on the surface. As the microtip is moving across the surface a physical coordinate for each data point is also given allowing the production of electrochemical surface maps. However, the fact that the

microtip is not in direct contact with the surface also provides the biggest disadvantage of the scanning techniques. The data signals received from the microtip are often complicated and inferences have to be made to interpret them and establish surface reactivities. However, as the microtip is not in contact with the surface this also means that the corrosion occurring on the surface under investigation is not affected and thus the scanning procedure can be repeated, allowing a study of the dynamic evolution of localized corrosion processes.

The scanning reference electrode technique (SRET) was the earliest of the scanning methods used to study corrosion in aqueous environments.[126-128] The SRET measures ohmic potentials generated in solution by passage of current from anodes to cathodes using a scanning reference electrode and a remote electrode. Whilst the technique is able to locate and detect anodic events its sensitivity and spatial resolution are somewhat limited.[126]

The scanning vibrating reference electrode technique (SVRET) is a derivative of the scanning reference electrode technique (SRET).[127] The difference is that the scanning micro-tip is vibrated relative to the sample surface and more often than not is a pseudo reference electrode and is thus abbreviated to SVET.[126] The technique has the ability to directly measure components of corrosion current density when spatially resolving areas of dissimilar electrochemical activity, which is a distinct advantage over the SRET technique. SVET also offers improved sensitivity and improved spatial resolution.[126]

Of these two techniques it is only the SVET that can give us limited information on the performance of organically coated metal substrates. However, a third technique, the scanning Kelvin probe technique (SKP) has also been developed. As an electrochemical technique the SKP is practically unique in that it does not require the presence of a bulk electrolyte and is capable of measuring localised free corrosion potentials (E_{corr}) beneath humidity films and/or polymer coatings. The SKP uses a vibrating capacitor method to measure the work function difference between a conducting sample and a microtip.

Of the scanning techniques mentioned here only the SVET and the SKP are used in this thesis and are therefore described in more detail in the following sections.

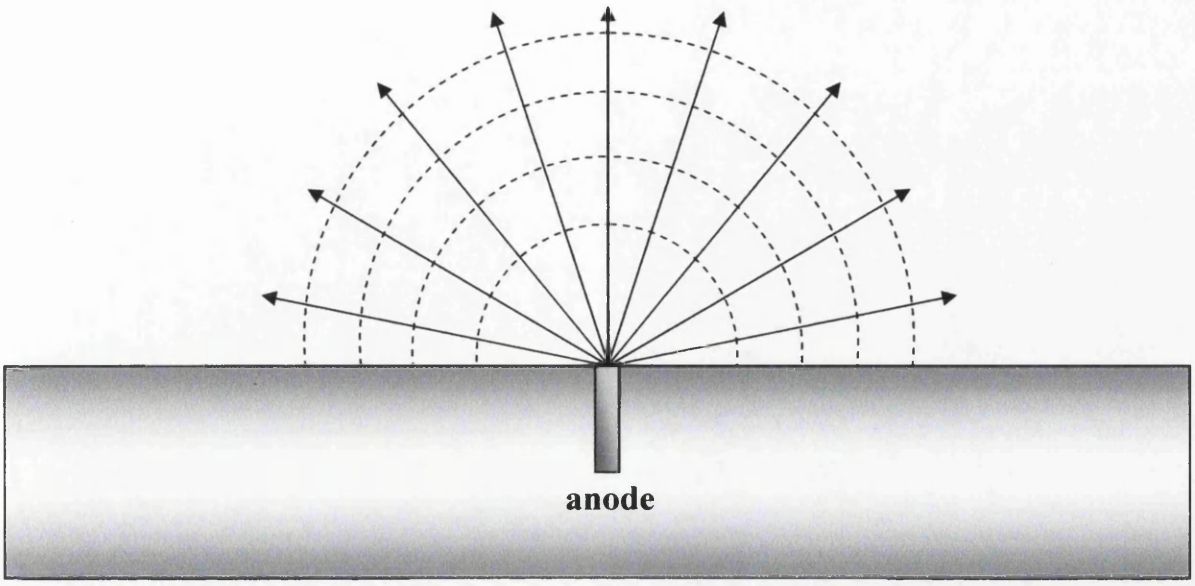

Figure 1.19: Schematic diagram showing lines of ionic current flux emanating from a localised anode setting up lines of iso-potential. The cathode in this instance is assumed to be "remote" giving radial distribution of current flux.

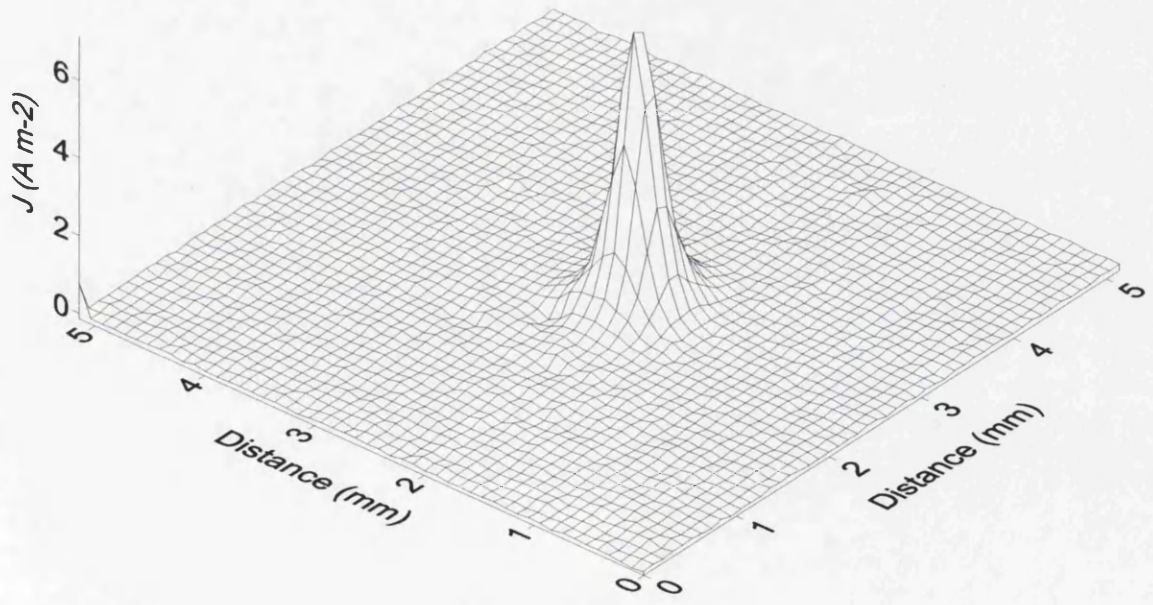

Figure 1.20: A typical experimental 3D SVET calibration plot of the point source cell.

1.6.1 Scanning Vibrating Electrode Technique

When immersed in an electrolyte localised corrosion can occur on a metal surface. If this happens the ionic current will flow from the more localised anodic features to the more general cathodic surface areas. The SVET measures ohmic potential differences in solution above a local corrosion cell. These potential differences arise because of the radially distributed ionic current flux generated by the localised anode of the cell, illustrated schematically in Fig. 1.19. The circuit is completed by electron flow through the metal substrate which has negligible resistance and is thus considered as a plane of constant potential. The aqueous electrolyte has a relatively high resistance, when compared with the bulk metal. This generates ohmic potential gradients within the electrolyte due to the passage of ionic currents. These are shown diagrammatically as iso-potential lines lying normal to the lines of ionic flux in Fig. 1.19.

The distribution of the current flux and lines of iso-potential gradient can be determined using the Laplace equation,[128]

$$\nabla^2 E = 0 \tag{1.17}$$

where E = electrical potential, and Ohm's law,

$$i = -\kappa \nabla E \tag{1.18}$$

where i = current and κ = solution conductivity.

However, analytical solutions to this problem are non-trivial and it is only when a point source model is considered that a solution can be obtained. If a point current source, i, is considered, situated at height z = 0 on a non-conducting x,y plane with the current drain at infinity it may be shown that the potential at any point (x,y,z) in solution is inversely proportional to the distance from the source and is given by,[129]

$$E = \frac{\mathrm{i}}{2\pi\kappa\sqrt{(\mathrm{x}^2 + \mathrm{y}^2 + \mathrm{z}^2)}} \tag{1.19}$$

When using the SVET technique the scanning microtip electrode is mechanically vibrated, via a loudspeaker, above the surface of the sample at constant amplitude. As the microtip electrode is oscillated through the lines of iso-potential in the solution, a potential difference at the vibration frequency is generated in the microtip. As this potential field is generated ohmically by the ionic current flux, the SVET signal is directly proportional to the normal component of ionic current density. As the microtip resides at a set distance above the corroding surface (*ca.* 100 μm in this work) it should be remembered that the signal measured is not proportional to the surface current density but rather the vector component of the current density in the electrolyte at the height of the probe.

For the anodic point current source described previously the normal electric field strength (F) measured by vibrating the SVET probe perpendicular to the sample surface is given by the z differential of Equation (1.19)[129] and hence,

$$F = \frac{dE}{dz} = \frac{iz}{2\pi\kappa(x^2 + y^2 + z^2)^{1.5}} \tag{1.20}$$

Furthermore, the maximum field strength (F_{max}) will be obtained when the SVET electrode is directly over the point source ($x = y = 0$):

$$F_{max} = \frac{i}{2\pi\kappa z^2} \tag{1.21}$$

A typical experimental SVET scan of a calibration point source is shown in Fig. 1.20 and shows the characteristically peaked shape that is centred over the current source. Equation (1.21) highlights that there is an inverse square relationship between maximum field strength (F_{max}) and probe height and thus control of probe height above the surface of a sample is critical. If the overall measurement is calibrated into current density units, this problem is removed and as such integrated SVET current density maps can be used for semi-quantitative measurements.

Spatial resolution is of great importance in assessing the localisation of corrosion features. The spatial resolution of the probe represents the minimum distance between two features that can be detected by the microtip. Theoretical spatial resolution of the SVET is determined by calculating the signal peak width at

half maximum peak height (*whm*). Considering a quantity r as the distance from a point current source on the x,y plane then,

$$r = (x^2 + y^2)^{0.5} \tag{1.22}$$

The value of r where F is equal to half the maximum value is found by combining equations (1.21) and (1.22), and thus,

$$0.5F_{max} = \frac{iz}{2\pi\kappa(r^2 + z^2)^{1.5}} \tag{1.23}$$

The ratio of equations (1.20) and (1.22) gives,

$$r = z(2^{2/3} - 1)^{0.5} \tag{1.24}$$

and the width of the SVET response peak is $2r$ hence,

$$whm = 2r = 1.533z \tag{1.25}$$

This shows that the limiting spatial resolution of the SVET is 1.533z.[129] Thus for a scanning height of 100μm the theoretical spatial resolution of the SVET is 153 μm. However, such resolution is difficult to achieve practically, due to the finite dimensionality of the microtip itself, typically 125 μm, and thus practical spatial resolution is generally around 100μm higher than the theoretical value. Therefore, features separated by a distance < ~225 mm will not be resolved individually by the SVET.

1.6.1.1 SVET Applications

The SVET has been used extensively in the investigation of localised corrosion and has been shown to be an effective tool for studying pitting corrosion on carbon-steel[130-133] and aluminium alloys.[78,134-137] Perhaps most importantly in terms of its use in this thesis, the SVET has been used effectively to investigate pitting

corrosion inhibitors on AA2024-T3. Aldykewicz *et al*[115] showed that in chloride containing solutions cerium inhibits corrosion of AA2024-T3 by reducing the rate of the cathodic reaction. This is due to the formation of cerium-rich films over copper containing intermetallics which act as local cathodic sites.

Tallman *et al* have also used the SVET to determine the effectiveness of Poly(3-octyl pyrrole) (a conducting polymer much like polyaniline, as discussed in Section 1.5.2) for corrosion control on AA2024-T3.[135,136]

1.6.2 Scanning Kelvin Probe Technique

The Scanning Kelvin Probe is based on work pioneered by William Thomson (later Lord Kelvin) in 1898[138], to measure the work function of a surface. The Work function is the minimum work required to extract an electron through a conducting phase to a surface. Under certain circumstances the work function is determined by the electrode potential and therefore the Kelvin probe is able to measure local electrode or corrosion potentials. These can then be used to produce a map of corrosion potentials existing on a surface. The major advantage of the SKP over SVET and many other electrochemical techniques is that it does not require either the presence of a bulk electrolyte or that any conducting pathway exists between the probe and the sample surface.[139-141] Therefore, unlike conventional reference electrode techniques, SKP is able to measure atmospheric corrosion that is occurring both *in-situ* and under intact organic coatings.

1.6.2.1 SKP Principles

The Kelvin probe can be described as a parallel plate capacitor with the metallic wire and the sample surface acting as the plates and the air gap separating them as the dielectric medium, as shown schematically in Fig. 1.21. One metal plate is covered with an electrolyte layer (known as the sample) and the other which vibrates, generally Au wire, is known as the vibrating probe electrode. The metals are connected by a conducting wire. When the surface is charged, a Volta potential, Ψ, exists between the surface electrolyte and the Au tip forming a capacitor.

The gold wire is vibrated via an actuator causing a change in the distance between the probe and sample and thus a corresponding variation in the capacitance

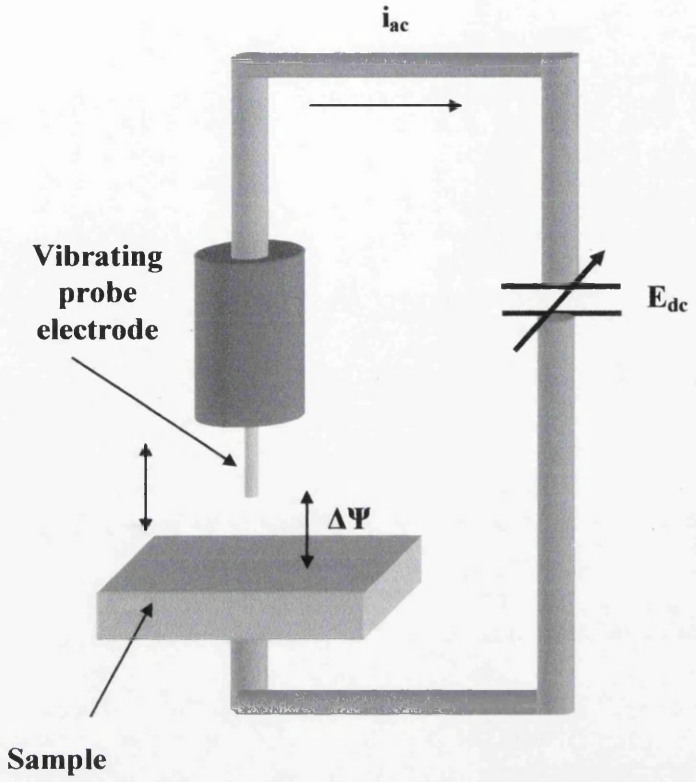

Figure 1.21: Schematic diagram of parallel plate capacitor Scanning Kelvin Probe.

across the air gap, so that an alternating current is set up in the circuit. The magnitude of this AC is dependent on the potential difference, $\Delta\psi_{\text{Sample}}^{\text{Ref}}$ between the sample and the reference probe, across the gap. The AC current, i_{ac}, is then given by[141]

$$i_{ac} = \frac{dQ}{dt} = \Delta\psi_{\text{Sample}}^{\text{Ref}} \frac{dC}{dt} \tag{1.26}$$

where Q is the electric charge on the plates and C is the capacitance. For a capacitor with parallel plates of area A, the distance between which changes sinusoidally, (as the probe is vibrated relative to the sample surface) such that the plate separation, d, is given by

$$d = d_0 + d_1 \sin(\omega t) \tag{1.27}$$

and capacitance is given by

$$C = \frac{\varepsilon\varepsilon_0 A}{d} \tag{1.28}$$

where d_0 is the average distance between the plates, d_1 the maximum amplitude of the vibration, ω frequency, ε_0 the permittivity of vacuum, and ε the dielectric of air.

The magnitude of the current can be used to determine $\Delta\Psi$ but because of the number of variables in this equation a more effective method is to apply a reverse bias voltage E reducing the signal current to 0. Under null conditions and for simplicity this is identified as the "Kelvin Probe Potential" and is designated as the E_{kp} value, such that

$$-E = E_{kp} = \Delta\psi_{\text{Sample}}^{\text{Ref}} \tag{1.29}$$

The E_{kp} value is then proportional to the corrosion potential of the metal specimen.[140] This proportionality will be explained in more detail in Section 2.5.4, but it is shown that[107,140]

$$E_{corr} \approx const + \Delta\psi_{El}^{Ref} \quad (1.30)$$

1.6.2.2 SKP Applications

In terms of corrosion the Kelvin probe technique was first applied by Stratmann[140] to study the kinetics of metals surfaces (iron and iron-copper alloy) covered by ultra thin electrolyte layers. A Kelvin probe was used to measure the corrosion potential at a point on a metal surface covered by a progressively thinner electrolyte layer. As the surface of the metal gradually dried, *i.e.* the electrolyte thinned, the rate of corrosion (shown by E_{kp} as measured by the SKP) at first increased and then subsided over time. As the rate of corrosion increases, the O_2 reduction is accelerated. The O_2 consumption was simultaneously measured using a differential pressure meter. Over time, passivation of the metal surface due to the build up of corrosion products occurs and the corrosion rate is reduced. Using these combined techniques, that is, the corrosion potential as measured by the Kelvin Probe and the decay of the partial pressure in a closed volume, it was possible to identify the corrosion rate of the system. It was shown that this is determined by 3 competing reactions:-

(a) The acceleration of diffusion limited reduction at the start of the wet-dry process.

(b) The passivation of the surface as drying continues.

(c) The decrease of the rate of oxygen reduction during the last stage of drying.

Further investigations were performed in this area over a number of years by Stratmann and others and forms the basis of the model for atmospheric corrosion.[139,142,143]

The technique was developed further by Stratmann and it was shown that the SKP could be used for identifying the electrochemical processes at metal / coating interfaces.[141] It was also shown that the SKP could be used as an *in-situ*, non-invasive way of determining corrosion induced delamination of a polymer coating from a metal substrate. Thus followed a series of work by several groups reporting on the corrosion inhibition properties of various coating systems primarily on iron and

steel.[107,111,144-147] However, studies have also been carried out on other substrates such as zinc[148,149] and aluminium.[88,94,97,98,150,151]

In terms of this thesis, it is the application of the SKP to study the mechanisms and kinetics of FFC that is perhaps most important. It has been shown that it is possible to use the SKP to identify individual filament heads and their associated free corrosion potentials.[97,98,150] Also, by repeatedly scanning *in-situ* it is possible to produce a series of time-dependent corrosion potential, E_{corr} maps.[94,95] These provide information on the initiation of FFC and can be used to generate kinetic data associated with filiform propagation.

The SKP has also been used in many other fields of study including semiconductor doping, organic semiconductors, biological systems, and heterogeneous catalysis.[152-155] Perhaps one of the most exciting possible future applications of the SKP is in the field of forensic science for the detection of latent fingerprints.[156]

1.7 References

1. S. Wernick, R. Pinner and P. G. Sheasby, The Surface Treatment and Finishing of Aluminium and its Alloys, Finishing Publicationsr Ltd, UK (1987).

2. The International Aluminium Institute, http://www.world-aluminium.org/production/index.html, Date accessed: 15/02/2006

3. J. R. Davies, Aluminum and Aluminum Alloys; prepared under the direction of the ASM International Handbook Committee, Materials Park, OH (1993).

4. http://www.direct.gov.uk/en/Motoring, Date accessed: 15/02/2007

5. A. Afseth, Metallurgical Control of Filiform Corrosion of Aluminium Alloys, 1999

6. A. Afseth, J. H. Nordlien, G. M. Scamans and K. Nisancioglu, *Corros. Sci.*, **43**, 2093 (2001).

7. A. Afseth, J. H. Nordlien, G. M. Scamans and K. Nisancioglu, *Corros. Sci.*, **43**, 2359 (2001).

8. A. Afseth, J. H. Nordlien, G. M. Scamans and K. Nisancioglu, *Corros. Sci.*, **44**, 145 (2002).

9. A. Afseth, J. H. Nordlien, G. M. Scamans and K. Nisancioglu, *Corros. Sci.*, **44**, 2491 (2002).

10. A. Afseth, J. H. Nordlien, G. M. Scamans and K. Nisancioglu, *Corros. Sci.*, **44**, 2529 (2002).

11. A. Afseth, J. H. Nordlien, G. M. Scamans and K. Nisancioglu, *Corros. Sci.*, **44**, 2543 (2002).

12. R. Ambat, A. J. Davenport, A. Afseth and G. Scamans, *J. Electrochem. Soc.*, **151**, B53 (2004).

13. H. Leth-Olsen, A. Afseth and K. Nisancioglu, *Corros. Sci.*, **40**, 1195 (1998).

14. H. Leth-Olsen and K. Nisancioglu, *Corros. Sci.*, **40**, 1179 (1998).

15. H. Leth-Olsen, J. H. Nordlien and K. Nisancioglu, *Corros. Sci.*, **40**, 2051 (1998).

16. M. Fishkis and J. C. Lin, *Wear*, **206**, 156 (1997).

17. A. Porter and K. E. Easterling, Phase Transformations in Metals and Alloys, (1992).

18. L. F. Mondolfo, Aluminium alloys : structure and properties, London (1976).

19. R. G. Buchheit, R. P. Grant, P. F. Hlava, B. McKenzie and G. L. Zender, *J. Electrochem. Soc.*, **144**, 2621 (1997).

20. K. R. Trethewey and J. Chamberlain, Corrosion for Science and Engineering, (1988).

21. W. R. Witney, *J. Am. Chem. Soc.*, **25**, 395 (1903).

22. M. Pourbaix, Atlas of Electrochemical Equilibria in aqueous solutions, Pergamon Press, Oxford (1966).

23. P. Van Rysselburg, *Electrochem. Acta*, **9**, 1343 (1964).

24. R. Parsons, *Pure Appl. Chem.*, **37**, 512 (1974).

25. J. O. M. Bockris, Modern Aspects of Electrochemsitry, J. O. M. Bockris and B. E. Conway, (1954).

26. C. Wagner and W. Traud, *Z. Electrochem.*, **44**, 391 (1938).

27. J. Tafel, *Z. Physik. Chem.*, **50**, 641 (1905).

28. T. Ramgopal, P. I. Gouma and G. S. Frankel, *Corrosion*, **58**, 687 (2002).

29. T. Ramgopal, P. Schmutz and G. S. Frankel, *J. Electrochem. Soc.*, **148**, B348 (2001).

30. G. Svenningsen, J. E. Lein, A. Bjorgum, J. H. Nordlien, Y. D. Yu and K. Nisancioglu, *Corros. Sci.*, **48**, 226 (2006).

31. G. Svenningsen, M. H. Larsen, J. C. Walmsley, J. H. Nordlien and K. Nisancioglu, *Corros. Sci.*, **48**, 1528 (2006).

32. G. Svenningsen, M. H. Larsen, J. H. Nordlien and K. Nisancioglu, *Corros. Sci.*, **48**, 258 (2006).

33. G. Svenningsen, M. H. Larsen, J. H. Nordlien and K. Nisancioglu, *Corros. Sci.*, **48**, 3969 (2006).

34. A. Shi, B. A. Shaw and E. Sikora, *Corrosion*, **61**, 534 (2005).

35. A. Perovic, D. D. Perovic, G. C. Weatherley and D. J. Lloyd, *Scripta Mater.*, **41**, 703 (1999).

36. G. Svenningsen, M. H. Larsen, J. H. Nordlien and K. Nisancioglu, *Corros. Sci.*, **48**, 258 (2006).

37. N. Birbilis and R. G. Buchheit, *J. Electrochem. Soc.*, **152**, B140 (2005).

38. J. R. Davies, Metals Handbook, ASM International, Ohio (1987).

39. K. Urushino and K. Sugimoto, *Corros. Sci.*, **19**, 225 (1979).

40. R. Ambat and E. S. Dwarakadasa, *J. Appl. Electrochem.*, **24**, 911 (1994).

41. T. J. Warner, M. P. Schmidt, F. Sommer and D. Bellot, *Zeitschrift Fur Metallkunde*, **86**, 494 (1995).

42. P. Leblanc and G. S. Frankel, *J. Electrochem. Soc.*, **149**, B239 (2002).

43. J. O. Park, C. H. Paik, Y. H. Huang and R. C. Alkire, *J. Electrochem. Soc.*, **146**, 517 (1999).

44. I. L. Muller and J. R. Galvele, *Corros. Sci.*, **17**, 179 (1977).

45. J. R. Galvele and De Micheli.S.M, *Corros. Sci.*, **10**, 795 (1970).

46. R. G. Buchheit, *J. Electrochem. Soc.*, **142**, 3994 (1995).

47. R. G. Buchheit, M. A. Martinez and L. P. Montes, *J. Electrochem. Soc.*, **147**, 119 (2000).

48. N. Dimitrov, J. A. Mann, M. Vukmirovic and K. Sieradzki, *J. Electrochem. Soc.*, **147**, 3283 (2000).

49. M. B. Vukmirovic, N. Dimitrov and K. Sieradzki, *J. Electrochem. Soc.*, **149**, B428 (2002).

50. T. Suter and R. C. Alkire, *J. Electrochem. Soc.*, **148**, B36 (2001).

51. Z. Szklarska-Smialowska, *Corros. Sci.*, **41**, 1743 (1999).

52. O. Schneider, G. O. Ilevbare, J. R. Scully and R. G. Kelly, *J. Electrochem. Soc.*, **151**, B465 (2004).

53. T. J. R. Leclere and R. C. Newman, *J. Electrochem. Soc.*, **149**, B52 (2002).

54. M. A. Jakab, D. A. Little and J. R. Scully, *J. Electrochem. Soc.*, **152**, B311 (2005).

55. H. H. Uhlig, Corrosion Handbook, New York (1948).

56. P. Hulser, U. A. Kruger and F. Beck, *Corros. Sci.*, **38**, 47 (1996).

57. K. Nisancioglu, K. Y. Davanger, O. Strandmyr and H. Holtan, *J. Electrochem. Soc.*, **128**, 1523 (1981).

58. P. Hulser and F. Beck, *Aluminum*, **67**, 999 (1991).

59. J. O. M. Bockris and S. U. M. Khan, Surface Electrochemistry, Plenum Press, New York (1993).

60. B. Mazurkiewicz and A. Piotrowski, *Corros. Sci.*, **23**, 697 (1983).

61. R. P. Wei, C. M. Liao and M. Gao, *Metallurgical and Materials Transactions a-Physical Metallurgy and Materials Science*, **29**, 1153 (1998).

62. A. Kolics, A. S. Besing and A. Wieckowski, *J. Electrochem. Soc.*, **148**, B322 (2001).

63. L. Xia, E. Akiyama, G. Frankel and R. McCreery, *Journal of the Electrochemical Society*, **147**, 2556 (2000).

64. J. Zhao, R. L. McCreery, G. S. Frankel and F. Allen, *Abstr. Pap. Am. Chem. Soc.*, **220**, 163 (2000).

65. J. V. Kloet, W. Schmidt, A. W. Hassel and M. Stratmann, *Electrochimica Acta*, **48**, 1211 (2003).

66. P. Schmutz and G. S. Frankel, *Journal of the Electrochemical Society*, **146**, 4461 (1999).

67. G. O. Ilevbare and J. R. Scully, *J. Electrochem. Soc.*, **148**, B196 (2001).

68. A. Sehgal, D. Lu and G. S. Frankel, *J. Electrochem. Soc.*, **145**, 2834 (1998).

69. H. A. Katzman, G. M. Malouf, R. Bauer and G. W. Stupian, *Applied Surface Science*, **2**, 416 (1979).

70. D. Chidambaram, C. R. Clayton and G. P. Halada, *J. Electrochem. Soc.*, **150**, B224 (2003).

71. P. M. Natishan, E. McCafferty and G. K. Hubler, *J. Electrochem. Soc.*, **133**, 1061 (1986).

72. P. M. Natishan, E. McCafferty and G. K. Hubler, *J. Electrochem. Soc.*, **135**, 321 (1988).

73. E. McCafferty, *Corros. Sci.*, **37**, 481 (1995).

74. N. Mikami, M. Sasaki, T. Kikuchi and T. Yasunaga, *J. Phys. Chem.*, **87**, 5245 (1983).

75. N. Spanos, S. Slavov, C. Kordulis and A. Lycourghiotis, *Langmuir*, **10**, 3134 (1994).

76. C. H. Wu, S. L. Lo and C. F. Lin, *Colloids and Surfaces a-Physicochemical and Engineering Aspects*, **166**, 251 (2000).

77. M. Kendig, R. Addison and S. Jeanjaquet, *J. Electrochem. Soc.*, **146**, 4419 (1999).

78. A. M. Cabral, W. Trabelsi, R. Serra, M. F. Montemor, M. L. Zheludkevich and M. G. S. Ferreira, *Corros. Sci.*, **48**, 3740 (2006).

79. C. F. Sharman, *Nature*, **153**, 621 (1944).

80. W. H. Slabaugh, W. Dejager, S. E. Hoover and J. Hutchinson, *Paint Tech.*, **44**, 76 (1972).

81. A. Bauista, *Prog. Org. Coat.*, **28**, 49 (1996).

82. R. T. Ruggeri and T. R. Beck, *Corrosion-NACE*, **39**, 452 (1983).

83. H. J. W. Lenderink, *PhD. Thesis* (1995).

84. G. M. Hoch, *NACE*, 134 (1974).

85. H. Kaeshe, *Werks. Korros.*, **10**, 668 (1959).

86. Morita J and Y. M, *Corrosion*, **50** (1994).

87. W. H. Slabaugh and M. Grotheer, *Ind. Eng. Chem.*, **46**, 1014 (1954).

88. N. LeBozec, D. Persson, A. Nazarov and D. Thierry, *J. Electrochem. Soc.*, **149**, B403 (2002).

89. M. Van Loo, D. D. Laiderman and R. R. Bruhn, *Corrosion*, **9**, 277 (1953).

90. G. M. Scamans, A. Afseth, G. E. Thompson, Y. Liu and X. Zhou, *Mater. Sci. Forum*, **519 - 521**, 647 (2006).

91. W. Funke, *Prog. Org. Coat.*, **9**, 29 (1981).

92. M. Huisert, PhD. Thesis, Electrochemical Characterisation of Filiform Corrosion on Aluminium Rolled Products, Delft University of Technology, The Netherlands, 2001

93. G. Williams and H. N. McMurray, *J. Electrochem. Soc.*, **148**, B377 (2001).

94. G. Williams and H. N. McMurray, *J. Electrochem. Soc.*, **150**, B380 (2003).

95. G. Williams, H. N. McMurray, D. Hayman and P. C. Morgan, *Phys. Chem. Comm.*, **6**, 1 (2001).

96. H. Leidheiser, *NACE*, **38(7)**, 374 (1982).

97. G. Grundmeier, W. Schmidt and M. Stratmann, *Electrochem. Acta*, **45**, 2215 (2000).

98. W. Schmidt and M. Stratmann, *Corros. Sci.*, **40**, 1441 (1998).

99. N. LeBozec, D. Persson and D. Thierry, *J. Electrochem. Soc.*, **151**, B440 (2004).

100. A. Afseth, PhD. Thesis, Metallurgical Control of Filiform Corrosion of Aluminium Alloys, Norwegian University of Science and Technology, 1999

101. G. M. Scamans, A. Afseth, G. E. Thompson and X. Zhou, *Mater. Sci. Forum*, **396-402**, 1461 (2002).

102. G. Scamans, A. Afseth, G. E. Thompson and X. Zhou, *DFO/DGO Conference on Light Alloy Applications, Dusseldorf* (2004).

103. W. Funke, *Ind. Eng. Chem. Prod. Res. Dev*, **24**, 343 (1985).

104. E. L. Koehler, *Corrosion-NACE*, **33**, 209 (1977).

105. G. Williams and H. N. McMurray, *Electrochem. Comm.*, **5**, 871 (2003).

106. R. R. Wiggle, A. G. Smith and J. V. Petrocelli, *J. Paint. Tech.*, **44**, 174 (1968).

107. A. Leng, H. Streckel and M. Stratmann, *Corros. Sci.*, **41**, 547 (1999).

108. A. P. Anderson and K. A. Wright, *33*, 991 (1941).

109. D. W. Davies, *Mod. Packaging*, **19**, 145 (1946).

110. C. R. Bacon, J. J. Smith and R. M. Rugg, *Ind. Eng. Chem.*, **40**, 161 (1948).

111. M. Loveridge, PhD. Thesis, The Scanning Kelvin Probe Applied to Mechanisms of Delamination in Organic Coated Steels, University of Wales-Swansea, 2004

112. T. Watson, EngD. Thesis, University of Wales - Swansea, 2006
113. E. Matteson, Basic Corrosion Technology for Scientists and Engineers, (1996).
114. S. O'Driscoll, *PhD. Thesis.*
115. A. J. Aldykiewicz, H. S. Isaacs and A. J. Davenport, *J. Electrochem. Soc.*, **142**, 3342 (1995).
116. D. E. Tallman, G. Spinks, A. Dominis and G. G. Wallace, *J. Solid-State Electrochem.*, **6**, 73 (2002).
117. D. E. Tallman, Y. Pae and G. P. Bierwagon, *Corrosion*, **56** (2000).
118. J. C. Seegmiller, J. E. Pereira da Silva, D. A. Buttry, S. I. Cordoba de Torresi and R. M. Torresi, *J. Electrochem. Soc.*, **152**, B45 (2005).
119. S. F. Cogan, M. D. Gilbert, G. L. Holleck, J. Ehrlich and M. H. Jilson, *J. Electrochem. Soc.*, **147**, 2143 (2000).
120. G. Williams and H. N. McMurray, *16th Inter. Corrosion Congress Proc.*, **Paper P-18 C-29** (2005).
121. R. J. Holness, *PhD. Thesis* (2003).
122. A. J. Epstein, J. A. O. Smallfield, H. Guan and M. Fahlman, *Synthetic Met.*, **102**, 1374 (1999).
123. N. A. Ogurtsov, A. A. Pud, P. Kamarchik and G. S. Shapoval, *Synthetic Met.*, **143**, 43 (2004).
124. K. G. Conroy and C. B. Breslin, *Electrochim. Acta*, **48**, 721 (2003).
125. R. Racicot, R. Brown and S. C. Yang, *Synthetic Met.*, **85**, 1263 (1997).
126. H. N. McMurray and D. A. Worsley, Scanning Electrochemical Techniques for the Study of Localised Metallic Corrosion Research in Chemical Kinetics, R. R. Compton and G. Hancock, (1997).
127. L. J. Gainer and G. R. Wallwork, *NACE*, **35** (1979).
128. H. S. Isaacs and B. Vyas, *Electrochemical Corrosion Testing, ASTM special technical publication*, **727**, 3 (1981).
129. H. S. Isaacs, *J. Electrochem. Soc.*, **138**, 722 (1991).
130. H. N. McMurray, S. M. Powell and D. A. Worsley, *British Corrosion Journal*, **36**, 42 (2001).
131. M. J. Franklin, D. C. White and H. S. Isaacs, *Corros. Sci.*, **33**, 251 (1992).
132. M. J. Franklin, D. C. White and H. S. Isaacs, *Corros. Sci.*, **32**, 945 (1991).
133. G. Williams and H. N. McMurray, *Corrosion*, **62**, 231 (2006).

134. D. Battocchi, J. He, G. P. Bierwagen and D. E. Tallman, *Corros. Sci.*, **47**, 1165 (2005).

135. J. He, D. E. Tallman and G. P. Bierwagen, *J. Electrochem. Soc.*, **151**, B644 (2004).

136. J. He, V. J. Gelling, D. E. Tallman and G. P. Bierwagen, *J. Electrochem. Soc.*, **147**, 3661 (2000).

137. J. He, V. J. Gelling, D. E. Tallman, G. P. Bierwagen and G. G. Wallace, *J. Electrochem. Soc.*, **147**, 3667 (2000).

138. W. T. Kelvin, *Philos. Mag*, **46** (1898).

139. M. Stratmann, *Corros. Sci.*, **30**, 681 (1990).

140. M. Stratmann, *Corros. Sci.*, **27**, 869 (1987).

141. Y. Shelgon, R. A. Oriani and M. Stratmann, *J. Electrochem. Soc.*, **138**, 55 (1991).

142. M. Stratmann, *Corros. Sci.*, **30**, 697 (1990).

143. M. Stratmann, K. T. Kim and S. Crockett, *Corros. Sci.*, **30**, 715 (1990).

144. M. Stratmann, A. Leng, W. Furbeth, H. Streckel and GroBe-Brinkhaus, *Prog. Org. Coat.*, **27**, 261 (1996).

145. A. Leng, H. Streckel, K. Hofmannn and M. Stratmann, *Corros. Sci.*, **41**, 599 (1999).

146. W. Furbeth and M. Stratmann, *Fresen. J. Anal. Chem.*, **353**, 337 (1995).

147. A. Nazarov and D. Thierry, *Electrochem. Acta*, **49**, 2955 (2004).

148. G. Williams, R. J. Holness, D. A. Worsley and H. N. McMurray, *Electrochem. Comm.*, **6**, 549 (2004).

149. H. N. McMurray, M. Loveridge and G. Williams, *Abstracts of the 206th Meeting of the Electrochemical Society* (2004).

150. N. Le Bozec, D. Persson, A. Nazarov and D. Thierry, *J. Electrochem. Soc.*, **149**, B403 (149).

151. K. Wapner, B. Schoenberger, M. Stratmann and G. Grundmeierz, *J. Electrochem. Soc.*, **152**, E114 (2005).

152. G. Koley and M. G. Spencer, *J.Appl. Phys.*, **90**, 337 (2001).

153. H. O. Jacobs, H. F. Knapp, S. Mueller and A. Stemmer, *Ultramicroscopy*, **69**, 39 (1997).

154. H. Heil, J. Steiger, S. Karg, M. Gastel, H. Ortner, H. von Seggern and M. Stossel, *J.Appl. Phys.*, **89**, 420 (2001).

155. C. G. Vayenas, S. Bebelis and S. Ladas, *Nature*, **343**, 625.

156. G. Williams, H. N. McMurray and D. A. Worsley, *J. Forensic Sci.*, **46**, 1085 (2001).

Chapter 2

Experimental Methods

2.1 Introduction

A general description of the materials and experimental procedures used throughout the experimental work in this thesis are given in this chapter. Any details specific to a particular experiment are given in that particular chapter. Unless otherwise stated all chemicals used were supplied by Sigma Aldrich Ltd.

2.2 Materials

2.2.1 Metals

Chapters 3 and 4 use aluminium alloys AA6016-T4 and AA6111-T4 (T4 temper designation described in Chapter 1, Table 1.2) which are predominantly used in the automotive industry to make closure panels (see Section 1.2.2). These are commercial AlMgSi(Cu) alloys and were supplied by supplied by Alcan, Inc. in the form of 1 mm thick rolled sheet product. Their respective compositions are given below:

Table 1.1 Composition of 6xxx series alloys

Alloy	Si	Fe	Cu	Mn	Mg	Cr	Ni	Zn	Ti	V
AA6016	0.98	0.20	0.06	0.08	0.34	0.003	0.003	0.017	0.022	0.005
AA6111	0.2	0.26	0.66	0.21	0.59	0.025	0.004	0.025	0.024	0.010

In Chapters 5 and 6 aluminium alloy AA2024-T3 which is a high copper containing aerospace alloy (see Section 1.2.3) is used. This alloy was supplied by BAE Systems Ltd. as 1.5 mm thick rolled sheet with composition by weight: 0.5% Si, 0.5% Fe, 3.8-4.9% Cu, 0.3-0.9% Mn, 1.2-1.8% Mg, 0.1% Cr, 0.25% Zn). In Chapter 5 high purity (99.999%) aluminium foil, supplied by Goodfellow Cambridge Ltd, as 1 mm thick foil is also used.

Finally Chapters 7 and 8 use 1.5mm thick iron foil, of purity 99.9% obtained from Goodfellow Cambridge Limited.

2.2.2 Polyvinyl-Butyral

Polyvinyl butyral-*co*-vinyl alcohol-*co*-vinyl acetate (PVB), molecular weight 70,000 – 100,000 was used as a model coating and also as a matrix for the suspension of inhibitors. There are a number of polymers that would have been suitable for these purposes but PVB was chosen for several reasons. PVB is generally inert and also dries as a clear lacquer allowing visual observations to be made of any underlying corrosion. PVB is also soluble in non-toxic solvent and ethanol is used for this purpose throughout, producing a 15.5 wt% ethanolic solution of PVB. PVB consists of hydrophilic and hydrophobic monomers which allow good adhesion to both the metal substrate and any organic coating that may be subsequently applied over the top. In addition, PVB is relatively low cost with low level health risks. The molecular structure of PVB is shown in Fig. 2.1.

2.2.3 Polyaniline Emeraldine Salt Pigments

Polyaniline Emeraldine base (PAni-EB), MW *ca.* 65,000, with agglomerates mean diameter of 3 - 100 μm was used. Polyaniline Emeraldine salt (PAni-ES) was created by doping (protonating) Pani-EB. The acids used to do this were: Camphor Sulphonic Acid (CSA), MW 232.3; phenylphosphonic acid (H_2PP), MW 158.1; and Ethylenediaminetetraacetic acid (EDTA), MW 292.24. Upon oxidising the surface PAni-ES is reduced with the release of the dopant anion which can then form metal salts. Therefore it is important to know the anion incorporated into the Pani-ES coating when protonated using an acid. PAni ES is weakly acidic, and a pK_a of 5.5 has been reported for ES titrated to EB in aqueous suspension.[1] The pK_a values of the acids used in this work are given below in Table 2.1.

Table 2.1: pK_a values for Brønsted acids used to protonate PAni

Acid	pK_{a1}	pK_{a2}	pK_{a3}	pK_{a4}
CSA [2]	<0	-	-	-
H_2PP [2,3]	2.3	7.8	-	-
EDTA[4]	1.7	2.6	6.3	10.6

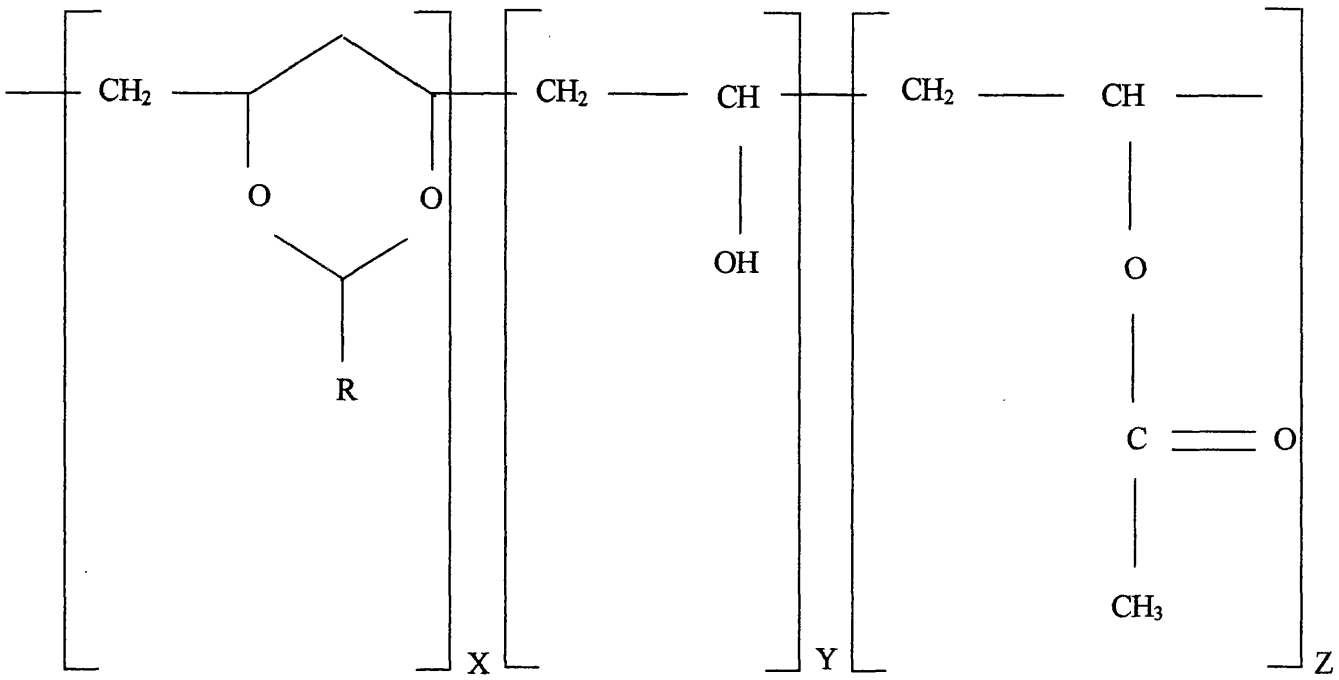

R = $CH_2 - CH_2 - CH_3$
X = No. of vinyl acetal groups
Y = No. of vinyl alcohol groups
Z = No. of vinyl acetate groups

Figure 2.1: Molecular Structure of PVB.

From this it may be seen that the monobasic CSA acid will efficiently protonate EB yielding CS^- anions. For H_2PP only the first pK_a is sufficiently acidic to efficiently protonate PAni-EB and the monovalent HPP^- anion will predominate in the resulting ES. Finally in the case of EDTA both the first two pK_a values are sufficiently low enough to pronate PAni-EB. This means that the dominant anion will be the divalent $EDTA^{2-}$ anion. The molecular structures of the dopant anions are shown in Fig. 2.2.

To fully dope PAni-EB with for example the HPP^- anion, 10 g of PAni-EB was dispersed in 200 cc of 0.5 M H_2PP dissolved in ethanol (analytical grade). This was stirred for 3 - 4 hours to allow sufficient time for full protonation producing PAni-HPP, before centrifugation to remove the ethanol. Repeated cycles of washing with distilled water were then carried out until the pH became non-acidic (> pH 5). The resultant powder was then air dried and ground to produce a particle size of < 20 μm. This was added to the PVB and mixed using a high shear blender for an hour to ensure even dispersion, before being placed in an ultrasound bath for a further hour to remove any trapped air bubbles.

The two part PAni-EB and PAni-ES coatings were loaded with a 0.2 volume fraction (Φ). The amount of pigment addition to be made to the PVB base coating system was calculated using Equation (2.1).

$$M_{pigment} = \frac{\Phi \cdot M_{PVB} \cdot \rho_{pigment}}{\rho_{PVB}(1-\Phi)} \qquad (2.1)$$

Where, M = Mass (g) and ρ = Density (g cm^{-3})

The following values of density were used:

ρ_{PVB} = Density of PVB = 0.8 g cm^{-3} [5]

$\rho_{PAni-EB}$ = Density of Polyaniline Emeraldine Base = 1.25 g cm^{-3} [6]

$\rho_{PAni-ES}$ = Density of Polyaniline Emeraldine Salt = 1.36 g cm^{-3} [6]

All weight measurements were carried out using a Sartorius digital balance.

This approach was used because of its significant practical implications, since this is commonly the form taken by conventional Cr(VI) primers. In so doing PAni-

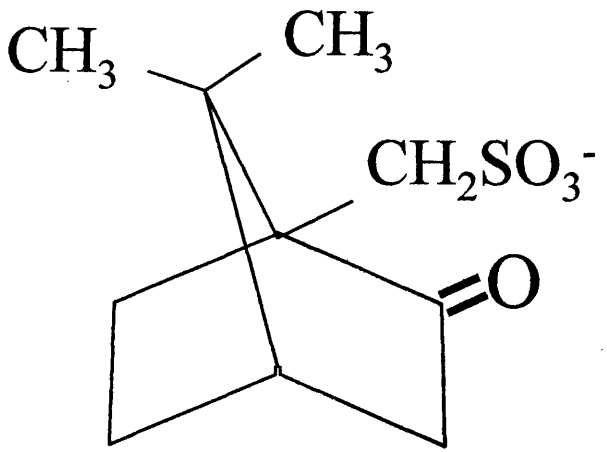

Camphor sulphonate
$pK_{a1} < 0$

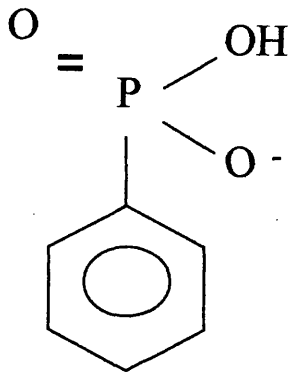

Phenyl Phosphonate
$pK_{a1} = 2.2$

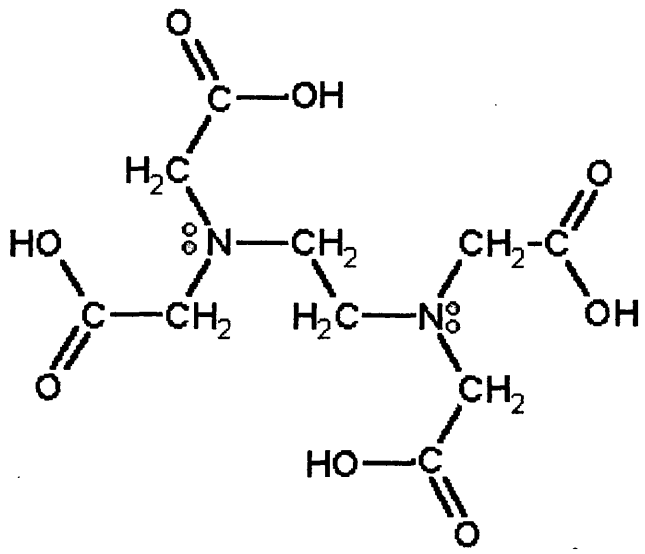

Ethylenediaminetetraacetic acid
$pK_{a2} = 2.6$

Figure 2.2: Molecular structure of dopant anions for PAni-ES pigment formulations.

ES was used as a straightforward replacement for conventional Cr(VI) inhibitor pigments such as $SrCrO_4$. The pigment/binder approach also circumvents practical difficulties from the intractability (insolubility and infusibility) of PAni-ES.

2.2.4 Phenylphosphonic Acid Coatings

Required weights of H_2PP were dissolved in a 15.5% w/w ethanolic solution of PVB. Coatings comprising 0.1%, 0.5%, 1%, 2.5% and 5% H_2PP w/w were prepared. The resulting mixture was bar cast onto the abraded AA6111-T4 surface to give dry films of thickness 30 μm. When applied to the substrate the resulting coatings were clear, homogeneous and strongly adherent

2.3 Potentiodynamic Measurements

Potentiodynamic polarisation measurements under conditions of electrolyte immersion were carried out using a Solartron SI 1280 potentiostat in conjunction with a gas-tight electrochemical cell incorporating a platinum gauze counter electrode and saturated calomel reference electrode (SCE). The electrolyte used was near neutral (pH 6.0 – 6.5) 0.5% w/v aqueous NaCl. When required, the electrolyte was deaerated by sparging with argon gas for 60 mins. The electrolyte was maintained at 25°C and stirred continuously throughout the duration of the experiment. Bare "surface deformed" and "bulk" AA6016-T4 sample coupons (detailed surface preparation given below in Section 2.5.5) were completely covered with an extruded PTFE adhesive tape (3490, 3M Ltd.) except for a 10 mm × 10 mm square area in the centre of the prepared surface. In all cases, potentiodynamic sweeps were carried out from a potential just above the onset of H_2 evolution (-1.7 V *vs.* SHE) to 0 V *vs.* SHE using a sweep rate of 5 mV/sec. This sweep rate was chosen to be sufficiently fast so that not all of the damaged layer, introduced by grinding, would have dissolved by the end of the experiment. All polarisation experiments showed excellent reproducibility with each experiment repeated a minimum of four times. In this thesis only one curve per surface/heat treatment experiment is shown to allow ease of data interpretation by the reader.

2.4 Scanning Vibrating Electrode Technique

The Scanning Vibrating Electrode Technique (SVET) has been extensively used in corrosion studies and the theory behind it is well known. The principles

behind the SVET are described in Section 1.6.1. This chapter will go over the basics and detail the specifics of apparatus used in this thesis.

2.4.1 SVET Introduction

The scanning vibrating reference electrode technique (SVRET) is a derivative of SRET.[7] The difference is that the scanning micro-tip is vibrated relative to the sample surface and more often than not is a pseudo reference electrode and is thus abbreviated to SVET.[8] The technique has the ability to directly measure components of corrosion current density when spatially resolving areas of dissimilar electrochemical activity, which is a distinct advantage over the SRET technique. SVET also offers improved sensitivity and improved spatial resolution.[8]

The micro-tip operates potentiometrically registering an alternating potential at the vibration frequency which is proportional to electrical field strength or potential gradient in the direction of vibration. The electric field generated ohmically by the ionic current flux passing through the electrolyte is shown in Fig. 2.3. The alternating potential measured by the SVET arises due to the oscillation through this electric field. Therefore the SVET signal is directly proportional to the ionic current flux which makes data interpretation easier than that received from SRET testing.[8]

2.4.2 SVET Apparatus

A schematic diagram of the SVET equipment is shown in Fig. 2.4. The SVET microprobe electrode is perhaps the most important part of the set-up and Fig. 2.5 shows the design in more detail. The probe tip consists of a 125 μm platinum wire encased in a glass shroud giving a maximum overall diameter of ~250 μm and ground flat at the end forming a micro-disc electrode. The tip is mechanically vibrated normal to the sample surface, via connection to an electromagnetic-loudspeaker. The speaker is vibrated at a frequency of 140 Hz using a Lock-In Amplifier (LIA), EG & G 7265, generating a microprobe amplitude of *ca.* 25 μm. The connection to the tip is made by attaching a glass rod to the loudspeaker using a two part marine epoxy. A Teflon coupler is then used to join the glass rod and the tip. This setup enables the loudspeaker to be encased in a *mu*-metal box which eliminates problems of magnetic flux leakage from the speaker to the probe.

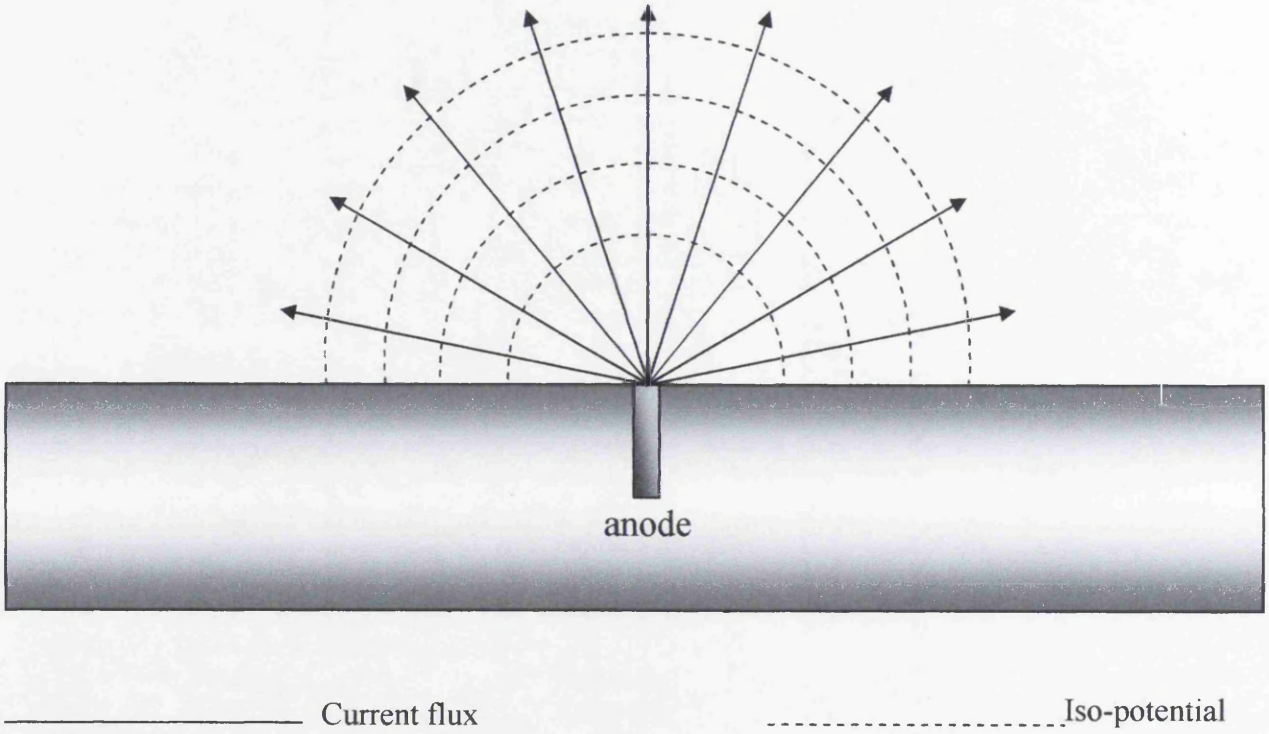

Figure 2.3: Schematic diagram showing lines of ionic current flux emanating from a localised anode setting up lines of iso-potential. The cathode in this instance is assumed to be "remote" giving radial distribution of current flux.

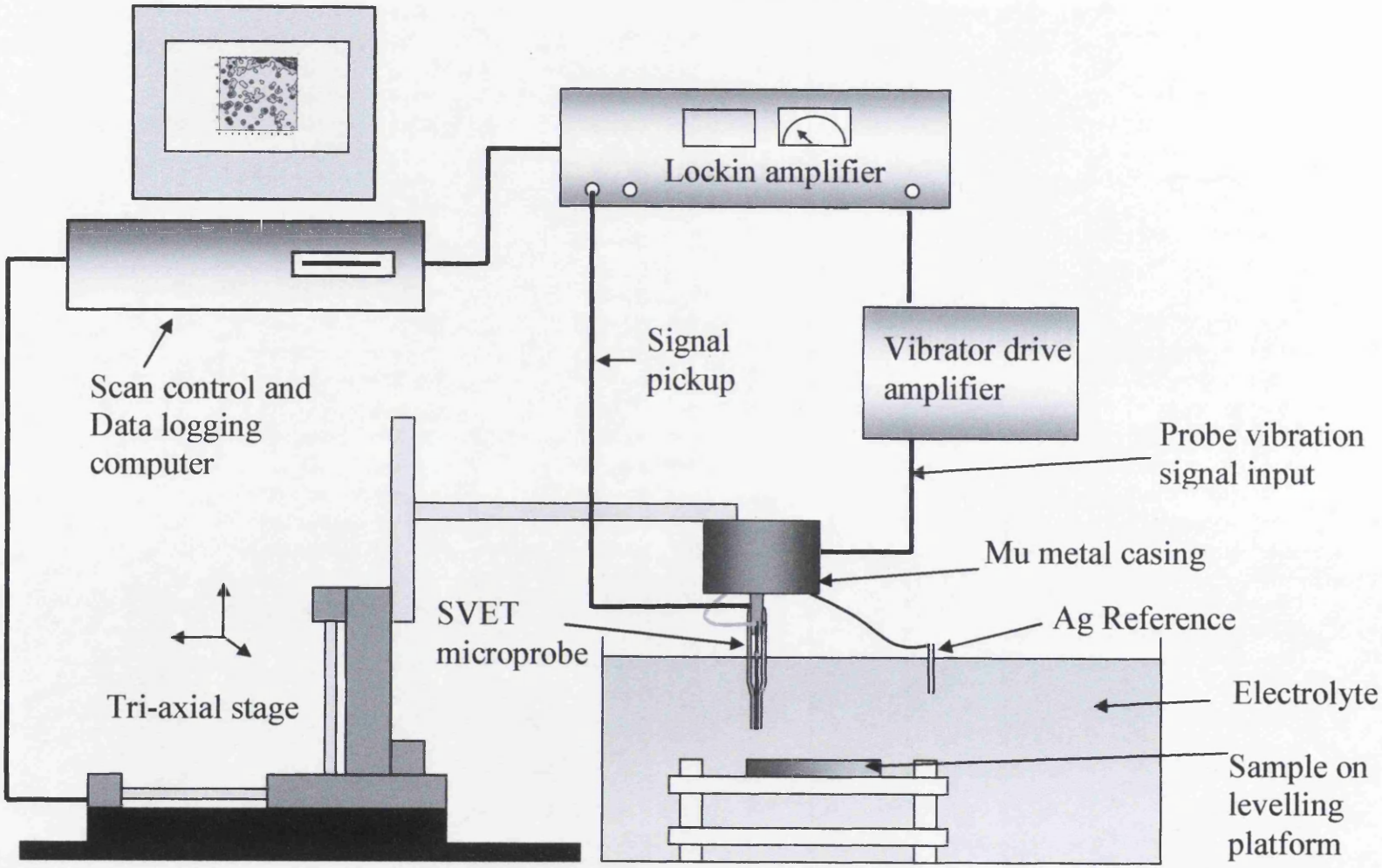

Figure 2.4: Schematic diagram of the most important features of the SVET equipment.

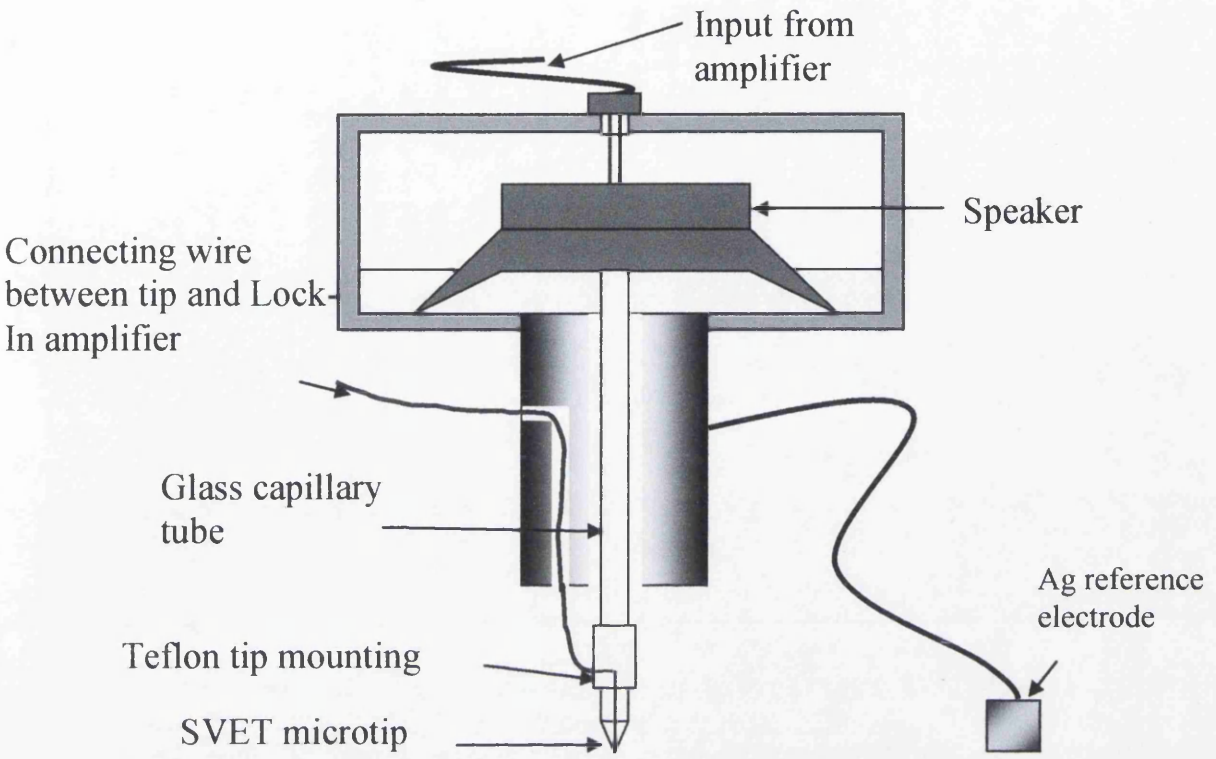

Figure 2.5: Schematic diagram of the SVET microtip.

The probe is moved over the sample surface in a step-wise manner, at user defined intervals, using a tri-axial micromanipulator stage (Time and Precision Ltd.). The scan height (probe – sample distance) used throughout these experiments was 100 μm as this has been shown to be the optimum height for maximum current detection.[9]

2.4.3 SVET Calibration

Throughout this thesis the SVET was calibrated using two different procedures. The first method uses the principals of the SVET as described in Section 1.6.1. Briefly, the SVET microtip records an alternating potential which is proportional to the electric field strength, F, or potential gradient in the direction of vibration. It has previously been shown that for a point current source, i, the value of F at any distance x,y and z from the point source, is given by,[10]

$$F = \frac{dE}{dz} = -\frac{iz}{2\pi\kappa(x^2 + y^2 + z^2)^{1.5}} \tag{2.2}$$

where E = electrical potential, i = current and κ = solution conductance.

The maximum field strength, F_{max}, at height z above the origin (x=0, y=0) from Equation (2.2) is given by

$$F_{max} = -\frac{i}{2\pi\kappa z^2} \tag{2.3}$$

The first calibration method utilises these principles to calibrate using a point current source cell (PCS). The PCS consists of a 25 μm platinum disc electrode, encased within a glass sheath within a Perspex block and connected to the positive or negative output from a nano-galvanostat and a large (2 cm^2) remote platinum gauze electrode. The cell was immersed in 0.86 mol dm^{-3} (5 wt%) NaCl and levelled with respect to the probe. Known currents, i, (typically 0.1 - 1 μA) were then passed through the point source using a galvanostat. The SVET probe was scanned over the point source at a constant height of 100 μm. The field strength distributions recorded around the point source exhibited the characteristic Gaussian distribution 360° (bell

(a)

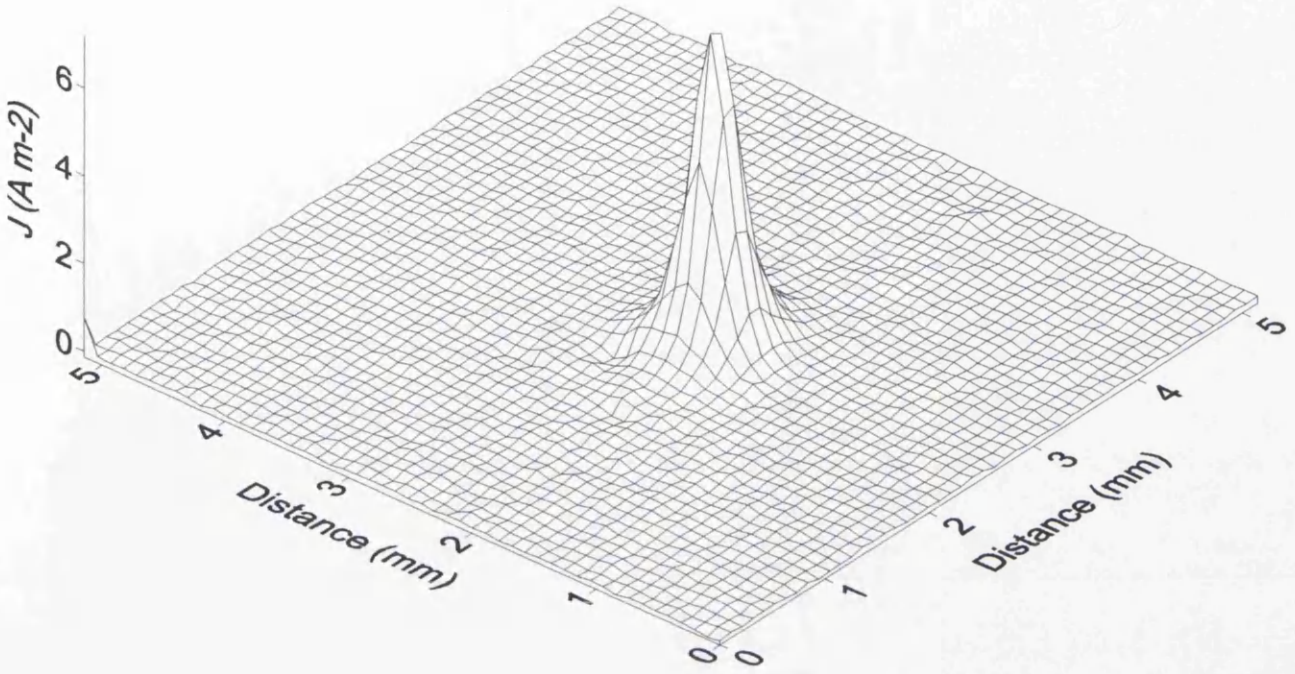

(b)

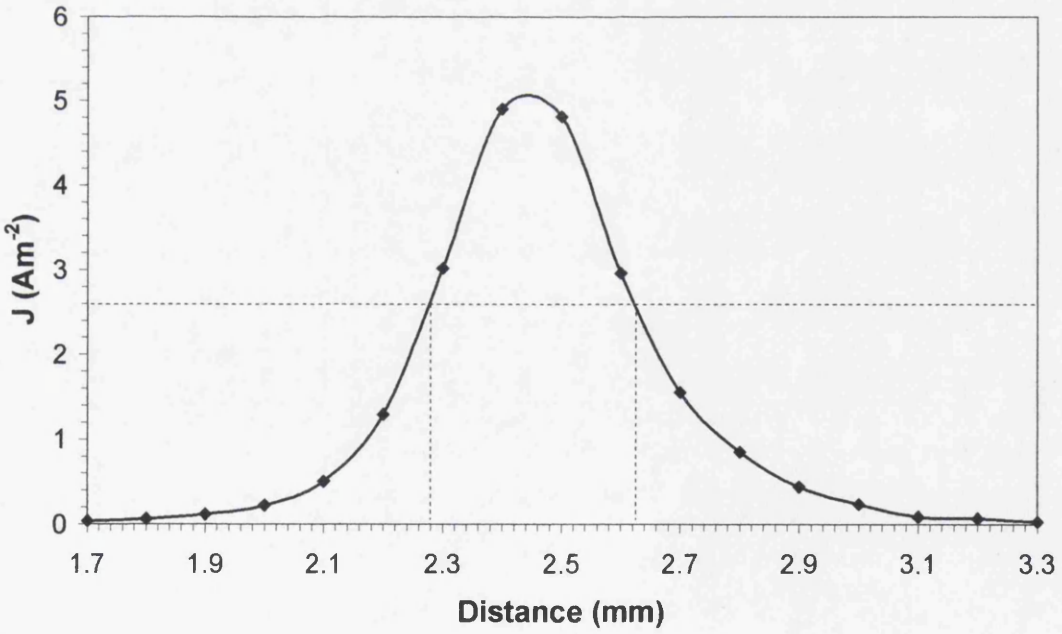

Figure 2.6: (a) 3D SVET calibration plot of a point source, in 5% NaCl with a scan height of 100μm and an applied current of 0.8μA. (b) Line scan taken across F_{max} used to determine *whm*.

shape) reported previously,[8] and is shown in Fig. 2.6(a), with a width at half maximum (*whm*) peak height of 0.36 mm as shown by the line scan in part (b) of Fig. 2.6. The maximum electric field strength values (F_{max}) were recorded when the probe was directly over the centre of point source (anode) and increased linearly with applied cell current, i.

As shown in Section 1.6.1, the theoretical value of the *whm* at z = 100μm is 0.153 mm. This is approximately half of the experimental value of 0.36 mm. This departure from theoretical performance derives from the finite dimensionality of the SVET probe since the tip consists of a 125 μm microdisc electrode. As the calibration cell anode may be considered as a point current source with a *whm* value of 0.36 mm this value is an indication of the limiting spatial resolution for the SVET.

The second calibration procedure, and the most often used in this thesis, was a specially designed two compartment cell, as shown in Fig. 2.7. Each compartment contains a $1cm^2$ Pt electrode and the aqueous electrolyte currently under investigation. The compartments are linked by a vertically oriented glass tube of length 7 cm and internal diameter 5 mm. During calibration the SVET probe was inserted a distance (*ca.* 5 mm) downwards into the tube lumen. At this position, current flux density is constant across the tube diameter and equal to the cell current divided by the internal area of cross-section (minus the cross-sectional area of the SVET probe). Furthermore, the glass tube allows the lines of current flux to align vertically along its length and thus the SVET tip is vibrated in an area of uniform current density. A range of currents were passed through this glass tube using a nano-galvanostat and for each current density the SVET voltage was measured and was found to vary linearly with applied current density. The gradient of a plot of current density *vs.* SVET voltage provides a calibration factor, G, for the instrument as shown in Fig.2.8 (where G = 562030). At all electrolyte concentrations and for j_z = -15 Am^{-2} to +15 Am^{-2} plots of SVET voltage versus j_z gave good straight lines (correl. coeff. > 0.998).

The advantage of this calibration procedure over the PCS is the speed of use allowing quick calibration before each experiment and most importantly, the calibration is independent of probe height.

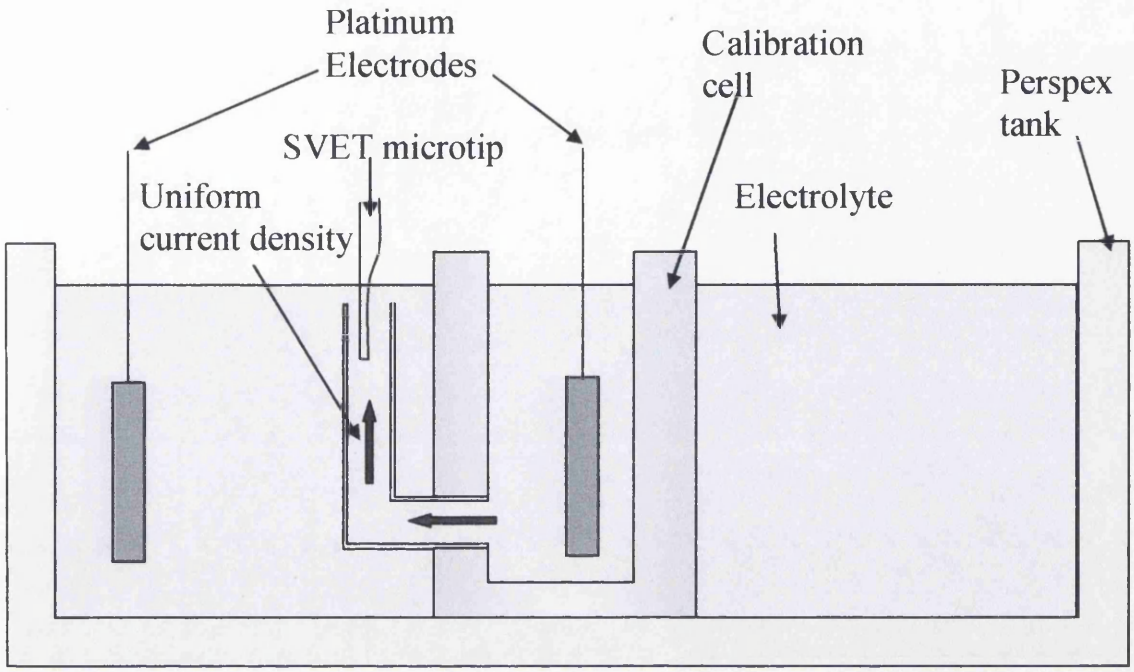

Figure 2.7: Schematic diagram of specially designed two compartment SVET calibration cell.

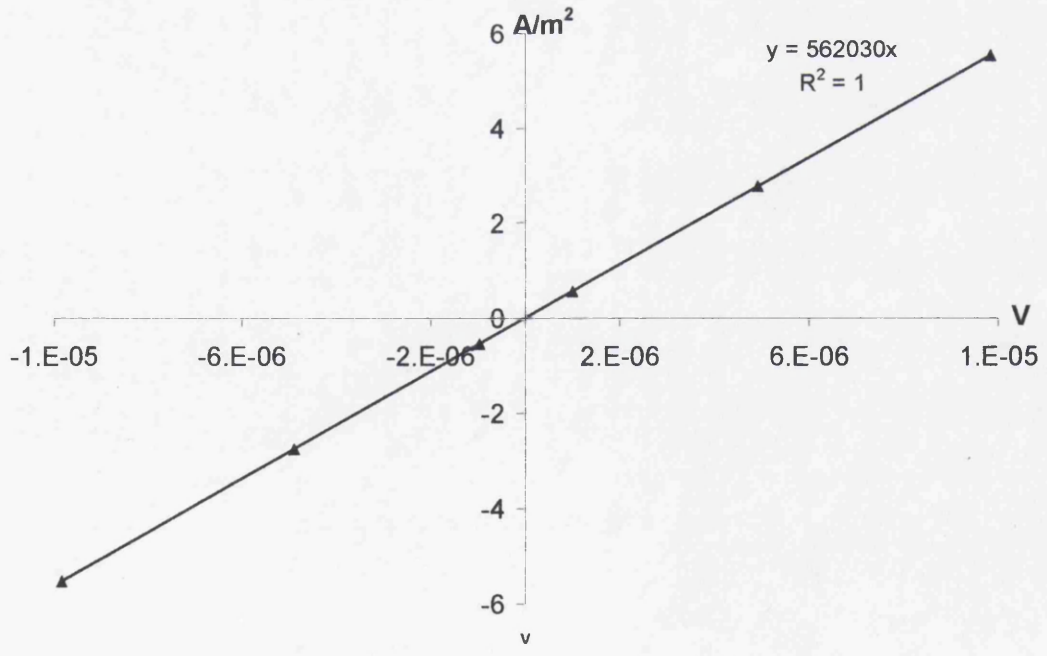

Figure 2.8: Typical calibration plot from data acquired using calibration cell shown in Fig. 2.7.

2.4.4 Sample Preparation

AA2024-T3 and pure aluminium as described in Section 2.2.1 were used for SVET experiments. Sodium chloride, and the following inhibitor chemicals; potassium ferrocyanide, sodium N,N-diethyldithiocarbamate trihydrate, benzotriazole, ethylenediammine-tetraacetic acid (disodium dihydrate), 2,5-dimercapto-1,3,4-thiadiazole (dipotassium salt) and all other chemicals were obtained from Sigma Aldrich Ltd. in their highest purity. Metal sample coupons measuring 3.5 cm × 3.5 cm were cleaned using an aqueous slurry of 5 μm polishing alumina (Struers) and non-ionic surfactant to remove any pre-formed oxide layer. The cleaned coupons were then rinsed with distilled water followed by ethanol and allowed to dry in air. The coupon surface was completely covered with 90 μm thick extruded polytetrafluoroethylene (PTFE) 5490 tape (3M Ltd), except for a 10 mm × 10 mm square area in the centre of one surface.

The samples were secured on a Perspex stage using rubber tensioning bands, as shown in Fig. 2.9, and levelled. This was achieved by using the noise made when the vibrating probe comes into contact with the metal surface. By checking each corner of the sample and adjusting the profile of the stage using the nylon screws shown, the sample could be levelled so that the probe was 100 μm above each corner, when positioned directly over it and thus in a parallel plane to that of the sample.

During SVET experiments metal samples were completely immersed, the exposed area uppermost, in an electrolyte bath containing 0.86 mol dm^{-3} (5% w/v) aqueous sodium chloride at pH 6.5. Additionally inhibitors (as listed above) were added to the electrolyte bath when required. Information concerning the quantities of each inhibitor used is discussed in the appropriate chapter. The bath was left unstirred and in contact with room air at a nominal temperature of 20°C. The SVET probe was held vertically and scanned at a fixed height (100μm) above the metal surface. Samples were scanned immediately following immersion, and at hourly intervals thereafter for a period of 24 hours. Each scan took *ca.* 15 minutes and produced a square matrix of 2500 SVET voltage data points. Upon removal from the experimental electrolyte after immersion experiments digital images of the surface were acquired using a Canon G3 Powershot digital camera.

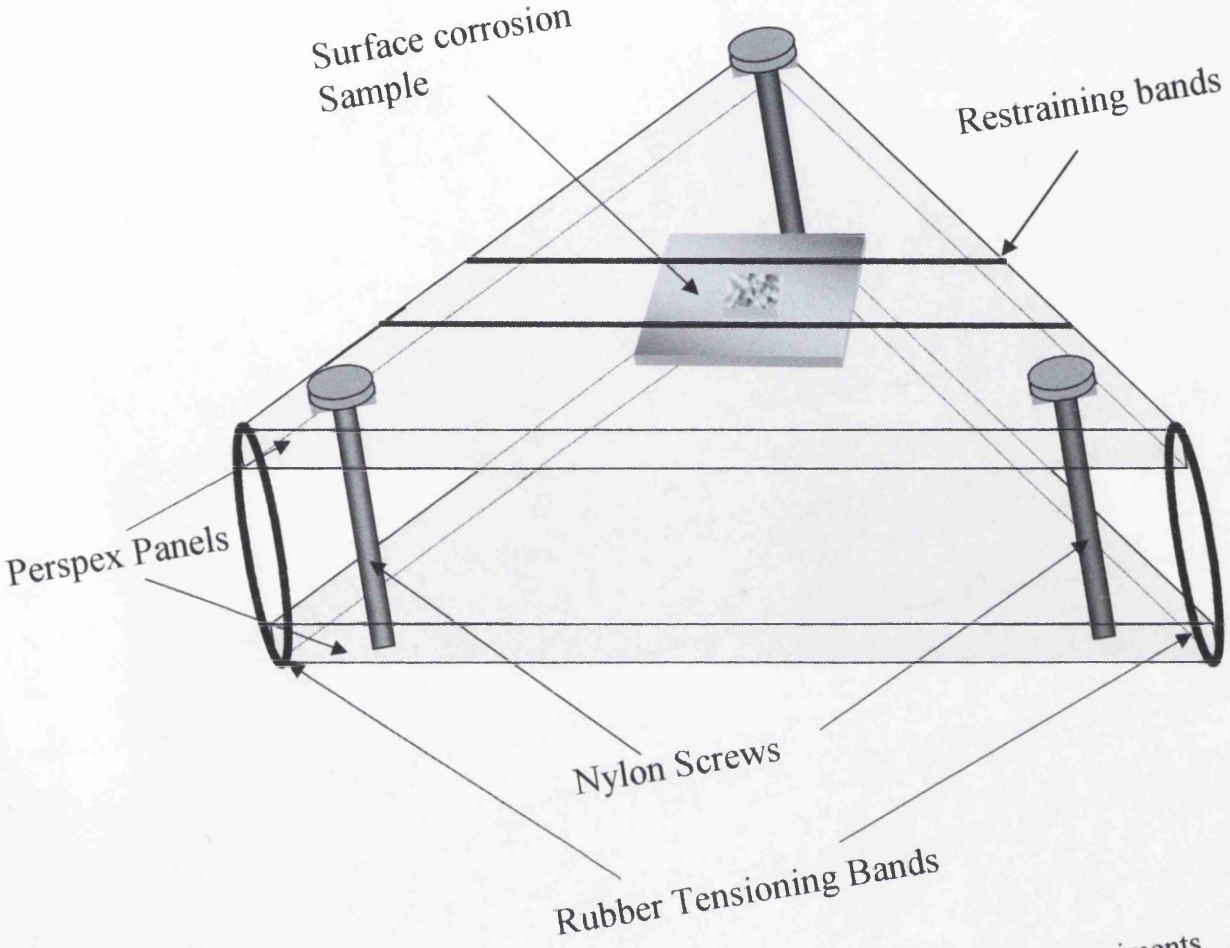

Figure 2.9: Schematic diagram of the leveling stage used for SVET experiments.

2.4.5 SVET Data Analysis

The raw data from the SVET scan is converted from units of nV to V, before being multiplied by calibration factor G converting raw data obtained from each scan into current density, j_z (Am^{-2}). This data is then plotted using a software cartography package, Surfer 8, to produce maps of the current densities present on the surface. Unfortunately, it is not possible to present j_z distribution plots in significant numbers within this thesis to adequately describe time-dependent pitting kinetics. Therefore an estimate of the time-dependent total (population) pitting currents was made through the numerical area integration of j_z distributions. It has previously been shown that a minimum estimate of the time-dependent total anodic current (I_a) and hence, area averaged anodic current density (J_t), may be obtained by numerically integrating j_z data, when distinct point anodes are detected.[11] This enables the compression of the very large quantity of j_z data acquired using SVET and enables a more compact depiction of pitting kinetics.[11] Data points are obtained by numerically integrating all the j_z values contained in a single SVET scan (obtained every hour from a 1 cm × 1 cm area) according to Equation (2.4):[11]

$$J_{(t)} = \frac{I_a}{A} = \frac{1}{A} \cdot \int_{x=0}^{x=X} \int_{y=0}^{y=Y} (jz_{(x,y)} > 0) dxdy \tag{2.4}$$

where A is the sample area, x and y are the length and width of the SVET scan. This data analysis may be taken further to consider the total metal loss from such an anodic current. Firstly, the total charge calculated from

$$Q = \int_0^t J.dt \tag{2.5}$$

where Q (Cm^{-2}) is the charge passed in time, t (seconds). By assuming that J(t) remains constant over time (that is to say over the hour between scans) the integral in Equation (2.5) can be simplified using the numerical approximation,

$$Q = 3600 \sum_{n=0}^{n=24} J_n \tag{2.6}$$

where J_n is the mean current density for each hourly scan and 3600 is the number of seconds per hour. The value n ranges from 0 to 24 to account for each hourly scan. By applying Faraday's Law this in turn may be used to calculate the total equivalent aluminium loss (teal) in gm^{-2}, from

$$teal = \frac{Q}{3F}.A \tag{2.7}$$

where F is Faraday's constant (96,500 coulomb mol^{-1}) and A is atomic weight (27g for Al). This equation assumes that aluminium is lost as Al^{3+}. Although a number of assumptions are made during these calculations, providing anode and cathode separations are > than the spatial resolution of the SVET recent studies have shown good results for the study of other materials.[11,12]

2.5 Scanning Kelvin Probe

As described in Section 1.6.2, the scanning Kelvin probe (SKP) is practically unique as an electrochemical technique in that it does not require the presence of a bulk electrolyte and is capable of measuring localised free corrosion potentials (E_{corr}) beneath humidity films and/or intact polymer layers. By moving the sample around beneath the probe a surface map of E_{corr} may be obtained. Continuous scanning allows the surface maps to be put sequentially in an animation allowing the dynamic evolution of E_{corr} to be studied. The SKP is used in this way to study FFC kinetics and also the effectiveness of different inhibitor coatings. The following section describes the apparatus used and the experimental procedures involved.

2.5.1 SKP Apparatus

A schematic diagram of the SKP apparatus is shown in Fig. 2.10. The reference probe (shown in Fig. 2.11) consists of a gold wire housed within a tapered glass capillary tube. Gold wire of diameter of 125 μm and 99.99% purity was used in this work unless otherwise stated. Wire was used as this produces the ideal tip geometry as if a truncated cone with a big vertex angle is used lateral resolution is reduced due to stray capacitance[13]. A 5 mm length of gold wire protrudes from the

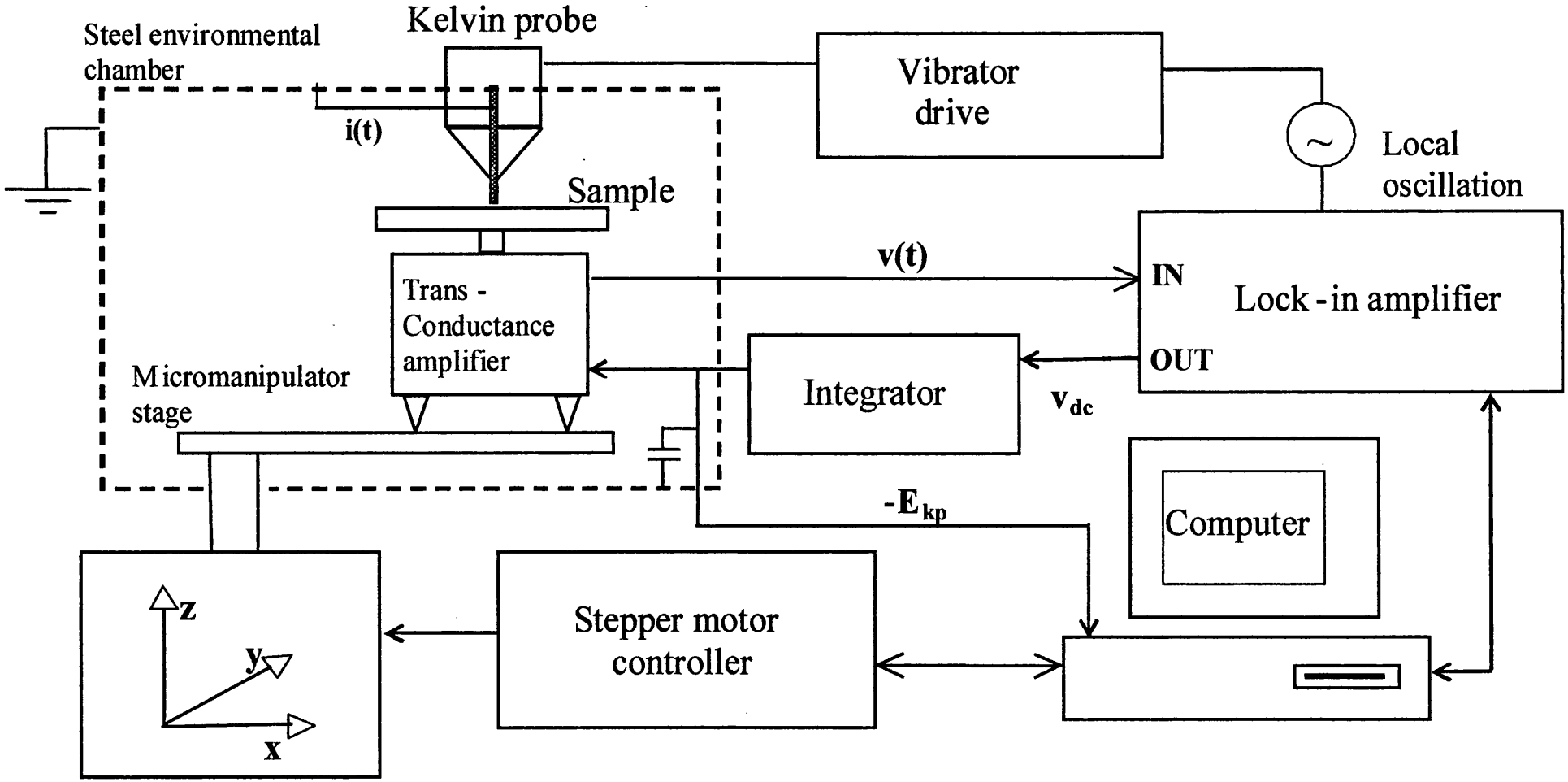

Figure 2.10: Schematic diagram of main scanning Kelvin probe (SKP) components.

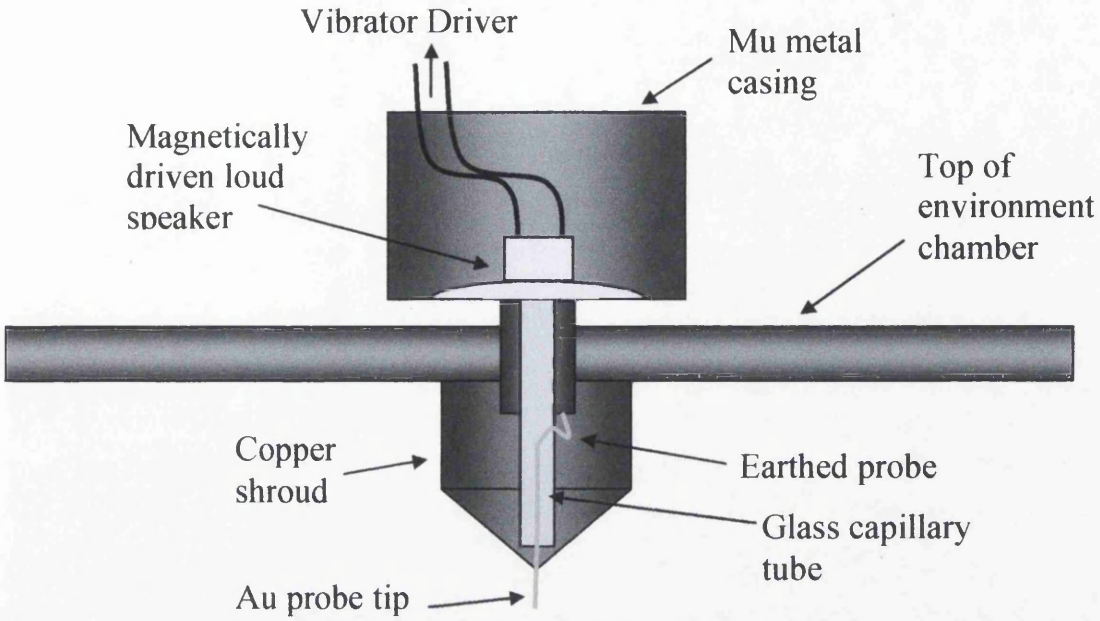

Figure 2.11: Schematic diagram of the SKP reference probe head.

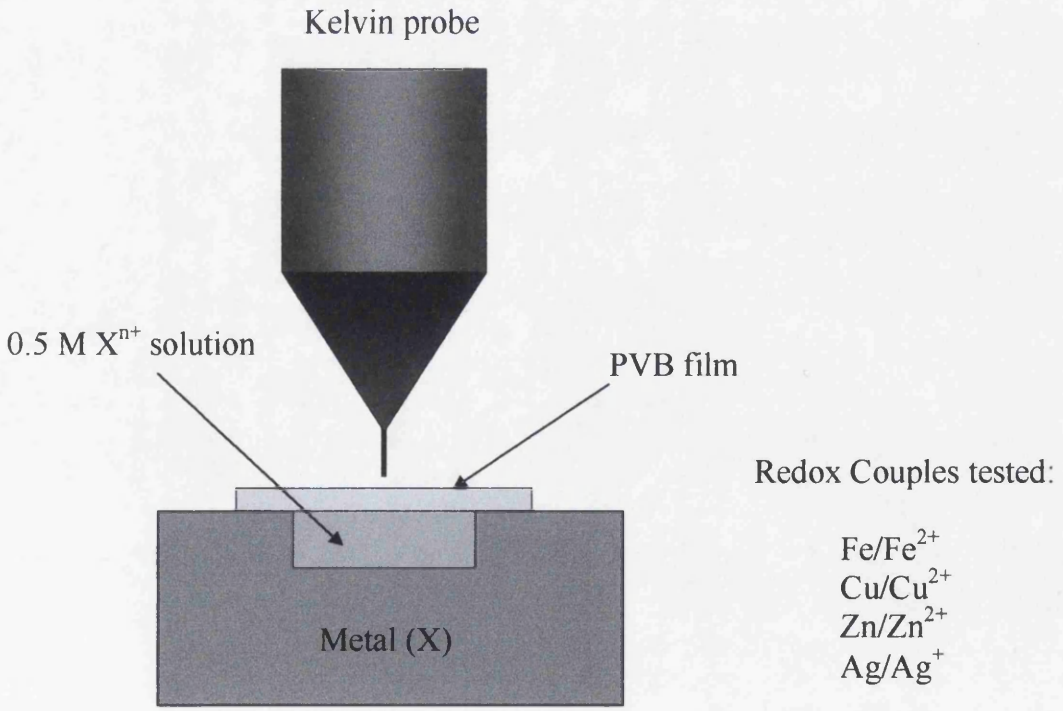

Figure 2.12: Schematic diagram of the SKP calibration with a PVB film present.

tapered end and is sealed with epoxy resin and then housed within a copper shroud. The other end of the tube is attached to a loudspeaker and connected to a vibrator drive, which consists of a magnetically driven loudspeaker vibrated sinusoidally, at a frequency of 280 Hz, and normal to the sample surface. The vibrations are generated from the oscillator function on a Lock-In Amplifier (LIA), EG & G 7265. The LIA also filters out any background interference frequencies. The vibrations are transmitted mechanically to the gold wire (via the loudspeaker) which is mounted parallel with the surface of the specimen and about 100 μm above it. A peak-to-peak vibration amplitude of 40 μm was generated from this setup.

The Kelvin probe is fixed to a computer controlled tri-axial (x,y,z) stage and the sample is fixed in its local position. As described in Section 1.6.2 it is important to maintain a constant tip to sample distance and this is maintained at its optimum value using the micrometer levelling stage. Finally the probe and sample are mounted inside a stainless steel environment chamber.

2.5.2 SKP Operation

If a Volta potential exists between the probe and the surface then a change in the distance between the probe and the surface will cause a change the magnitude of the charge between the two. If the change is periodic, *i.e.* by vibrating the probe sinusoidally with respect to the test sample, then dC/dt and any non-zero Volta potential difference between the two produces an a.c. current as shown in Equation 1.26. Thus the vibration of the gold wire may cause an a.c. current generated in the external circuit connecting the sample and the reference probe and is initially amplified and converted to a.c. voltage. A corresponding d.c. output is sent from the amplifier to an integrator which adjusts the d.c. bias applied to the sample by the Trans-conductance amplifier so as to automatically null it (E_i=0) and thus a "loop" is created.

The integrator makes the finite changes to equalise the Galvani potentials of the probe and the specimen in order to nullify the a.c. current. When the integrator alters the bias d.c. voltage, the system determines the effect it has on the a.c. current, gradually with smaller and smaller changes the system reaches null conditions. Once the stable condition is reached the integrator sends the magnitude of the reverse bias required ($-E_{kp}$), converted to a digital signal by the lock-in amplifier, to a computer.

2.5.3 SKP Calibration

The recorded $\Delta\psi_{Pol}^{Ref}$ value is a measurement of the difference in localised potential existing between the surface and the probe. However, in terms of corrosion it is important to be able to get a measurement of the electrode potential, or the free corrosion potential, existing at point on the surface during corrosion experiments. Therefore it is necessary to calibrate the SKP.

The probe electrode used in the SKP is made of gold wire, thus to ensure consistent results a calibration with a standard redox couple is required. In these experiments a series of redox couples have been used and also the effect of the PVB coating on $\Delta\psi_{Pol}^{Ref}$ determined. The SKP was calibrated in terms of electrode potential using Ag/Ag^{+}, Cu/Cu^{2+}, Fe/Fe^{2+} and Zn/Zn^{2+} couples. A schematic diagram of a calibration cell is shown in Fig. 2.12. Calibration cells were prepared by machining wells (8mm diameter, 2mm deep) in discs of the relevant metal (15 mm diameter, 5 mm thick). These wells were then filled with a 0.5 mol dm^{-3} aqueous solution of the respective metal chloride salt (0.5 mol dm^{-3} nitrate salt in the case of Ag) and Volta potential difference values $\Delta\psi_{Pol}^{Ref}$ obtained with the SKP reference probe positioned 100 μm above the solution-air interface in the centre of the well. It is found that there exists a linear relationship between recorded $\Delta\psi_{Pol}^{Ref}$ values and the free corrosion potential. A value for the redox couple can be identified using an electrochemical analyser and as such has proven and known potential results.

2.5.4 SKP Calibration Procedure

The metal X base plate with a reservoir (shown in Fig. 2.12) is attached to the SKP in place of a sample. The reservoir is then filled with a 0.5M X^{n+} aqueous and allowed to equilibrate after lowering the probe 100 μm above the reservoir surface and closing the SKP environment chamber. The $\Delta\psi_{Pol}^{Ref}$ value is recorded at one point above the surface.

The corrosion experiments are carried out with the presence of an organic coating which is primarily a poly-vinyl-butyral (PVB) coating. Therefore it is also

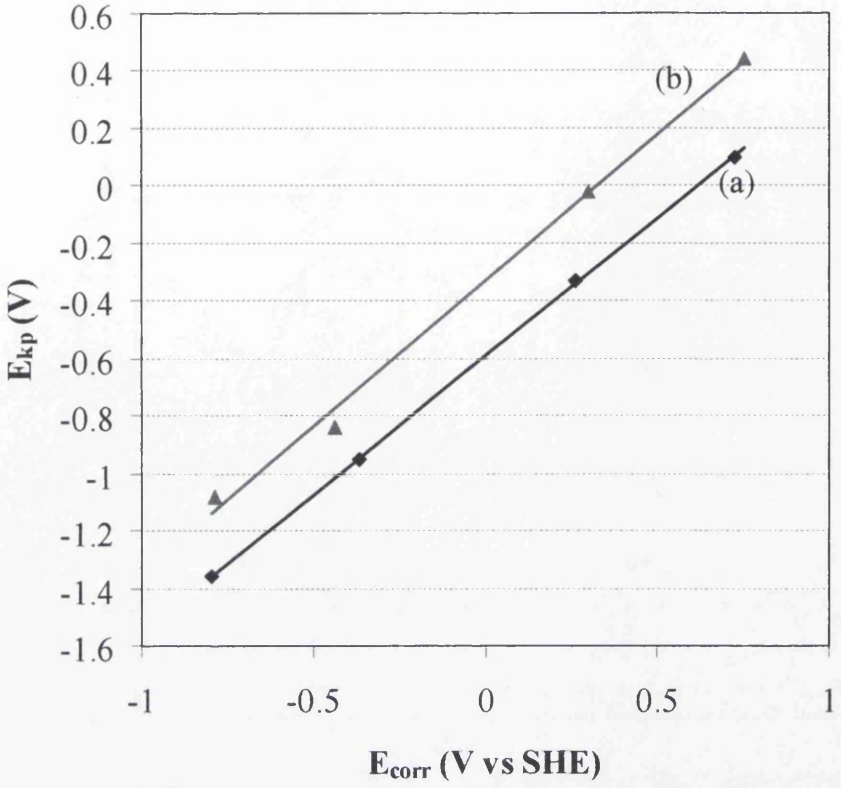

Figure 2.13: Typical SKP calibration plots for various redox cells. (a) no PVB and (b) PVB present.

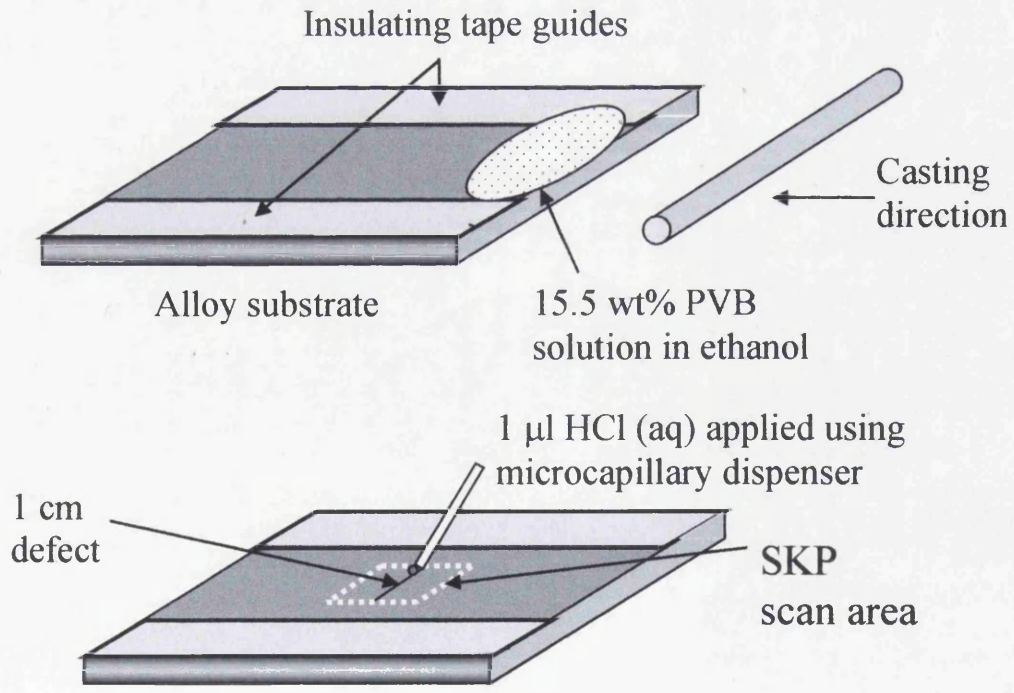

Figure 2.14: Schematic diagram of bar casting a PVB coating onto a AA6016 substrate using tape guidelines.

necessary to identify what effect the coating has on $\Delta\psi_{Pol}^{Ref}$ values. For this reason the calibration experiment is repeated - but with a self supporting PVB coating over the reservoir. This coating is made by bar casting PVB onto a glass sheet using tape guidelines and then peeling off when dried to place a 30 μm thick coating over the calibration cell. With the coating in place the $\Delta\psi_{Pol}^{Ref}$ value is recorded, after allowing 2 hours for the coating to equilibrate with the electrolyte, and the probe positioned 100 μm above it. Finally, the coating is removed and a saturated calomel electrode is dipped into the electrolyte. The electrode potential of the metal is then recorded using a Solatron 1280 pontentiostat.

Fig. 2.13 shows $\Delta\psi_{Pol}^{Ref}$ values both with and without a PVB coating plotted against the relative free corrosion potential for each calibration cell. It can be seen that there is a very good linear relationship between $\Delta\psi_{Pol}^{Ref}$ and the free corrosion potential. There is also a constant change of +0.22 V for the free corrosion potential of each redox cell in the presence of a PVB coating. Therefore the value of free corrosion potential can easily be calculated though

$$E_{corr} = \Delta\psi_{Pol}^{Ref} + C \tag{2.8}$$

where C is a constant. This value is then added to the matrix of $\Delta\psi_{Pol}^{Ref}$ data recorded during the SKP experiment and through the use of a software cartography package (Surfer™ 8, Golden Software) it is possible to produce interpolated grey scale maps of the free corrosion potential on the metal surface. Calibration was repeated before and after each SKP experiment and C was found to exhibit values of 0.33 ± 0.05 volts. Calibration was independent of probe – polymer surface distance over the range 50 – 500μm.

2.5.5 SKP Experimental Setup

AA6016-T4 sheet of 1 mm thickness (see Section 2.2.1) was provided by Alcan Inc. and had been alkali cleaned on-line to remove any rolling-induced surface deformed layer. As received AA6016-T4 was cut into 40 mm x 40 mm coupons and degreased using acetone. "Surface deformed" AA6016 was prepared by subjecting

the as received surface to 2 minutes of vigorous manual abrasion with 180 grit silicon carbide (SiC) paper. "Bulk" AA6016-T4 was prepared by etching the abraded surface for 45 secs at 60°C in 10% w/v aqueous NaOH, to remove any deformed layer, followed by desmutting for 30 secs in concentrated nitric acid at 25°C. Coupons were then washed with distilled water and dried in air. When required, substrates were also dipped in 2 M H_2PP for 60 mins prior to rinsing with distilled water, air drying. Any required heat treatment was carried out on "surface deformed" and "bulk" surfaces in air for 2 hours at temperatures (T_{HT}) between 180°C and 350°C, with coupons being allowed to cool naturally in room air. Coupons to be PVB coated were bar cast using a 15.5% w/w ethanolic PVB solution and tape guidelines to produce an air-dried coating thickness of 30 ± 5 μm, as determined using a micrometer screw gauge. This process is shown schematically in Fig. 2.14 and was done within 60 mins of any heat treatment. PAni (see Section 2.2.3) and PVB coatings containing HPP (see Section 2.2.4) were also bar cast when required producing a dry film coating thickness of 30 ± 5 μm. A 10 mm long linear penetrative defect, running normal to the substrate rolling direction, was created in the centre of each coated coupon using a scalpel blade. When required, FFC was initiated using 1 μl of 2 M aqueous HCl, distributed evenly along the defect using a glass microcapillary.[14] Following initiation, samples were held initially in room air [*ca.* 20°C and 50% relative humidity (r.h.)] for 30 mins - then transferred to the SKP environment chamber. Conditions of 40°C ± 1°C and 80% r.h. in isopiestic equilibrium with a saturated aqueous ammonium sulphate, $(NH_4)_2SO_4$, reference solution, were maintained for the duration of the experiment.[15]

The SKP probe was vibrated normal to the surface at 280 Hz frequency, a 40 μm peak-to-peak amplitude giving a mid-amplitude probe-sample distance of 120μm. Calibration was carried out, as described in Section 2.5.4, before each experiment. Scanning began immediately after the sample was placed in the environment chamber and was continuous with an average scan taking *ca.* 4 hours, for up to 150 hours. Each scan comprised a square grid of 120 x 120 data points over a 12 mm x 12mm area centred on the coating defect. At the end of the experiment the samples were removed and a digital image was acquired.

2.6 Image Analysis of FFC Experiments

Additional samples of AA6016-T4 and AA6111-T4 were also prepared as described in Section 2.5.5 but were not scanned using SKP. Following FFC initiation these samples were put in an environment chamber maintained at 40°C and 80% r.h. After the required duration the PVB coating was removed by immersion in n-methyl-2-pyrrolidinone at 60°C for 5 minutes. The samples were then optically imaged using a Canon G3 camera, before the images were analysed using a software image analysis package (Sigma Scan v5.0), to determine the total area of FFC on the surface.

2.7 Secondary Electron Microscope

Micrographs were taken of AA6016-T4 samples following corrosion experiments using a Phillips XL30CP scanning electron microscope (SEM). To prepare the samples for SEM analysis following corrosion experiments, the PVB coating was removed by placing the sample in n-methyl-2-pyrrolidinone heated to 60°C for 5 minutes before the sample was rinsed off with distilled water and dried. Corrosion products were removed by immersion in a hot (60°C) chromic-phosphoric acid solution for 5 mins according to ASTM G135 before again being rinsed with distilled water and allowed to dry.

AA2024-T3 samples subject to immersion experiments were examined by SEM following emersion from the experimental solution, rinsing with distilled water and drying in air.

2.8 Phase Contrast Interference Microscopy

Phase-contrast (PC) interference micrographs were taken of AA2024-T3 samples following immersion experiments using a Reichert-Jung MeF3 widefield microscope. PC microscopy is a technique used to show structural details on substrates which exhibit only minimal reflection differences and which can not be differentiated by chemical treatment. However, most structures of this type do have a height relief line whose fine level differences show up clearly in the bright/dark contrast or in interference colours.

2.9 Atomic Force Microscope

A Topometrix Explorer atomic force microscope (AFM) was used in contact mode for surface topography analysis. A silicon nitride mico-cantilever with a sharp tip (probe) was used and tip deflection measured using a laser spot reflected from the top of the cantilever into an array of photodiodes. In contact mode, the tip scans across the surface in direct physical contact with the sample. As the probe tip scans, varying topographic features cause deflection of the tip and cantilever. A light beam from a small laser is bounced off of the cantilever and reflected on to a four section photodetector. The amount of deflection of the cantilever – or the force it applies to the sample – can then be calculated from the difference in light intensity on the sectors.

2.10 Dual Chamber Gas Cell (Watson-Coleman device)

A specially designed novel gas cell is used to allow O_2 partial pressure (pO_2) in contact with the head and tail portions of an individual filiform to be varied independently. Coupled with time-lapse imagery, a study of the mechanism and growth kinetics of a filiform corrosion are made.

2.10.1 Sample Preparation

A 15.5% w/w ethanolic solution of PVB, was applied to the clean iron surface using a bar casting technique (shown in Fig. 2.14), leaving an air dried film thickness of *ca.* 30 μm, as measured using a micrometer screw gauge. FFC was initiated by creating an artificial defect 4 mm away from a centre hole (radius 2 mm) that had previously been drilled through the iron sample. Aqueous $FeCl_2$ (2μl of 0.0025 M or 0.025 M) was carefully dispensed using a glass microcapillary along a linear 2 mm scribe cut through the coating by using a clean scalpel blade. When the solution had dried along the penetrative defect the sample was maintained at a constant humidity of 93% and temperature of 20°C for 14 days to allow growth and propagation of the FFC.

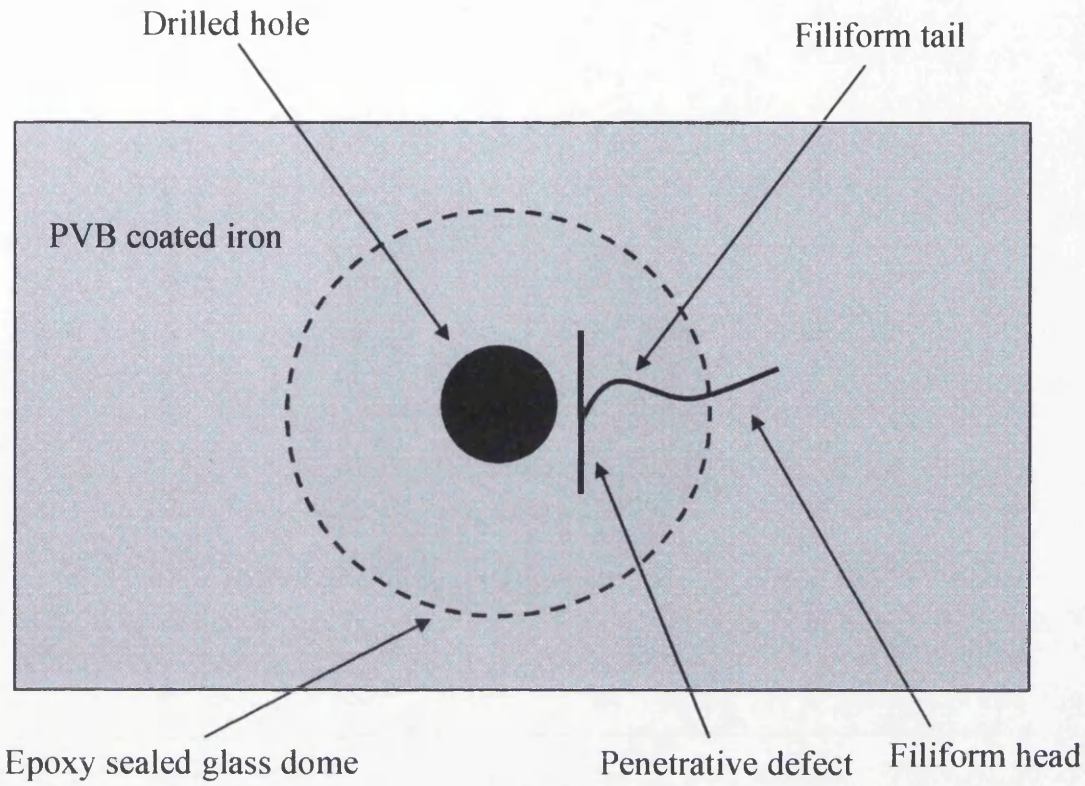

Figure 2.15: Schematic diagram of sample preparation for dual-compartment cell.

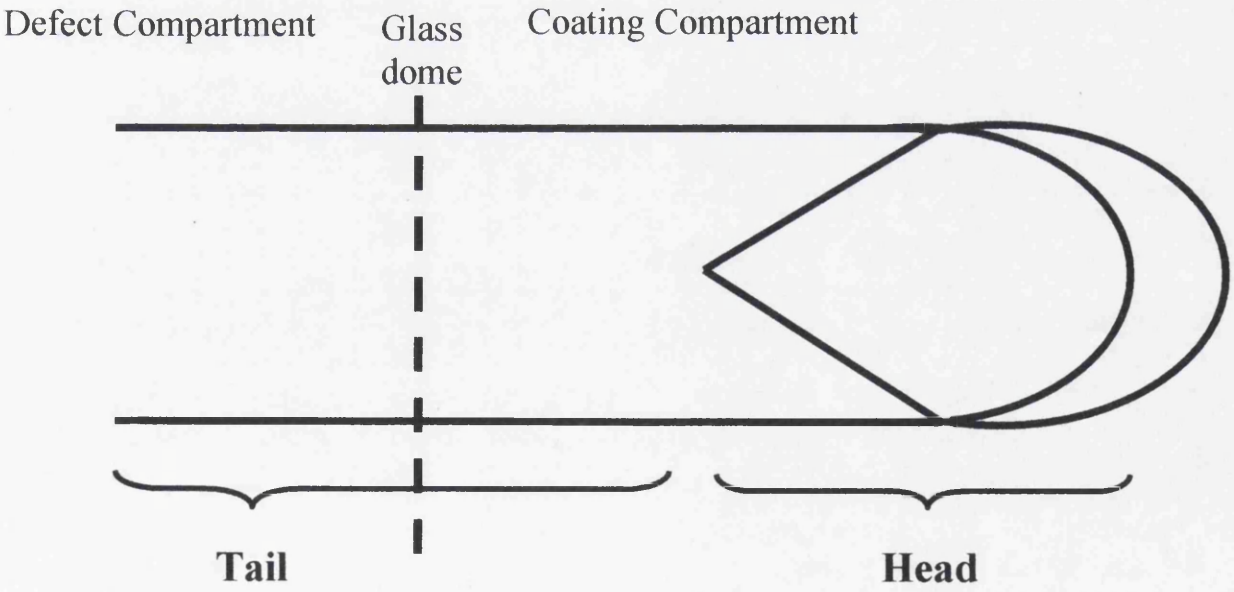

Figure 2.16: Filiform corrosion on iron. The vertical dotted line represents the demarcation of head and tail areas in preparation for exposure to different atmospheres.

2.10.2 Experimental Design

When a suitable individual filament had grown a distance of at least 2 mm away from the defect line a glass dome was sealed onto the surface of the coated iron sample using a two-part epoxy, ensuring that the filament head was outside the dome (*i.e.* present in the coating compartment) with the scribe defect inside the defect compartment, as shown in Fig. 2.15. However it is necessary to clarify at this point the meaning of the term "coating compartment" and "defect compartment" is. Clearly it is not possible to isolate the small droplet of electrolyte that constitutes the true head of a FFC filament. In this experiment "defect compartment" in actual fact means the break in the coating and a certain amount of porous tail that follows whereas "coating compartment" means the head droplet and a certain amount of preceding tail. This portions of the filament exposed to each chamber are shown schematically in Fig. 2.16

The sample was then installed into the three piece compartment setup shown schematically in Fig. 2.17. This consists of two 100 mm wide, 20 mm deep nylon chambers and a third top piece of clear Perspex that allowed the sample to be viewed during testing. The chambers are made air-tight using rubber O-rings placed between the chambers and then clamped together by eight bolts. This setup was primarily designed to allow the head and tail of the filament to be exposed to different atmospheres and secondly to allow large internal pressures to be applied to the compartments. The head of the filament, outside of the sealed dome, is exposed to the upper coating compartment atmosphere, sealed by the clear Perspex top piece. The tail of the filament (inside the dome) is exposed to the lower defect compartment atmosphere via the centre hole (2 mm radius) drilled in the iron sample which maintains the atmosphere in the dome environment. Conditions of *ca.* 25°C and 93% r.h. in isopiestic equilibrium with a saturated sodium sulphate (Na_2SO_4) reference electrolyte were maintained in both compartments throughout all experiments. However, the gas supplied to both the coating compartment and defect compartment was controlled separately and could be varied. This was achieved using a separate gas supply system for the coating and defect chambers. This allowed pre-humidified Air, Argon and Oxygen to be supplied to each chamber as required and gas outlet pipes allowed a constant flow rate to be introduced. The air was pre-humidified by passing the gas through three dreschel bottles (with frit ends) containing $Na_2SO_{4\,(aq)}$.

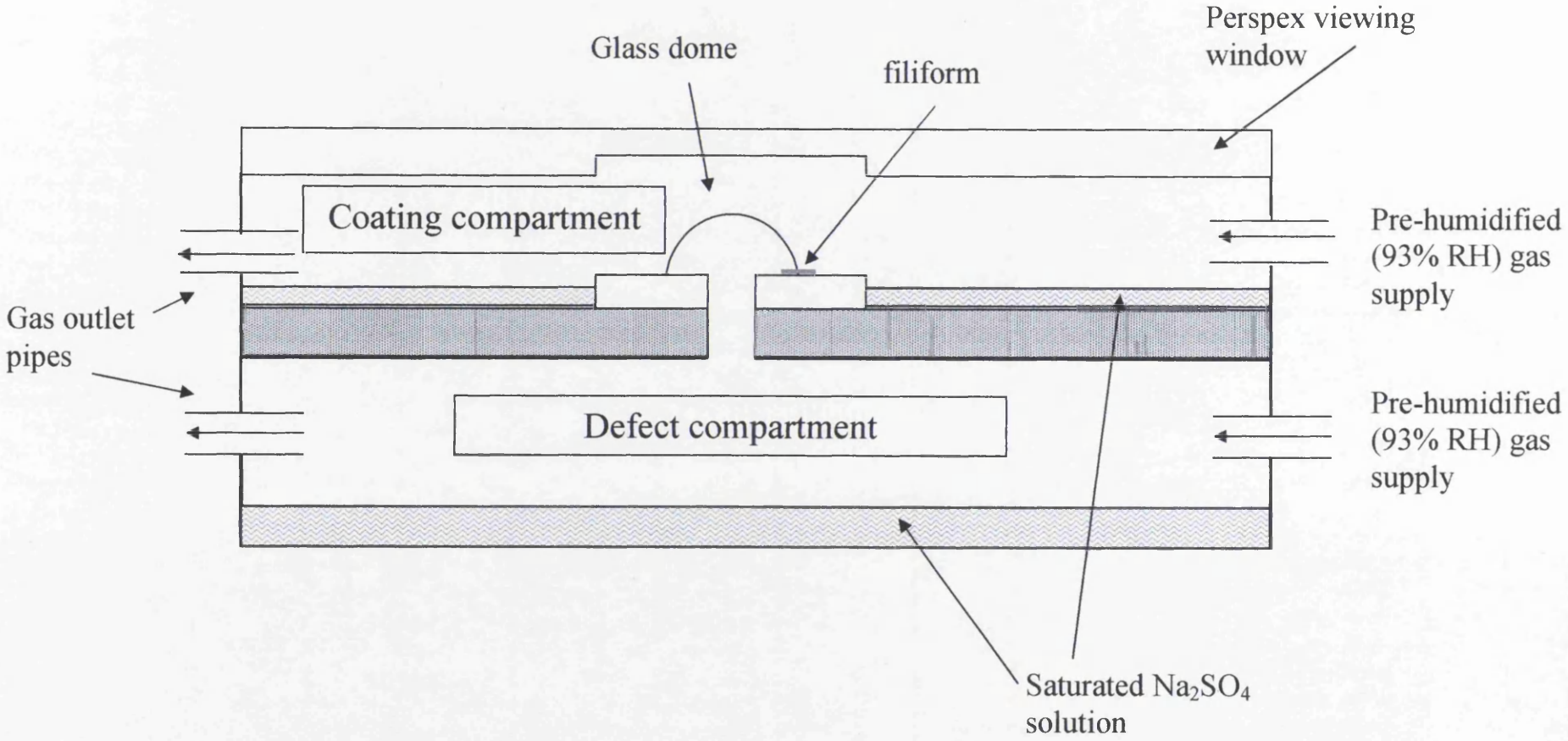

Figure 2.17: Schematic diagram of the 3-piece Dual-Compartment (Watson-Coleman) cell used to isolate the tail and head sections of a filiform.

2.10.3 Imaging

Images were taken *in-situ* of the filiform head at 10 minute intervals using a Nikon Coolpix 4500 digital camera in conjunction with a Meiji reflective light microscope. The visual images produced were subjected to computerised image analysis. In order to calibrate the images, a graticule (Ticules Ltd, cs515) image (1 mm) was taken at the end of every experiment using identical camera settings to those of the experiment. The images were imported into a software image analysis program, Sigma Scan v5.0. The data image was calibrated by using an image of the graticule to correlate image pixel size with actual size.

Following calibration the filament length can be determined at set time intervals according to Fig. 2.18. A line can be drawn between a point that was formerly the front of the filament and the new front of the filament. The software then allows an actual length (in mm) to be attributed to the length of the line. Using this method the cumulative growth of the filament can be determined over set time periods. The width of the filament is determined by drawing a line from the uppermost point of the filament to the lower (as shown in Fig. 2.18).

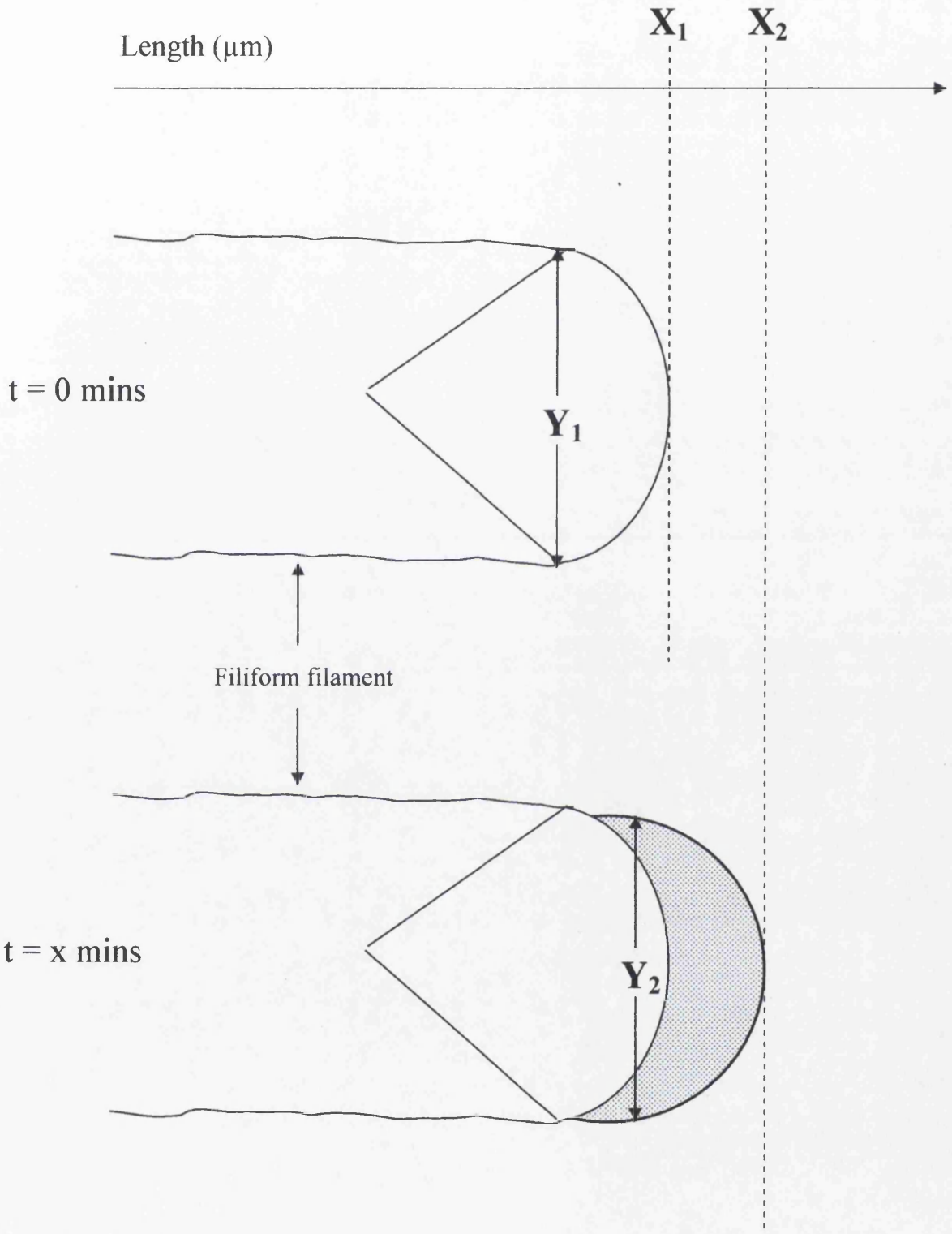

Figure 2.18: Schematic diagram of time lapse imaging of filiform corrosion. Distance $X_2 - X_1$ is the distance grown in 300 minutes. Y_1 is the width of the filiform at t = 0 mins and Y_2 is the width at t = x mins.

2.11 References

1. C. Menardo, M. Nechtscein, A. Rousseau, J. P. Travers and P. Hany, *Synthetic Met.*, **25**, 311 (1988).

2. G. Williams, A. Gabriel, A. Cook and H. N. McMurray, *J. Electrochem. Soc.*, **153**, B425 (2006).

3. L. D. Freedman and G. O. Doak, *Chem. Rev.*, **57**, 479 (1957).

4. http://www.petrik.com/PUBLIC/library/misc/acid_base_pk.htm, Date accessed: 19/09/2006

5. H. Dominghaus, Plastics for Engineers, Munich (1988).

6. J. Stejskal and R. G. Gilbert, *Pure Appl. Chem.*, **74**, 857 (2002).

7. L. J. Gainer and G. R. Wallwork, *NACE*, **35** (1979).

8. H. N. McMurray and D. A. Worsley, Scanning Electrochemical Techniques for the Study of Localised Metallic Corrosion Research in Chemical Kinetics, R. R. Compton and G. Hancock, (1997).

9. J. H. Sullivan, H. N. McMurray, D. J. Penney and D. A. Worsley, *ECS trans.*, **1**, 413 (2006).

10. H. S. Isaacs, *J. Electrochem. Soc.*, **138**, 722 (1991).

11. G. Williams and H. N. McMurray, *Corrosion*, **62**, 231 (2006).

12. D. A. Worsley, H. N. McMurray, J. H. Sullivan and I. P. Williams, *Corrosion*, **60**, 437 (2004).

13. S. Yee, R. A. Oriani and M. Stratmann, *J. Electrochem. Soc.*, **138**, 55 (1991).

14. G. Williams and H. N. McMurray, *J. Electrochem. Soc.*, **150**, B380 (2003).

15. F. E. M. O'Brien, *Journal of Scientific Instruments*, **25**, 73 (1948).

Chapter 3

Scanning Kelvin Probe Studies of Filiform Corrosion on Automotive Aluminium Alloy AA6016-T4

3.1 Introduction

As discussed in Section 1.2.2, there has been an increase in the use of aluminium alloys for automotive skin (enclosure) panels. It is the dual requirement of a relatively low strength, which allows sufficient formability to make a body panel, and a high strength after final painting which has meant that the current alloys of choice in the automotive industry are the 6000 series (Al-Mg-Si(Cu)) alloys. In Europe skin panel gauges tend to be thicker than those used in North America, where a 1 mm or less outer skin gauge is used. This means that in North America a higher strength alloy is needed and they tend to opt for AA6111 which has a final strength of approximately 220MPa.[1] In Europe where the thicker gauge panel is used, alloy AA6016 is generally chosen which has a final strength after final painting of approximately 190MPa.[1] However, both alloys possess a good combination of strength and formability in the solutionised, T4 temper (see Chapter 1, Table 1.2), and strengthen further by precipitation hardening during the final paint-bake process (typically carried out in air at 180°C).

The 6000 series alloys are relatively corrosion resistant, but an integral part of the manufacturing process of automotive enclosure panels involves the mechanical abrasion of the alloy surfaces immediately prior to pre-treatment and painting.[2] Surface abrasion during grinding reintroduces a micrograined deformed layer which reactivates the surface with respect to filiform corrosion (FFC)[2-4] (described in Section 1.4.3.4). Studies of microstructure and corrosion morphology in deformed layers developed by grinding the surface of AA6016 sheet have suggested that the mechanism of activation after paint baking is similar to that for development of intergranular corrosion (IGC) susceptibility in the bulk alloys.[2]

In this chapter, scanning Kelvin probe (SKP) potentiometry in humid air is used to systematically investigate the effect of surface abrasion and subsequent heat treatment on the open-circuit potential of both bulk AA6016-T4 and the shear-deformed surface layer. SKP is also used to follow the kinetics of chloride-induced FFC on organic coated AA6016-T4 and to determine characteristic potentials associated with the FFC localised corrosion cell. The original aim was to establish the relationship between abrasion-induced surface deformation, heat treatment and FFC susceptibility. However, it became a further aim to elucidate the mechanism(s) by which FFC occurs on surface deformed AA6016-T4 and determine more exactly

how the deformed layer acts to increase FFC susceptibility.

3.2 Experimental

All the main experimental procedures and techniques used in this chapter are described in more detail in Chapter 2. Aluminium alloy AA6016-T4 (see Section 2.2.1) was prepared and heat treated for FFC experiments as described in Section 2.5.3. Briefly, "Surface deformed" AA6016-T4 was prepared by subjecting the as received surface to 2 minutes of vigorous manual abrasion with 180 grit silicon carbide (SiC) paper. "Bulk" AA6016-T4 was prepared by etching the abraded surface for 45 secs at 60°C in 10% w/v aqueous NaOH, to remove any deformed layer, followed by desmutting for 30 secs in concentrated nitric acid at 25°C. Any required heat treatment was carried out in air for 2 hours at temperatures (T_{HT}) between 180°C and 350°C, with coupons being allowed to cool naturally in room air. The SKP equipment, calibration and FFC initiation procedures are described in Section 2.5. Unless stated otherwise, all subsequent SKP measurements were carried out in static air at 40°C ± 1°C and 80% relative humidity (r.h.) in isopiestic equilibrium with a saturated aqueous $(NH_4)_2SO_4$ reference solution. The experimental conditions were chosen following extensive preliminary investigations which found that these conditions produced very reproducible results. Therefore, the long FFC SKP experiments shown in this chapter were known to be representative of the susceptibility of the alloy substrate following a particular surface/heat treatment. At the end of each FFC experiment samples were photographed in room air. The polyvinylbutyral (PVB) coating and corrosion products were removed for scanning electron microscope (SEM) analysis as detailed in Section 2.7.

Potentiodynamic polarisation measurements under conditions of electrolyte immersion (near neutral (pH 6.0 – 6.5) 0.5% w/v aqueous NaCl) were carried out as detailed in Section 2.3, using a Solartron SI 1280 potentiostat in conjunction with a gas-tight electrochemical cell incorporating a platinum gauze counter electrode and saturated calomel reference electrode (SCE).

3.3 Results and Discussion

3.3.1 Electrochemical Characterisation of AA6016 Surfaces

Values of $\Delta\psi_{Pol}^{Ref}$ obtained through SKP scanning of PVB covered AA6016 were used in conjunction with Equation 2.8 to calculate E_{corr} at the metal surface, as described in Section 2.5.4. For the purpose of discussion, the term "intact potential" (E_{intact}) designates E_{corr} measured over uncorroded portions of the sample (where the organic coating remains adherent). Typical plots of E_{intact} *vs.* time for samples which have been heat treated at various T_{HT} are given in Fig. 3.1. Each E_{intact} value has been calculated from an average of 480 $\Delta\psi_{Pol}^{Ref}$ data points. Fig. 3.1a shows data for "surface deformed" AA6016 and Fig. 3.1b shows data for "bulk" AA6016, as defined in the Experimental section above. It may be seen that E_{intact} initially changes with time, but becomes approximately constant as samples reach a steady state with the humid SKP atmosphere (air at 80% r.h. and 40°C). Time independent E_{intact} values (calculated as an average over the period of 20 to 35 hours following humid air contact) are summarised in Fig. 3.2. Time independent E_{intact} is significantly lower for surface deformed AA6016 than for bulk AA6016 at all values of T_{HT}. The E_{intact} difference ($\Delta E_{intact} = E_{intact}$ surface deformed - E_{intact} bulk) is *ca.* -0.2 V when $T_{HT} \leq 180°C$ and increases in magnitude to *ca.* -0.5 V when T_{HT} = 350°C.

On the basis of mixed potential theory, the trends in Fig. 3.2 may be understood in terms of the abrasion-induced surface deformed layer being anodically activated and/or cathodically deactivated relative to bulk AA6016 - with these changes being further magnified when post-abrasion $T_{HT} \geq 180°C$. However, caution is necessary when interpreting potentials measured in the absence of a well defined electrolyte and a series of polarisation experiments was therefore carried out in dilute (0.5%), near neutral (pH 6 - 6.5) aqueous NaCl. Figs. 3.3 and 3.4 show polarisation data obtained under aerated and de-aerated conditions respectively. Parts **a)** of Figs. 3.3 and 3.4 derive from surface deformed AA6016 and parts **b)** from bulk AA6016. The individual polarisation curve labels in Figs. 3.3 and 3.4 correspond to: (i) $T_{HT} \leq$ 25°C, (ii) T_{HT} = 180°C and (iii) T_{HT} = 350°C.

For purposes of comparison, values of cathodic current density at -0.76 V *vs.* SHE (j_{ca}) were obtained from the various cathodic polarisation curves in Figs. 3.3a

a)

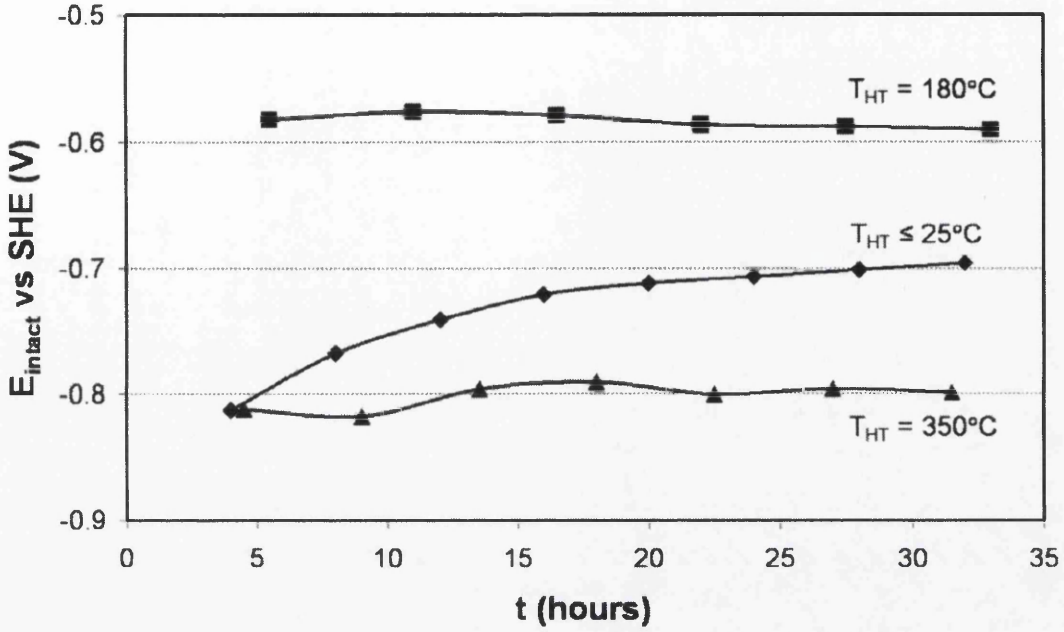

b)

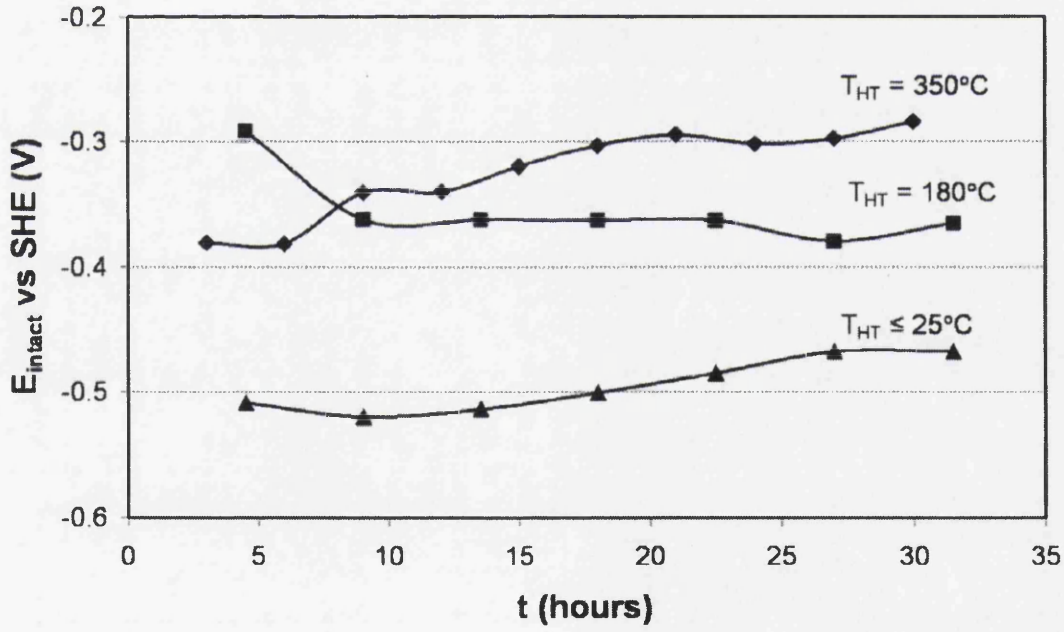

Fig. 3.1: Time-dependent E_{intact} for PVB coated AA6016 in air at 80% r.h. and 40°C. Time is the period elapsed since first contact with the humid SKP atmosphere. **(a)** Surface deformed AA6016. **(b)** Bulk AA6016.

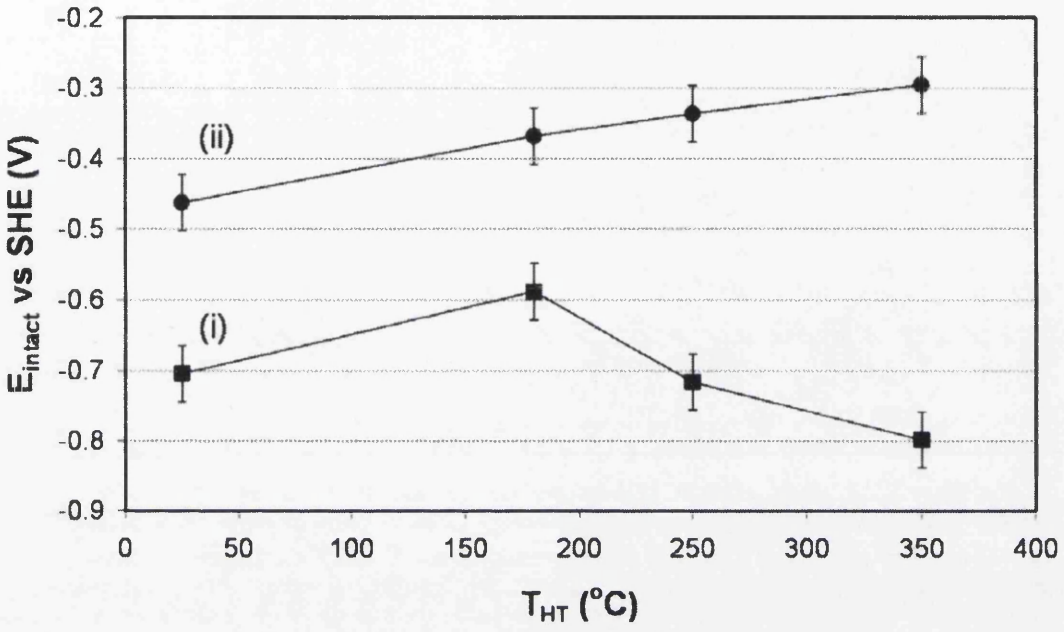

Fig. 3.2: Time-independent E_{intact} for PVB coated AA6016 plotted *vs.* heat treatment temperature (T_{HT}). Each E_{intact} value is calculated from the arithmetic mean of corresponding time-dependent data in Fig. 3.1 between 20 and 30 hours, error bars ± 1 s.d. Curve **(i)** surface deformed AA6016. Curve **(ii)** Bulk AA6016.

a)

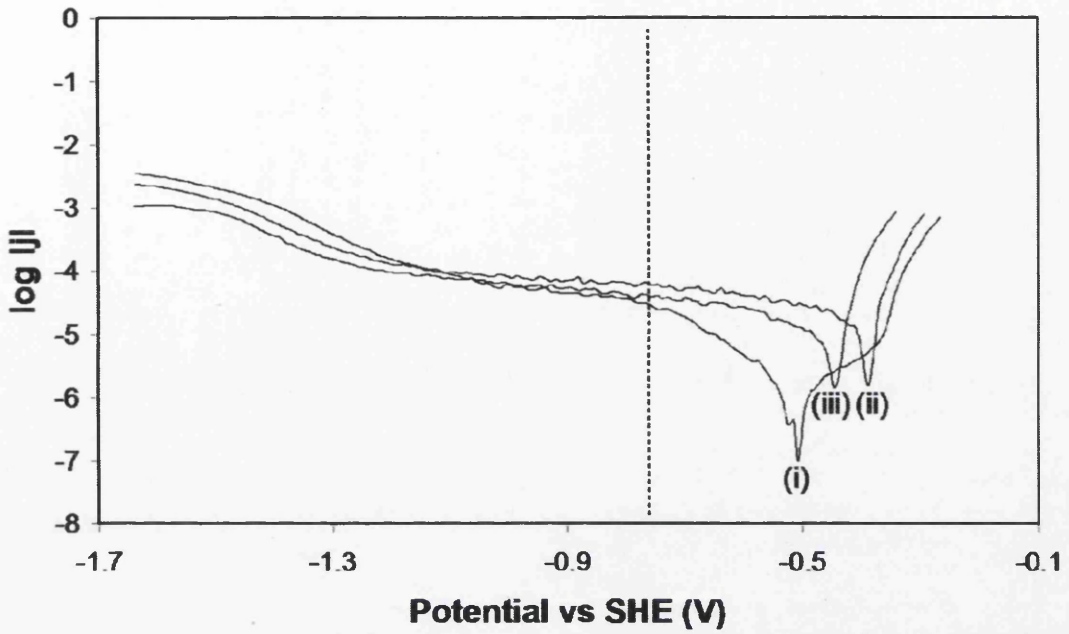

b)

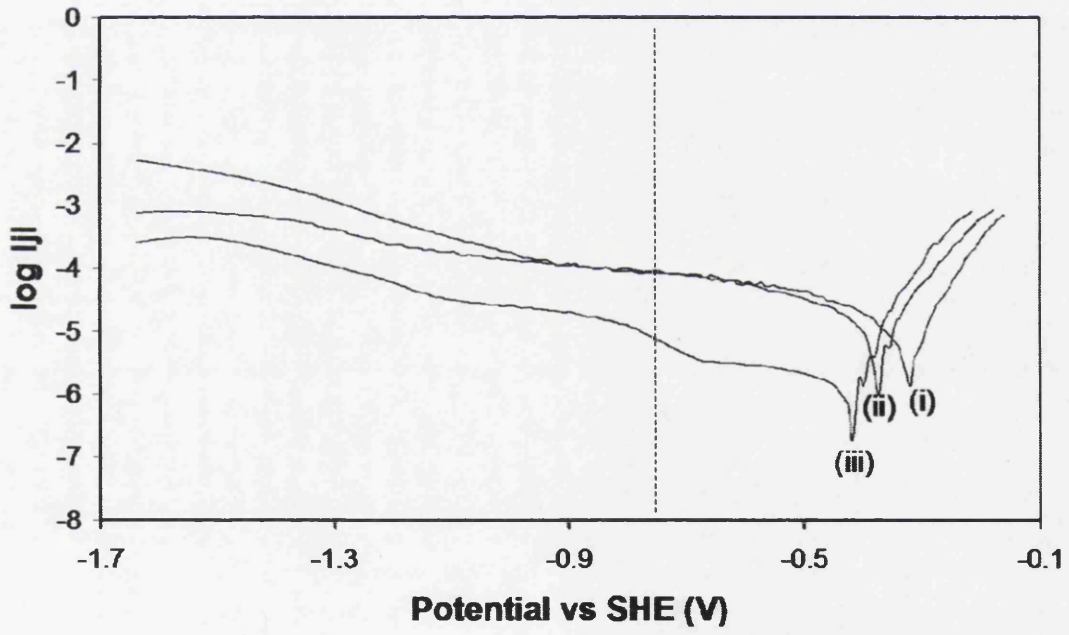

Fig. 3.3: Potentiodynamic polarization curves for AA6016 in aerated 0.5% aqueous NaCl at pH 6.5. **a)** Surface deformed AA6016. **b)** Bulk AA6016. Heat treatment temperature key: T_{HT} = **(i)** $\leq 25^{o}C$ **(ii)** $180^{o}C$ and **(iii)** $350^{o}C$.

a)

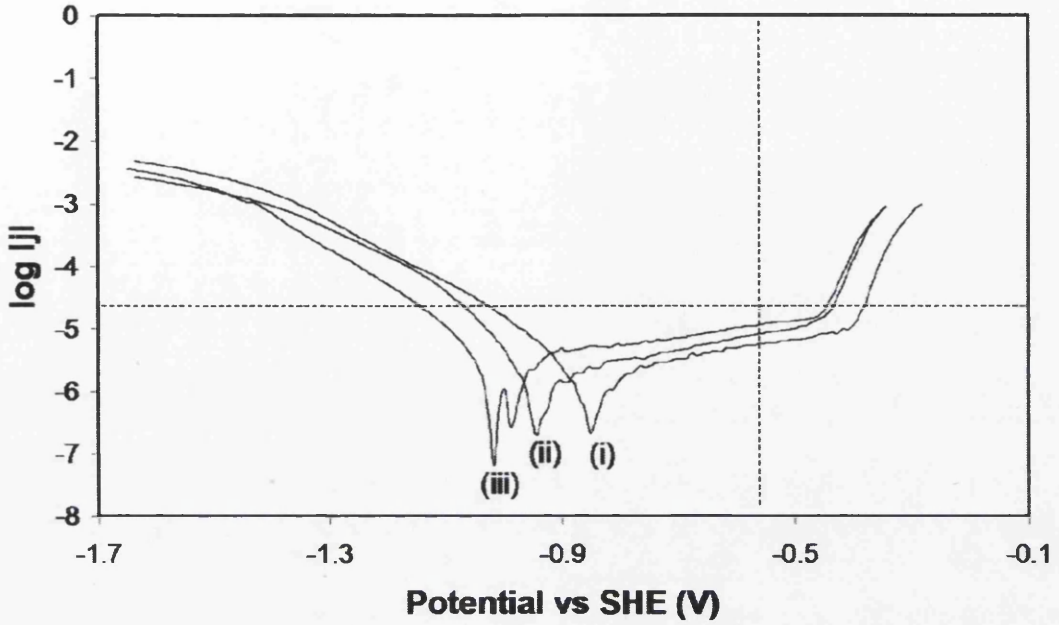

b)

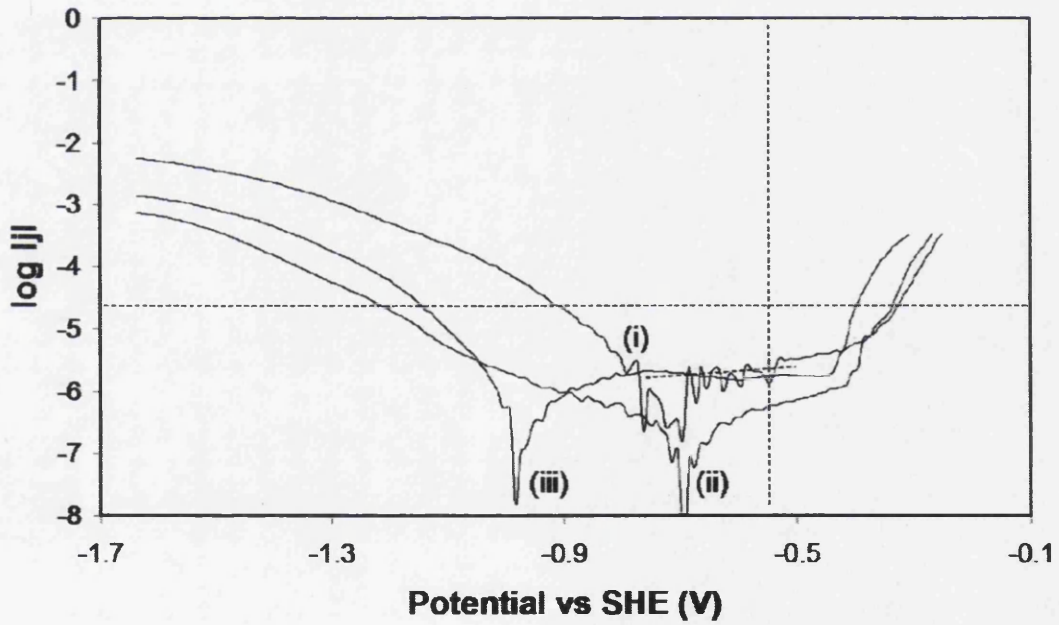

Fig. 3.4: Potentiodynamic polarization curves for AA6016 in de-aerated 0.5% aqueous NaCl at pH 6.5. **a)** Surface deformed AA6016. **b)** Bulk AA6016. Heat treatment temperature key: T_{HT} = **(i)** $\leq 25^{o}C$ **(ii)** $180^{o}C$ and **(iii)** $350^{o}C$.

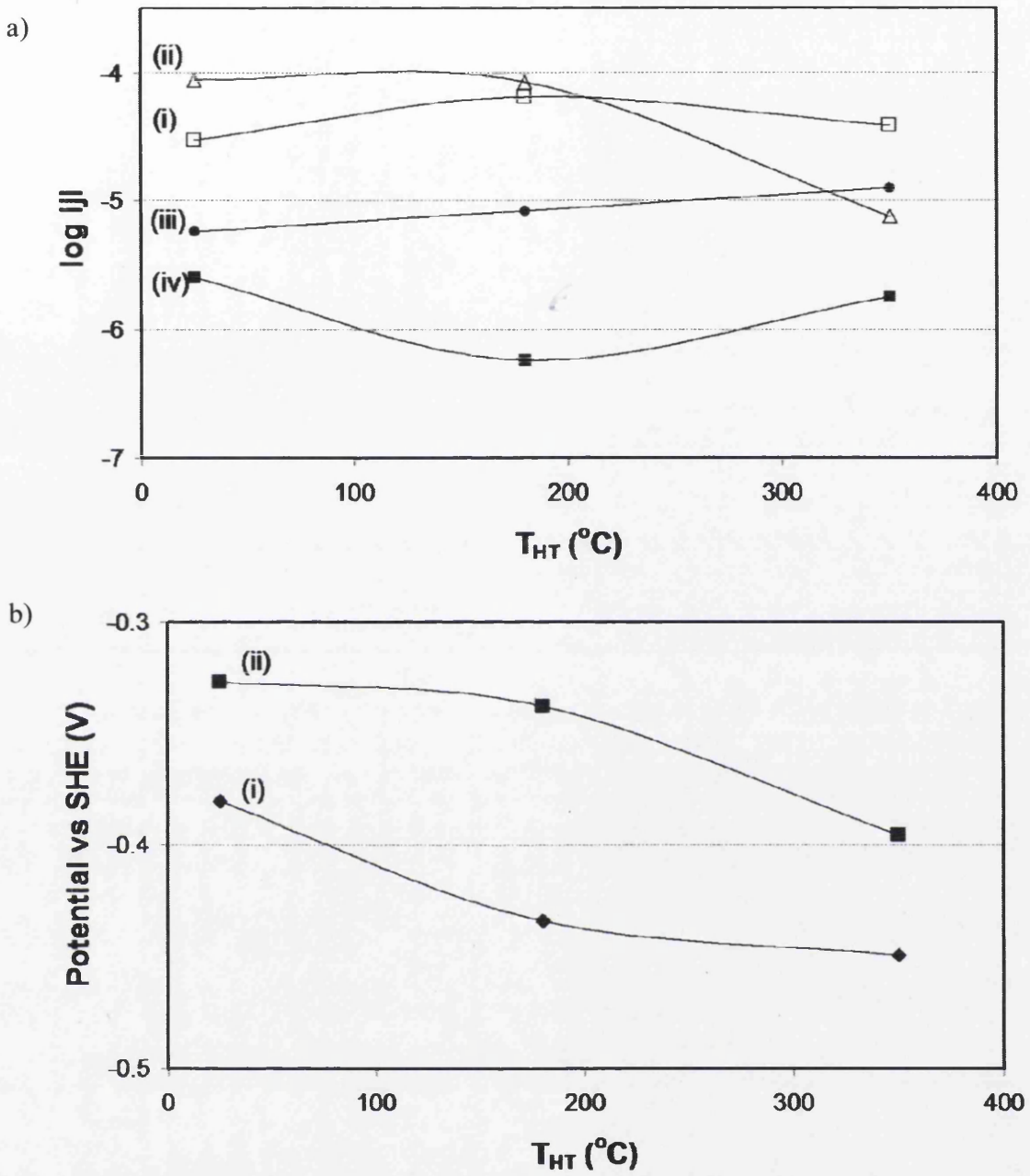

Fig. 3.5 Part **a)** Cathodic (j_{ca}) and anodic (j_{an}) current densities as a function of T_{HT}. **(i)** j_{ca} for surface deformed AA6016, **(ii)** j_{ca} for bulk AA6016, **(iii)** j_{an} for surface deformed AA6016 and **(iv)** j_{an} for bulk AA6016. Part **b)** Anodic breakdown potentials (E_b) for **(i)** surface deformed AA6016 and **(ii)** bulk AA6016. Note: j_{ca} values obtained at -0.76V *vs.* SHE (vertical dotted line in Figs. 3.3a and 3.3b), j_{an} values obtained at -0.55V *vs.* SHE (vertical dotted line in Figs. 3.4a and 3.4b). E_b obtained at $j_{an} = 2 \times 10^{-5}$ A cm^{-2} (horizontal dotted line in Figs. 3.4a and 3.4b).

and 3.3b., and are plotted as a function T_{HT} in curves (i) and (ii) of Fig. 3.5a respectively. There is no evidence of any significant increase in j_{ca} with T_{HT} for either bulk or surface deformed AA6016. Consequently, and in contrast to Al alloys which contain significant quantities of Fe and Mn,[5-8] (as discussed in Section 1.4.3.4) there is no reason to suggest that preferential precipitation of cathodically active intermetallic phases occurs within the deformed layer on AA6016. This finding is consistent with the observation that copper-containing Q phase precipitates do not form in low-copper AA6016[9] (see Section 1.4.1). The decrease in j_{ca} values observed on bulk AA6016 when T_{HT} = 350°C possibly results from a thermally promoted growth of surface oxide and a partial blocking of cathodic electron transfer by the resulting oxide film.

All the anodic polarisation curves in Figs. 3.4a and 3.4b exhibit passivity, with passive current densities in the range 10^{-6} to 10^{-5} Acm^{-2}. The charge calculated by integrating under each anodic curve between E_{corr} and the breakdown potential, E_b (here defined as the potential at which current density becomes $\geq 2 \times 10^{-5}$ Acm^{-2}) was < 10% of the anodic charge required to dissolve 1 μm of aluminium as Al^{3+} (note: this calculation is shown in Appendix A). The data in Fig. 3.4a may therefore be assumed to derive primarily from the abrasion-induced surface deformed layer; whereas, the data in Fig. 3.4b derive from the bulk. Values of E_b obtained from the various curves in Figs. 3.4a and 3.4b are plotted *vs.* T_{HT} in curves (i) and (ii) of Fig. 3.5b. When $T_{HT} \leq 25°C$ the value of E_b on surface deformed AA6016 is *ca.* 0.05 V lower than E_b on bulk AA6016. This E_b difference increases when $T_{HT} > 25°C$ and reaches *ca.* 0.1 V at the "paint bake" temperature T_{HT} = 180°C.

The above findings are immediately explicable on the basis of a thermally promoted grain boundary (gb) precipitation of ß″ Mg_2Si particles, as described in Section 1.4.1. It is reasonable to expect that a preferential anodic dissolution of the ß″ phase will leave behind a population of microscopic surface "cracks" or "crevices" and so facilitate gb attack. The finding that E_b becomes significantly lowered in the presence of a deformed layer is then consistent with the micrograined nature of deformed layers on AA6016 and the consequently higher number density of grain boundaries. It is also possible that high levels of strain present within the deformed layer actively promote gb ß″ precipitation. Strain induced precipitation would also explain the finding that surface deformation lowers E_b even when $T_{HT} \leq$

25°C.

For the purpose of comparison passive anodic current densities at -0.55 V *vs.* SHE (j_{an}) were obtained from the various polarisation curves in Figs. 3.4a and 3.4b, and are plotted *vs.* T_{HT} in curves (iii) and (iv) of Fig. 3.5a respectively. When $T_{HT} \leq$ 25°C the value of j_{an} on surface deformed AA6016 is only *ca.* 1.6 times > j_{an} on bulk AA6016. However, this difference increases when T_{HT} > 25°C and reaches a factor of *ca.* 10 when T_{HT} = 180°C. As argued previously in the case of E_b changes, the precipitation of ß″ Mg_2Si and subsequent preferential anodic ß″ dissolution may be responsible for the steady increase in j_{an} with T_{HT} seen for surface deformed AA6016 in Fig. 3.5a. The failure to observe (in the same Fig.) a parallel trend for bulk AA6016 could reflect the lower gb number density in the bulk alloy. However, other factors, such as thermally promoted oxide growth, might also influence passive current density and oppose the effects of ß″ precipitation.

It is evident from Figs. 3.5a and 3.5b that deformed layers introduced by surface abrasion of AA6016 are anodically activated relative to the underlying bulk alloy. The extent of anodic activation increases upon heat treatment at T_{HT} > 25°C and becomes very pronounced at the automotive "paint bake" temperature of T_{HT} = 180°C. The anodic activation of surface deformed AA6016 shown in Figs. 3.4 and 3.5 under immersion conditions is immediately consistent with the changes in E_{intact} shown in Fig. 3.2 under atmospheric conditions. There is no evidence of any cathodic activation process, so that any increase in corrodibility which is observed to accompany the surface abrasion of AA6016 may be confidently ascribed to anodic activation alone. This is, in turn consistent with the predicted absence of cathodic Q phase $Cu_2Mg_8Si_7Al_4$ in low copper AA6016.[9]

3.3.2 Filiform Corrosion Kinetics

The 1 µl aliquot of 2 M aqueous HCl injected to initiate FFC is expected to react stoichiometrically with the metal substrate to produce the various (partially hydrolysed) chloride salts (principally $AlCl_3$) which subsequently constitute the filament-head electrolyte.[10] This electrolyte exists in equilibrium with the humid SKP atmosphere and therefore in equilibrium with the saturated $(NH_4)_2SO_4$ reference solution. The filament-head and reference electrolytes will be isopiestic, *i.e.* their concentrations will be such that they exhibit an equal vapour pressure (of water)[11-15]

and hence water activity.[11] Consequently, similar quantities and compositions of filament head electrolyte should result from each initiation and any differences in subsequent FFC propagation result entirely from differences in substrate corrosion resistance.[16] As such, the aqueous HCl injection method is intended to create greater reproducibility than methods involving sample exposure to salt fog,[17] exposure to HCl vapour,[18] or immersion in aqueous electrolyte (including aqueous NaCl, $AlCl_3$, and HCl).[19-22]

When subject to FFC initiation as above, PVB coated bulk AA6016 samples in the as-received T4 temper ($T_{HT} \leq 25°C$) were found to be effectively corrosion resistant, *i.e.* no FFC filaments could be detected, either visually or using SKP over a 7 day experimental period. In contrast, all the surface deformed AA6016 samples were found to exhibit a rapid, superficial attack consistent with "surface-active" FFC. That is to say, a form of FFC in which metal dissolution is restricted to the depth of the abrasion-induced surface deformed layer. Surface-active FFC was observable regardless of heat treatment temperature, over the range $T_{HT} \leq 25°C$ to $T_{HT} = 350°C$. However, surface deformed samples with T_{HT} between 180°C and 350°C were also found to exhibit a slower, more deeply penetrating, secondary mode of attack consistent with "successive-pitting"[23] FFC. The mechanisms underlying both surface-active and successive-pitting FFC will be discussed further in Section 3.3.3.

The matrix of $\Delta\psi_{Pol}^{Ref}$ values obtained in the course of each SKP scan was used in conjunction with Equation 2.8 to calculate the instantaneous distribution of E_{corr} values existing at the AA6016 surface. SKP data obtained at different times (t) following FFC initiation could then be used to visualise the dynamic evolution of E_{corr} patterns associated with filament propagation (see Section 1.6.2.2). Fig. 3.6 shows representative grey-scale maps of E_{corr} distribution obtained at (a) t = 4 hours (b) t = 84 hours and (c) t = 132 hours over PVB coated surface deformed AA6016 with $T_{HT} \leq 25°C$. Fig. 3.6d shows a photographic image of the same sample at the end of the experimental period. Figs. 3.7 and 3.8 show similar data for surface deformed samples with $T_{HT} = 180°C$ and $T_{HT} = 350°C$, respectively. It should be noted that the SKP calibration constant (C in Equation 2.8) for PVB covered metal has been used throughout. Consequently E_{corr} values associated with the scribed defect (*i.e.* bare metal) in Figs. 3.6-3.8 may be underestimated by up to 0.22 V.[24]

In parts a-c of Figs. 3.6, 3.7 and 3.8 E_{intact} is *ca.* -0.7V, -0.6V and –0.8V *vs.*

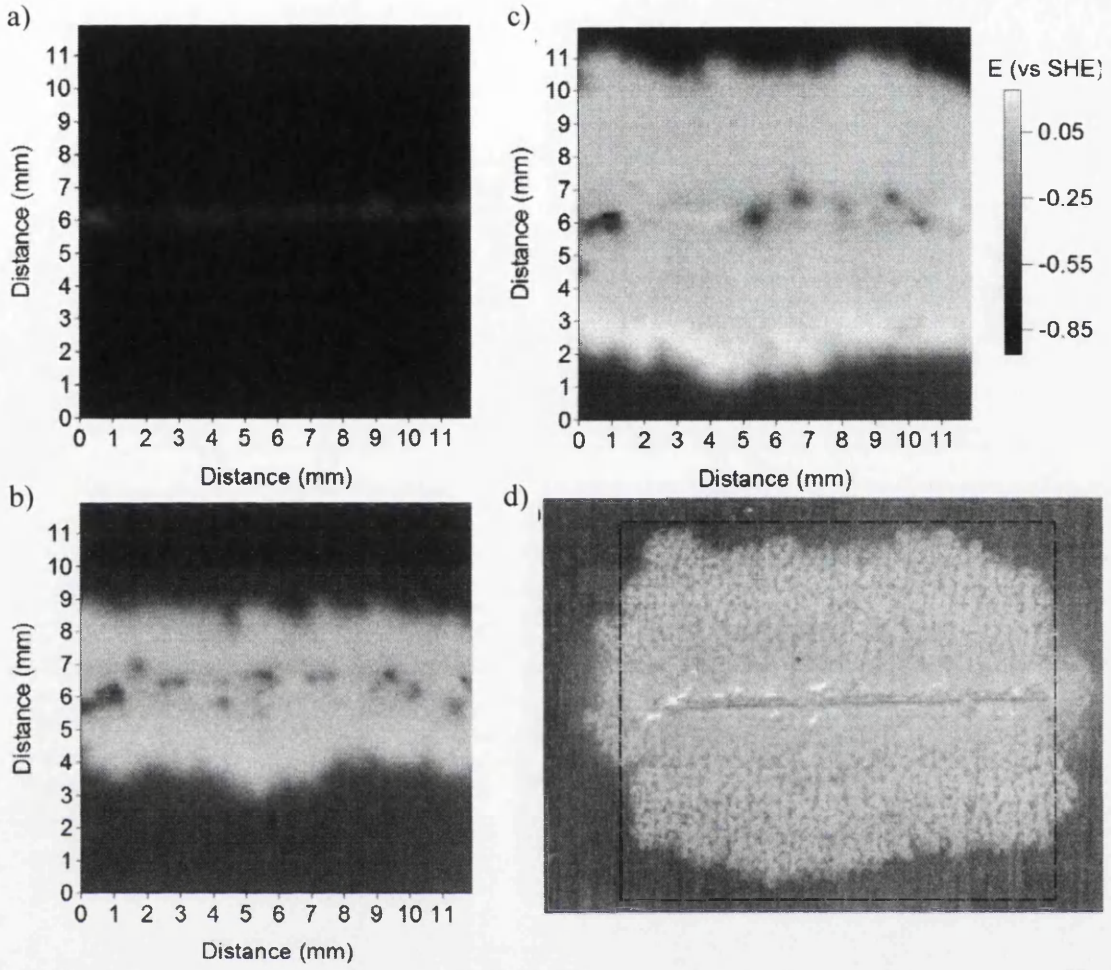

Fig. 3.6: Interpolated greyscale maps showing E_{corr} distribution measured in air at 80% *r.h.* and 40°C over PVB coated, surface deformed AA6016 ($T_{HT} \leq 25^{o}C$). Time key: (a) t = 4 hours (b) t = 84 hours and (c) t = 132 hours following FFC initiation. A photographic image of the sample at t = 132 hours is shown in (d); the area scanned using SKP is indicated by a dashed line.

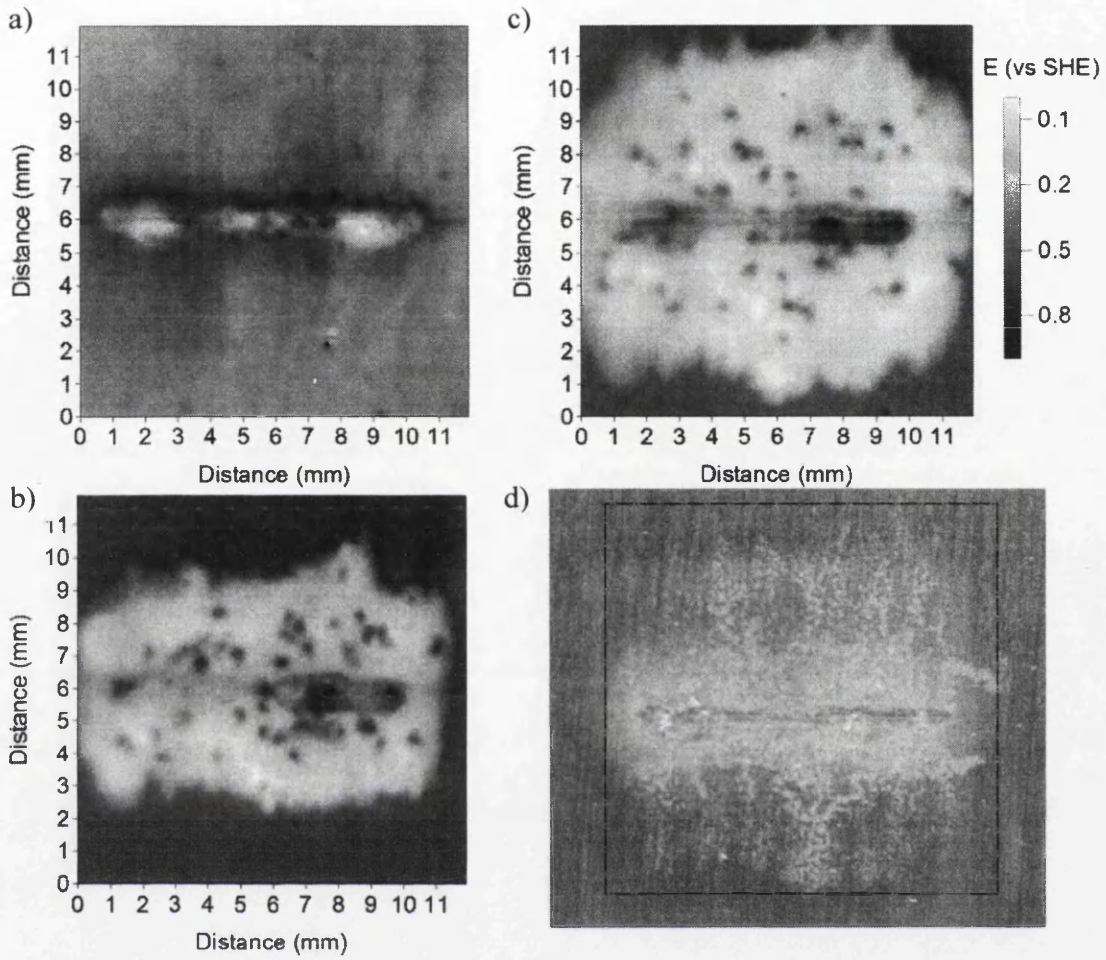

Fig. 3.7: Interpolated greyscale maps showing E_{corr} distribution measured in air at 80% *r.h.* and 40°C over PVB coated, surface deformed AA6016 (T_{HT} = 180°C). Time key: (a) t = 4 hours (b) t = 84 hours and (c) t = 132 hours following FFC initiation. A photographic image of the sample at t = 132 hours is shown in (d); the area scanned using SKP is indicated by a dashed line.

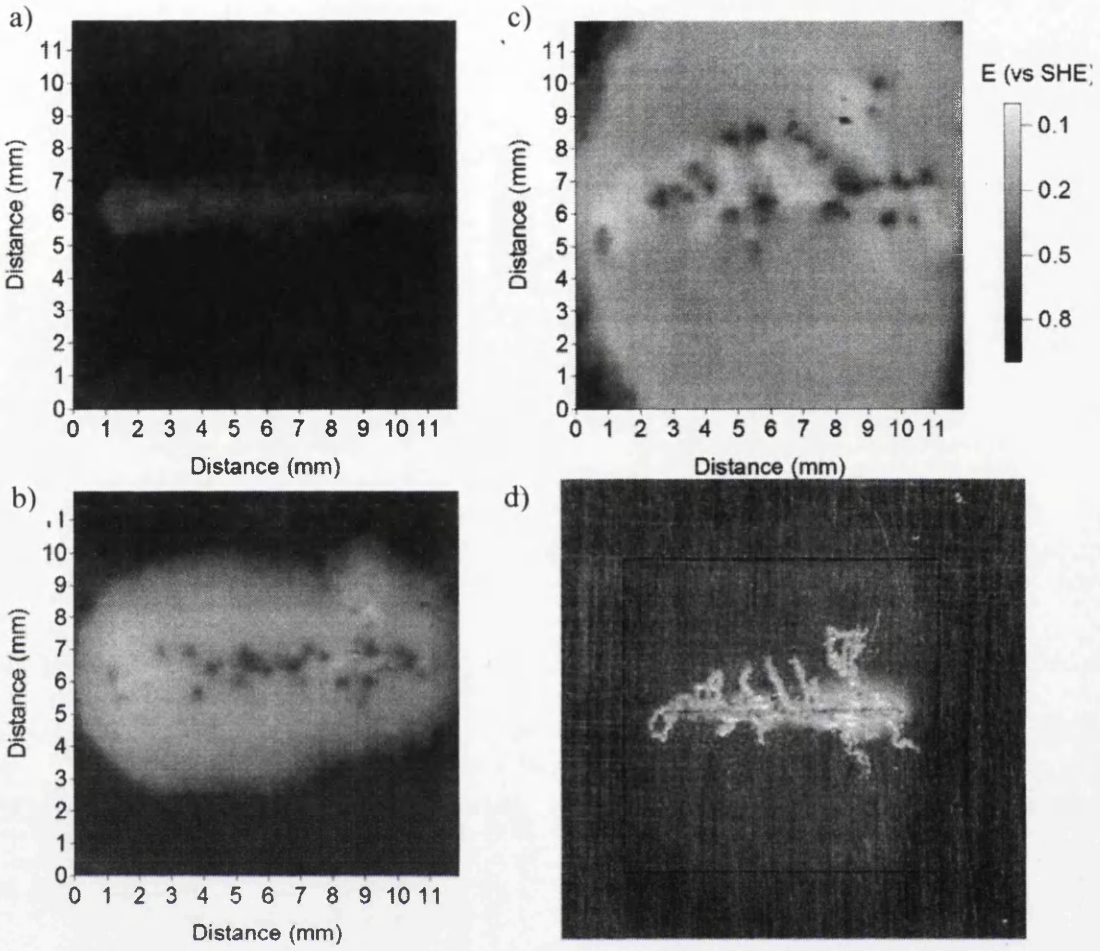

Fig. 3.8: Interpolated greyscale maps showing E_{corr} distribution measured in air at 80% *r.h.* and 40°C over PVB coated, surface deformed AA6016 (T_{HT} = 350°C). Time key: (a) t = 4 hours (b) t = 84 hours and (c) t = 132 hours following FFC initiation. A photographic image of the sample at t = 132 hours is shown in (d); the area scanned using SKP is indicated by a dashed line.

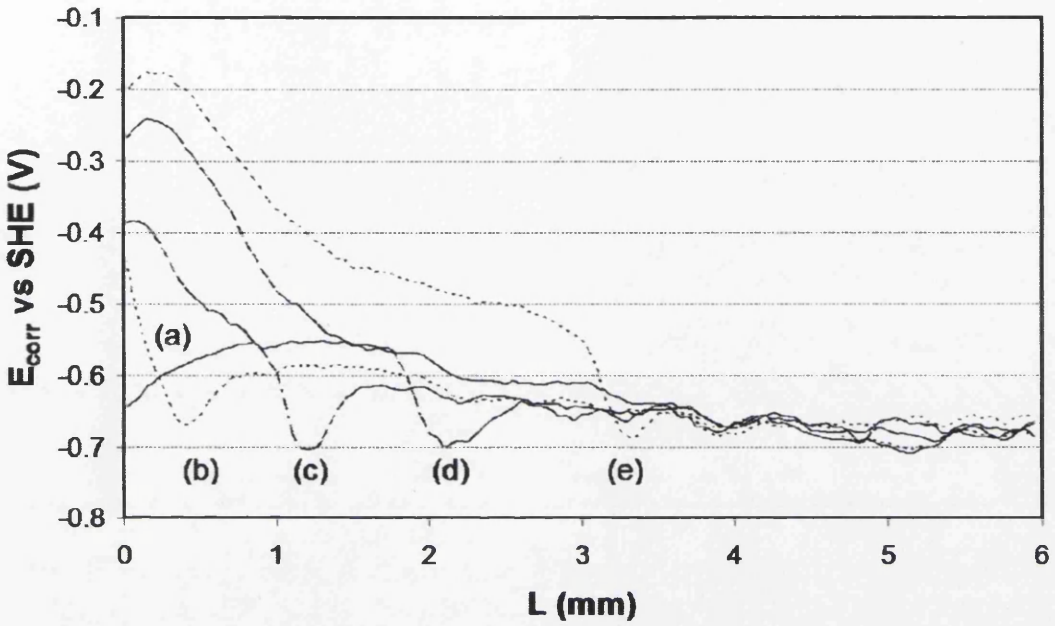

Fig. 3.9: Profiles of E_{corr} as a function of distance (L) from the defect edge plotted centrally along the axis of filament propagation for "surface-active" FFC on PVB coated, surface deformed AA6016 (T_{HT} = 180°C). Time key: (a) 25, (b) 55, (c) 110, (d) 160 and (e) 245 hours after FFC initiation. Note, SKP probe diameter is 50 μm and experimental temperature is non-standard (20°C).

SHE respectively. Individual surface-active corrosion filaments are not resolved by the SKP probe.[25] Surface-active FFC therefore appears as a continuous narrow front (*ca.* 0.3 mm from front to back) of relatively low potential (E_{corr} = *ca.* -0.8V) propagating away from the coating defect and leaving in its wake an area of increased potential (E_{corr} = *ca.* -0.1V *vs.* SHE). The time-dependent potential relationships in surface-active FFC are, however, best understood in Fig. 3.9, which shows E_{corr} profiles measured along the axis of filament propagation. The filament-head E_{corr} minimum moves at constant velocity from left to right, while E_{corr} values in the wake of the advancing head increase with time. In part d of Figs. 3.6-3.8 a whitish corrosion product is distributed over a partially coalesced mass of narrow (0.1 – 0.2 mm diameter) filaments which extend up to 12 mm away from the coating defect. A comparison of SKP and photographic data supports the notion that the corrosion front in parts a-c of Figs. 3.6-3.9 corresponds to the surface-active FFC filament head and the wake region corresponds to the surface-active FFC tail.

The propagation kinetics of surface-active FFC were followed by using SKP derived E_{corr} maps to determine surface-active filament length L_s. The value of L_s at any time (t) following FFC initiation was taken to be the mean distance (measured normal to the coating defect) between the defect and the advancing corrosion front - visible as a potential minimum in the corresponding E_{corr} map. Fig. 3.10 shows L_s plotted *vs.* t for PVB coated surface deformed AA6016 with heat treatment temperatures of: a) $T_{HT} \leq 25°C$, b) $T_{HT} = 180°C$, c) $T_{HT} = 250°C$ and d) $T_{HT} = 350°C$. Curves a)-d) are all reasonably straight lines, implying that rates of filament propagation (dL_s/dt) remain approximately constant over the experimental period. Values of dL_s/dt gradient obtained by least squares analysis of individual data sets in Fig. 3.10 are plotted *vs.* T_{HT} in Fig. 3.11, and increase from 0.35 mm/hour when $T_{HT} \leq 25°C$ to 0.1 mm/hour when $T_{HT} = 350°C$. Values of ΔE_{intact} (E_{intact} surface deformed - E_{intact} bulk) are also plotted in Fig. 3.11 and a correlation is apparent whereby increasing dL_s/dt coincides with increasingly negative ΔE_{intact} when $T_{HT} > 180°C$.

In parts a-c of Figs. 3.6, 3.7 and 3.8 small circular regions (*ca.* 0.2 mm diameter) of relatively low potential (E_{corr} = *ca.* -0.55V *vs.* SHE) are seen to become established on or near the coating defect. On samples with $T_{HT} \leq 25°C$ (Fig. 3.6) these low E_{corr} "discs" remain near the defect edge throughout. However, on

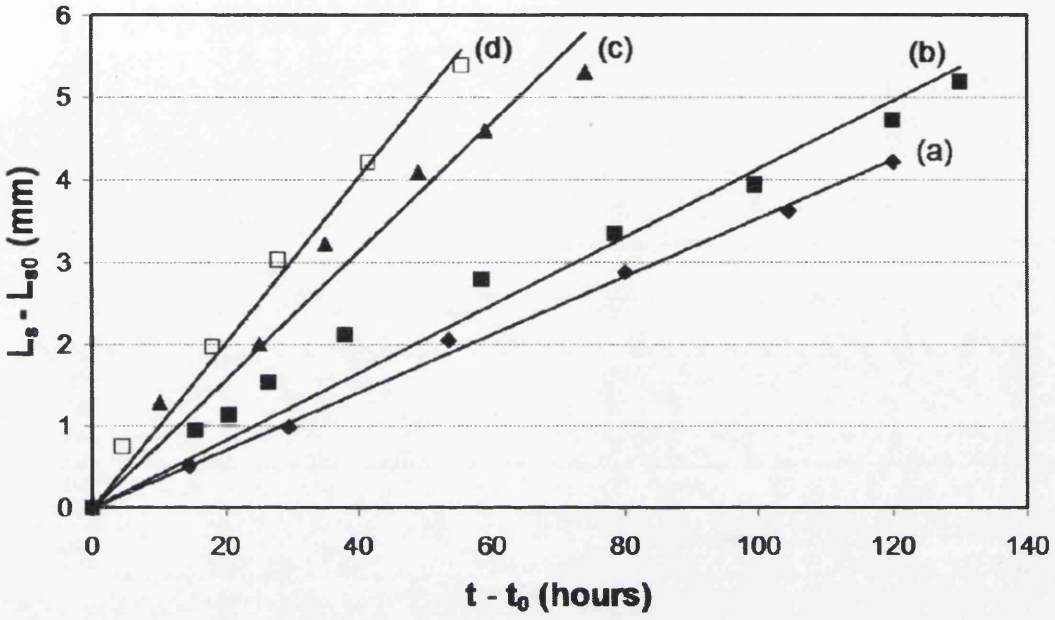

Fig. 3.10: Plot of "surface-active" filament length (L_s) *vs.* time (t) since FFC initiation on PVB coated, surface deformed AA6016. Heat treatment temperature key: T_{HT} = a) ≤ 25°C, b) 180°C, c) 250 °C and d) 350°C. The quantity L_{s0} is the value of L_s in the first SKP scan, acquired at time t_0.

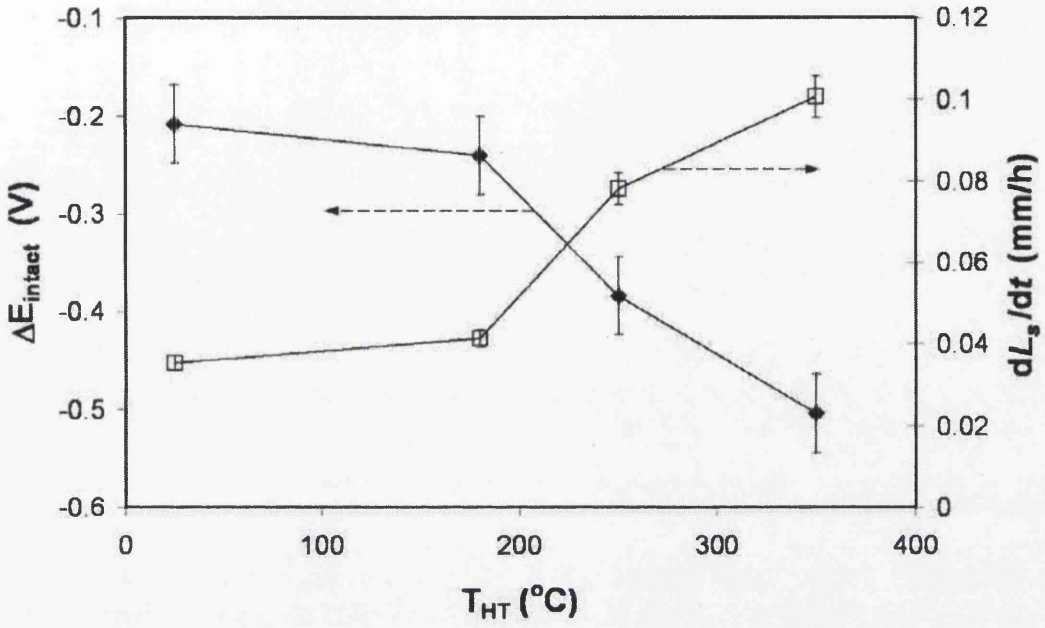

Fig. 3.11: Summary plots of surface-active filament propagation rate (dL_s/dt) and ΔE_{intact} (E_{intact} surface deformed - ΔE_{intact} bulk) *vs.* heat treatment temperature (T_{HT}) for PVB coated, surface deformed AA6016. Values of dL_s/dt calculated as least squares gradient of corresponding data sets in Fig. 3.10, with error bars ± 5%. Values of ΔE_{intact} calculated from corresponding data sets in Fig. 3.2.

samples with $T_{HT} \geq 180°C$ (Figs. 3.7 and 3.8) low E_{corr} discs propagate away from the defect and over the high E_{corr} region left in the wake of primary, surface-active, FFC. When the PVB coating was finally removed these low E_{corr} discs were found to co-locate with the heads of "successive-pitting" type FFC filaments, as will be discussed more fully in the following subsection. In Fig. 3.8 "tails" of increased E_{corr} (*ca.* 0.05V) may just be distinguished behind the successive-pitting FFC heads. The time-dependent potential relationships are, however, best understood in Fig. 3.12, which shows E_{corr} profiles measured centrally along the axis of filament propagation. The successive-pitting filament-head E_{corr} minimum moves at constant velocity from left to right, whilst E_{corr} values in the wake of the advancing head increase with time to form the tail. Similar E_{corr} profiles have been reported elsewhere for FFC on aluminium alloy AA2024.[24,26]

Parts a-c of Figs. 3.7 and 3.8 indicate that successive-pitting FFC propagates in a region of the sample where any deformed surface layer has already been substantially removed by preceding surface-active FFC. This suggests that susceptibility to successive-pitting FFC is independent of surface deformation and depends instead upon the temper of underlying bulk AA6016. In order to test this hypothesis a PVB coated bulk AA6016 sample was prepared with $T_{HT} = 180°C$. Fig. 3.13a shows an E_{corr} map and Fig. 3.13b a photographic image of the same sample 90 hours after FFC initiation. Comparison of Fig. 3.13b and Fig. 3.8d shows that successive-pitting FFC has indeed occurred. However, in contrast to Figs. 3.7c and 3.8c, Fig. 3.13a shows no evidence of preceding surface-active FFC. It therefore seems reasonable to conclude that susceptibility to successive-pitting FFC is indeed determined by the temper of bulk AA6016 and that neither a pre-existing deformed surface layer nor preceding surface-active FFC is required for successive-pitting FFC to occur.

The propagation of successive-pitting, filaments followed a "random walk" pattern (although filaments were not observed to cross), *i.e.* there was no evidence of directionality along the original rolling or grinding directions. The true length of successive-pitting filaments was therefore estimated as the geometric length of the tail (as opposed to the defect-head distance). An arithmetic mean length (L_p) was calculated for the 5 most significant (longest) successive-pitting filaments on each experimental sample. Fig. 3.14 shows plots of L_p *vs.* time since FFC initiation (t) for PVB coated surface deformed AA6016 with heat treatment temperatures of: a) $T_{HT} \leq$

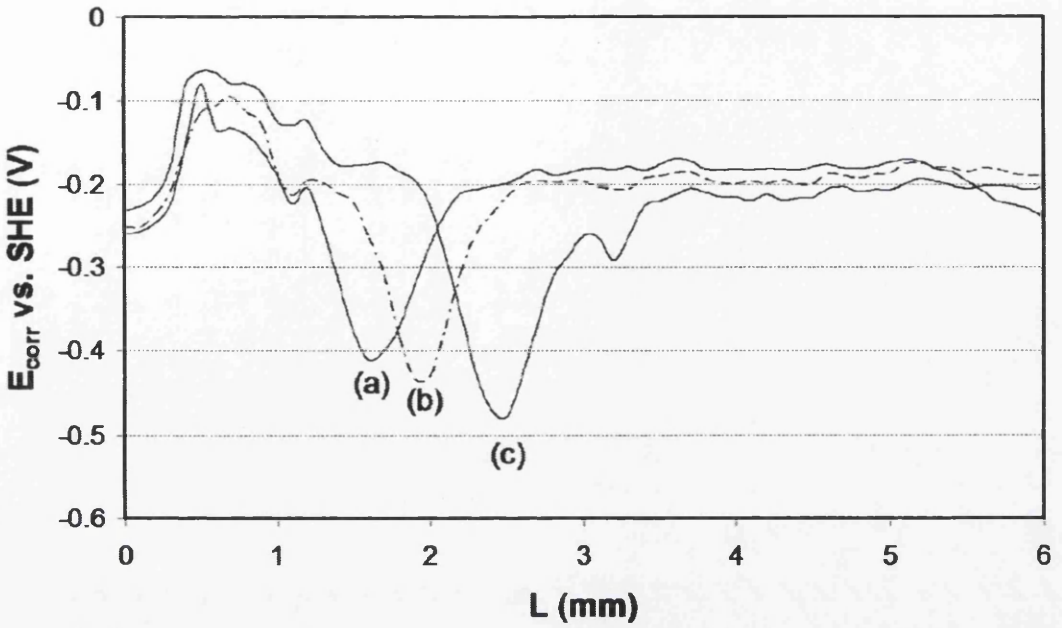

Fig. 3.12: Profiles of E_{corr} as a function of distance (L) from the defect edge plotted centrally along the axis of filament propagation for "successive-pitting" FFC on PVB coated, surface deformed AA6016 T_{HT} = 350°C. Time key: (a) 74, (b) 93 and (c) 120 hours after FFC initiation.

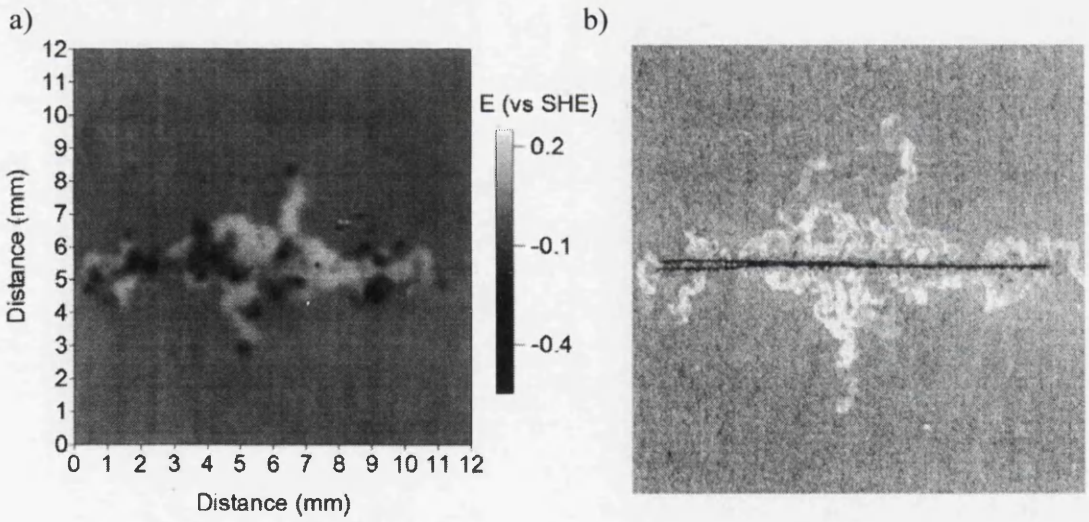

Fig. 3.13. a) Interpolated greyscale maps showing E_{corr} distribution measured 90 hours after FFC initiation on PVB coated, bulk AA6016 (T_{HT} = 180°C) in air at 80% *r.h.* and 40°C. **b)** A photographic image of the same sample.

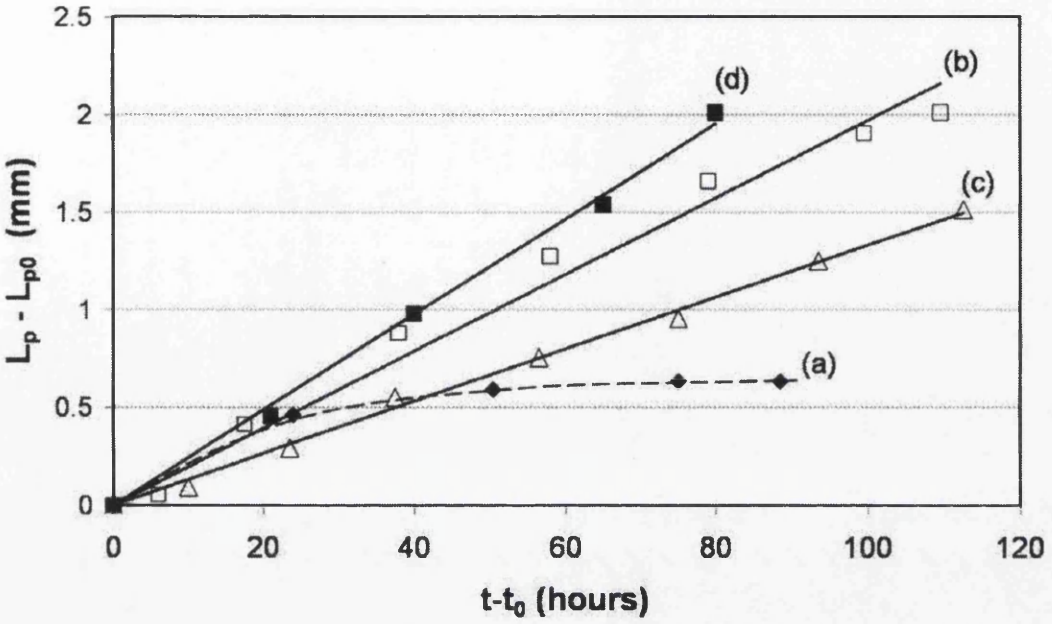

Fig. 3.14: Plot of mean "successive-pitting" filament length (L_p) *vs.* time (t) since FFC initiation on PVB coated AA6016. **a)** surface deformed AA6016, $T_{HT} \leq 25^{o}C$: **b)** surface deformed AA6016, $T_{HT} = 180^{o}C$ and **c)** surface deformed AA6016, $T_{HT} = 350^{o}C$ and **d)** bulk AA6016, $T_{HT} = 180^{o}C$. The quantity L_{p0} is the value of L_p in the first SKP scan, acquired at time t_0.

25°C, b) T_{HT} = 180°C, and c) T_{HT} = 350°C (note: data derived from the samples shown in Figs. 3.6-3.8). In curve a) L_p reaches a constant value of *ca.* 0.5mm after 25-50 hours. In contrast, curves b) and c) are reasonable straight lines, *i.e.* dL_p/dt gradients remain constant over the experimental period. Curve d) in Fig. 3.14 derives from the sample shown in Fig. 3.13, *i.e.* bulk AA6016 with T_{HT} = 180°C. Comparing curves a) and d) shows that $T_{HT} \geq$ 180°C is necessary for successive-pitting FFC to propagate over any distance. Comparing curves b), c) and d) shows that the initial presence of a deformed layer has little or no effect on propagation rate (dL_p/dt gradient) which remains in the range 0.02 – 0.025 mm/hour throughout. Furthermore, unlike the surface-active FFC case illustrated in Figs. 3.10 and 3.11, successive-pitting propagation rates do not increase with T_{HT} above 180°C.

3.3.3 Corrosion Mechanisms

Fig. 3.15a and b shows an SEM micrograph obtained from the Fig. 3.6 surface deformed AA6016 sample ($T_{HT} \leq$ 25°C) in the region of the surface-active FFC front after removing the PVB coating and corrosion products. The intact, uncorroded, surface is seen to the right of the image and the corroded surface to the left. The surface-active FFC front is seen as a zone in which porosity steadily increases (from right to left). The dimension and spacing of the pores which develop across the FFC front is consistent with intergranular attack and/or selective grain dissolution if grain size is of the order 0.1 – 1 μm. The depth of surface-active FFC attack, *i.e.* the thickness of metal dissolved in Fig. 3.15b, was estimated to be 1 - 1.5 μm by tilting the sample under SEM. The depth of attack and pore development morphology are entirely consistent with the layer thickness and grain size which have been demonstrated elsewhere for abrasion-induced surface deformed layers on AA6111 and AA6016.[2]

Given the above, and given the arguments presented earlier regarding anodic activation of the deformed surface layer relative to bulk AA6016, the mechanism underlying surface-active FFC may be understood in terms of Fig. 3.16. The lower portion of Fig. 3.16 shows, in schematic form, the characteristic E_{corr} – distance profile typified in Fig. 3.9. The upper portion of Fig. 3.16 correlates the E_{corr} – distance profile with physical regions within the surface-active FFC corrosion-cell. Region (i) in Fig. 3.16 corresponds to that part of the sample where the deformed

a)

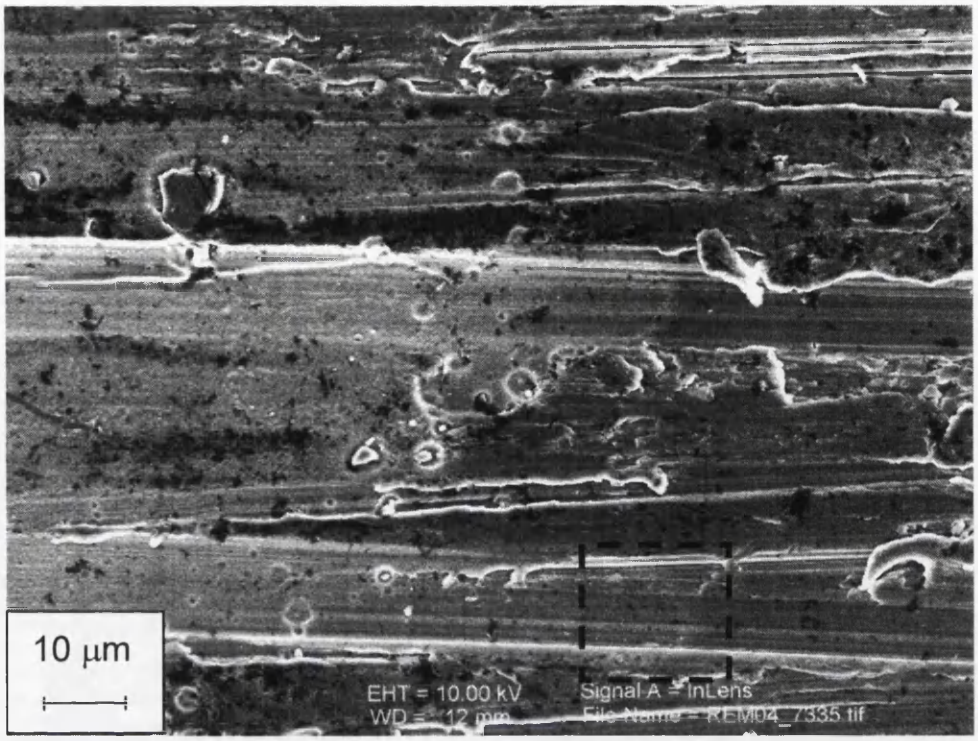

b)

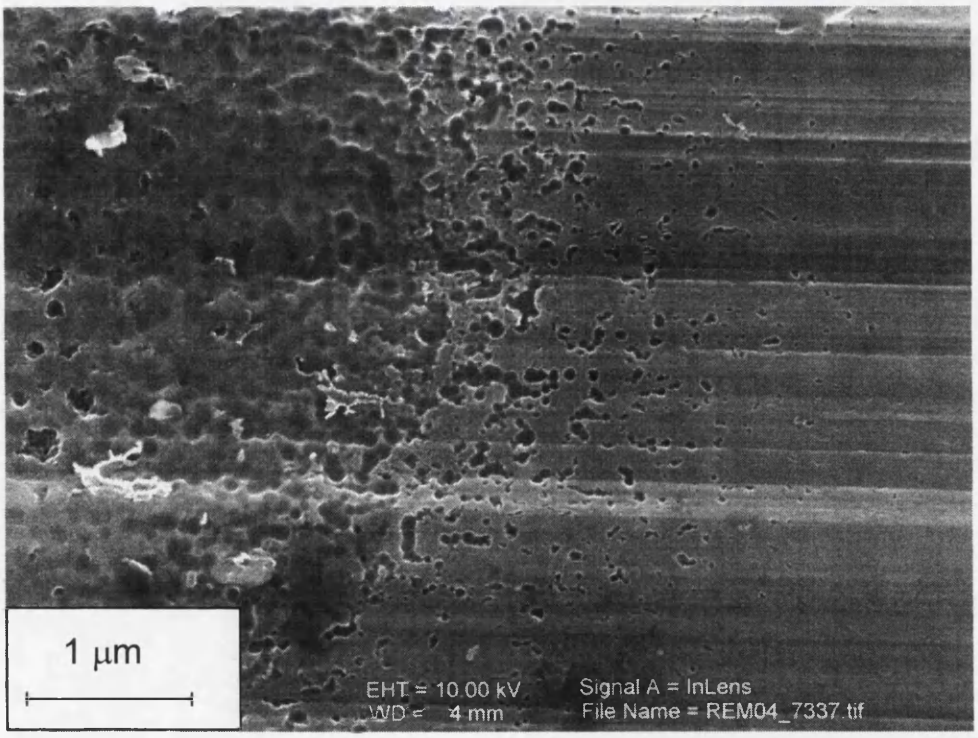

Fig. 3.15: SEM images of the "surface-active" FFC front (propagating from left to right) on corroded AA6016 surface ($T_{HT} \leq 25^{o}C$) after N-methyl pyrrolidinone removal of the PVB coating and removal of corrosion product with chromate inhibited phosphoric acid. **b)** Higher magnification image of hatched area indicated on **a)**.

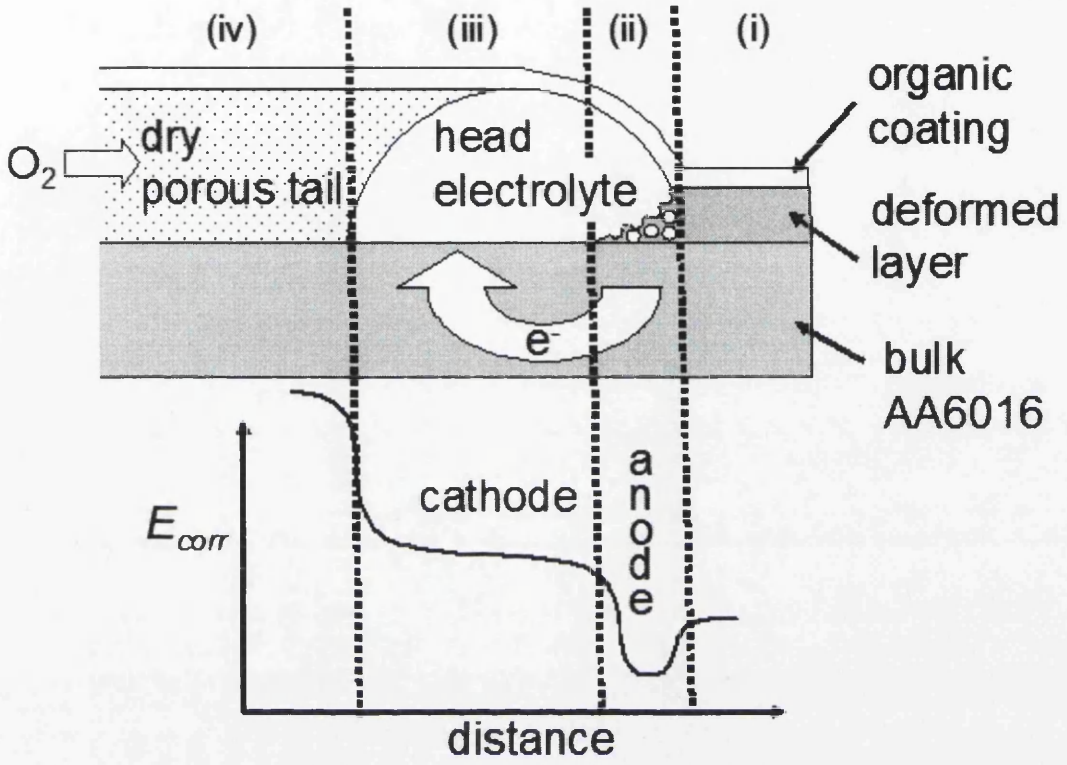

Fig. 3.16: Schematic representation of proposed relationship between SKP measured E_{corr} – distance profiles and physical regions within the "surface-active" FFC corrosion-cell.

surface layer is still present, the PVB film is still adherent, and the SKP registers $E_{intact.}$ In region (ii) the filament-head electrolyte droplet (comprising aqueous HCl and partially-hydrolysed aqueous $AlCl_3$) comes into contact with the surface layer, which undergoes anodic dissolution. In region (iii) the surface layer has dissolved and the filament-head electrolyte lies in contact with bulk AA6016, which - because of a facile diffusion of gases along the filament tail, acts as the primary site of cathodic O_2 reduction.[27,28] In region (iv) Al^{3+} aquocations become fully hydrolysed, precipitating solid Al(III) (hydr)oxide corrosion product. No water-soluble electrolyte is present in region (iv) and the corrosion product dries through osmosis - so permitting the rapid diffusion of atmospheric O_2[27,28] (see Section 1.4.3.3).

In common with most FFC, differential aeration is likely to be an important driving force underlying the Fig. 3.16 mechanism. However, anodic activation of the deformed surface layer relative to bulk AA6016 will necessarily give rise to a significant additional driving force. That is to say, the FFC cell potential will contain a contribution arising from the dissimilar electrochemical characteristics of the surface deformed layer present at the leading edge of the surface-active filiform head and the bulk alloy exposed by layer dissolution. This notion is immediately consistent with the correlation between increasing dL_s/dt and increasingly negative ΔE_{intact} seen in Fig. 3.11. It is also consistent with the potential difference of 0.1 - 0.2 V seen in Fig. 3.9 between regions (ii) and (iii) of the E_{corr} – L profile (regions defined in Fig. 3.16). Furthermore, the failure to observe measurable rates of surface-active FFC on bulk AA6016 samples suggests that this additional driving force is, in fact, essential for surface-active FFC to occur. Anodic activation of the deformed surface layer also explains the superficial nature of surface-active FFC, since bulk AA6016 becoming exposed to the aggressive filament-head electrolyte will be cathodically protected whilst galvanically coupled to the dissolving surface layer. Anodic attack is therefore restricted to the surface layer and the underlying bulk AA6016 remains effectively unscathed.

Fig. 3.17 shows SEM micrographs obtained from Fig. 3.7 sample (surface deformed, T_{HT} = 180°C) in the region of a secondary, successive-pitting, filiform head. The appearance of the corroded surface is consistent with intergranular attack, with a grain size of *ca.* 10 - 20 μm – *i.e.* similar to the bulk alloy. The overall depth of attack, *i.e.* the thickness of metal removed as the filiform advanced, was estimated

a)

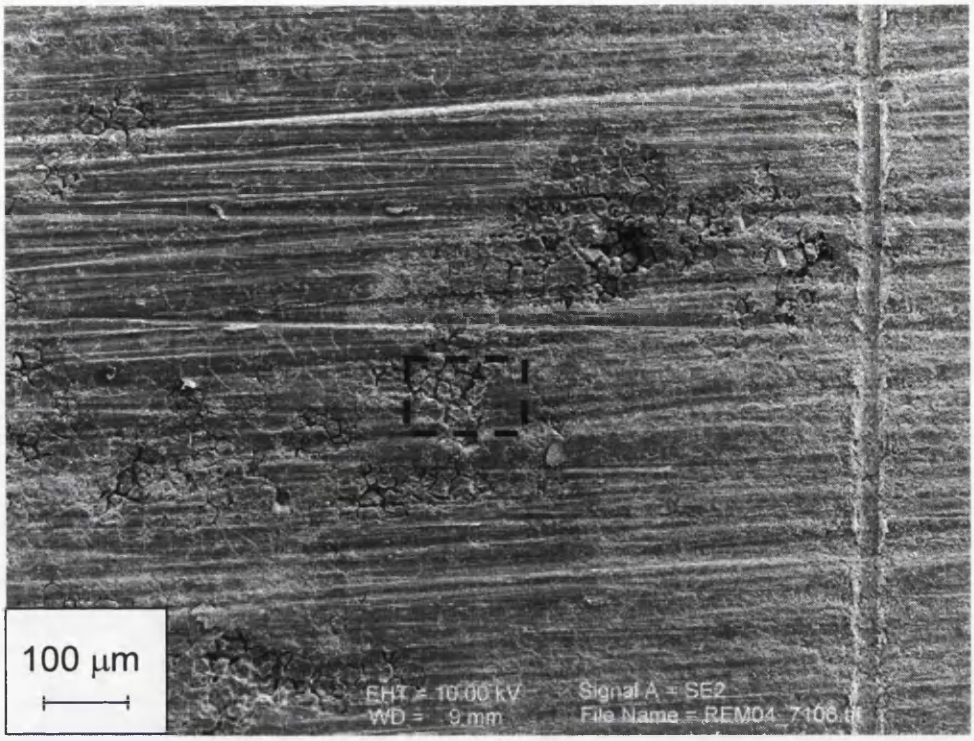

b)

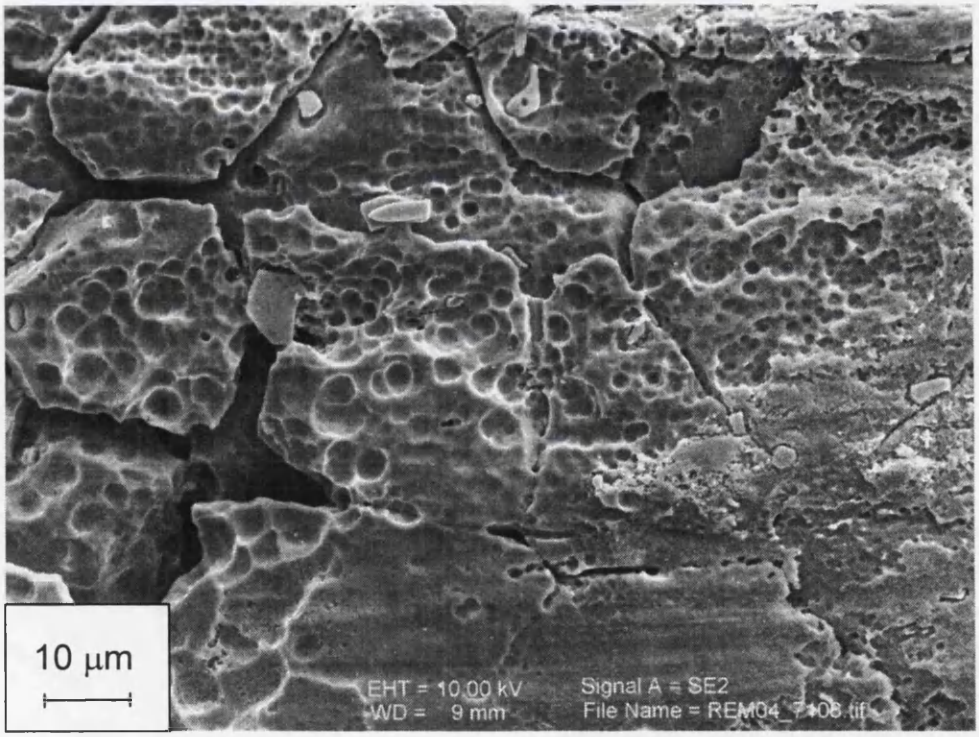

Fig. 3.17: SEM images of a "successive-pitting" FFC head (propagating from right to left) on surface deformed AA6016 (T_{HT} = 180°C) after N-methyl pyrrolidinone removal of the PVB coating and removal of corrosion product with chromate inhibited phosphoric acid. **b)** Higher magnification image of hatched area indicated on **a)**.

by tilting the SEM stage and lay in the range 10 μm – 50 μm. Similarly corroded surfaces were observed for successive-pitting filiform heads on all AA6016 samples with post-abrasion T_{HT} between 180°C and 350°C. These findings are entirely consistent with the notion of bulk AA6016 becoming sensitised to intergranular attack though grain boundary precipitation of Mg_2Si, as discussed previously. The mechanism underlying successive-pitting FFC may be understood therefore in terms of Fig. 3.18.

The lower portion of Fig. 3.18 shows, in schematic form, the characteristic E_{corr} – distance profile typified in Fig. 3.12. The upper portion of Fig. 3.18 correlates the E_{corr} – distance profile with physical regions within the successive-pitting FFC corrosion-cell. Thus, region (i) corresponds to that part of the sample where the PVB coating overlies the thin (< 2 μm thick) layer of corrosion product left in the wake of the preceding surface-active FFC front. In region (ii) the filament-head electrolyte droplet ingresses beneath the PVB coating and contacts bulk AA6016. The pre-existing corrosion product layer either dissolves or mechanically breaks away from the metal surface. Anodic dissolution of bulk AA6016 occurs, initially at least, through intergranular attack. Cathodic O_2 reduction also occurs on bulk AA6016. In region (iii) Al^{3+} cations precipitate as Al(III) (hydr)oxide which becomes progressively dehydrated through osmosis – as in the case of surface-active FFC.

The successive-pitting FFC mechanism proposed in Fig. 3.18 can only occur when bulk AA6016 is not cathodically protected by an anodically activated deformed layer. Consequently, successive-pitting FFC will only become initiated when the deformed layer is either absent initially or has been removed by preceding surface-active FFC. As in most FFC, the principal driving force is likely to be differential aeration arising from facile diffusion of atmospheric O_2 through porous corrosion product in the filament tail.[27,28] This would be the case despite the presence of a pre-existing corrosion product layer left in the wake of surface-active FFC because the greater thickness (*ca.* 10 μm) of corrosion product in the successive-pitting filament tail would allow correspondingly greater rates of O_2 transport. The same differential aeration effect would tend to force net anodic activity towards the front of the filament head droplet.[27,28]

At first sight the morphology of the corroded surfaces in Fig. 3.15 and Fig. 3.17 appears to conflict with predictions[5,29-31] that, with Cu << 0.1 wt%, the AA6016

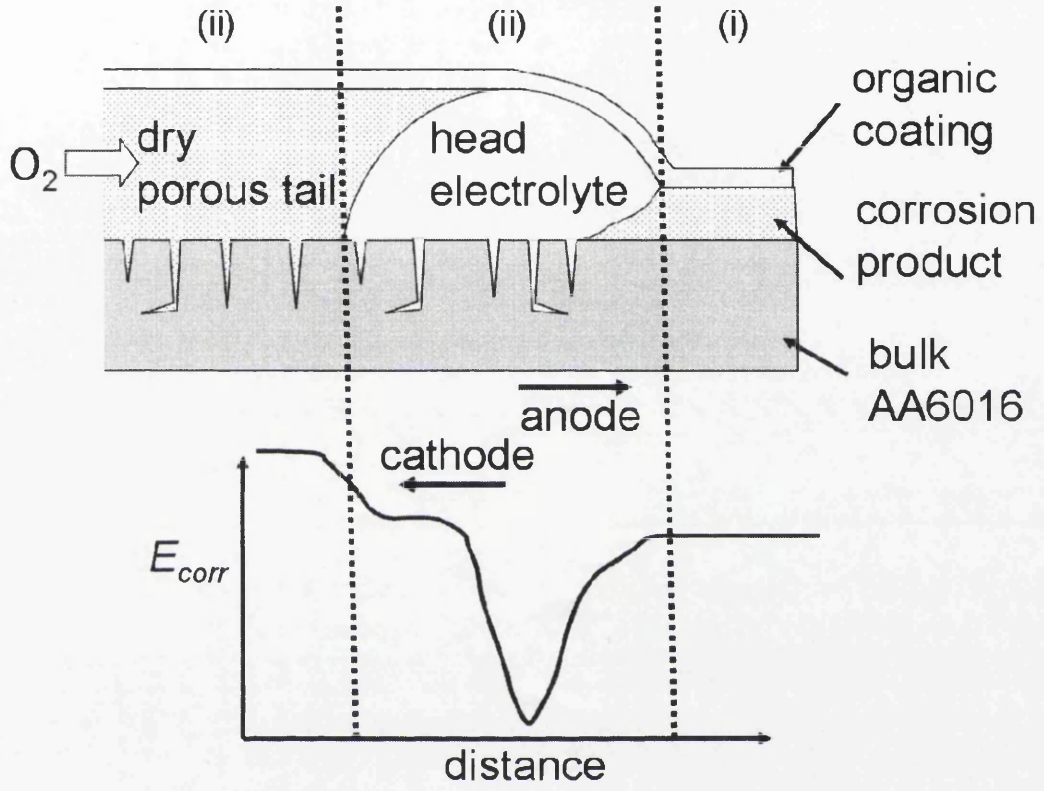

Fig. 3.18: Schematic representation of proposed relationship between SKP measured E_{corr} – distance profiles and physical regions within the "successive-pitting" FFC corrosion-cell.

used in our experiments should have a high resistance to intergranular attack. However, it should be noted that intergranular corrosion experiments are typically carried out under immersion conditions, in near neutral aqueous NaCl. By comparison the FFC head electrolyte, consisting as it does of aqueous HCl and partially hydrolysed $AlCl_3$, is likely it be significantly more aggressive. Furthermore, FFC occurs in the absence of a bulk electrolyte, under conditions of aeration which are likely to increase E_{corr} values and hence the driving force for anodic dissolution. Certainly, the notion that that intergranular corrosion underlies the mechanisms of both surface-active FFC and successive-pitting FFC provides an immediate explanation for the greater anodic activation, and sacrificial behaviour, of the abrasion-induced surface deformed layer in AA6016, since the micrograined structure of this layer necessarily implies a much greater density of grain boundaries.

3.4 Conclusions

- In humid air at 80% r.h. and 40°C, SKP has been used to quantify localised free corrosion potentials (E_{corr}) on AA6016 aluminium alloy which has been overcoated with a thin (30μm) layer of PVB. The kinetics of filiform corrosion (FFC), initiated by aqueous HCl injection, have similarly been quantified by following the subsequent evolution of E_{corr} patterns.

- Bulk AA6016 in the solutionised and naturally aged T4 temper is effectively corrosion resistant. However, when an abrasion-induced surface deformed layer is present AA6016 exhibits a rapid, superficial, "surface-active" FFC, in which metal loss is limited to the thickness of the deformed layer (*i.e.* < *ca.* 2μm). Heat treatment at temperatures in the range T_{HT} = 180°C to 350°C increases surface-active FFC propagation rates by 17% to 184 % respectively.

- Potentials (E_{intact}) measured over the intact, uncorroded, PVB coated surface are lower for surface deformed AA6016 than for bulk AA6016. The potential difference (ΔE_{intact} = E_{intact} surface deformed - E_{intact} bulk) is *ca.* -0.2V when $T_{HT} \leq 180$°C but increases to *ca.* -0.5V when $T_{HT} \geq 350$°C. This is consistent with a thermally enhanced anodic activation of the abrasion-induced deformed layer. Anodic activation has been confirmed by potentiodynamic

- polarization measurements in near-neutral 0.5% aqueous NaCl.

- A mechanistic scheme has been proposed in which the deformed layer reacts as a sacrificial anode with respect to bulk AA6016. The potential difference between the deformed layer and bulk alloy exposed by layer dissolution (estimated as ΔE_{intact}) contributes significantly to the thermodynamic driving force for surface-active FFC.

- PVB coated AA6016 with T_{HT} between 180°C and 350°C is also subject to a slower, more deeply penetrating, "successive-pitting" type of FFC in which the bulk alloy is penetrated to a depth of 10 - 50 μm. Successive-pitting FFC only occurs in the absence of a sacrificial deformed layer, *i.e.* either directly on bulk AA6016 on as a secondary process following surface-active FFC on surface deformed AA6016.

- In both surface-active and successive-pitting FFC the appearance of the corroded surface under SEM is consistent with intergranular corrosion. In successive-pitting FFC the apparent grain size is typical of the bulk alloy, *i.e.* *ca.*20 μm. In surface-active FFC the apparent grain size is reduced to *ca.*1 μm, as would be expected for a "micro-grained" surface layer.

- The exact mechanism whereby AA6016 becomes sensitised to intergranular corrosion remains unclear. However, given the low copper content (0.06%) of the samples used in our studies, it seems likely that sensitisation involves precipitation of anodically active Mg_2Si at grain boundaries. The greater anodic activation of the abrasion-induced surface deformed layer is therefore explicable on the basis of the greater density of grain boundaries in this layer.

3.1 Further Work

Further work will be required to determine how the surface becomes activated in the absence of post-abrasion heat treatment. Abrasion of AA6016 in the naturally aged T4 condition presumably results in dissolution of precipitates of metastable ß″ in the deformed layer and the transport of Mg and Si solute to grain boundaries.

3.2 References

1. S. M. Hirth, G. J. Marshall, S. A. Court and D. J. Lloyd, *Mat. Sci. Eng. A*, **319-321**, 452 (2001).

2. G. M. Scamans, A. Afseth, G. E. Thompson, Y. Liu and X. Zhou, *Mater. Sci. Forum*, **519 - 521**, 647 (2006).

3. G. Svenningsen, M. Hurlen Larsen, J. E. Lein, J. H. Nordlien and K. Nisancioglu, *9th International Conference on Aluminium Alloys, Aluminium Alloys their Physical and Mechanical Properties*, **818-824** (2004).

4. H. N. McMurray, A. Coleman, G. Williams, A. Afseth and G. Scamens, *Mater. Sci. Forum*, **519-521**, 679 (2006).

5. G. Svenningsen, M. H. Larsen, J. H. Nordlien and K. Nisancioglu, *Corros. Sci.*, **48**, 3969 (2006).

6. R. Ambat, A. J. Davenport, A. Afseth and G. Scamans, *J. Electrochem. Soc.*, **151**, B53 (2004).

7. A. Shi, B. A. Shaw and E. Sikora, *Corrosion*, **61**, 534 (2005).

8. A. Afseth, J. H. Nordlien, G. M. Scamans and K. Nisancioglu, *Corros. Sci.*, **43**, 2359 (2001).

9. A. Perovic, D. D. Perovic, G. C. Weatherley and D. J. Lloyd, *Scripta Mater.*, **41**, 703 (1999).

10. G. Williams and H. N. McMurray, *J. Electrochem. Soc.*, **150**, B380 (2003).

11. C. B. Monk, Electrolytic Dissociation, Academic Press, London (1961).

12. R. A. Robinson, Electrolyte Solutions, Butterworths, London (1955).

13. H. S. Harned and B. B. Owen, The Physical Chemistry of Electrolyte Solutions, Reinhold Publishing Corporation ACS monograph series, NY (1943).

14. K. S. Pitzer, Activity Coefficeints in Electrolyte Solutions, CRC Press, Boca Raton, FL (1991).

15. D. A. Sinclair, *J. Phys. Chem.*, **37**, 495 (1933).

16. G. Williams and H. N. McMurray, *J. Electrochem. Soc.*, **150**, B380 (2003).

17. 'Standard test method for filiform corrosion resistance of organic coatings on metal', ASTM Standard D2803 (1982).

18. 'Aerospace: filiform corrosion test of coatings on aluminium alloys', DIN 65 472-A (1996).

19. H. Leth-Olsen and K. Nisancioglu, *Corrosion*, **53**, 705 (1997).

20. 'Paint and Varnishes - filiform corrosion test on steel', ISO 4623 (1984).

21. N. LeBozec, D. Persson and D. Thierry, *J. Electrochem. Soc.*, **151**, B440 (2004).

22. W. H. Slabaugh, W. Dejager, S. E. Hoover and J. Hutchinson, *Paint Tech.*, **44**, 76 (1972).

23. A. Afseth, J. H. Nordlien, G. M. Scamans and K. Nisancioglu, *Corros. Sci.*, **43**, 2093 (2001).
24. G. Williams, H. N. McMurray, D. Hayman and P. C. Morgan, *Phys. Chem. Comm.*, **6**, 1 (2001).
25. H. N. McMurray and G. Williams, *J.Appl. Phys.*, **91**, 1673 (2002).
26. W. Schmidt and M. Stratmann, *Corros. Sci.*, **40**, 1441 (1998).
27. A. Bautista, *Prog. Org. Coat.*, **28**, 49 (1996).
28. R. T. Ruggeri and T. R. Beck, *Corrosion-NACE*, **39**, 452 (1983).
29. G. Svenningsen, M. H. Larsen, J. C. Walmsley, J. H. Nordlien and K. Nisancioglu, *Corros. Sci.*, **48**, 1528 (2006).
30. G. Svenningsen, M. H. Larsen, J. H. Nordlien and K. Nisancioglu, *Corros. Sci.*, **48**, 258 (2006).
31. G. Svenningsen, J. E. Lein, A. Bjorgum, J. H. Nordlien, Y. Yu and K. Nisancioglu, *Corros. Sci.*, **48**, 226 (2006).

Chapter 4

Inhibition of Filiform Corrosion on AA6111-T4

4.1 Introduction

Section 1.4.3.4 and Chapter 3 have demonstrated the susceptibility of AA6016 series rolled sheet aluminium alloys to filiform corrosion (FFC) when the surface is abraded which is unfortunately common practice during automotive assembly. In this chapter a 6000 series alloy regularly used in North American car production, namely AA6111, is investigated. As of yet, it has proved neither practical nor economically viable to remove the damaged surface layers introduced by grinding, by introducing a specific post-grinding etch or cleaning process. Consequently, coating systems and/or pre-treatment systems need to be found to inhibit filiform attack on the ground surface. The initial approach decided upon was to attempt to locally inhibit FFC on areas of the alloy surface where the damaged layer had been introduced by using a localised "self-oxidising" coating. Thus, by converting the active surface layer into an oxide or through the formation of a metal salt layer it was hoped that the susceptibility of the ground surface areas would be eliminated/minimised. The second coating system was prepared in an attempt to produce a "localised etching" of the damaged surface layer.

Both coating systems used required the use of Brønsted acids. Three acids were chosen for use in this chapter; camphorsulfonic (HCS), phenylphosphonic (H_2PP) and ethylenediaminetetraacetic acid (EDTA). These were chosen with the possible inhibitory properties of their associated anions in mind. HCS was chosen primarily as a control acid as in previous studies[1] the sulphonate anion has shown little inhibitory effects on aluminium alloy surfaces. Conversely, H_2PP was chosen as the phosphonate anion is often incorporated into coating systems on aluminium alloy surfaces. Finally, EDTA was used in an attempt to "scavenge" or complex transition metals released during the corrosion process. It was hoped that by removing these metals (primarily copper) it may be possible to slow down or even eliminate the propagation of filiform. Two different delivery mechanisms are chosen for the acids. The first was an "intelligent" coating system using an intrinsically conducting polymer (ICP) called Polyaniline (PAni). The second delivery mechanism was a simple dispersion of the acid in a polyvinylbutyral (PVB) matrix applied directly onto the metal surface.

PAni is described in detail in Section 1.5.2 and the main developments in this field are also reviewed by Tallman *et al* .[2,3] Polyaniline exists in several states as

shown in Fig. 4.1 but it is the Emeraldine Salt (ES) form which is electrically conductive and most widely used for corrosion control. The Emeraldine Base (EB) form of PAni can be "doped" or protonated with the Brønsted acids described above to form PAni-ES. It has been shown that PAni-ES can partially inhibit filiform corrosion on aluminium alloy AA2024-T3 by the formation of a thin oxide film at the metal/polymer interface.[4] If PAni-ES coatings exhibited a similar localised "self-anodisation" effect on ground 6000 series alloy surfaces then it is feasible to suggest there would be a conversion of the active surface layer into oxide and thus an inhibitory effect on the rate of fast (cosmetic) filiform attack. However, it has also been claimed by other authors that doping is unnecessary and that the PAni-EB provides superior protection [5] and therefore PAni-EB is also tested.

The second coating system simply dissolves H_2PP in PVB as only the HPP^- anion was found to show any inhibitory properties when released from a PAni-ES coating. It is also known that the hydrogen phenylphosphonate (HPP^-) and phenylphosphonate (PP^{2-}) anions are strongly adsorbed on aluminium (hydr)oxide.[6-8]

To study the inhibitory and polarising effects of the coating systems, a combination of *in-situ* scanning Kelvin probe (SKP) and optical analysis experiments were used. The ability of the SKP technique to spatially and temporally resolve potential distributions beneath intact organic coatings is well documented[9-11] and is summarised in Section 1.6.2.2.

4.2 Experimental

All the main experimental procedures and techniques used in this chapter are described in more detail in Chapter 2. Aluminium Alloy AA6111-T4 was prepared as described in Section 2.6.3. Two-part PAni/PVB coatings were prepared as described in Section 2.2.3 producing coatings represented as PAni-EB, PAni-CS, PAni-HPP and PAni-EDTA. H_2PP/PVB coatings were prepared as described in Section 2.2.4.

The coating, SKP equipment, calibration and FFC initiation procedures are described in Section 2.5. At the end of each SKP experiment the coatings were removed by immersion in n-methyl-2-pyrrolidinone at 60°C for 5 minutes. The corroded metal surface was then photographed using a digital camera.

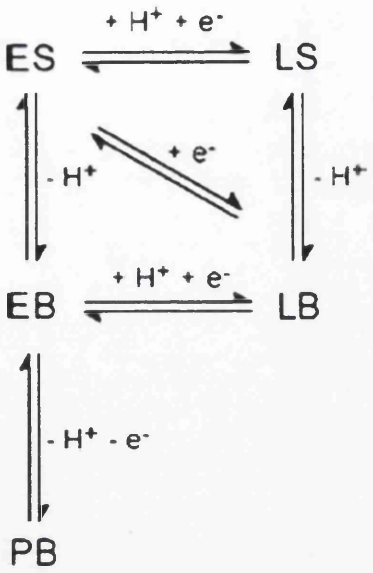

Figure 4.1: Redox and acid-base equilibria in polyaniline: ES = emeraldine salt, LS = leuco salt, EB = emeraldine base, LB = leuco base, and PB = pernigraniline base. The number of protons and electrons shown are for every two aniline residues.

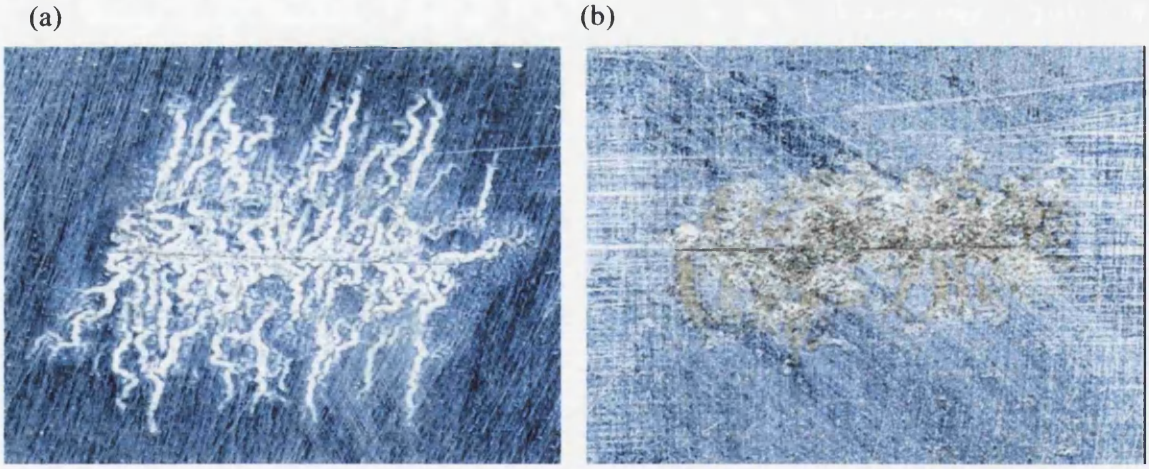

Figure 4.2: Digital images of AA6111 surfaces following PVB coating removal, 100 hours after FFC initiation. Surface preparation: (a) Abraded (180 grit SiC paper) and (b) abraded and caustic etched. FFC initiated using 1 μl of 2 M HCl. Conditions of 80% RH and 40°C maintained during corrosion testing.

Up to four additional samples were prepared with each coating as described in Section 2.5.5. However, these samples were not scanned using SKP but placed into an environment chamber after FFC initiation and maintained at 40°C and 80% r.h. for 100 hours before digital image analysis of the surfaces was carried out, as described in Section 2.6.[12] This second type of experiment was intended purely to compare the inhibition efficiency of differently formulated PVB/H_2PP coatings.

4.3 Results and Discussion

4.3.1 Polyaniline Coatings

Initial corrosion experiments were carried out to determine the susceptibility of the bulk alloy and the damaged surface layer to FFC. When a damaged surface layer was introduced to the alloy by surface abrasion a significant amount of surface active FFC corrosion was visible on the surface as shown in Fig. 4.2a. This finding is entirely consistent with those reported previously for abraded AA6111-T4.[13] However, when the FFC corrosion experiments were carried out on bulk AA6111 alloy (prepared by abrading the surface and then removing the damaged layer via a caustic etch process) it became apparent that the bulk alloy was inherently susceptible to corrosion as shown in Fig. 4.2b. There was no surface active (cosmetic) filiform visible but only a deeper successive pitting FFC attack. The susceptibility of the bulk AA6111 alloy to successive pitting FFC is consistent with observations made by Scamans *et al* [14] and described in Section 1.4.3.4. However, as stated in the same section this type of FFC may be controlled by proper application of the pre-treatment layer and coating system currently in use by the automotive industry. Therefore from this point on only samples where the surface has been abraded and that are therefore susceptible to surface active FFC attack are studied.

The distribution of free corrosion potential (E_{corr}) values existing at the AA6111 surface were calculated from the matrix of $\Delta\psi_{Pol}^{Ref}$ values recorded during each SKP scan (see Section 2.5.5) in combination with Equation 2.8. For the purpose of discussion, the term "intact potential" (E_{intact}) designates E_{corr} measured over uncorroded portions of the sample (where the organic coating remains adherent). E_{corr} distributions obtained at different times (t) following FFC initiation using 2 M aqueous HCl could then be used to visualise the dynamic evolution of

E_{corr} patterns associated with filament propagation.[15] Fig. 4.3 shows representative E_{corr} distributions obtained at t = (a) 12, (b), 52 and (c) 96 h following FFC initiation for an abraded PVB coated AA6111 surface. The results are very similar to that of alloy AA6016 shown in Chapter 3. E_{intact} values are approximately uniform and time-independent ranging from -0.65 to -0.7 V vs. SHE. A broad uniform front of fast filiform attack may be seen that propagates away from the defect with time with a region of higher potentials following behind. This region consists of filiform tails that have become intertwined and are irresolvable due to the resolution of SKP apparatus (~100μm). The potentials existing in this region are between -0.5 and 0.1 V *vs.* SHE. In the area where fast filiform attack has occurred secondary filiform heads are visible as small dark regions of low potential close to the defect as described in more detail in Chapter 3. Sample appearance at the end of the experiment is shown in Fig. 4.3d and was consistent with the filament distribution observed by the SKP. The attack observed on a ground AA6111 surface is entirely similar to the fast superficial FFC observed on abraded AA6016 shown in Chapter 3. The most notable difference is the increased amount of deeper successive pitting filiform attack on the substrate following the superficial surface active FFC. However, this would be expected given the increased susceptibility of bulk AA6111 alloy to successive pitting FFC.

Fig. 4.4(a-d) shows digital images of the samples after corrosion testing with various polyaniline coatings. The images were taken immediately after FFC experiments, following coating removal. It may be seen that PAni-EB, PAni-CS and PAni-EDTA shown by Fig. 4.4(a-c) respectively, were all ineffective corrosion inhibitors. In fact when present these PAni coatings increased the amount of FFC attack occurring on the surface as compared to the uninhibited case shown in Fig. 4.3d. Only PAni-HPP (Fig. 4.4d) shows a significant reduction in the level of FFC on the alloy surface. These results suggest that rather than inhibiting FFC, PAni coatings supply an additional cathodic driving force for FFC. This is probably as a result of the reduction of the PAni-ES coating to its leuco-base form (as described in Section 1.5.2) providing an easier path for electron transfer. However, although this explanation may be given for the electrically active PAni-ES coatings used it does not explain the increased amount of attack observed when the AA6111-T4 substrate was coated with the electrically inactive PAni-EB coating. If the coating is

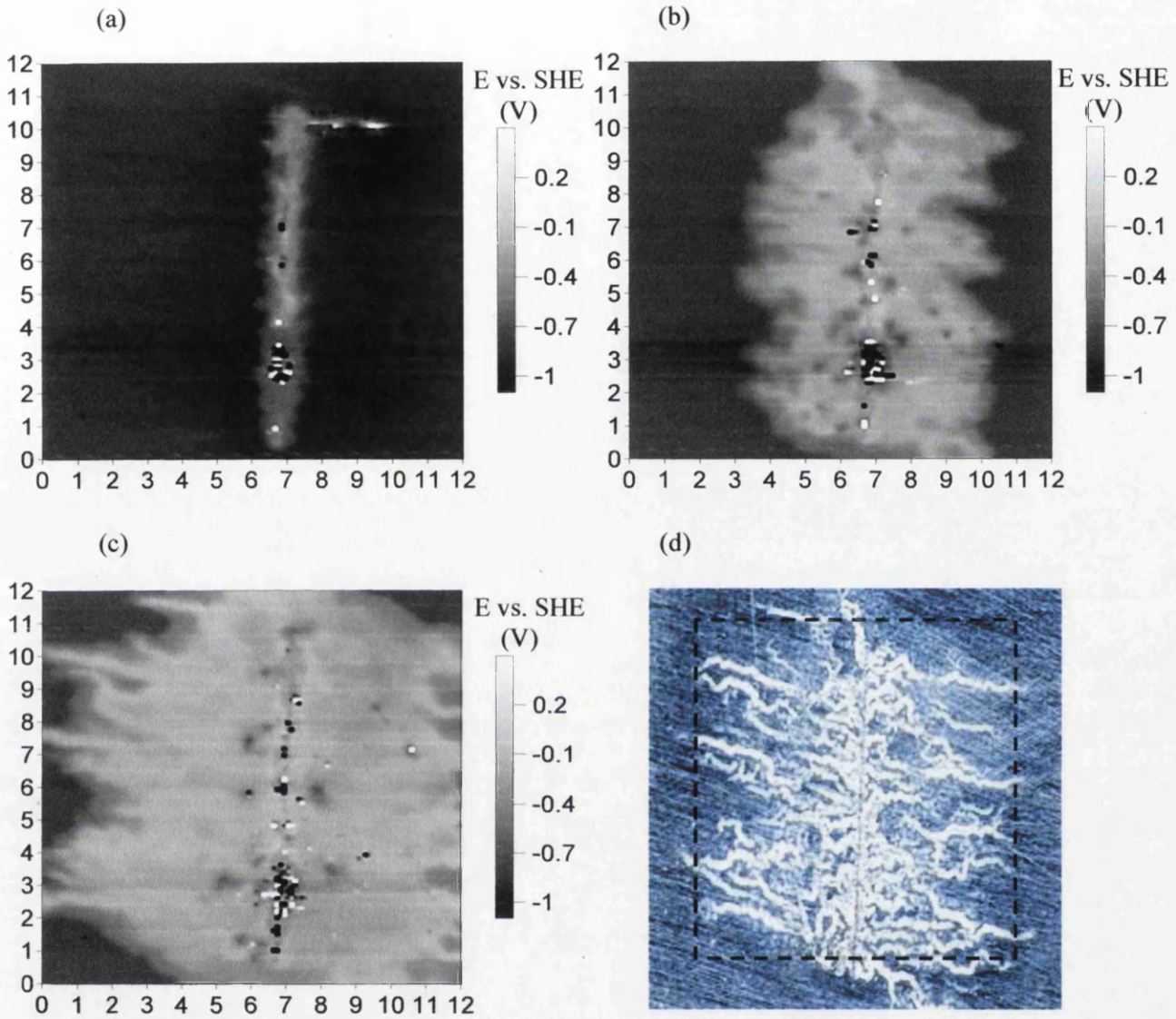

Figure 4.3: Interpolated greyscale maps showing E_{corr} distributions measured over a AA6111 surface ground with 180 grit SiC paper and coated with PVB at t = (a) 12, (b) 52 and (c) 96 h following FFC initiation using 1 µl of 2 M aqueous HCl. Conditions of 40°C and 80% r.h. were maintained for the duration of the experiment. (d) Photographic image taken of the sample upon removal from the SKP environment chamber. The SKP scanned area is indicated by the dotted line.

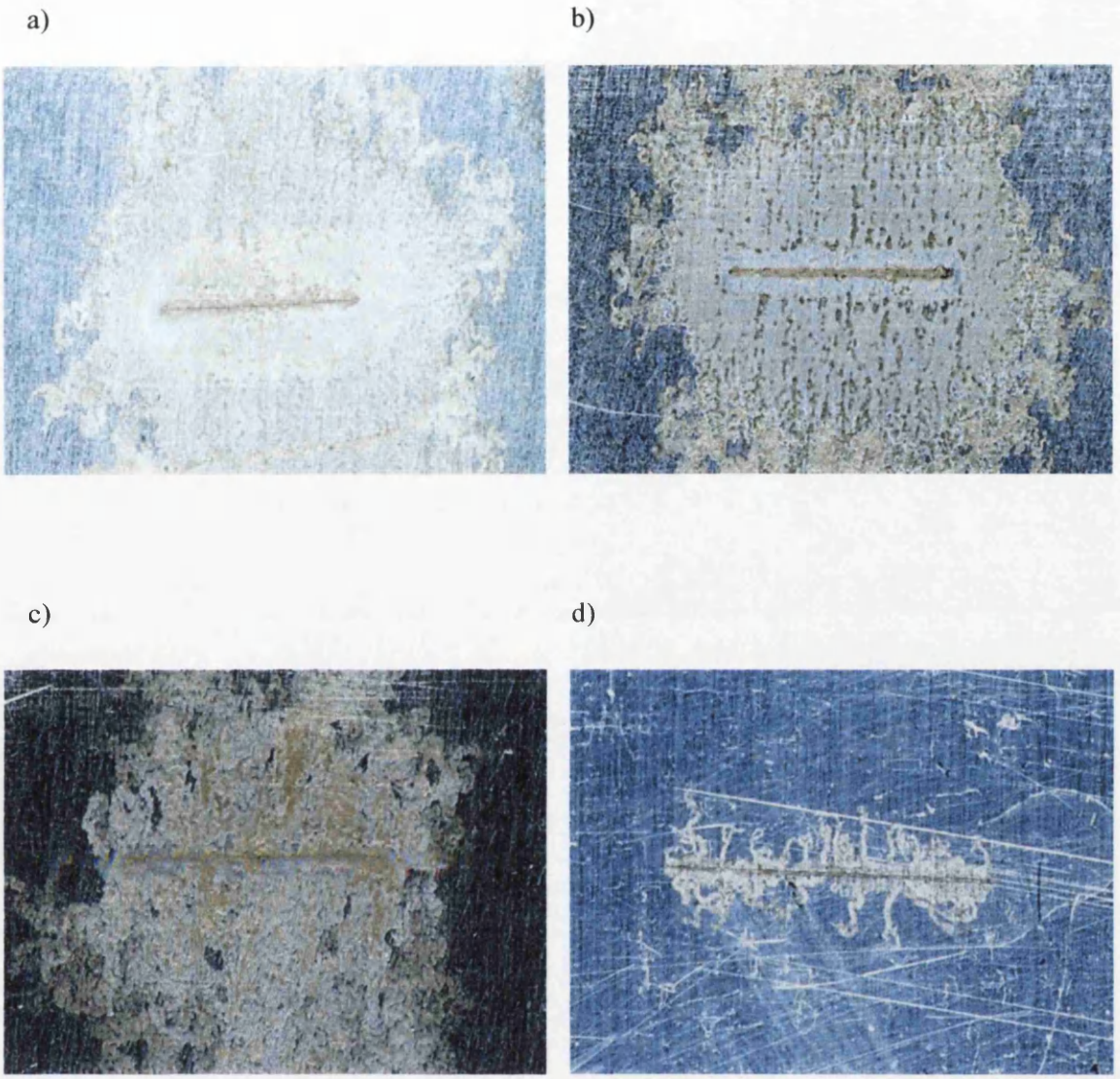

Figure 4.4: Digital images of ground AA6111 samples following FFC corrosion experiments for 100 hours under conditions of 40°C and 80% r.h. FFC initiated with 2 M HCl. Coating removed using n-methylpyrrolidinone. Samples were coated with (a) PAni-EB, (b) PAni-CS, (c) PAni-EDTA and (d) PAni-HPP

electrically inert with no dopant anion present then it would be expected that there would be no increase in the amount of FFC on the surface when compared to a PVB only coated sample. However, upon initiating FFC a significant number of protons are introduced into the defect through the addition of 1μl of 2 M HCl. These protons are available to locally dope or protonate the PAni-EB coating. Appendix B shows that for a 30 μm coating used in these experiments this equates to a total area of 0.47 cm^2 of PAni-EB coating around the defect that could be protonated. This is a significant area of coating, but it must also be remembered that this value is for protonation of the full coating thickness. In reality it is feasible that only the coating close to the delaminated region and also directly in contact with the electrolyte will be doped and hence a larger area of the coating may be affected. Therefore, even when a PAni-EB coating is used it is possible that the coating can be protonated and thus electrically active (as in the case of the PAni-ES coatings) providing a facile reduction reaction. When FFC initiates, the coating close to the defect is delaminated exposing new PAni-EB coating which can in turn be protonated. The now electrically active PAni-ES coating may participate in electron transfer with the alloy and be reduced, providing a cathodic driving force for filiform attack, thus increasing the level of FFC observed on the surface.

The results shown in Fig. 4.4 also give an indication as to the effectiveness of the dopant anion as a secondary mode of protection. As described above it appears that the PAni coating itself is not inhibiting attack through oxidation of the active surface layer. However, there is also a possible secondary mode of protection with PAni coatings, through the release of the dopant anion (see Section 1.5.2). The dopant anion released depends on the acid used to protonate PAni-EB. The sulphonate anion introduced using camphor sulphonic acid shows no inhibitory properties as expected. As discussed above it appears that the primary cathodic reaction is that of the reduction of the PAni-ES and thus the possible removal of transition metals by using EDTA is also ineffective as a dopant anion in this instance. However, it may have applications in the protection of AA2024 where copper replating is an important part of the filiform mechanism.

In the case of PAni-HPP shown in Fig. 4.4d there is a significant reduction in the amount of filiform attack. There is a total cessation of the uniform filiform attack observed on a PVB ground surface and the other PAni-ES coated systems. There is

some attack on the surface but this is limited to areas close to the defect and occurs as individually identifiable filaments. As no other PAni coating was an effective inhibitor this result indicates that the inhibition of FFC must be linked to the HPP^- anion released upon the reduction of PAni. The inhibitory properties and possible mechanism of protection of the HPP^- anion are discussed in more detail below in Section 4.3.2.

Although the PAni coatings were not effective inhibitors the coated samples were subjected to SKP scans to try and identify what effect the coating was having on the surface. When scanned in air the SKP potential recorded in the E_{intact}, region was found to be substantially heterogeneous over each coated surface. Fig. 4.5(a-d) shows interpolated greyscale maps of E_{corr} distributions measured over an abraded AA6111 surface coated with a PAni-HPP coating ($\phi = 0.2$) at t = (a) 12, (b) 48, (c) 92 and (d) 136 h following FFC initiation using 1 μl of 2 M aqueous HCl. It may be seen that the heterogeneity of the E_{intact} region is unstable and changes with time. Fig. 4.6 shows representative E_{intact} SKP line scans taken across the sample parallel and far away from the defect after 50 hours corrosion testing. It may be seen that E_{intact} for a sample coated with uninhibited PVB is very homogeneous with a mean average of ~-0.7V *vs.* SHE. Conversely the PAni-CS and PAni-HPP coated samples are very heterogeneous with values ranging from -0.5 to 0.1V *vs.* SHE for PAni-CS and -0.4 to 0.4V *vs.* SHE for PAni-HPP.

The significance of E_{intact} for polymer-coated metal has been discussed at length elsewhere.[16,17] Briefly, for non-conducting polymers E_{intact} reflects the open-circuit potential of the oxide covered metal surface, influenced as this may be by reaction with atmospheric O_2 and/or Brønsted acid-base interactions occurring between the oxide and polymer coating. However, ICP's such as PAni-ES may enter into electron transfer with the metal substrate and, under these circumstances, E_{intact} tends towards the redox potential (or Fermi level) of the ICP.[16] The redox potential of PAni-ES on an aluminium substrate has been reported elsewhere at *ca.* 0.5V *vs.* SHE.[18] The redox potential of the alloy surface can be taken as E_{intact} for a PVB coated surface which is *ca.* -0.7V *vs.* SHE as shown in Fig. 4.6. If the values of E_{intact} recorded on the surface are thought of in terms of mixed potential theory then they are falling in between these two outer limits (-0.7 and 0.5V). We are able to think of the potentials in this way as they are dynamic, *i.e.* they are not in

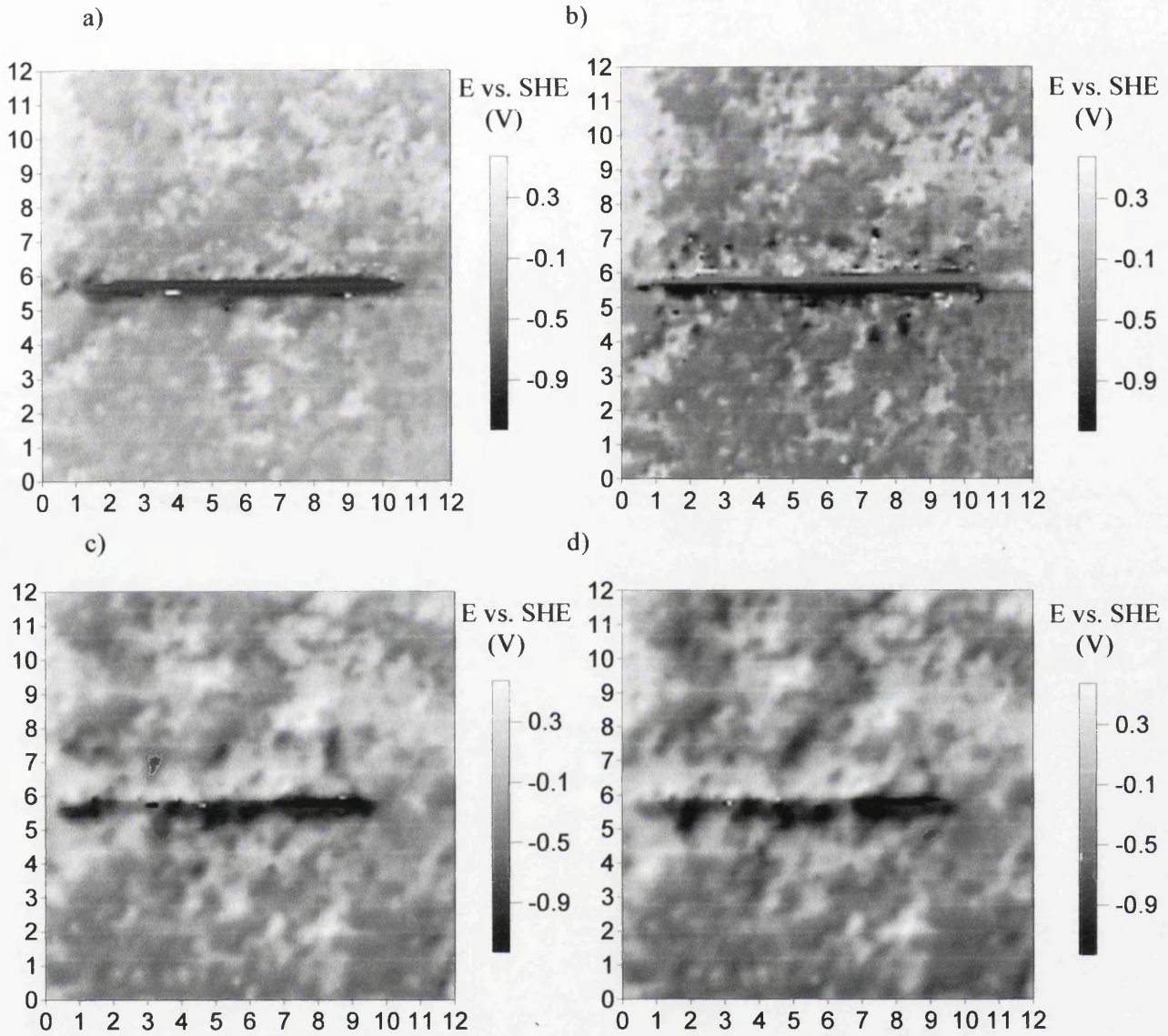

Figure 4.5: Interpolated greyscale maps showing E_{corr} distributions measured over a AA6111 surface ground with 180 grit SiC paper and coated with a PAni-HPP coating (ϕ = 0.2) at t = (a) 12, (b) 48, (c) 92 and (d) 136 h following FFC initiation using 1 µl of 2 M aqueous HCl.

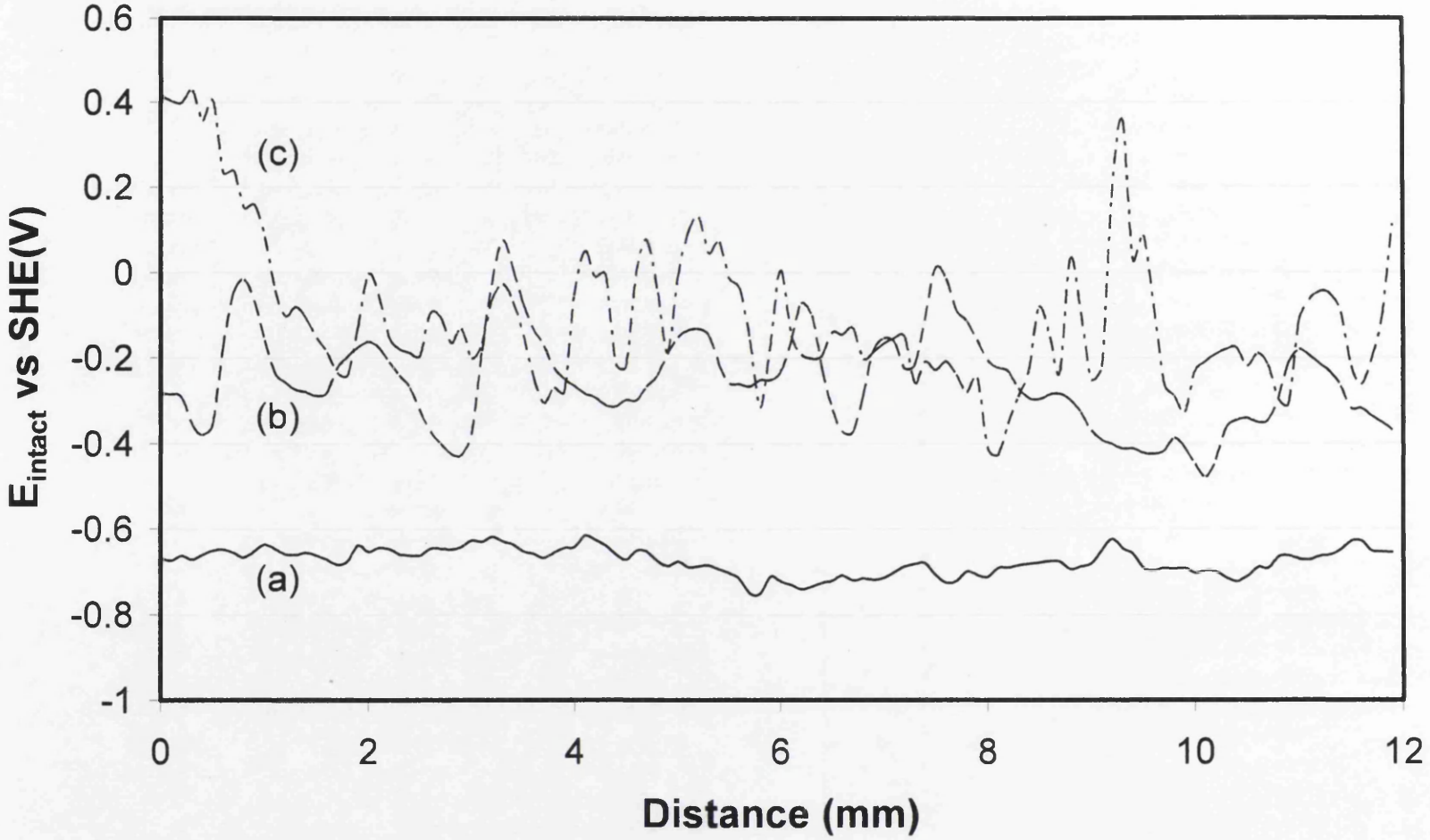

Figure 4.6: SKP line scans of E_{intact} values for AA6111 ground (180 grit SiC paper) surfaces coated with (a) PVB, (b) Pani-CS and(c) PAni-HPP 50 hours after coating application. Sample maintained at 40°C and 81% r.h.

thermodynamic equilibrium, as shown in Fig. 4.5 where E_{intact} may be seen to be changing with time. Therefore the process of oxidation occurring on the surface is continuous and dynamic. This continuous process of oxidation produces a heterogeneous surface that increases susceptibility to corrosion due to localised differences in E_{intact} unless there is an inhibitory effect of the dopant anion as in the case of the PAni-HPP coated surface.

It is possible that the corrosion inhibition properties of these PAni coatings may have been enhanced by increasing the pigment volume fraction to try and achieve a more homogeneous E_{intact} value closer to or equal to that of the redox potential of PAni-ES. A similar observation of heterogeneous E_{intact} values has been made on AA2024 where increasing pigment volume fraction of PAni resulted in more homogenous E_{intact} values.[4] However, the inhibitory properties of the coating were already becoming apparent before the critical level of pigment volume fraction required for homogenous E_{intact} close to the redox potential of PAni-ES was observed. Therefore it was decided to remove the PAni from the coating system and concentrate on the one acid whose dopant anion had showed inhibitory properties, that is H_2PP. A secondary motivation for this was that in terms possible future commercial use as a further increase in the pigment volume fraction of PAni would render it even more expensive and therefore unappealing to industry. H_2PP on the other hand is relatively very cheap and easily obtainable.

4.3.2 Phenylphosphonic acid/PVB Coating System

In the work to be described in this section the primary aim has been to examine the possibility of using H_2PP simply dissolved in an organic polymer "primer" coating to inhibit FFC on ground AA6111. The polymer chosen was polyvinylbutyral (PVB), which has been widely used as a binder in commercial "etch primer" formulations. PVB has also been used as the basis of model coatings, formulated with the intention of following FFC kinetics[19,20] and better understanding the operation of corrosion inhibitor pigments such as chromate[21] and hydrotalcite.[1,12,22] It was a further aim to probe the possible mechanism(s) by which H_2PP acts to inhibit FFC on aluminium alloys.

Fig. 4.7(a-f) shows the appearance of PVB coated AA6111-T4 samples 100 hours after FFC initiation in the presence and absence of H_2PP inhibition. In the

uninhibited case (Fig. 4.7a) the sample exhibits a rapid, superficial attack consistent with "surface-active" FFC as described in Fig. 4.2a. The mean distance (measured normal to the defect) between the defect and the advancing filiform front was 3.9 mm. When the PVB coating contained 0.1% w/w H_2PP (Fig 4.7b) the extent of attack was similar, in that filaments propagated a mean distance of 3.6mm. However, the FFC morphology was changed to produce narrower, more widely spaced filaments which were more orientated along the rolling/grinding direction. This is possibly due to a partial inhibition of FFC propagation forcing filaments to take a "path of least resistance". Increasing H_2PP content to 0.5% w/w (Fig. 4.7c) reduced mean filament lengths to < 1.5mm. Increasing H_2PP content above 0.5% w/w (up to 5% w/w, as shown in Fig. 4.7(d-f) did not appear to further increase the efficiency of FFC inhibition.

FFC experiments were repeated up to 4 times for each in-coating H_2PP concentration, and images similar to those shown in Fig. 4.7 were subject to digital image analysis in order to determine the visible area of coating delamination. Fig. 4.8 shows a bar chart of mean delaminated area after 100 hours. The error bars are ± 1 standard deviation units on the mean, and correspond to a fractional error of *ca* ± 9%. It may be seen that 0.1% w/w in-coating H_2PP reduces delaminated area by *ca.* 60% relative to the uninhibited case. Increasing in-coating H_2PP to 0.5% w/w reduces delaminated area by *ca.* 95% relative to the uninhibited case. However, increasing in-coating H_2PP content above 0.5% w/w does not produce any further significant decrease in delaminated area.

The extent to which in-coating H_2PP influences the distribution of E_{corr} values was determined using calibrated *in-situ* SKP measurements.[20,21] Fig. 4.9 shows E_{corr} profiles for individual filaments, each with a visible length of *ca.* 1.5mm, measured centrally along the axis of filament propagation. The in-coating H_2PP concentration for each profile was: (a) zero, (b) 0.1%, (c) 1% w/w. The location of filament heads and tails was assigned by registration of SKP potential maps and photographic images of corrosion filaments.[22,23] The lateral resolution of the SKP used (~100 μm) is such that the values reported for E_{intact} and for E_{corr} associated with filament tails will be reasonably accurate. Conversely, the E_{corr} contrast associated with individual filiform heads is likely to be significantly underestimated.

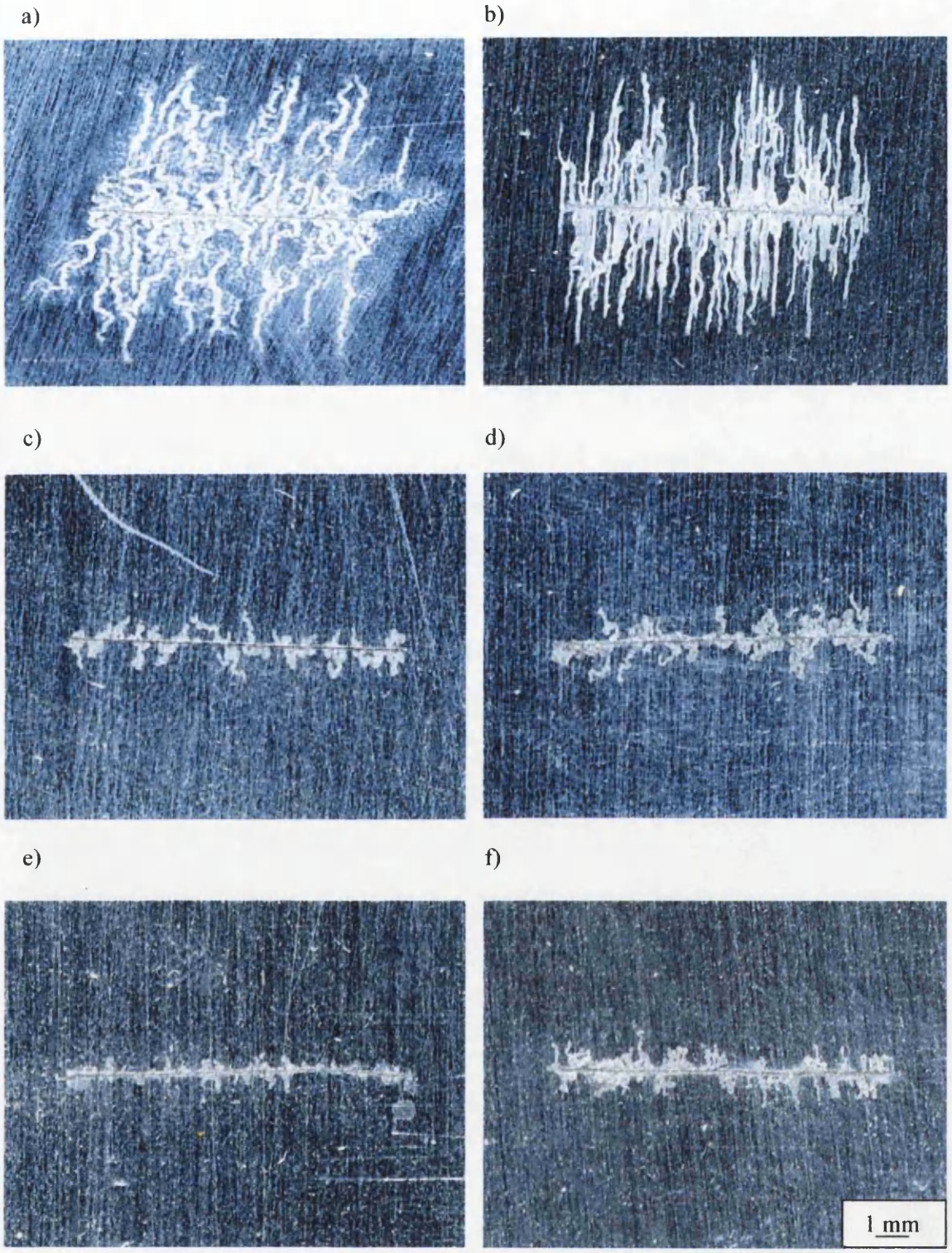

Figure 4.7: Photographic images, each showing the area surrounding the 1 cm penetrative defect on PVB/H_2PP coated, abraded AA6111-T4 100 hours following FFC initiation. H_2PP concentration key: (a) none, (b) 0.1%, (c) 0.5%, (d) 1%, (e) 2.5% and (f) 5% w/w

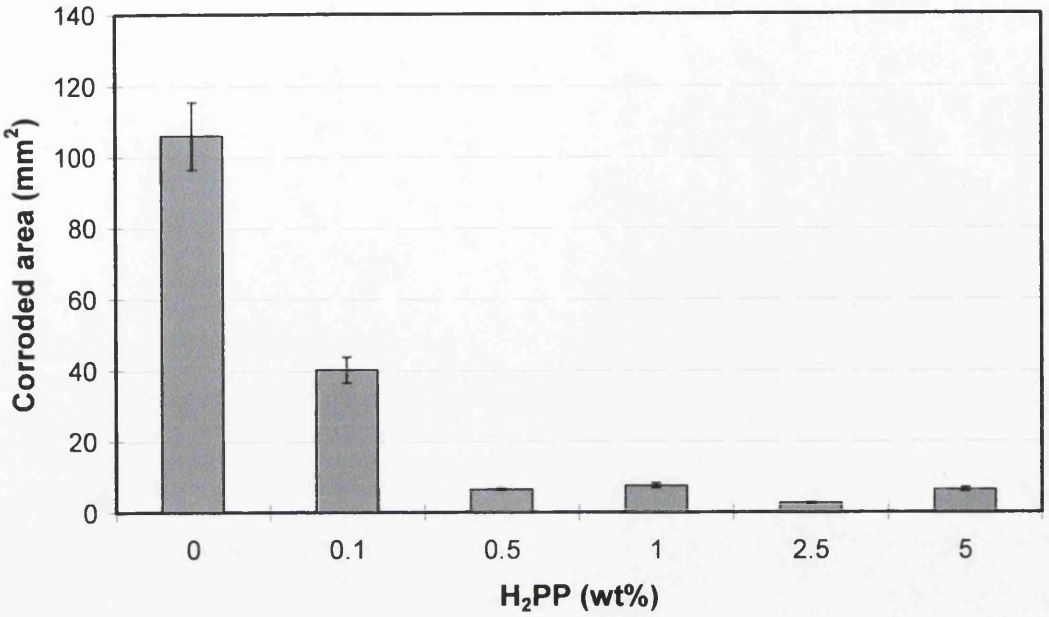

Figure 4.8: FFC delaminated area, as determined by optical image analysis of PVB/H_2PP coated, abraded AA6111-T4 100 hours following FFC initiation. Error bars are ± 1 standard deviation units on the mean, corresponding to fractional error of ca ± 9%.

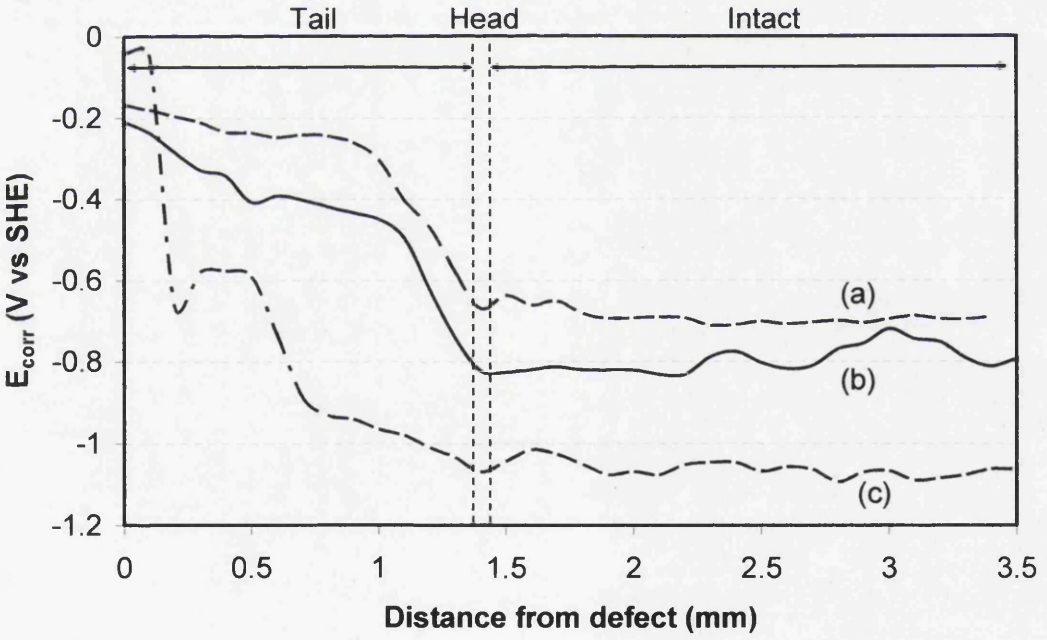

Figure 4.9: SKP derived E_{corr} vs. distance profiles for individual 1.5 mm long filaments on PVB/H_2PP coated, abraded AA6111-T4 - measured centrally along the axis of propagation. H_2PP concentration key: (a) none, (b) 0.1%, (c) 1%.

The uninhibited E_{corr} profile shown by curve (a) of Fig 4.9 is entirely similar to profiles obtained for surface-active FFC on AA6016-T4 (shown in Chapter 3, Fig. 3.9), with an E_{intact} of *ca.* -0.68 V *vs.* SHE rising to a E_{corr} maximum of *ca.* -0.2 V in the filament-tail region. In curve (b), the introduction of 0.1% w/w in-coating H_2PP produces a relatively small depression (of *ca.* 0.1V) in both E_{intact}, and filament E_{corr} values. In curve (c), increasing in-coating H_2PP to 1% w/w depresses E_{intact} to *ca.* -1.1V *vs.* SHE and also depresses E_{corr} values by *ca.* 0.35 V (relative to the uninhibited case) over much of the filament length. Profiles entirely similar to curve (c) were obtained for all in-coating H_2PP concentrations between 0.5% and 5% w/w and values of E_{intact} were found to be substantially uniform over the sample surface. Fig. 4.10 shows plots of E_{intact} *vs.* time for the various coatings tested. Each time-dependent E_{intact} value has been calculated from an average of 480 data points (arranged as a series of 4 rows remote from, and parallel to, the coating defect). It may be seen that as in Chapter 3, E_{intact} values initially change with time as sample coatings come into equilibrium with humid air, but are approximately constant thereafter. Time-independent E_{intact} values (calculated as an average over the period of 40 to 48 hours humid air contact) are summarised in Fig. 4.11, plotted *vs.* in-coating H_2PP concentration and delaminated area data from Fig. 4.8. It may be seen that the decrease in E_{intact} coincides with a decrease in delaminated (corroded) area after 100 hours of FFC. However, it remains unclear whether these two phenomena are causally related or merely coincidental.

FFC kinetics may be quantified by following the time-dependent area of coating delamination – as determined by numerical integration of sample areas for which $E_{corr} \neq E_{intact}$.[20,24] Delaminated area (A) *vs.* time (t) plots thus obtained are shown in Fig. 4.12, where t_0 is the time taken for surface active FFC to become initiated (typically *ca.* 800 minutes). Curve (a) shows that, in the absence of inhibition, FFC propagation kinetics are linear with a delamination rate (dA/dt) of 2.4 x 10^{-2} mm^2/min. Curve (b) shows that 0.1% w/w in-coating H_2PP does not affect the linearity of FFC kinetics but reduces the rate of delamination to 1.9 x 10^{-3} mm^2/min. Curve (c) shows that 1% w/w in-coating H_2PP allows surface active FFC to initiate but completely inhibits subsequent FFC propagation. This last finding was similar for all in-coating H_2PP concentrations in the range 0.5 – 5% w/w. Absolute values of delaminated area may be underestimated in Fig. 4.12 due to limitations of SKP

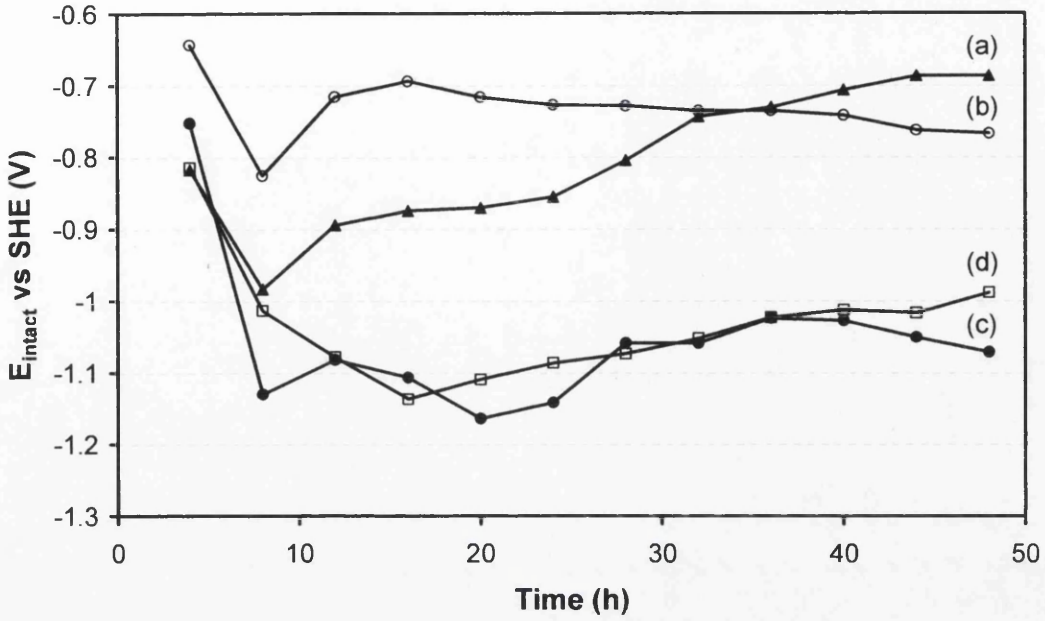

Figure 4.10: Time-dependent E_{intact} for PVB coated AA6111 in air at 80% r.h. and 40°C. Time is the period elapsed since first contact with the humid SKP atmosphere. H_2PP concentration key: (a) none, (b) 0.1%, (c) 1% and (d) 5%.

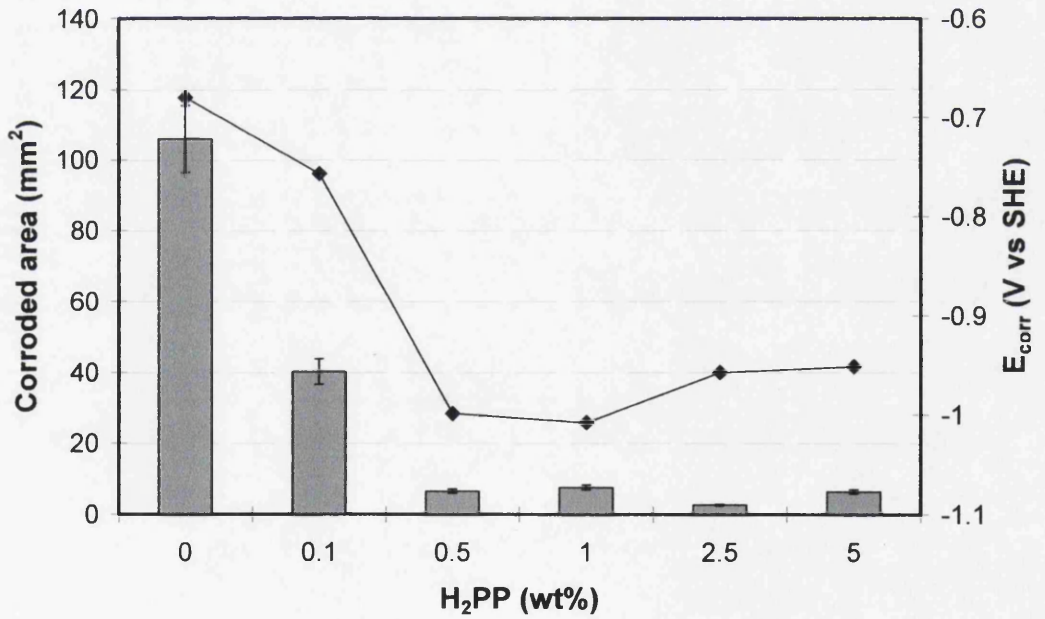

Figure 4.11: *Bar graph* – FFC delaminated area as shown in Fig. 4.8. *Line plot* – SKP derived time-independent E_{intact} for abraded PVB/H_2PP coated AA6111. Each E_{intact} value is calculated from the arithmetic mean of 480 data points for each of the final 3 scans (between 40 and 48 hours after FFC initiation from Fig. 4.12).

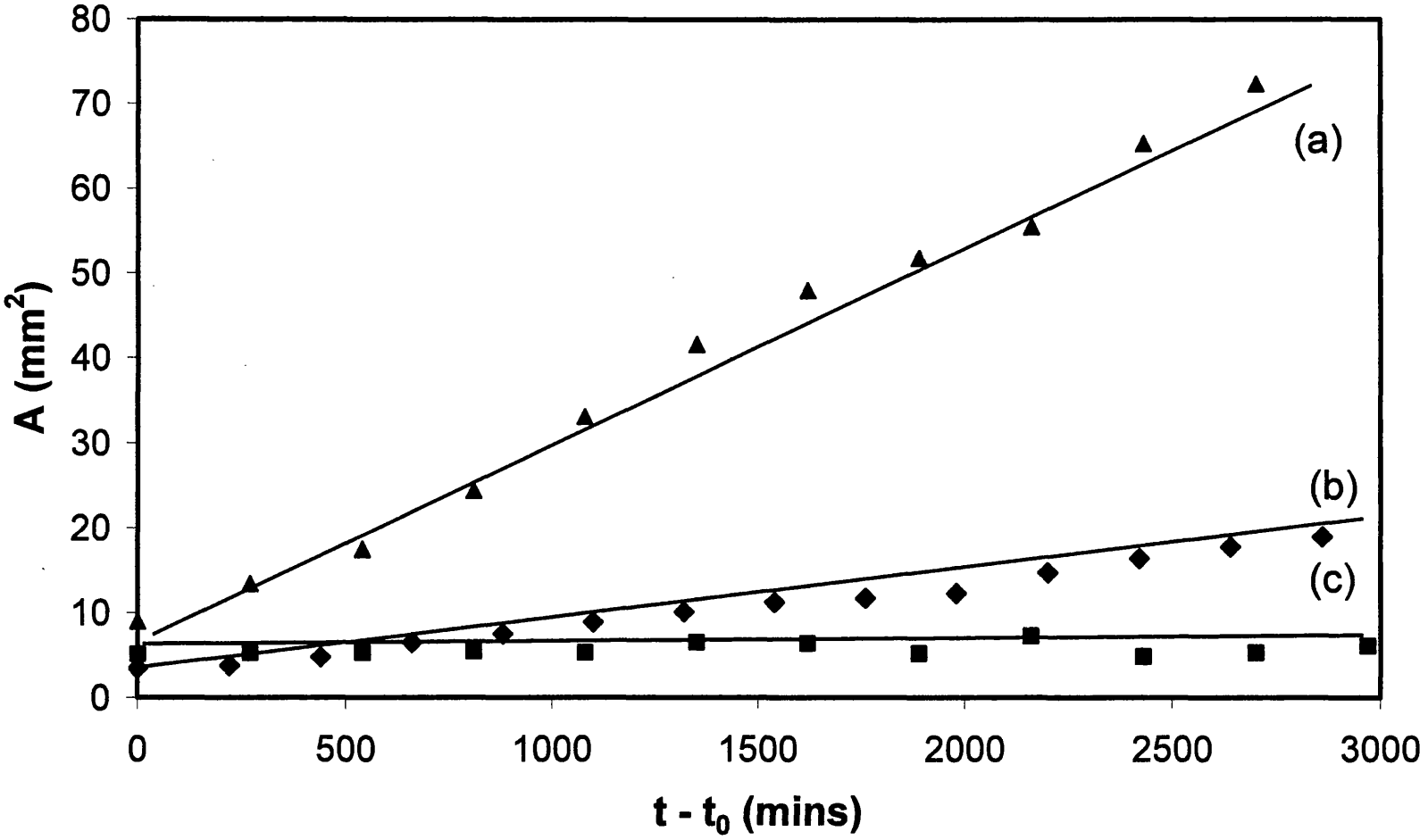

Figure 4.12: Time dependent FFC delaminated area for PVB coated AA6111-T4, quantified by in-situ SKP scanning. H_2PP concentration key: (a) none, (b) 0.1%, (c) 1%. The quantity t_0 is the time taken for FFC to become initiated typically *ca.* 800mins.

resolution. However, the final (3000 min) delaminated areas follow the same trend with in-coating H_2PP content as seen in Fig. 4.8.

On the basis of mixed potential theory, the E_{corr} depression seen in Fig. 4.9 is consistent with H_2PP acting to inhibit cathodic reactions (O_2 reduction and/or H_2 evolution) associated with FFC on AA6111. Furthermore, this would be a reasonable hypothesis in regions where the PVB coating has already become delaminated and aqueous electrolyte may contact the underlying metal. Under these circumstances, H_2PP could diffuse from the PVB coating into the FFC electrolyte, and inhibition could arise from the non-Faradic adsorption of H_2PP derived anions[6-8,25] and/or the precipitation of H_2PP/metal (principally aluminium) salts.[26,27] Such a mechanism is consistent with the observation, in Fig. 4.12, that in-coating H_2PP cannot prevent FFC initiation but acts rapidly and efficiently to inhibit FFC propagation.

A question then arises as to whether H_2PP adsorption or salt formation during coating deposition could similarly be responsible for the H_2PP-induced depression of E_{intact} and also contribute to FFC inhibition. To test this hypothesis an abraded AA6111 substrate was immersed in 2 M aqueous H_2PP for a period of 1 hour and then rinsed with distilled water prior to coating with PVB. The resulting sample exhibited neither significant E_{intact} depression nor significant FFC inhibition relative to the normal uninhibited case, (H_2PP = 0 wt%) shown in Fig. 4.11. Specifically, the value of E_{intact} was *ca.* -0.7V vs. SHE *cf.* -0.68V vs. SHE and 100 hours delaminated area was 100 ±9 mm^2 *cf.* 106 ±10 mm^2 for the normal uninhibited case. This suggests that neither chemical reaction nor irreversible adsorption processes involving H_2PP occur to any significant extent during coating deposition. Instead it would seem likely that E_{intact} depression results from a metal-coating dipole, arising in turn from a reversible adsorption of H_2PP derived species – possibly HPP^- and/or PP^{2-} anions – at the metal/coating interface.[6-8] Nevertheless, E_{intact} depression might conceivably contribute to FFC inhibition by Coulombically disfavouring the adsorption of aggressive Cl^- anions from the FFC electrolyte.[21,25]

The fact that the adsorption of H_2PP derived anion species is occurring from the coating also has implications if this concept was to be further developed for commercial applications. The acid may be released both up and down normal to the metal substrate meaning that as well as being adsorbed onto the underlying substrate

the acid may also be released into an overcoated top paint layer. This is likely to have a detrimental effect on the appearance of any overlaying topcoat paint layers.

4.4 Conclusions

- The damaged surface layer introduced by grinding increases the susceptibility of AA6111 to "surface active" filiform attack. In the absence of an inhibitor, FFC propagates with linear kinetics over an indefinite period. The bulk alloy is also inherently susceptible to the slower, deeper "successive pitting" type attack. This leads to more secondary FFC on the bulk in the corroded area behind the surface active filiform front.

- "Self-anodisation" of an abraded AA6111 surface through the use of PAni coatings was ineffective as a corrosion inhibition mechanism. In fact the PAni coating itself increased the rate of surface active FFC by providing a facile cathodic reaction through the reduction of PAni-ES. Of the dopant anions used only HPP^- showed any inhibitory properties.

- Phenylphosphonic acid (H_2PP) dissolved in a PVB primer can efficiently inhibit HCl induced FFC on an abraded AA6111-T4 surface. When H_2PP is present at concentrations $\geq$ 0.5% FFC initiation still occurs but filament propagation is inhibited such that no single filament was observed to reach a length > 1.5 mm, even after 100 hours testing.

- Increasing in-coating H_2PP concentration over the range 0.5% - 5% w/w confers no additional benefit. One possible explanation for the inhibition of FFC would be that a complete coverage of electrochemically active sites by adsorption of HPP^- or PP^{2-}anions has already been achieved at the critical level of 0.5% w/w H_2PP.

- In-coating H_2PP acts to suppress E_{intact} and filament E_{corr} values by up to 0.35 V – an observation which has tentatively been attributed to the adsorption of

HPP^- or PP^{2-} anions on the oxide-covered aluminium surface, although metal/H_2PP salt formation may also contribute in the filament region.

4.5 Further Work

The efficiency of in-coating H_2PP as an inhibitor of FFC on AA6111-T4 is such that the exact mechanism(s) of inhibition and the determination of optimum inhibitor concentration seems worthy of further investigation, with a possible view to developing new coating and/or pre-treatment systems. However, current electrophoretic bath coating systems used in the automotive industry would render the soluble acid unusable without a microencapsulating delivery mechanism.

4.6 References

1. G. Williams and H. N. McMurray, *Electrochem. Solid-State Lett.*, **6**, B9 (2003).

2. G. M. Spinks, A. J. Dominis, G. G. Wallace and D. E. Tallman, *J. Solid-State Electrochem.*, **6**, 85 (2002).

3. D. E. Tallman, G. Spinks, A. Dominis and G. G. Wallace, *J. Solid-State Electrochem.*, **6**, 73 (2002).

4. G. Williams and H. N. McMurray, *16th Inter. Corrosion Congress Proc.*, **Paper P-18 C-29** (2005).

5. A. J. Dominis, G. M. Spinks and G. G. Wallace, *Prog. Org. Coat.*, **48**, 43 (2003).

6. P. Persson, E. Laiti and L. O. Ohman, *Journal of Colloid and Interface Science*, **190**, 341 (1997).

7. E. Laiti and L. O. Ohman, *Journal of Colloid and Interface Science*, **183**, 441 (1996).

8. E. Laiti, L. O. Ohman, J. Nordin and S. Sjoberg, *Journal of Colloid and Interface Science*, **175**, 230 (1995).

9. M. Stratmann, A. Leng, W. Furbeth, H. Streckel and GroBe-Brinkhaus, *Prog. Org. Coat.*, **27**, 261 (1996).

10. M. Stratmann, R. Feser and A. Leng, *Electrochemica Acta*, **39**, 1207 (1994).

11. W. Furbeth and M. Stratmann, *Fresen. J. Anal. Chem.*, **353**, 337 (1995).

12. H. N. McMurray and G. Williams, *Corrosion*, **60**, 219 (2004).

13. G. M. Scamans, A. Afseth, G. E. Thompson and X. Zhou, *DFO/DGO Conference on Light Alloy Applications, Dusseldorf* (2004).

14. G. Scamans, A. Afseth, G. E. Thompson and X. Zhou, *DFO/DGO Conference on Light Alloy Applications, Dusseldorf* (2004).

15. G. Williams, H. N. McMurray, D. Hayman and P. C. Morgan, *Phys. Chem. Comm.*, **6**, 1 (2001).

16. A. Nazarov and D. Thierry, *Protecting Metals*, **39** (2003).

17. A. Leng, H. Streckel and M. Stratmann, *Corros. Sci.*, **41**, 547 (1999).

18. G. Williams and H. N. McMurray, *Electrochem. Solid-State Lett.*, **8**, B42 (2005).

19. H. N. McMurray, A. J. Coleman, G. Williams, A. Afseth and G. M. Scamans, *J. Electrochem. Soc.*, submitted to Journal of the Electrochemical Society.

20. G. Williams and H. N. McMurray, *J. Electrochem. Soc.*, **150**, B380 (2003).

21. H. N. McMurray, G. Williams and S. O'Driscoll, *J. Electrochem. Soc.*, **151**, B406 (2004).

22. G. Williams and H. N. McMurray, *Electrochem. Solid-State Lett.*, **7**, B13 (2004).

23. W. Schmidt and M. Stratmann, *Corros. Sci.*, **40**, 1441 (1998).

24. H. N. McMurray, G. Williams and S. O'Driscoll. in *Corrosion and Corrosion Protection*, J. D. Sinclair, R. P. Frankenthal, E. Kalman and W. Plieth, PV 2001-22, p.891, The Electrochemical society Proceedings Series, Pennington, NJ (2001).

25. M. Sheffer, A. Groysman, D. Starosvetsky, N. Savchenko and D. Mandler, *Corros. Sci.*, **46**, 2975 (2004).

26. S. Rajendran, B. V. Apparao and N. Palaniswamy, *Anti-Corrosion Methods and Materials*, **45**, 158 (1998).

27. J. E. P. da Silva, S. I. C. de Torresi and R. M. Torresi, *Corros. Sci.*, **47**, 811 (2005).

Chapter 5

Inhibition of Pitting Corrosion on AA2024-T3 by Copper Complexing Compounds

5.1 Introduction

Aluminium alloys such as AA2024-T3 are widely used in the aerospace industry due to their high strength to weight ratio. A large concentration of copper (up to 5 wt.%) is used which leads to the formation of intermetallic particles (IMP) such as Al_2Cu, Al_2CuMg and $Al_{20}Cu_2(Mn,Fe)_3$. These enhance the mechanical properties of the alloys as a consequence of age-hardening (as described in Section 1.2.3). However, the presence of these same copper containing IMP's increases the susceptibility of the alloys to localised corrosion which has been extensively investigated and is discussed in detail in Section 1.4.2. Briefly, galvanic interactions between copper-rich intermetallic particles and the aluminium matrix renders precipitation hardened Al-alloys, such as AA2024-T3, highly susceptible to localized corrosion in aqueous chloride containing electrolytes. The most abundant IMP, the S-phase IMP, is initially anodic to the matrix but dealloying S-phase occurs when the constituent Mg dissolves as Mg^{2+}. This transiently inhibits re-passivation, allowing aluminium to dissolve, leaving behind a high surface area, porous copper sponge.[1] Over time, nano-scale Cu clusters may become detached and transported either by convection in solution or by the mechanical action of growing corrosion product, to other locations on the corroding AA2024 surface (see Section 1.4.2.2) In addition, once Cu clusters become electrically disconnected from the alloy, they can adopt free corrosion potentials representative of pure copper. In aggressive Cl^- containing electrolytes, anodic dissolution may occur to give aqueous Cu^{2+} ions, which subsequently replate on the alloy surface.[2]

In contrast, matrix dealloying occurs as a result of elevated local pH at sites of cathodic oxygen reduction, such as Cu-rich S-phase remnants.[3,4] Local alkalisation destroys the passivity of the Al matrix by promoting the dissolution of Al as the soluble aluminate anion, AlO_2^- (aq).[4-7] Dealloying by so called "cathodic corrosion" (see Section 1.4.2.3) may also lead to significant levels of Cu exposure, resulting in agglomeration of solid solution Cu to form cathodically active particles which serve as additional sites of oxygen reduction. Furthermore, matrix dissolution will also reveal new IMPs, which anodically activate and transform into oxygen reduction cathodes by the processes already described above.

As described in Section 1.4.2.5, it is widely accepted that water soluble chromium (VI) oxyanions are highly effective in inhibiting localised corrosion of

precipitation hardened Al alloys such as AA2024-T3. Inhibition has been shown to occur by many mechanisms but it is the inhibition of electrochemical processes, especially the oxygen reduction reaction (ORR), on Cu-rich IMPs by Cr(VI) which is receiving significant current attention from researchers keen to mimic the action of Cr(VI) using environmentally benign alternatives.[8]

It has recently been shown (see Section 1.4.2.5) that copper complexants such as 2,5-dimercapto-1,3,4-thiadiazolate (DMTD) effectively stifle oxygen reduction on pure copper. It has also been demonstrated that the benzotriazolate anion (BTA), a well known inhibitor of copper corrosion, can inhibit both localized corrosion on bare AA2024-T3 immersed in Cl^- containing solution and filiform corrosion when exchanged into hydrotalcite pigment and dispersed in an organic coating.

In this chapter a systematic and comparative study is made of DMTD and BTA along with other reagents which specifically interact with Cu(II) aquo-cations, including ferrocyanide, N,N-diethyl dithiocarbamate (DEDTC) and ethylenediamminetetraacetic acid (EDTA), as inhibitors of pitting corrosion on bare AA2024-T3 in chloride containing solution. A scanning vibrating electrode technique (SVET) is used to follow the kinetics of stable pitting on non-polarised samples as a function of inhibitor concentration in aerated 5% w/v aqueous sodium chloride solution at room temperature. The initial aim was to draw up a ranking order of inhibitor efficiencies and identify the mode of action by which each reagent influenced local corrosion activity. However, it became a further aim to differentiate between inhibition arising from either the de-activation of Cu-rich IMPs or the prevention of copper re-plating, thus highlighting their relative importance within the overall process of stable pitting on AA2024-T3.

5.2 Experimental Details

AA2024-T3 aluminium alloy sheet of 2 mm thickness (composition given in Section 2.2.1) was provided by BAe Systems Plc and prepared for SVET experiments as described in Section 2.4.4. Sodium chloride, potassium ferrocyanide, sodium N,N-diethyldithiocarbamate trihydrate, benzotriazole, ethylenediammine-tetraacetic acid (disodium dihydrate), 2,5-dimercapto-1,3,4-thiadiazole (dipotassium salt) and all other chemicals were obtained from the Aldrich Chemical Co. in their highest purity.

Scanning vibrating electrode measurements were carried out using the SVET apparatus described in Section 2.4 where a detailed description of the calibration procedure is also given. Briefly, the probe comprised a 125 μm diameter platinum wire sealed in a glass sheath, so that the active portion of the probe tip consisted of a 125 μm diameter Pt micro-disc electrode with a total tip diameter of ~ 250μm. The probe vibration frequency was 140 Hz and the peak-to-peak vibration amplitude (A_{pp}), as measured stroboscopically in air was 30 ± 5 μm. Movement of the SVET probe-vibrator assembly was achieved using three orthogonal linear bearings driven by stepper motors (Time and Precision Ltd). The SVET voltage signal was detected using a Perkin Elmer 7265 lock-in amplifier and subject to digital signal averaging (typically of 10 successive measurements) to further enhance signal-to-noise ratio.

AA2024-T3 samples were completely immersed, exposed area uppermost, in an electrolyte bath containing 0.86 M (5% w/v) aqueous sodium chloride at pH 6.5, unless otherwise stated. The bath was left unstirred and in contact with room air at a nominal temperature of 20°C. Samples were scanned immediately following immersion and at hourly intervals thereafter for a period of 24 hours.

5.3 Results and Discussion

5.3.1 Uninhibited Corrosion of AA2024-T3

Current density distributions were determined as a function of time above the surface of an unpolarised AA2024-T3 alloy sample, freely-corroding in aerated 0.86 M aqueous NaCl at pH6.5, by repetitive *in-situ* SVET scanning. This approach enabled pit propagation kinetics to be studied for a population of stable pits. It should be noted that because of the time taken to complete a scan of the exposed AA2024-T3 surface (*ca.* 20 min), the SVET is largely ineffective at detecting metastable pitting. Fig. 5.1 shows representative current density, j_z, maps obtained 1h and 6h following electrolyte immersion and at 6 hourly intervals thereafter up to the termination of the experiment at 24 hours. A SVET scan carried out immediately following immersion revealed limited local anodic activity ($j_z \leq 0.5$ Am^{-2}) at several points on the AA2024-T3 surface, indicating that localised corrosion is initiated within minutes of exposure to chloride containing solution. Within 1h, stable pitting becomes established, as evidenced by the anodic j_z peaks in Fig. 5.1a where *ca.* 25 pits per cm^{-2}

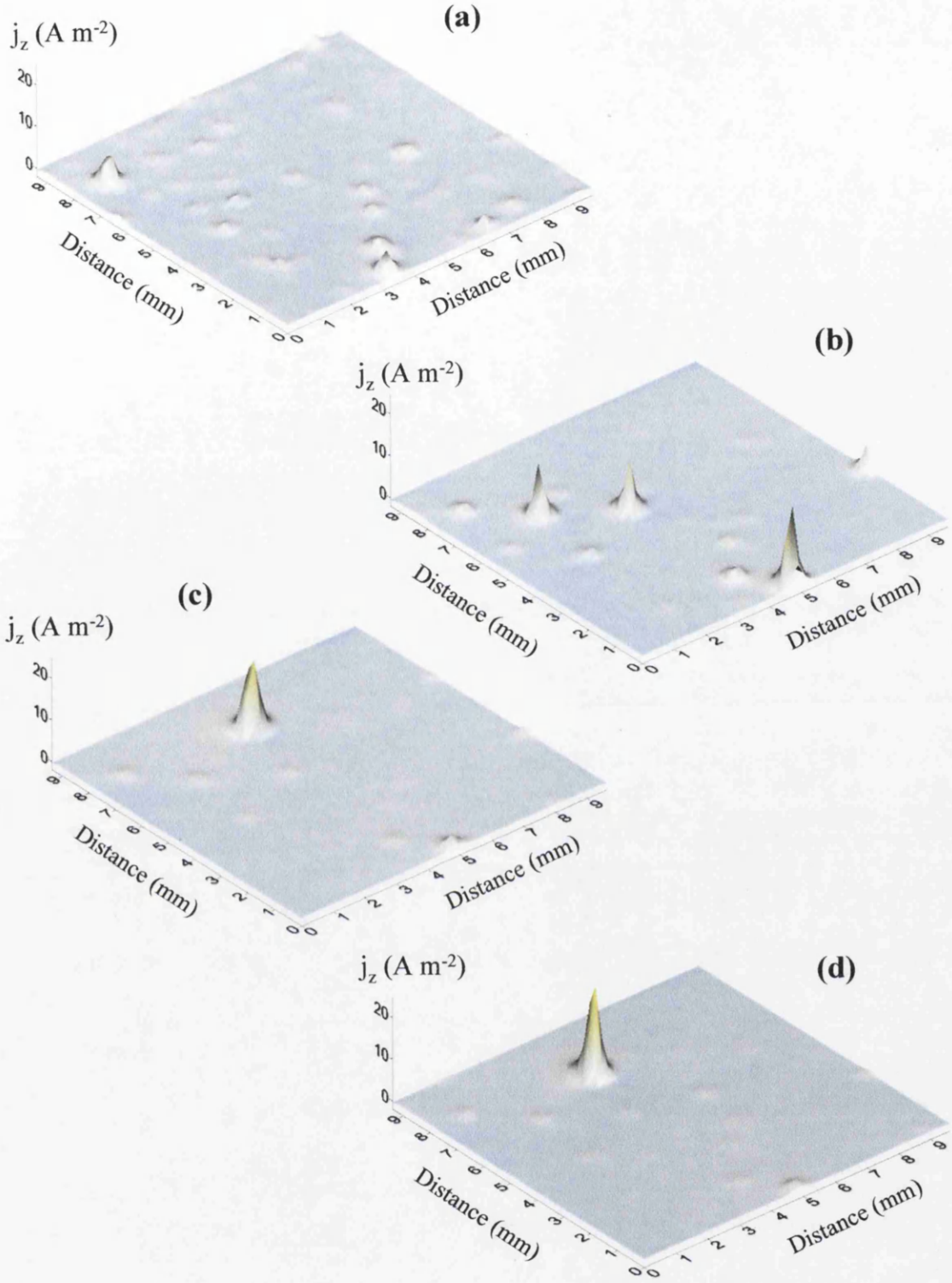

Figure 5.1: Surface plots showing the distribution of normal current density j_z above an AA2024-T3 alloy sample freely corroding in aerated 0.86 M aqueous NaCl at pH 6.5 and 20°C. Data were obtained from SVET scans carried out **(a)** 1, **(b)** 6, **(c)** 12, **(d)** 18 and (e) 24 hours after sample immersion. **(f)** Shows the visual appearance of the same sample after 24 hours immersion.

are detected with current densities in the range $0.5 \geq j_z \geq 5\ Am^{-2}$. Subsequent scans show that following initiation, individual pits propagate for varying periods of time before passivating. Thus it may be seen from Fig. 5.1(a-e) that some pits remain active over a 12 hour period or longer whereas many others do not. The visual appearance of the sample surface at the end of the 24h immersion period is shown in Fig. 5.1f. The pit openings, visible at the centre of roughly circular deposits of white corrosion product, coincide with the location of the anodic current density maxima seen in Fig. 5.1(a-e). The remainder of the surface is covered with a dark tarnish.

Unfortunately, j_z surface plots of the type shown in Fig. 5.1 are too numerous to allow the time dependent evolution of local corrosion currents to be comprehensively described in a compact manner. An estimation of time dependent total local corrosion currents was obtained through the numerical area integration of j_z distributions using an approach detailed in Section 2.4.5. A minimum estimate of time-dependent total anodic current (I_a) and hence area-averaged anodic current density (J_t) associated with each of the current density distribution j_z maps exemplified in Fig. 5.1, was obtained by numerical integration according to Equation (5.1),

$$I_a = A \cdot J_t \geq \int_0^x \int_0^y [\, jz_{(x,y)} > 0 \,]\, dxdy \qquad (5.1)$$

where A is the sample area, x and y are the length and width of the SVET scan. Numerical integration was carried out using the trapezium rule, allowing one J_t value to be obtained from each hourly SVET scan. To compensate for a small but finite level of random electrical noise superimposed on the SVET signal (typically 1 μV peak-to-peak, corresponding to ± 0.06 Am^{-2}), a J_t value carried out for a blank experiment was subtracted from each individual area averaged anodic J_t current density value, calculated according to Equation (5.1). The blank J_t value used was a mean value obtained from five separate SVET scans carried out over a glass slide immersed in test electrolyte.

From area averaged anodic J_t current density values, the total equivalent aluminium loss could be calculated by applying Faraday's law. The total quantity of charge emitted from corrosion pits over the 24 hour experimental period was calculated using,

$$Q = \frac{3F \times teal}{27} = \int_{t=0}^{t=tm} Jt\ dt \qquad (5.2)$$

where Q is the charge in Cm^{-2}, tm is the immersion period (in seconds), F is the Faraday constant and *teal* is the total equivalent aluminium (atm. wt 27g) loss in gm^{-2}.

The mean value of Q obtained from 3 repetitions of the uninhibited 24 hour immersion experiment, using a freshly prepared AA2024-T3 sample each time, was $3300 \pm 430\ Cm^{-2}$, which corresponds to a *teal* value of $0.31 \pm 0.04\ g\ m^{-2}$. It should be stressed that SVET-derived j_z area integrals systematically underestimate corrosion currents whenever lines of current flux between galvanically coupled anodic and cathodic regions pass under the plane of scan (*i.e.* < 100 μm). Therefore SVET-derived *teal* values are minimum estimates, arising from a situation where areas of local anodic and cathodic activity are physically separated by distances of > 100 μm and as such do not take into account any contribution due to generalised corrosion.

5.3.2 Corrosion Inhibition by Copper Complexing Reagents

A series of experiments were carried out where AA2024-T3 samples were immersed in aerated 0.86 M NaCl (aq) solutions containing reagents capable of either precipitating and/or sequestering copper ($Fe(CN)_6^{4-}$, DMTD, DEDTC, BTA and EDTA) at concentrations ranging between 10^{-4} and 10^{-2} M. The chemical structures of the latter four compounds are given in Fig. 5.2. As in the uninhibited experiment, SVET scanning was carried out immediately on immersion and at 1 hour intervals thereafter for 24 hours.

5.3.2.1 Inhibition by Ferrocyanide

Fig. 5.3 shows a selection of representative j_z maps recorded in the presence of a 10^{-3} M $K_4Fe(CN)_6$ addition at various time intervals following immersion. The choice of $K_4Fe(CN)_6$ as a potential inhibitor of pitting corrosion on AA2024-T3 was based on the ability of ferrocyanide ions to combine with aqueous Cu^{2+} to form an insoluble precipitate.

(a) BTA

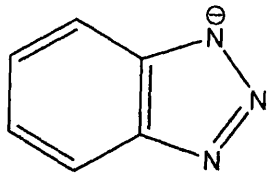

(b) DMDT

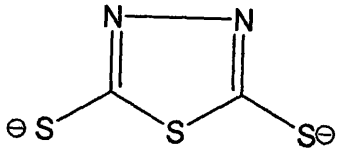

(c) DEDTC

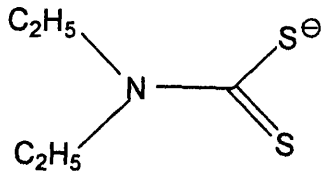

(d) EDTA

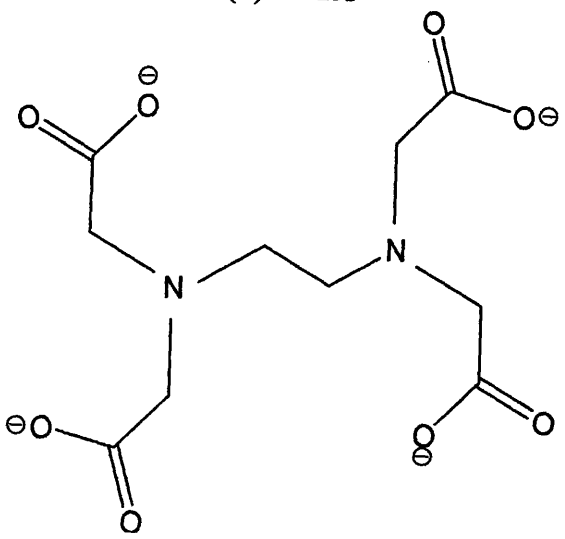

Figure 5.2: Chemical structures of selected copper chelating reagents used for the inhibition of AA2024-T3 pitting corrosion in NaCl containing electrolyte.

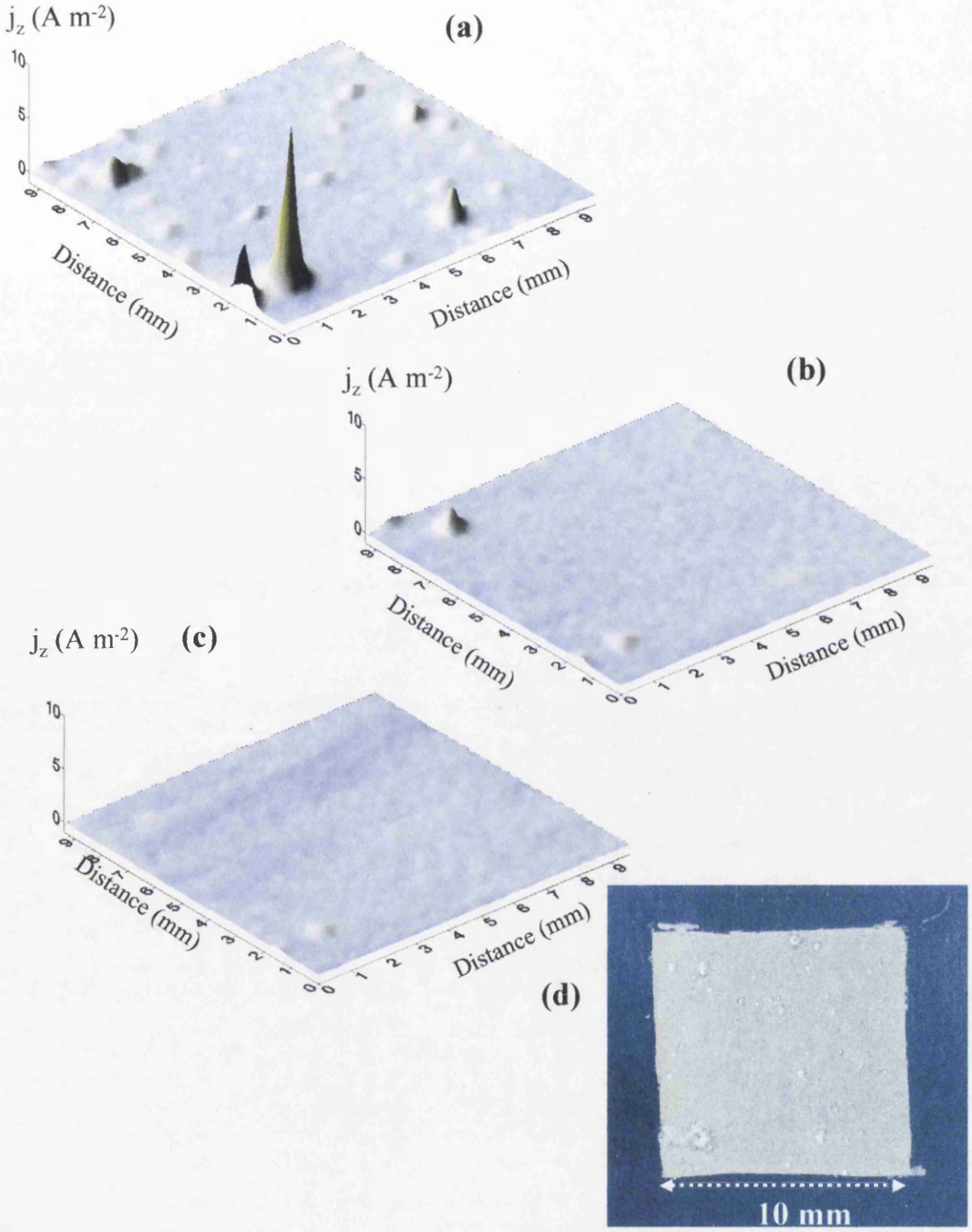

Figure 5.3: Surface plots showing the distribution of normal current density j_z above an AA2024-T3 alloy sample freely corroding in aerated 0.86 M aqueous NaCl containing 10^{-3} M potassium ferrocyanide at pH 6.5 and 20°C. Data were obtained from SVET scans carried out **(a)** 2, **(b)** 12, and **(c)** 24 h after sample immersion. **(d)** Shows the visual appearance of the same sample after 24 hours immersion

$$2Cu^{2+}_{(aq)} + Fe(CN)_6^{4-}(aq) \rightarrow Cu_2[Fe(CN)_6]_{(s)} \quad (5.3)$$

As discussed previously, Cu^{2+} ions are released when nano-scale copper ligaments become physically detached from dealloyed S-phase IMPs and undergo anodic dissolution independently of the matrix.[2,9] Therefore, where local concentrations of Cu^{2+} and ferrocyanide are sufficiently high that the solubility product of $Cu_2[Fe(CN)_6]$ is exceeded ($K_{sp} = 1.3 \times 10^{-16}$ mol^3 dm^{-9}),[10] then an insoluble film may be formed on the alloy surface. The j_z map in Fig. 5.3a shows that several stable pits are observed on the AA2024-T3 surface within 2h of immersion in the presence of a 10^{-3} M ferrocyanide concentration. However, over a further 3h period these pits are seen to passivate and for the remainder of the 24h experiment the AA2024-T3 shows little evidence of local corrosion activity (see Fig. 5.3b and c). A photographic image of the corroded surface following 24h immersion is given in Fig. 5.3d. The surface is covered with a white film, while the short lived stable pits observed by SVET at immersion times $\leq$ 5h are marked by spots of thicker white corrosion product.

Time-dependent area-averaged corrosion current density J_t values were obtained as before using Equation (5.1), for SVET immersion experiments carried out in the presence of varying concentrations of $K_4Fe(CN)_6$. Fig. 5.4(b-d) shows J_t versus time plots obtained in the presence of ferrocyanide at concentrations of 10^{-4}, 10^{-3} and 10^{-2} M respectively, along with results obtained in the absence of inhibitor shown in Fig. 5.4a. A limited degree of inhibition is afforded by a 10^{-4} M ferrocyanide addition (as shown in Fig. 5.4b), where time-dependent J_t values are typically reduced by *ca.* 50% compared to the control experiment carried out in 0.86 M NaCl electrolyte only (as shown in Fig 5.4a). Increasing the ferrocyanide concentration by an order of magnitude leads to a more complete inhibition of pitting, where marked anodic activity, peaking at 2h immersion, is observed to cease within 6h and is effectively zero for the duration of the experiment (see Fig 5.4c). Interestingly, a 10^{-2} M ferrocyanide concentration is significantly less efficient in inhibiting pitting. Fig. 5.4d shows that although J_t values are low upon initial immersion, they increase progressively with time and attain values characteristic of uninhibited AA2024-T3 at immersion times $\geq$ 20h. The reasons for this behaviour are unclear, but may be

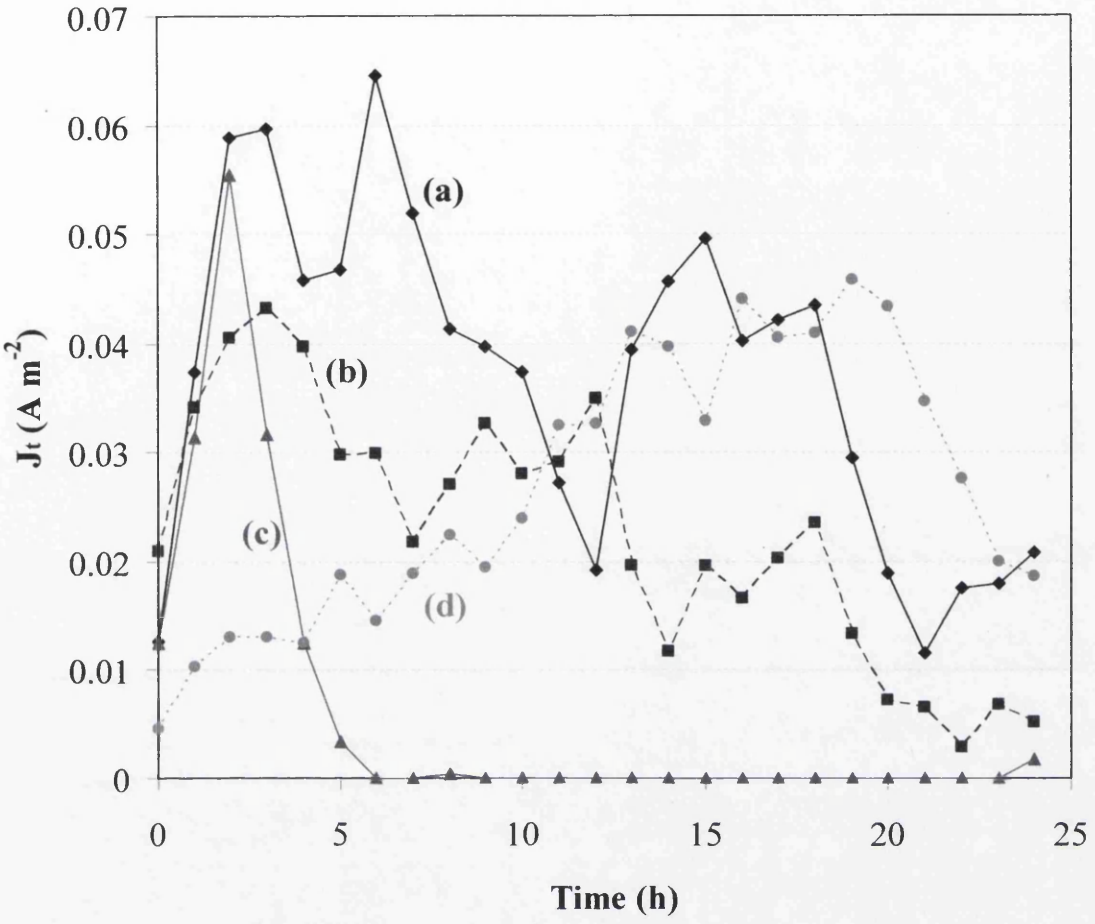

Figure 5.4: Plots of area-averaged anodic current density J_t versus immersion time for AA2024-T3 samples freely corroding in 0.86 M aqueous NaCl in the absence (a) and presence of potassium ferrocyanide at concentrations of (b) 10^{-4}, (c) 10^{-3} and (d) 10^{-2} M.

associated with the stability of ferrocyanide in acidic media.[11] As stable pits propagate, $Fe(CN)_6^{4-}$ anions can migrate from the bulk electrolyte to the interior of a pit, thus becoming exposed to a low pH environment. A certain degree of ferrocyanide decomposition may occur, accompanied by the formation of ferricyanide which may diffuse back into bulk solution with time. The presence of a ferrocyanide/ferricyanide redox couple in solution (E^o = +0.36V vs SHE[10]) provides an alternative facile cathodic reaction to oxygen reduction, and may contribute to an increase in pit currents. At bulk ferrocyanide concentrations $\leq 10^{-3}$ M, insufficient ferricyanide may be formed to have a perceptible effect.

Although ferrocyanide was selected as a possible inhibitor due to the low solubility product of its copper(II) salt, the appearance of an inhibited AA2024-T3 sample post-immersion, shown in Fig. 5.3d, is inconsistent with Cu^{2+} precipitation being the principal mode of inhibition. The absence of any reddish coloured surface deposits suggests that relatively little insoluble $Cu_2[Fe(CN)_6]$ is formed during immersion. A simple test carried out by mixing equal quantities of aqueous 10^{-2} M $CuCl_2$ (aq) and $K_4Fe(CN)_6$ solutions confirmed that a red coloured insoluble product was formed. A question therefore arises about the primary mode of inhibition of ferrocyanide at concentrations $\leq 10^{-3}$ M. There is no evidence to suggest that ferrocyanide can combine with Al^{3+} ions to form an inhibitor film. A second spot test, substituting $AlCl_3$ (aq) for the $CuCl_2$ (aq) solution, did not yield an insoluble product when mixed with a $Fe(CN)_6^{4-}$ (aq) solution. However, it has been reported that ferrocyanide anions adsorb strongly on to aluminium oxides, especially γ-Al_2O_3 at pH values of ≤ 7.[12] Therefore, inhibition may be due in part to strongly adsorbed ferrocyanide on the Al surface oxide film acting to disfavour Cl^- adsorption, in an analogous manner to a proposed mode of inhibition of AA2024-T3 by Cr(VI) oxy-anions.[8,13-20]

5.3.2.2 Inhibition by copper-specific chelating agents

Two organic reagents, namely sodium N,N-diethyl dithiocarbamate (DEDTC) and potassium 2,5-dimercapto-1,3,4-thiadiazolate (DMTD) were selected as potential inhibitors of AA2024-T3 corrosion on the basis of their properties as strong chelating agents for Cu^{2+} in aqueous solution. Chelation is the process of reversible binding (complexation) of a ligand (*i.e.* the chelating agent) to a metal ion by two or more

atoms, forming a metal complex (chelate).[21] Since the products of their respective reactions with Cu^{2+} are highly coloured, both compounds have been used as analytical spectrophotometric agents for the determination of copper in aqueous solution. [22-24] The Cu^{2+} – DEDTC chelate has low solubility in aqueous solution and is typically extracted into a chlorinated organic solvent for spectrophotometric analysis.[23,24] Its solubility in neutral aqueous solution was estimated by a simple titration of a 10^{-3} M DEDTC solution with $CuSO_4$ (aq), where a yellow-brown coloured chelate was observed to precipitate from solution at $[Cu^{2+}] \geq 5 \times 10^{-5}$ M. A similar test was carried out using 10^{-3} M DMTD (aq) and gave a yellow-green soluble product at $[Cu^{2+}] \leq 2 \times 10^{-4}$ M, which precipitated from solution at higher concentrations. DMTD has already been demonstrated to effectively inhibit oxygen reduction on copper,[8] with a view to its incorporation into anti-corrosion pigments for AA2024.[8] In this section the inhibitory effect of the addition of varying concentrations of DMTD to 0.86 M NaCl electrolyte on the pitting corrosion of unpolarised AA2024-T3 is compared with that of a second Cu^{2+} chelator (DEDTC) under the same experimental conditions.

Again, DEDTC and DMTD concentrations were systematically varied in the range 10^{-4} to 10^{-2} M and numerical integration of anodic j_z values according to Equation (5.1) was used to produce a semi-quantitative measure of corrosion rate. A representative selection of current density distribution maps obtained for unpolarised AA2024-T3 in inhibited 0.86 M NaCl electrolyte, using a DEDTC addition of 10^{-3} M, is given in Fig. 5.5. A small amount of anodic activity is observed over the first 3h following immersion as shown by Fig. 5.5a, where there are *ca.* 8 pits cm^{-2} exhibiting local anodic current density values in the range $0.3 \leq j_z \leq 0.6$ A m^{-2}. However, all anodic activity ceases at immersion times $\geq$ 4h as evidenced by the j_z maps given in Figs. 5.5b and c. A photographic image of the corroded sample surface following 24h immersion (see Fig. 5.5d), shows that the majority of the sample surface is coated with a light brown film,. However, there are some small pits surrounded by circular deposits of white product on the surface. The effect of systematically increasing the DEDTC concentration by 2 orders of magnitude is shown by the J_t versus time plots in Fig. 5.6. Again, results obtained for uninhibited AA2024-T3 are also plotted for comparison. The plots show that systematically increasing the DEDTC concentration serves to progressively decrease the extent of local anodic activity. At a DEDTC

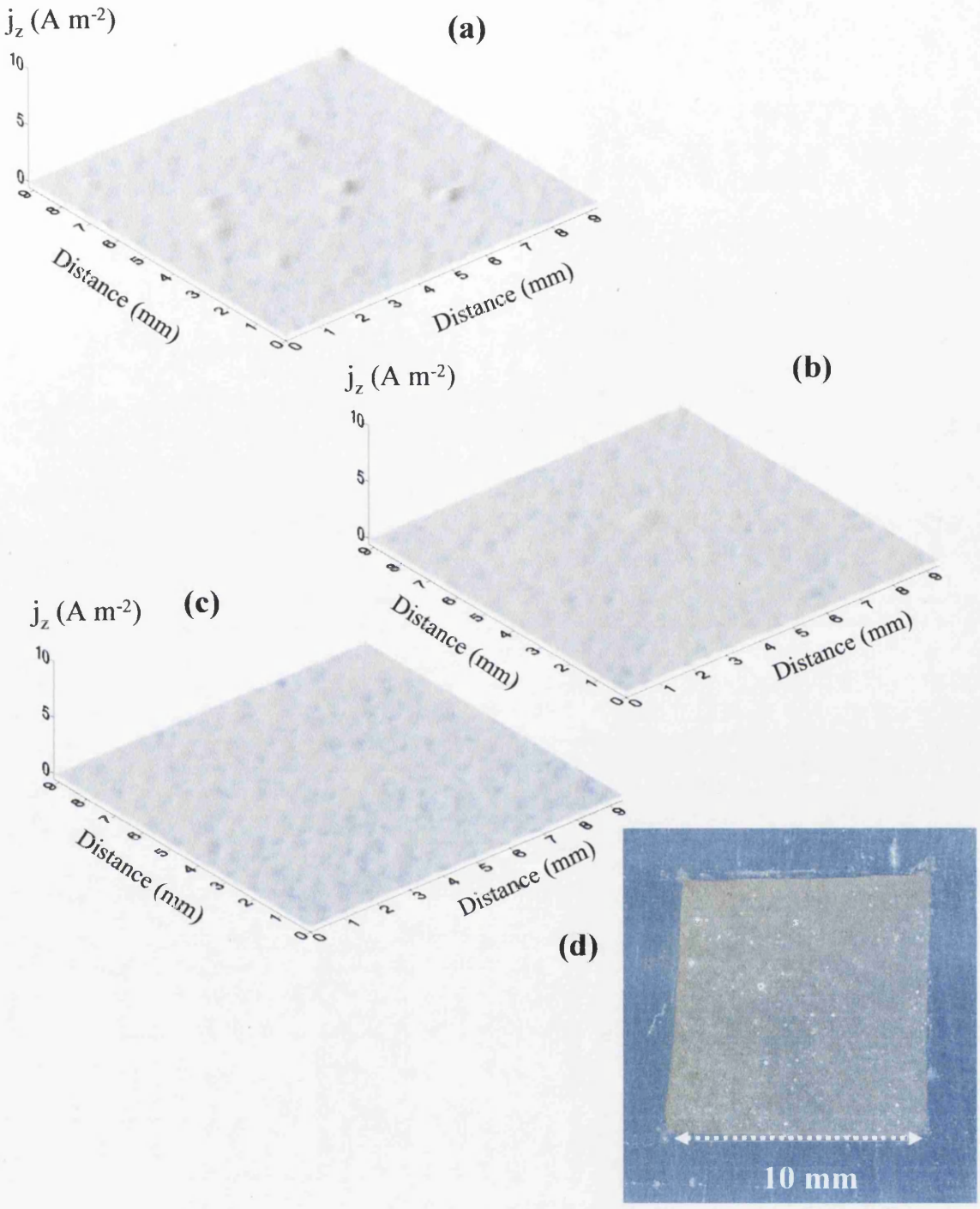

Figure 5.5: Surface plots showing the distribution of normal current density j_z above an AA2024-T3 alloy sample freely corroding in aerated 0.86 M aqueous NaCl containing a 10^{-3} M sodium N,N-diethyl dithiocarbamate (DEDTC) salt addition at pH 6.5 and 20°C. Data were obtained from SVET scans carried out **(a)** 2, **(b)** 12, and **(c)** 24 h after sample immersion. **(d)** Shows the visual appearance of the same sample after 24 hours immersion.

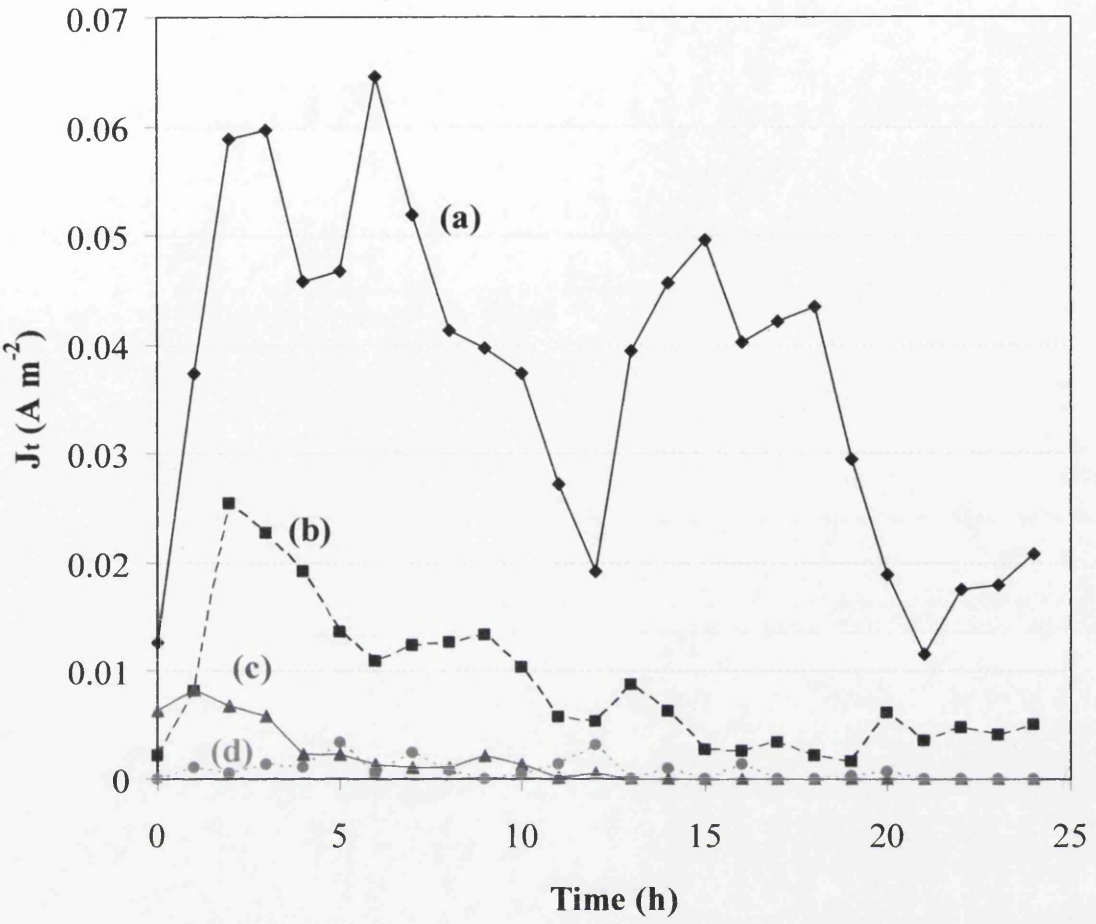

Figure 5.6: Plots of area-averaged anodic current density J_t versus immersion time for AA2024-T3 samples freely corroding in 0.86 M aqueous NaCl in the absence (a) and presence of sodium N,N-diethyl dithiocarbamate (DEDTC) at concentrations of (b) 10^{-4}, (c) 10^{-3} and (d) 10^{-2} M.

concentration of 10^{-2} M, time-resolved J_t values are effectively zero over the immersion period. The profound inhibition observed at this concentration is accompanied by the formation of a yellow-brown surface film.

Identical experiments carried out using DMTD gave entirely similar results. J_t versus time plots obtained in the presence of DMTD at concentrations of 10^{-4}, 10^{-3} and 10^{-2} M respectively, along with results obtained in the absence of inhibitor are given in Fig. 5.7. These plots show that DMTD is an excellent inhibitor of AA2024-T3 pitting corrosion when present at concentrations $\geq 10^{-3}$ M. At the end of the immersion period the DMTD-inhibited AA2024-T3 samples were again covered with a light brown film and little visual evidence of pitting could be observed.

5.3.3 Inhibition by Benzotriazolate

Benzotriazole (BTA) has been known as an efficient inhibitor of copper corrosion for 40 years [25-27] and forms the subject of numerous recent studies.[28-31] The benzotriazolate (BTA^-) anion is known to inhibit anodic copper dissolution by forming protective polymeric Cu^+BTA^- films.[29-31] In addition, it is known that BTA^- inhibits cathodic O_2 reduction on copper through competitive adsorption at the metal surface.[28] Because of the importance of Cu-rich IMP dealloying and subsequent copper redistribution in AA2024 corrosion, researchers are now starting to study BTA^- as an inhibitor of aluminium alloy corrosion.[32]

As for the inhibitor systems described previously, the effect of BTA additions in the range 10^{-4} to 10^{-2} M was studied. However, in order to dissolve BTA (*i.e* undissociated benzotriazole) in aqueous solution, the pH of the 0.86 NaCl M electrolyte was adjusted to pH 8. (*i.e.* equal to the pK_a value for BTA).[33] For comparison, a control experiment was carried out in the absence of BTA at the same elevated pH. A mean Q value of 3820 Cm^{-2} (corresponding to a *teal* of 0.36 g m^{-2}), obtained for this uninhibited 24 hour immersion experiment carried out at pH 8, was in reasonable agreement with values determined at near neutral pH (see section 5.3.1). Plots of area averaged anodic current density versus time for unpolarised AA2024-T3 in the presence and absence of BTA are given in Fig. 5.8. A comparison of the plots in Fig. 5.8a and b show that a 10^{-3} M inhibitor concentration has little or no effect on corrosion rate. For the sake of clarity, results obtained for a 10^{-4} M BTA addition are not included, but show a similar lack of inhibition. However, at concentrations $\geq 5 \times$

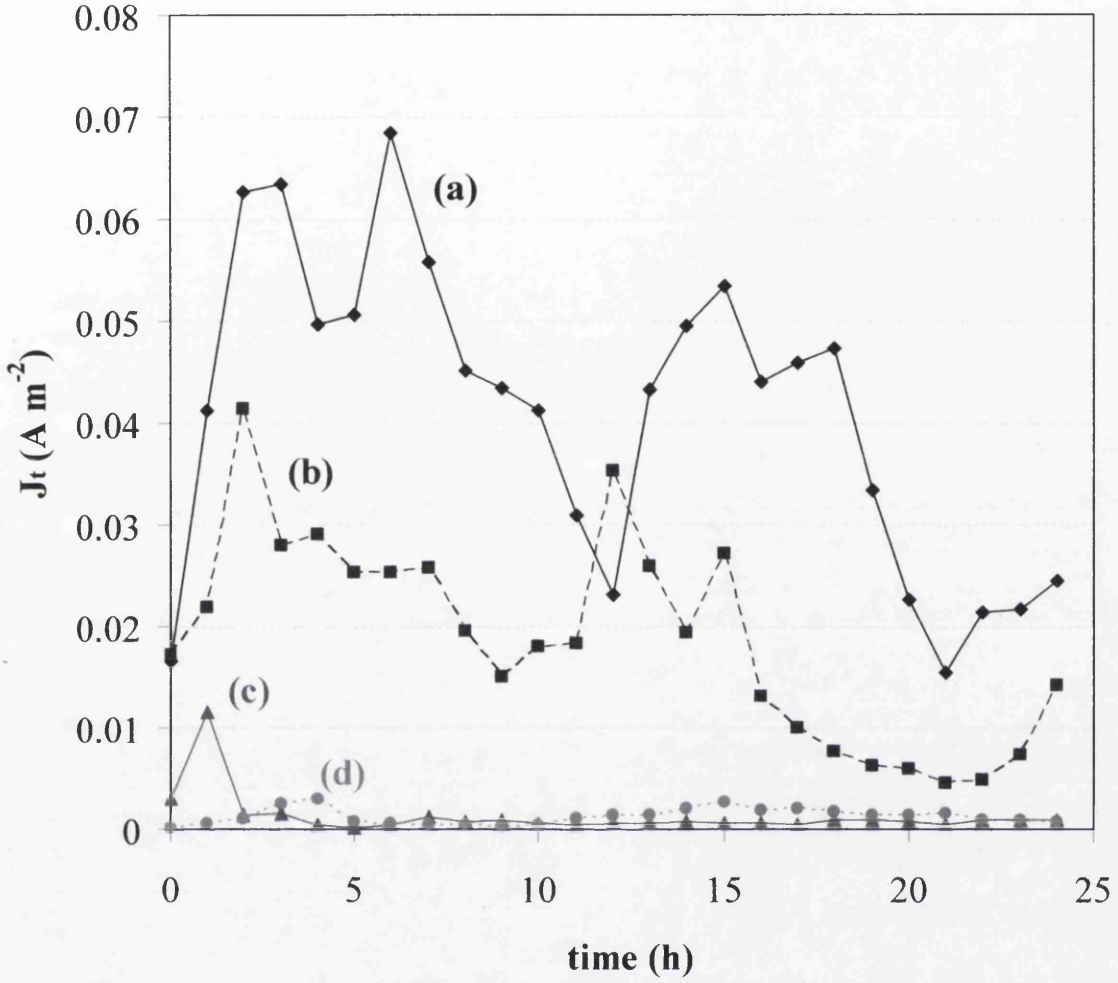

Figure 5.7: Plots of area-averaged anodic current density J_t versus immersion time for AA2024-T3 samples freely corroding in 0.86 M aqueous NaCl in the absence (a) and presence of odium 2,5 dimercapto 1,3,4, thiadiazolate (DMTD) at concentrations of (b) 10^{-4}, (c) 10^{-3} and (d) 10^{-2} M.

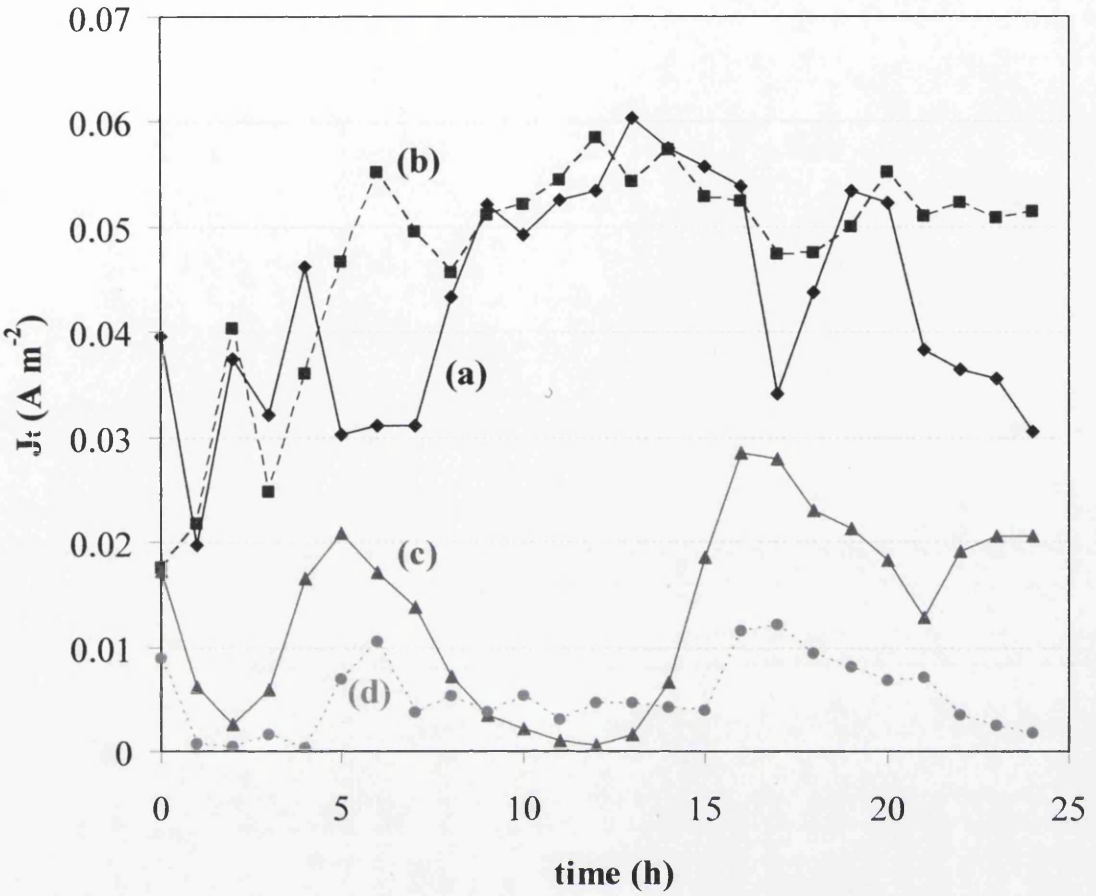

Figure 5.8: Plots of area-averaged anodic current density J_t versus immersion time for AA2024-T3 samples freely corroding in 0.86 M aqueous NaCl at pH 7.8 in the absence (a) and presence of benzotriazole at concentrations of (b) 10^{-3}, (c) 5×10^{-3} and (d) 10^{-2} M.

10^{-3} M, increasing BTA leads to a progressive decrease in the magnitude of time-resolved anodic current densities, as shown by Fig. 5.8c and d. The onset of inhibition at BTA $\geq 5 \times 10^{-3}$ M, is marked by the formation of dark brown surface films on the exposed AA2024-T3 surface during immersion. This supports the notion that BTA^- adsorbs strongly onto Cu-rich IMPs which are electrically connected with the AA2024-T3 matrix, thus stifling cathodic O_2 reduction and preventing Cu^{2+} ion formation (with consequent Cu replating) from electrically disconnected Cu particles.

5.3.4 Inhibition by EDTA

EDTA is probably the most well known and widely used chelating agent in the field of chemical analysis[21] and can form water soluble hexadentate complexes with a wide range of metal cations. In this work, the effect of EDTA additions on the corrosion of unpolarised AA2024-T3 in 0.86 M NaCl electrolyte was studied by repetitive *in-situ* SVET scanning. Electrolyte pH was adjusted from the natural pH of the EDTA solution (*ca.* pH 4 – 4.5) to 6.5 by dropwise addition of NaOH (aq). Experiments carried out using 10^{-3} and 10^{-2} M inhibitor concentrations showed that AA2024-T3 samples immersed in EDTA containing solution retained their original polished finish. However, despite the apparent lack of visual evidence of corrosion when EDTA is present, SVET analysis of the immersed AA2024-T3 surface tells a slightly different story. Fig. 5.9 shows SVET-derived j_z distribution maps obtained when scanning over a AA2024-T3 sample immersed in 0.86 M NaCl electrolyte containing a 10^{-2} M addition of EDTA at pH 6.5, at various times following immersion. The bright appearance of the AA2024-T3 surface following 24h immersion can be seen in Fig. 5.9d and may be directly compared with the highly pitted, uninhibited sample shown in Fig. 5.1f. It is evident from the j_z maps shown in Fig. 5.9(a–c) that EDTA does not inhibit pitting corrosion of AA2024-T3 and comparison with Fig. 5.1 indicates that peak anodic intensities remain $\geq$ the uninhibited sample over a 24h immersion period. Fig. 5.10 shows area-averaged corrosion current density J_t values plotted as a function of time, for experiments carried out in the presence of different EDTA concentrations. In the presence of a 10^{-3} M addition of EDTA, time resolved J_t values shown in curve (b) are comparable to those estimated for the control experiment given in curve (a). However, when 10^{-2} M EDTA was added to the immersion electrolyte, J_t peaked after 5h at a value of 0.15

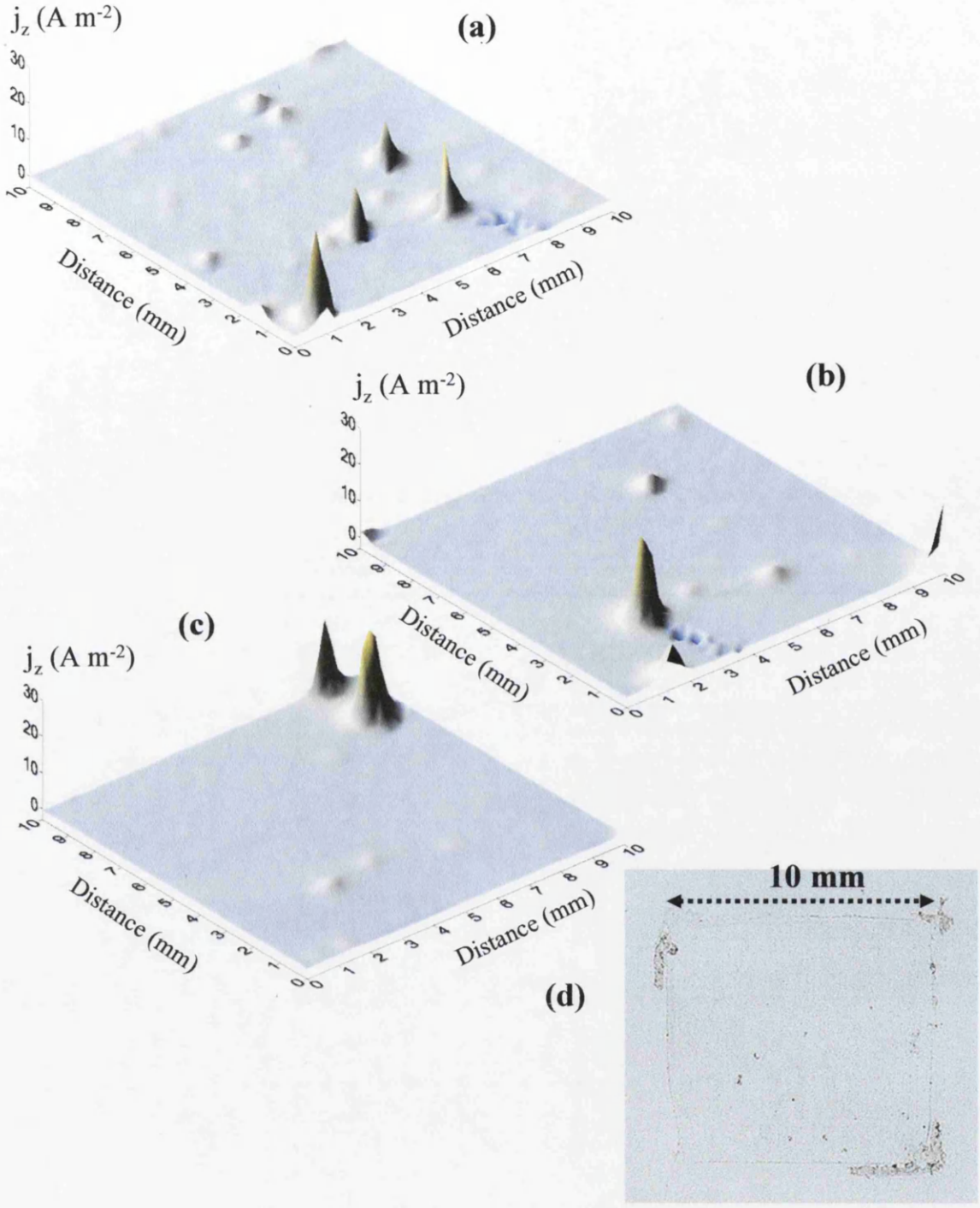

Figure 5.9: Surface plots showing the distribution of normal current density j_z above an AA2024-T3 alloy sample freely corroding in aerated 0.86 M aqueous NaCl containing a 10^{-2} M EDTA at pH 6.5 and 20°C. Data were obtained from SVET scans carried out (a) 2, (b) 12, and (c) 24 h after sample immersion. (d) Shows the visual appearance of the same sample after 24 hours immersion.

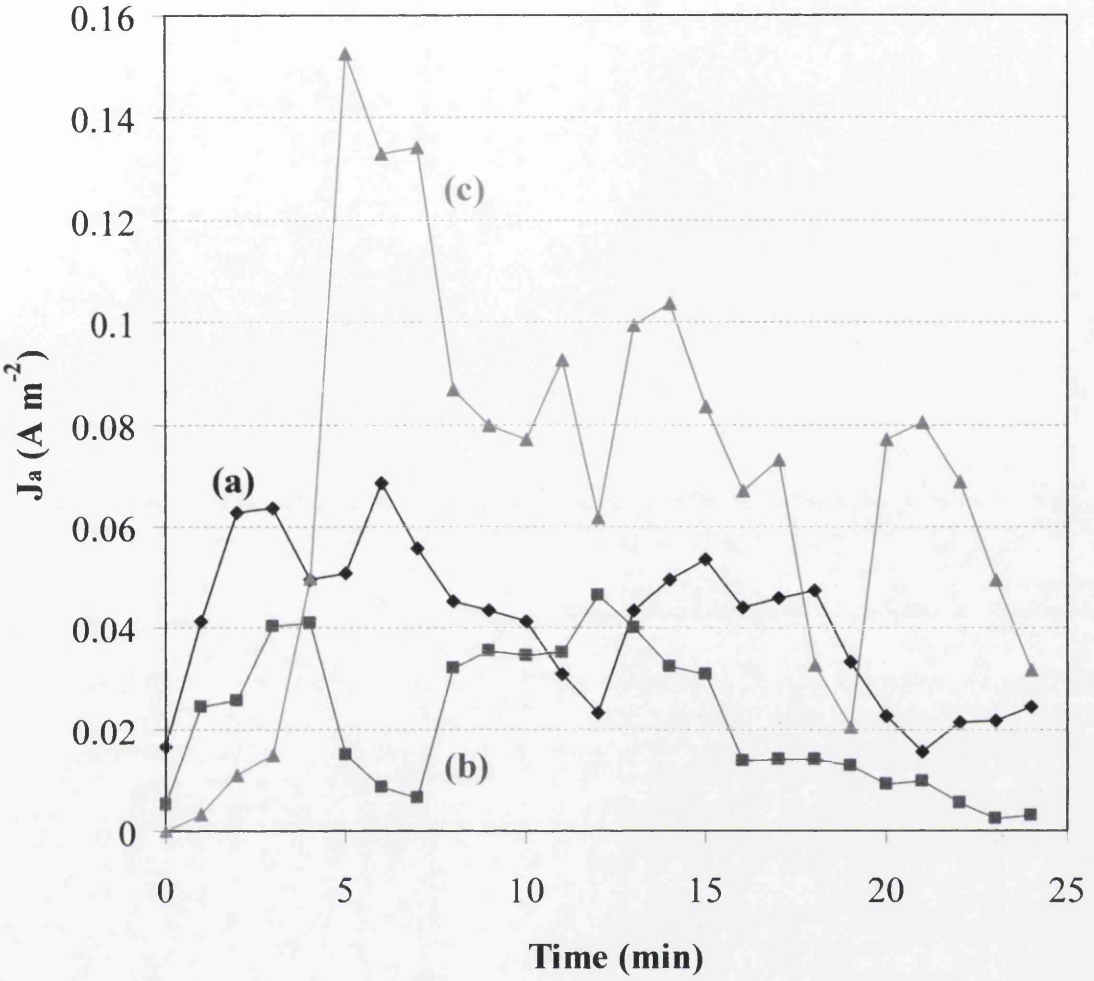

Figure 5.10: Plots of area-averaged anodic current density J_t versus immersion time for AA2024-T3 samples freely corroding in 0.86 M aqueous NaCl in the absence (a) and presence of EDTA at concentrations of (b) 10^{-3}, and (c) 10^{-2} M.

Am^{-2}, representing a *ca.* 250% increase as compared to the sample in the absence of EDTA. Thereafter J_t was observed to progressively decrease with time, though consistently maintaining higher values than the control experiment.

The observation of a bright metal surface, covered with clean clearly defined pits, as shown by the image given in Fig. 5.9d, is consistent with EDTA complexing Cu^{2+} ions ejected from corrosion pits, thus preventing replating onto the alloy surface. To prove this hypothesis, immersion tests were carried out using pure aluminium (99.999%) in 0.86 M NaCl (aq) at pH 6.5. SVET analysis over a 24h period showed that unpolarised, pure aluminium was effectively electrochemically inert over the entirety of the experimental period as shown by the j_z distribution map in Fig. 5.11a. However, in the presence of a 10^{-3} M $CuSO_4$ addition to the electrolyte, pure Al rapidly undergoes pitting as shown in Fig. 5.11b where the j_z map was recorded 5 min after immersion. Within 1h of exposure to Cu^{2+}, the exposed area became dominated by one intense stable pit showing j_z = 70 A m^{-2} (see Fig. 5.11c). This single pit remained active with peak anodic current densities ranging between 60 and 80 A m^{-2} over a further 23h immersion period. The visual appearance of the sample after 24h immersion, shown in Fig. 5.11d, confirmed that copper had plated onto the pure Al surface. A large proportion of the surface was coated with a light tarnish, while numerous small areas, presumably associated with short lived or metastable pitting events occurring < 1h immersion, showed a thicker copper deposit. The long-lived stable pit is located in the lower left corner of the exposed sample area (see Fig. 5.11d) and has a pit opening diameter of *ca.* 400 μm. When this immersion experiment was repeated in the presence of an additional 10^{-2} M EDTA concentration, the pure aluminium did not show evidence of stable pitting for the duration of the 24h immersion experiment and the exposed surface remained bright and free of dark deposits.

The finding that stable pitting occurs on AA2024-T3 despite the absence of copper replating when EDTA is added to a chloride containing electrolyte, concurs with the observations of other researchers on the role of copper re-distribution in AA2024-T3 corrosion.[3,34] The implication from this study is that cathodic oxygen reduction occurring on Cu-rich IMPs is sufficient to sustain stable pitting and that subsequent copper redistribution is not pivotal to stable pit propagation. The brightly polished yet pitted appearance of AA2024-T3 after immersion in EDTA suggests that Al^{3+} ions released by anodic activity are also efficiently sequestered by EDTA. The

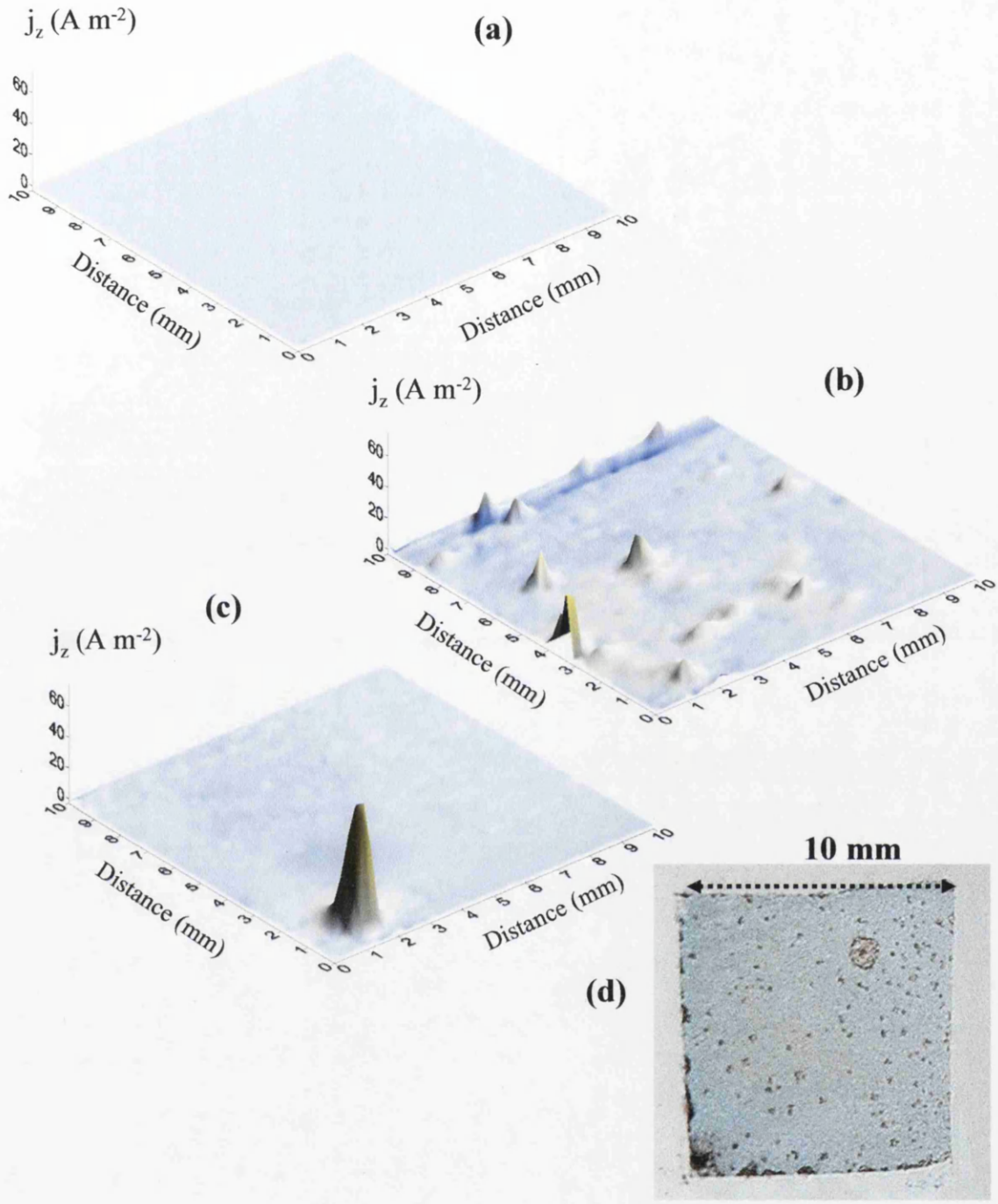

Figure 5.11: Surface plots showing the distribution of normal current density j_z above a pure aluminium sample immersed in (a) 0.86 M aqueous NaCl after 24h, (b) and (c) 0.86 M aqueous NaCl containing 10^{-3} M $CuSO_4$ after 5min and 1h immersion respectively. The visual appearance of the sample after 24h immersion in theCu^{2+} containing electrolyte is given in (d).

absence of corrosion build-up around stable pits may account in part for some of the increased anodic activity observed in the presence of 10^{-2} M EDTA. However, EDTA may also act as a pH buffer, thus moderating the elevated pH values usually observed in the vicinity of Cu-rich IMPs. As discussed previously, high pH leads to so-called cathodic corrosion and eventual trenching around cathodically active particles.[3,4] In unbuffered electrolyte, cathodic oxygen reduction on Cu-rich IMPs can galvanically couple with anodic dissolution of the surrounding matrix to give aluminate ions. If the separation of coupled anodic and cathodic regions is less *ca.* 100 μm, then corrosion currents will not be detected by SVET scanning. However, as demonstrated by other researchers,[4] immersion of AA2024-T3 in buffered electrolyte leads to a moderation of cathodic corrosion and a significantly greater proportion of cathodic activity arising from oxygen reduction on Cu-rich IMPs is available to couple with remote sites of anodic activity. Under such circumstances, SVET detection of localised corrosion events will be significantly more effective. Therefore, the apparent rise in corrosion activity observed in the presence of EDTA shown in Fig. 5.10 may be accounted for in terms of increased SVET detection efficiency, rather than an overall increase in rate of localised corrosion. The effect of EDTA on "cathodic corrosion" and SVET current density detection will be discussed further in the following chapter.

5.3.5 A Rationale for Effective AA2024-T3 Pitting Corrosion Inhibition

A summary of the results obtained for all inhibitor systems tested in terms of *teal* values, calculated according to Equation (5.2) over a 24h immersion period, is given in Fig. 5.12. From the findings presented, a ranking order can be drawn up in terms of increasing inhibition efficiency whereby EDTA << Ferrocyanide < BTA < DMTD = DEDTC. The latter three systems all appear to profoundly inhibit AA2024-T3 pitting at a concentration of 10^{-2} M although BTA is less effective than DMTD or DEDTC when present at lower concentrations. Reagents such as EDTA which sequester Cu^{2+} as water soluble chelates are the least effective AA2024-T3 corrosion inhibitors, whereas compounds such as ferrocyanide which precipitate Cu^{2+} from solution are more efficient. However, in the case of ferrocyanide it should also be noted that competitive adsorption onto aluminium surface oxides may also play a substantial role in the overall mechanism of inhibition.

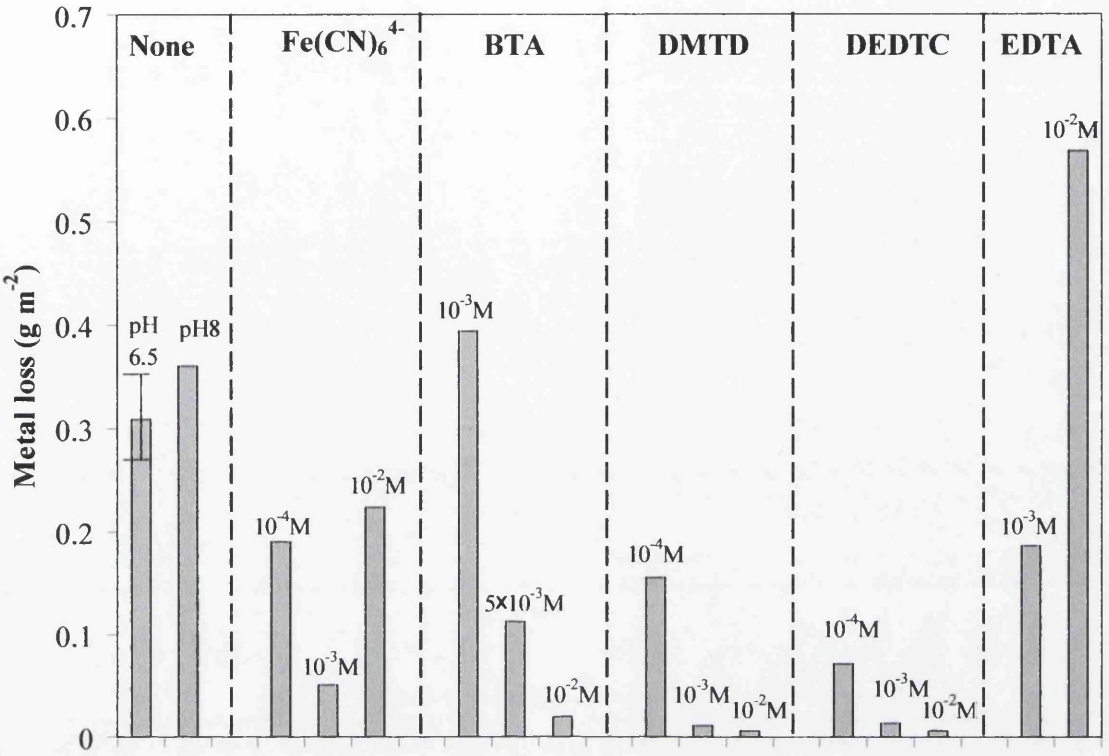

Figure 5.12: The effect of various inhibitors on pitting corrosion of AA2024-T3 in 0.86 M aqueous NaCl summarised by 24h total equivalent aluminium loss values calculated from SVET data.

The similarity of Fig. 5.6 and Fig. 5.7 (and consequently the *teal* values given in Fig. 5.12), coupled with the fact that both DEDTC and DMTD are Cu^{2+} selective chelators, suggests that both inhibit AA2024-T3 pitting in an identical manner. Given the finding that EDTA is an ineffective inhibitor, it appears that the ability of both DEDTC and DMTD to sequester Cu^{2+} and hence prevent copper replating is probably of secondary importance to the overall mechanism of inhibition. It should be noted however that although all three reagents form Cu^{2+} chelates, both the DEDTC and DMTD-derived products have limited water solubility and this may have a bearing on their inhibiting properties. Despite this however, it therefore seems reasonable to propose that the primary mode of inhibition for both DEDTC and DMTD involves the formation of blocking films on the surface of Cu-rich IMPs, thus hindering cathodic oxygen reduction.

Since BTA is well known as a copper inhibitor which functions by forming a surface film of polymeric $Cu^{+}BTA^{-}$, it seems logical to presume that inhibition also results from a slowing of cathodic oxygen reduction on Cu-rich IMPs. The more complete inhibition by both DMTD and DEDTC suggests that the nature of the inhibitor film formed on Cu-rich IMPs differs from the BTA system. This is highly likely given that DMTD/DEDTC combine with Cu^{2+} cations whereas BTA interacts with monovalent copper.

The work outlined here may have implications for the future design of effective AA2024-T3 corrosion inhibitors. The apparent critical factor in pitting inhibition is not the prevention of copper redistribution, but rather the stifling of cathodic oxygen reduction on Cu-rich IMPs. This work demonstrates that an effective method of so doing appears to be that of incorporating species which either adsorb strongly onto, or form, insoluble films on the surface of copper containing intermetallics.

5.4 Conclusions

- The scanning vibrating electrode technique (SVET) has been used to perform a systematic and comparative study of a series of copper complexing reagents (ferrocyanide, DMTD, DEDTC, BTA and EDTA). This was done to determine their relative efficiencies as inhibitors of pitting corrosion on

unpolarised AA2024-T3 immersed in near-neutral, aerated 0.86 M NaCl (aq) electrolyte.

- Of the inhibitors tested, only EDTA produced little or no inhibition of AA2024-T3 pitting corrosion. However, samples immersed in EDTA containing NaCl electrolyte retained a bright polished surface finish despite undergoing significant pitting activity. This finding confirms that copper is effectively sequestered by EDTA, and no re-plating occurs on the aluminium surface. Furthermore it supports the idea that copper re-plating is not necessary for stable pitting to be maintained on AA2024-T3, and that sufficient cathodic activity can be sustained on Cu-rich IMPs to drive any observed local anodic activity.

- The most effective inhibitors of AA2024-T3 pitting were Cu specific chelators (DMTD and DEDTC) which form Cu^{2+} complexes of limited aqueous solubility and appear to adsorb strongly onto Cu-rich IMPs, as evidenced by the formation of brownish surface films on immersion. Benzotriazole, an effective copper corrosion inhibitor was also shown to inhibit localised corrosion, though less efficiently than both DEDTC and DMTD. A Cu^{2+} precipitation agent, such as ferrocyanide, was far less effective and any inhibiting effects were ascribed to a competitive adsorption onto the aluminium surface oxide acting to disfavour chloride ion uptake.

- It is suggested that the apparent critical factor in pitting inhibition is not the prevention of copper redistribution, but rather the stifling of cathodic oxygen reduction on Cu-rich IMPs. This work demonstrates that an effective method of doing so appears to be that of incorporating species which either adsorb strongly onto, or form, insoluble films on the surface of copper containing intermetallics.

5.5 Future work

The results in this chapter have identified effective pitting corrosion inhibitors for use with alloys where cathodic oxygen reduction occurs on copper containing

IMPs. In terms of filiform corrosion, the next step would be to use the knowledge gained from this work to develop novel coating systems containing these inhibitors so as to prevent "successive pitting" type FFC on AA2024-T3 and other high copper containing automotive alloys susceptible to this type of corrosion attack, such as AA6111-T4.

5.6 References

1. N. Dimitrov, J. A. Mann, M. Vukmirovic and K. Sieradzki, *J. Electrochem. Soc.*, **147**, 3283 (2000).

2. R. G. Buchheit, M. A. Martinez and L. P. Montes, *J. Electrochem. Soc.*, **147**, 119 (2000).

3. M. B. Vukmirovic, N. Dimitrov and K. Sieradzki, *J. Electrochem. Soc.*, **149**, B428 (2002).

4. T. J. R. Leclere and R. C. Newman, *J. Electrochem. Soc.*, **149**, B52 (2002).

5. H. H. Uhlig, Corrosion Handbook, New York (1948).

6. P. Hulser and F. Beck, *Aluminum*, **67**, 999 (1991).

7. P. Hulser, U. A. Kruger and F. Beck, *Corros. Sci.*, **38**, 47 (1996).

8. M. Kendig, R. Addison and S. Jeanjaquet, *J. Electrochem. Soc.*, **146**, 4419 (1999).

9. R. G. Buchheit, R. P. Grant, P. F. Hlava, B. McKenzie and G. L. Zender, *J. Electrochem. Soc.*, **144**, 2621 (1997).

10. R. A. Weast, Editor, CRC Handbook of Chemistry and Physics, Boca Raton, FL (1987).

11. Y. Ono, T. Abiko, M. Ohta and M. Yasuda, *Electrochemistry*, **69**, 122 (2001).

12. J. T. Bushey and D. A. Dzombak, *Journal of Colloid and Interface Science*, **272**, 46 (2004).

13. D. Chidambaram, C. R. Clayton and G. P. Halada, *J. Electrochem. Soc.*, **150**, B224 (2003).

14. E. McCafferty, *Corros. Sci.*, **37**, 481 (1995).

15. N. Mikami, M. Sasaki, T. Kikuchi and T. Yasunaga, *J. Phys. Chem.*, **87**, 5245 (1983).

16. P. M. Natishan, E. McCafferty and G. K. Hubler, *J. Electrochem. Soc.*, **133**, 1061 (1986).

17. P. M. Natishan, E. McCafferty and G. K. Hubler, *J. Electrochem. Soc.*, **135**, 321 (1988).

18. N. Spanos, S. Slavov, C. Kordulis and A. Lycourghiotis, *Langmuir*, **10**, 3134 (1994).

19. Z. Szklarska-Smialowska, *Corros. Sci.*, **41**, 1743 (1999).

20. C. H. Wu, S. L. Lo and C. F. Lin, *Colloids and Surfaces a-Physicochemical and Engineering Aspects*, **166**, 251 (2000).

21. G. D. Christian, Analytical Chemistry, John Wiley & Sons, Inc., USA (1994).

22. M. J. Ahmed, I. Jahan and S. Banoo, *Analytical Sciences*, **18**, 805 (2002).

23. M. Silva, *Analyst*, **99**, 408 (1974).

24. T. Nomura, M. Kumagai and A. Sato, *Analytica Chimica Acta*, **343**, 209 (1997).

25. J. B. Cotton and I. R. Scholes, *British Corrosion Journal*, **2**, 1 (1967).

26. I. Dugdale and J. B. Cotton, *Corros. Sci.*, **3**, 69 (1963).

27. G. W. Poling, *Corrosion Sci.*, **10**, 359 (1970).

28. A. T. Al-Hinai and K. Osseo-Asare, *Electrochem. Solid State Lett.*, **6**, B23 (2003).

29. P. G. Cao, J. L. Yao, J. W. Zheng, R. A. Gu and Z. Q. Tian, *Langmuir*, **18**, 100 (2002).

30. W. Qafsaoui, C. Blanc, N. Pebere, H. Takenouti, A. Srhiri and G. Mankowski, *Electrochim. Acta*, **47**, 4339 (2002).

31. D. Tromans and G. H. Li, *Electrochem. Solid State Lett.*, **5**, B5 (2002).

32. A. M. Cabral, W. Trabelsi, R. Serra, M. F. Montemor, M. L. Zheludkevich and M. G. S. Ferreira, *Corros. Sci.*, **48**, 3740 (2006).

33. E. Fagel Jr. and G. R. Ewing, *J. Amer. Chem. Soc.*, **73**, 4360 (1951).

34. M. A. Jakab, D. A. Little and J. R. Scully, *J. Electrochem. Soc.*, **152**, B311 (2005).

Chapter 6

The Anomalous Influence of EDTA on Localised Corrosion of AA2024-T3

6.1 Introduction

In Chapter 5 Ethylenediaminetetraacetic (EDTA) acid was shown to have an anomalous effect when tested as a corrosion inhibitor. Firstly, it enhances localised current densities (as detected by the SVET – see Section 1.6) on AA2024-T3 freely corroding in near neutral NaCl electrolyte. Secondly, EDTA does this whilst inhibiting metal (Cu) replating by virtue of its properties as a complexing agent. It was for this ability to complex metal cations (Cu) that EDTA was used in Chapter 5. However, as a tetraprotic acid, EDTA has 4 pK_a values;[2] 2.0, 2.7, 6.2 and 10.3 – and can therefore function as a pH buffer at each pK_a value. A question arises as to how the particular properties of EDTA, *i.e.* buffering capacity and metal cation complexation might contribute (or not) to its enhancement of localised corrosion current densities on AA2024-T3. It has been shown elsewhere that pH buffers may increase the (net) cathodic current available to drive remote anodes on AA2024 by reducing rates of matrix dissolution due to so called "cathodic corrosion". In this chapter the influence of EDTA on "cathodic corrosion" is described in relation to its properties as a pH buffer, and the pH gradients produced by cathodic O_2 reduction on Cu-rich intermetallic particles (IMPs).

The concept of "cathodic corrosion" is discussed at length in Section 1.4.2.3. Briefly, cathodic oxygen reduction occurring on this alloy whether it occurs on intact IMPs, copper-rich (dealloyed) intermetallics, detached and re-deposited copper clusters or replated copper, generates high local solution pH's.[1,3] The high pH results in the depassivation and dissolution of the Al-matrix in the area adjacent to the localised cathode.[1,3-9] The term "cathodic corrosion" is actually a misnomer because aluminium undergoes anodic dissolution at high pH with the generation of AlO_2^- ions as shown by the Pourbaix diagram in Fig. 6.1. Furthermore, it has been shown that while matrix Cu enrichment is to be expected as a result of alkaline aluminium dissolution at or near cathodic regions, the anodic current contribution arising from that same aluminium dissolution would tend to consume the greater part of any additional cathodic current contribution arising from oxygen reduction on the Cu enriched surface.[1] It is likely therefore that Cu enrichment due to "cathodic corrosion" of the AA2024-T3 matrix could make only a limited contribution to the maintenance of remote anodic sites such as

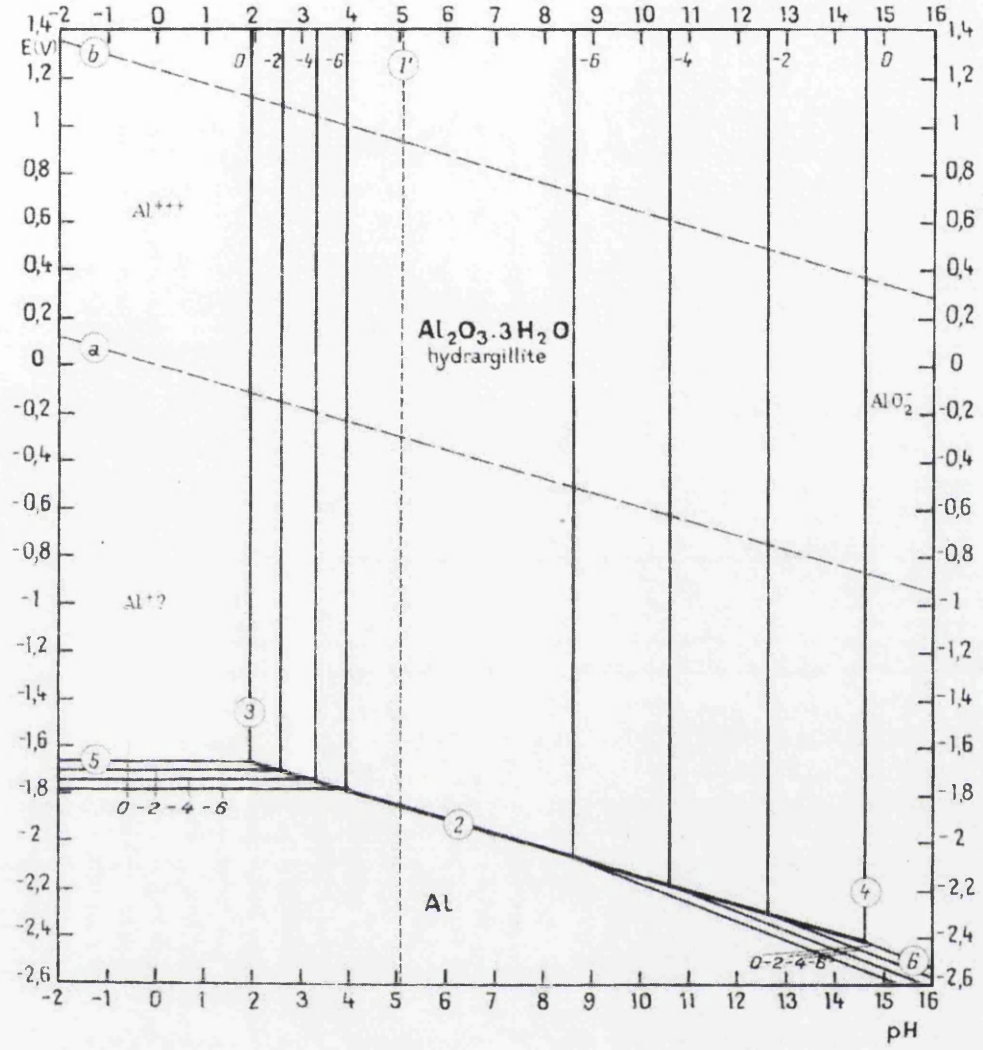

Figure 6.1: Pourbaix (E *vs.* pH) equilibrium diagram for the system aluminium-water, at 25°C.[17]

stable corrosion pits.[1] Park *et al*[8] have also shown that in buffered electrolyte trench formation around cathodic IMPs (through "cathodic corrosion") was suppressed near iron-rich inclusions within aluminium alloy AA6061 but that this resulted in the generation of anodic sites at the crevice formed between the mounted specimen and the alloy. A similar result was shown for both copper containing and iron containing IMPs in buffered electrolyte by Seegmiller *et al.*[10]

In order to elucidate the possible role of EDTA in suppressing "cathodic corrosion" the following approach has been taken. AA2024-T3 samples were subject to immersion in 0.86 M NaCl containing various concentrations of EDTA followed by emersion and microscopic analysis. The primary aim was to examine "cathodic corrosion" and associated trench formation around cathodic sites. In so doing the complexing properties of EDTA proved extremely useful because in the presence of EDTA, Cu replating does not occur. Consequently cathodic activity remains localised at pre-existing IMPs for long periods of time. Also, the matrix surface remains bright and substantially free of transition metal-rich corrosion product. This last effect obviates the need to remove corrosion product before microscopically examining the corroded surface and permits facile visualisation of "cathodic corrosion" related features.

6.2 Experimental

Aluminium alloy AA2024-T3 was supplied by BAe Systems Plc as 2mm thick rolled sheet (composition by weight; 0.5% Si , 0.5% Fe, 3.8 – 4.9% Cu, 0.3 – 0.9% Mn, 1.2 – 1.8% Mg, 0.1% Cr, 0.25% Zn), and sectioned into 40 mm x 40 mm coupons. All other chemicals and materials were obtained from Sigma Aldrich Ltd. Samples of AA2024-T3 were prepared as described in Section 2.4.4. During the experiments samples were immersed in an electrolyte bath containing aqueous 0.86 M NaCl and required concentrations of the disodium salt of Ethylenediaminetetraacetic (EDTA) acid. Three solutions were used; 0 M EDTA, 10^{-3} M EDTA and 10^{-2} M EDTA. No pH adjustment was employed so that at EDTA conc. = zero, solution pH was 6.3, with 10^{-3} M EDTA solution pH was 4.3 and when EDTA concentration was 10^{-2} M, pH was pH 4.2.

After emersion the corroded AA2024-T3 surface was rinsed in distilled water and dried in air. The surface was characterised by optical macro photography, phase contrast interference Microscopy (IM) using a Reichert-Jung MeF3 microscope (Section 2.8), scanning electron microscopy (SEM) analysis using a Phillips XL30CP (Section 2.7) and Atomic Force Microscopy (AFM) using a Topometrix Explorer instrument (Section 2.9).

A full description of all the materials and experimental techniques used are outlined in Chapter 2.

6.3 Results

Digital macro photographs of AA2024-T3 samples corroded in the presence of various concentrations of EDTA are shown in Fig. 6.2(a-c). The AA2024-T3 sample corroded in the absence of EDTA, shown in Fig. 6.2a, darkened by surface coverage with corrosion products and redeposited copper. However, when corroded in the presence of 10^{-3} M EDTA the AA2024-T3 surface remained relatively clean with minimal corrosion product deposits as shown in Fig. 6.2b. At the highest EDTA concentration of 10^{-2} M the surface remained brighter still with the sample almost completely retaining its mirror polish finish as shown in Fig.6.2c. However, all three samples showed evidence of pitting corrosion (as expected from Chapter 5) with pit mouths appearing as dark circles of 50 and 90 μm diameter. Pit mouths formed in the absence of EDTA have rings with white deposits of Al-rich corrosion product (0.2 and 1.2 mm diameter). This is due to the hydrolysis of Al^{3+} cations ejected from corrosion pits as described in Chapter 5. When EDTA concentrations of 10^{-3} M and 10^{-2} M solutions were used, these white rings of aluminium (hydr)oxides were absent, probably due to complexation of Al^{3+} by EDTA and consequent suppression of Al^{3+} hydrolysis. In the absence of EDTA the alloy surface outside the immediate vicinity of corrosion pits is darkened due to transition metal rich deposits. These will arise from hydrolysis of (iron, copper) cations and electrochemical reduction (replating) of Cu^{2+}. When EDTA = 10^{-3} M surface darkening is greatly reduced and at 10^{-2} M surface darkening is almost completely suppressed. This is presumably due to cation complexation suppressing

a)

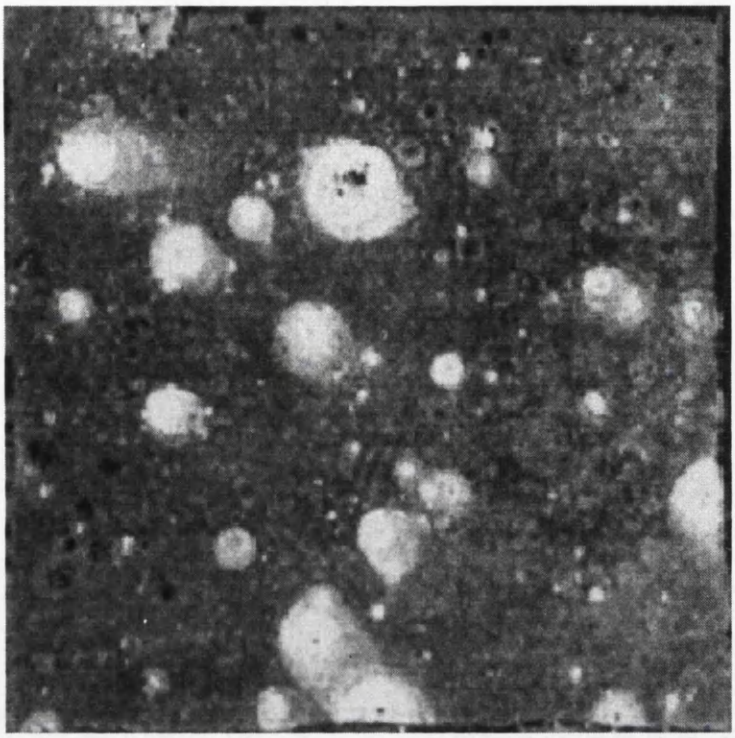

b)

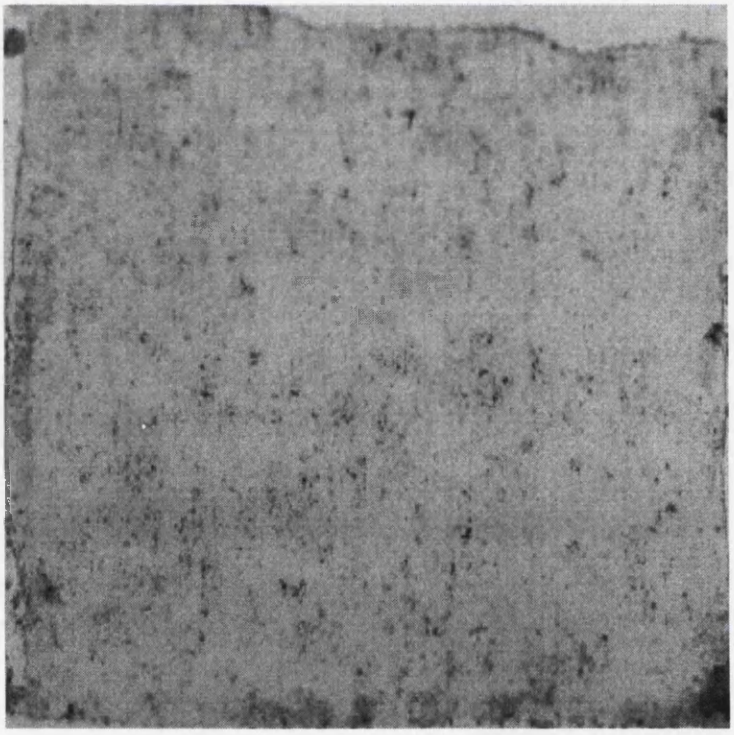

Figure 6.2: Grey-scale digital images of AA2024-T3 substrates following 24 hour corrosion experiments in 0.86 M NaCl electrolyte. EDTA concentration key: (a) 0 M (b) 10^{-3} M and (c) 10^{-2} M

c)

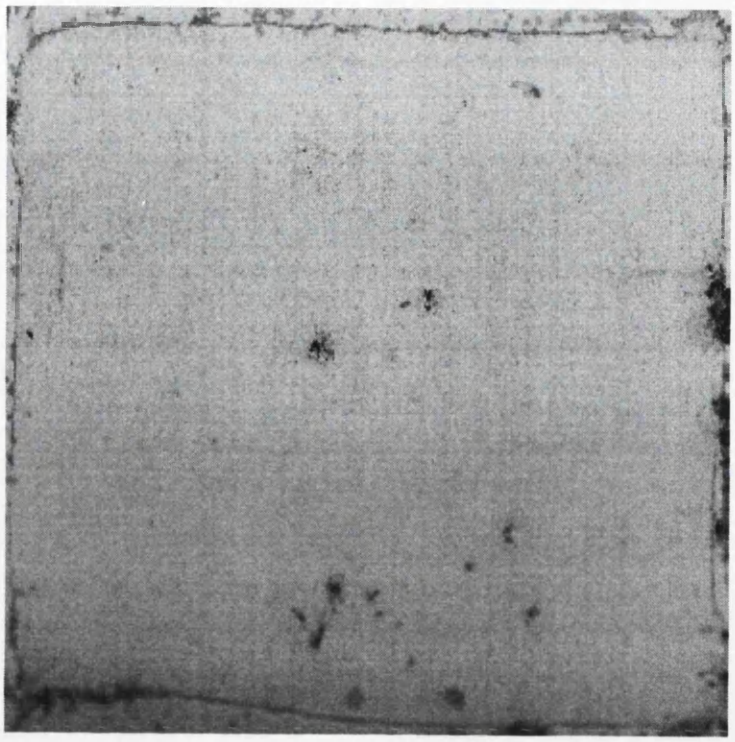

Figure 6.2 (cont.): Grey-scale digital images of AA2024-T3 substrates following 24 hour corrosion experiments in 0.86 M NaCl electrolyte. EDTA concentration key: (a) 0 M (b) 10^{-3} M and (c) 10^{-2} M

hydrolysis and Cu replating. This suppression of corrosion products and copper replating enabled further optical analysis of the substrate following corrosion testing without the need for further surface treatment.

Fig. 6.3(a-c) shows typical optical micrographs of the surfaces from Fig. 6.2(a-c) taken using brightfield illumination. The sample areas imaged in Fig. 6.3(a-c) were all selected to be remote (> 2 mm away) from the mouth of any macroscopically conspicuous corrosion pits. As such they are representative of that portion of the sample surface which experiences a net (overall) cathodic current for the greater part of the corrosion period. The dark features in Fig. 6.3d of a polished non-corroded surface are the IMPs typically present in AA2024-T3. A comparison of Fig. 6.3d and Fig. 6.3c shows that in the presence of 10^{-2} M EDTA, the number, size and location of particles remains substantially unchanged. Conversely, Fig. 6.3a shows a significant enlargement of the dark features associated with some individual IMPs. This is most probably due to dealloying of S-phase particles followed by subsequent cu particles ejection and also dissolution of the surrounding Al-matrix through "cathodic corrosion". Some IMPs are ringed with light coloured regions, probably due to Mg and Al (hydr)oxide deposition arising from the hydrolysis of ejected Al^{3+} and Mg^{2+} cations. Others are ringed with dark deposits due to hydrolysis of ejected Fe^{2+}, Mn^{2+} and Cu^{2+} cations and/or Cu replating. The extent of these dark deposits is such that the alloy matrix is almost completely covered. Fig. 6.3b shows that when the concentration of EDTA is 10^{-3} M there is only very slight evidence of dark deposition on the alloy matrix. However, some interesting additional features are present. These take the form of clearly defined "halos" (examples labelled 'A' in Fig. 6.3b) around some, but not all, IMPs. These halos do not have the appearance of a light or dark coloured deposit but instead have the appearance of a topographical feature. Alternatively, they could be a deposit of transparent, colourless material which is acting as a "lens" – refracting light by virtue of having a refractive index > 1 (*i.e.* > air). One obvious candidate for such a material would be aluminium (hydr)oxide.

In order to better characterise the halo features formed in the presence of 10^{-3} M EDTA the surface in Fig. 6.3b was re-imaged using phase contrast microscopy. This technique has the specific property of rendering visible differences in refractive index, as

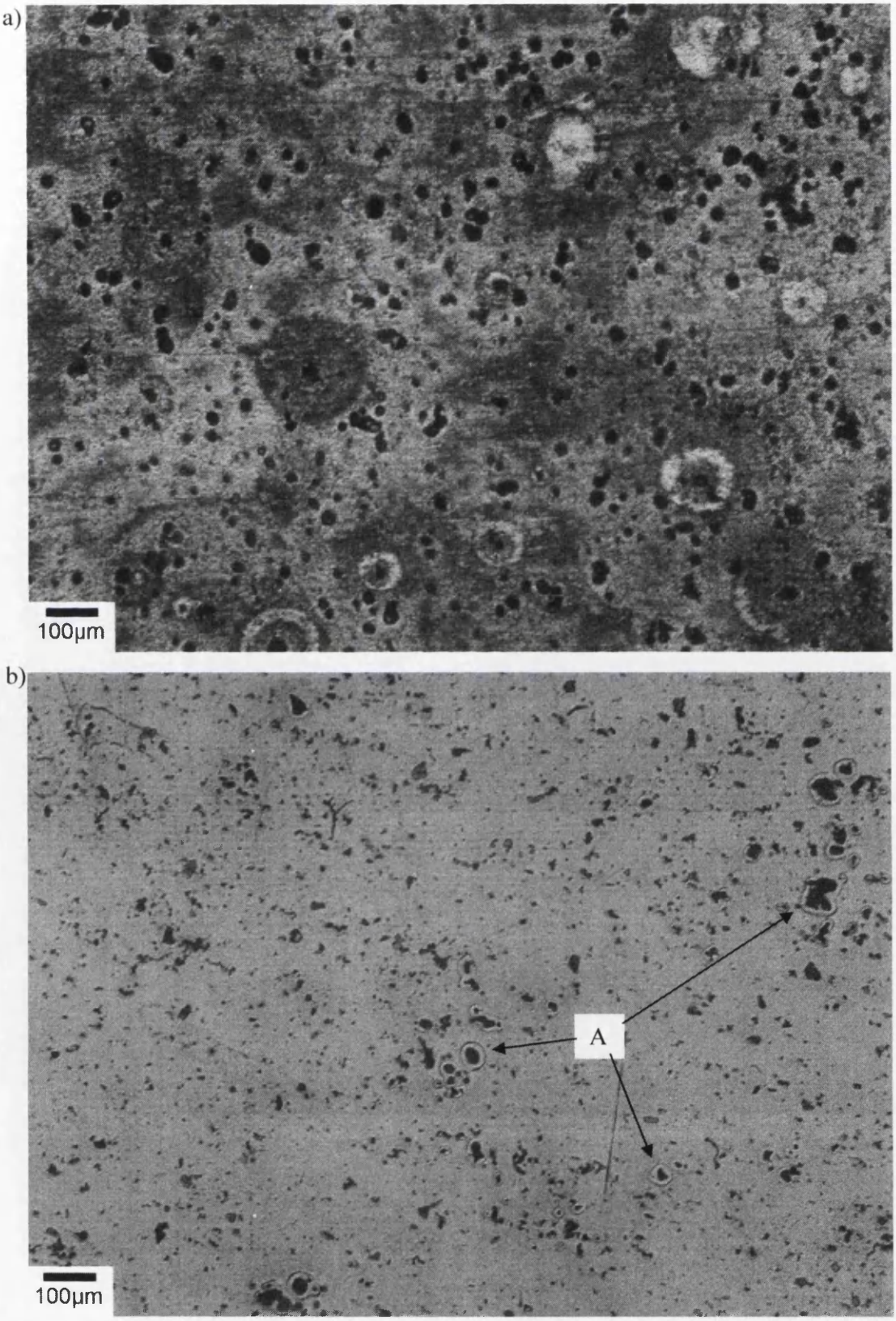

Figure 6.3: Brightfield illumination microscope images of AA2024-T3 after 24 hours immersion in 0.86 M NaCl. EDTA concentration key: (a) 0 M (b) 10^{-3} M and (c) 10^{-2} M. Image (d) is of the uncorroded surface following polishing.

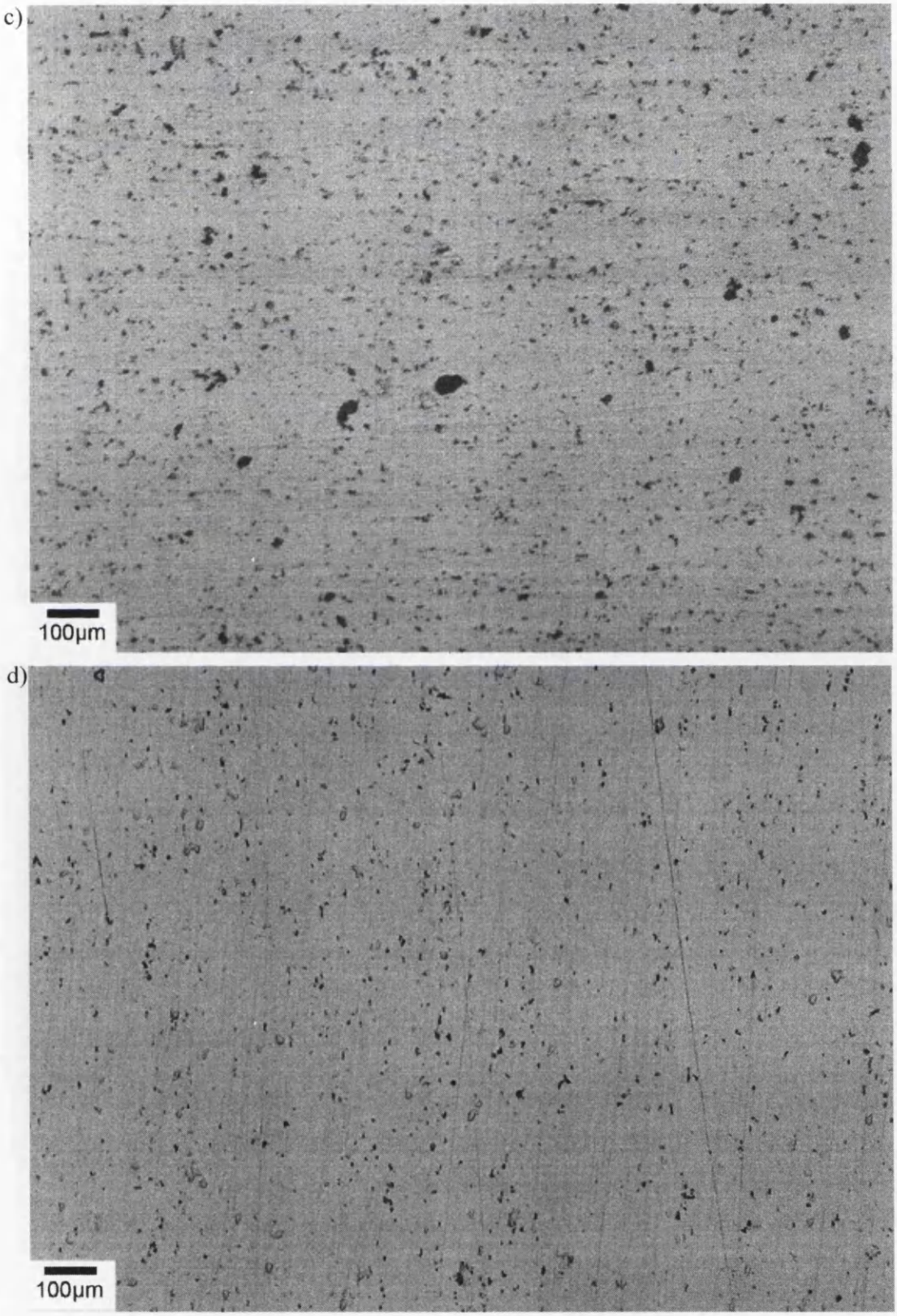

Figure 6.3(cont.): Brightfield illumination microscope images of AA2024-T3 after 24 hours immersion in 0.86 M NaCl. EDTA concentration key: (a) 0 M (b) 10^{-3} M and (c) 10^{-2} M. Image (d) is of the uncorroded surface following polishing.

described in Section 2.8. The results are shown in Figs. 6.4b and c. For comparison the zero EDTA and 10^{-2} M EDTA corroded surfaces are shown in Figs. 6.4a, and d respectively. It may be seen that whereas Figs. 6.4a and d are essentially flat, Figs. 6.4b and c show apparently raised features surrounding some of the IMPs. However, one must be careful when interpreting the phase contrast images in Fig. 6.4b and c as features can take on either a topographically raised or depressed appearance depending on the phase adjustment and image orientation. [Note: To convince themselves of this fact the reader should view Figs. 6.4b and c with the page held upside down.] Thus it would seem most likely that the halos surrounding IMPs are deposits of transparent aluminium (hydr)oxide but it is still not clear whether these deposits lie on top of the surrounding matrix or within a trench cut into that matrix.

In order to resolve the above issue regarding the topography of the features, AFM topographical scanning was used. Fig. 6.5a shows a typical surface map of an area of the surface centred on a cathodic IMP such as those shown in Fig. 6.4b and 6.4c. In the lower half of the figure a line plot is shown, taken along line L–L* from the surface map. From both of these plots it may be seen that there are two distinct phases to the deposits as indicated by Region A and Region B on the line plot and that they are both topographically raised features with respect to the substrate. Region A is a narrow lip *ca.* 4 μm wide and *ca.* 0.4 μm high, whilst Region B is a wider disc area radially extending *ca.* 10 μm further and is only *ca.* 0.1 μm in height. In the centre of the formation the remnants of an IMP may be seen surrounded by a trench, consistent with high local pH generation at a cathodic IMP and the subsequent dissolution of the immediately adjacent matrix.[10,11]

An attempt to further characterise the corroded surfaces was made by imaging the samples shown in Fig. 6.2(a-c) using SEM. The SEM images shown in Fig. 6.6a and Fig 6.6b allow a clear view into the pit features and it is possible to see the remnants of IMPs in trenches as described for the AFM topography maps. Surrounding the "cathodic pits" are dark "halos" consistent with the dimensions of the deposits around cathodic IMPs shown in Fig 6.5. However, there is minimal distinction between Region A and Region B in these images. This suggests that the deposit is "transparent" to the electron beam and thus the underlying metal substrate is primarily being observed. The

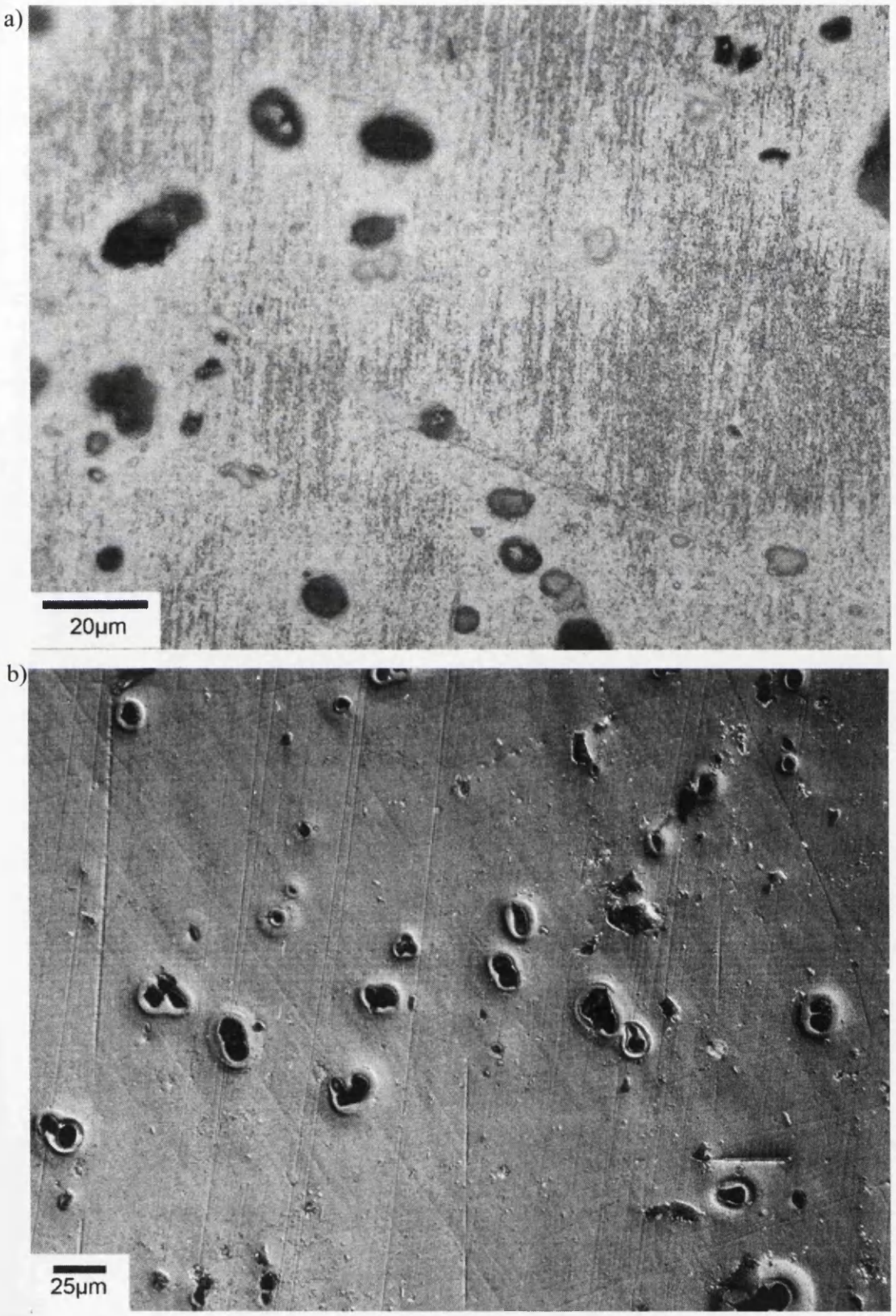

Figure 6.4: Phase contrast interference microscope images of AA2024-T3 after 24 hours immersion in 0.86 M NaCl. EDTA concentration key: (a) 0 M, (b) and (c) 10^{-3} M, (d) 10^{-2}M

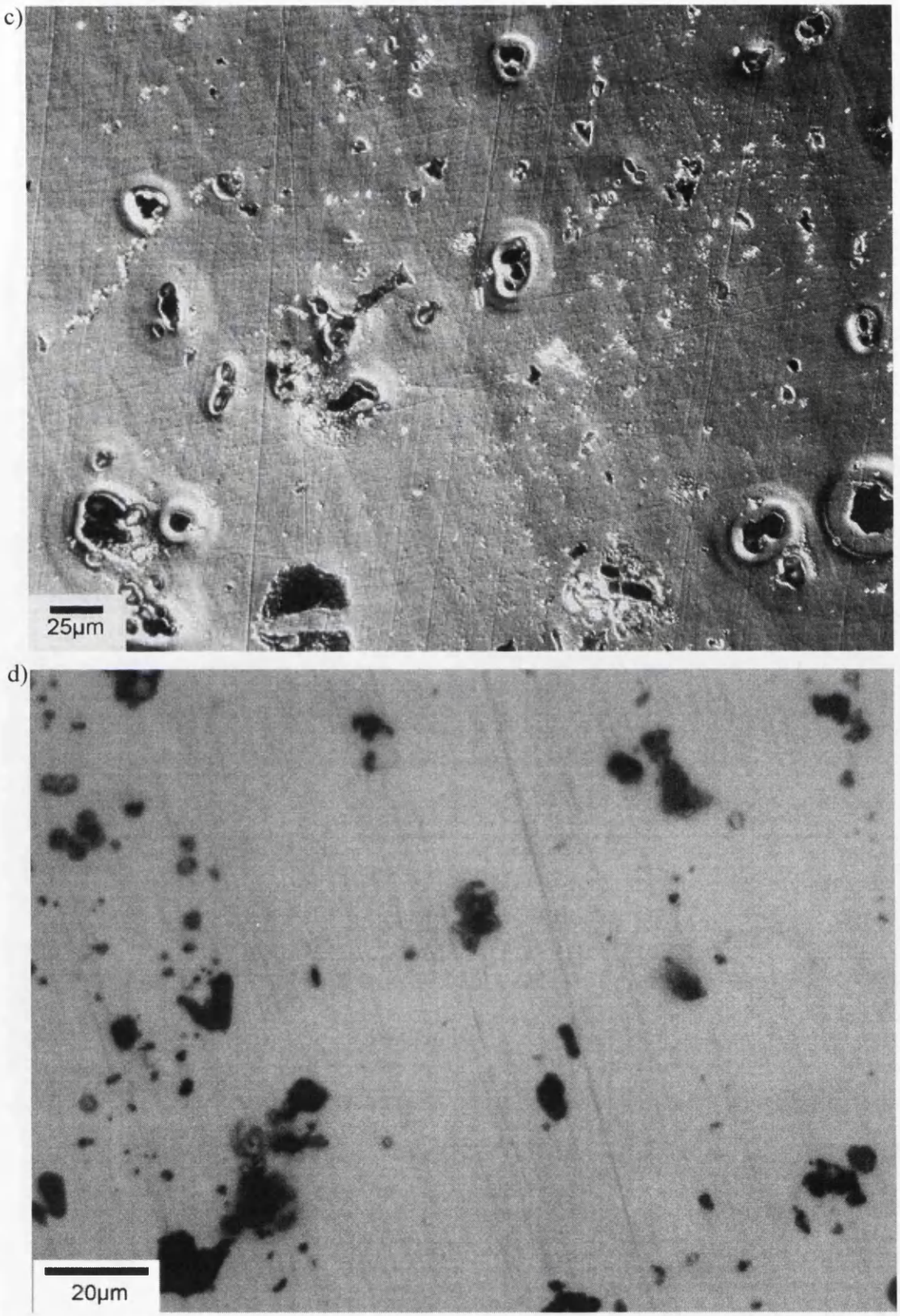

Figure 6.4(cont.): Phase contrast interference microscope images of AA2024-T3 after 24 hours immersion in 0.86 M NaCl. EDTA concentration key: (a) 0 M, (b) and (c) 10^{-3} M, (d) 10^{-2}M

a)

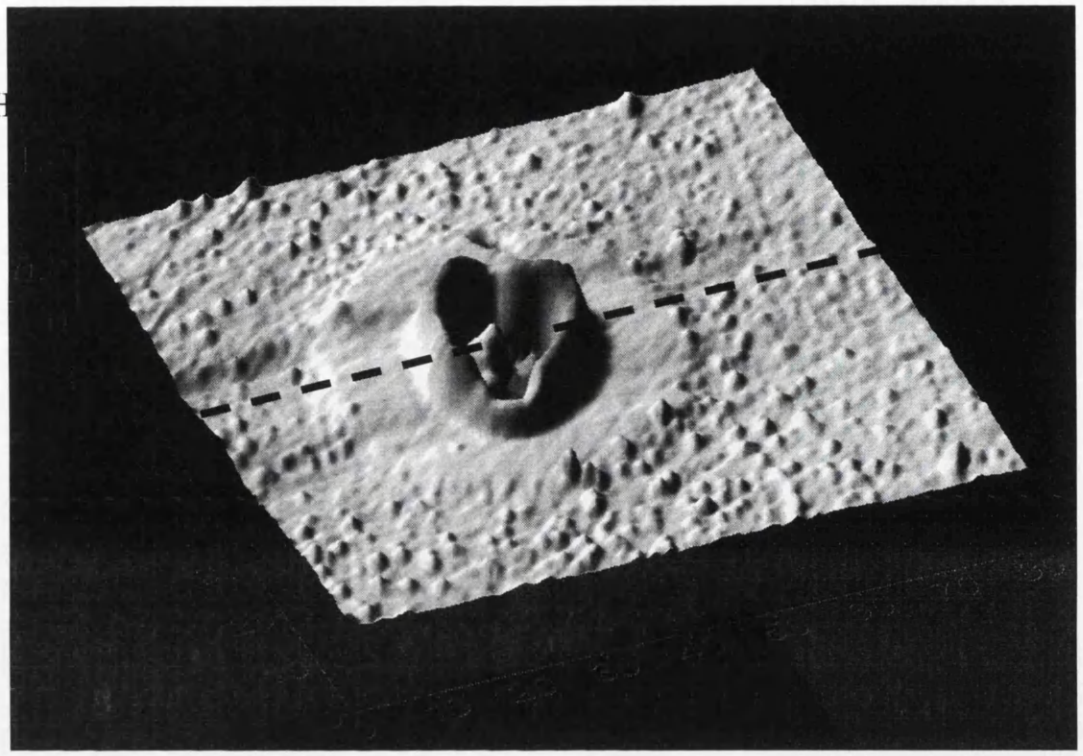

b)

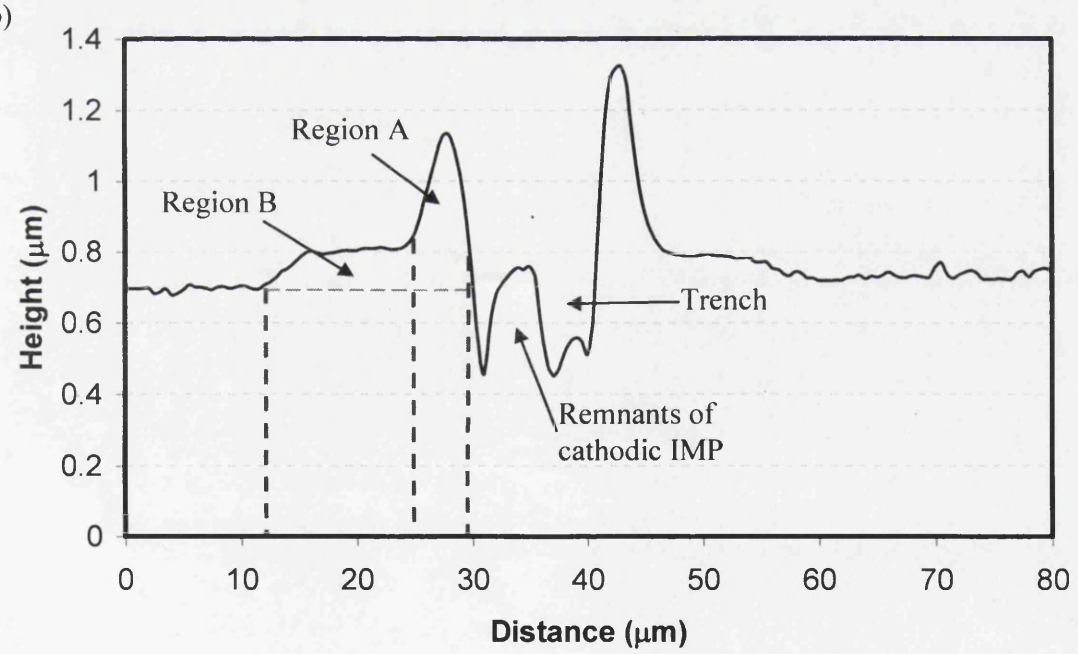

Figure 6.5: Surface analysis using AFM. (a) Topographical map of a cathodic IMP and surrounding area on AA2024-T3 following 24 hours immersion in 0.86 M NaCl electrolyte containing 10^{-3} M EDTA. (b) Line scan taken from (a) along the line L-L*

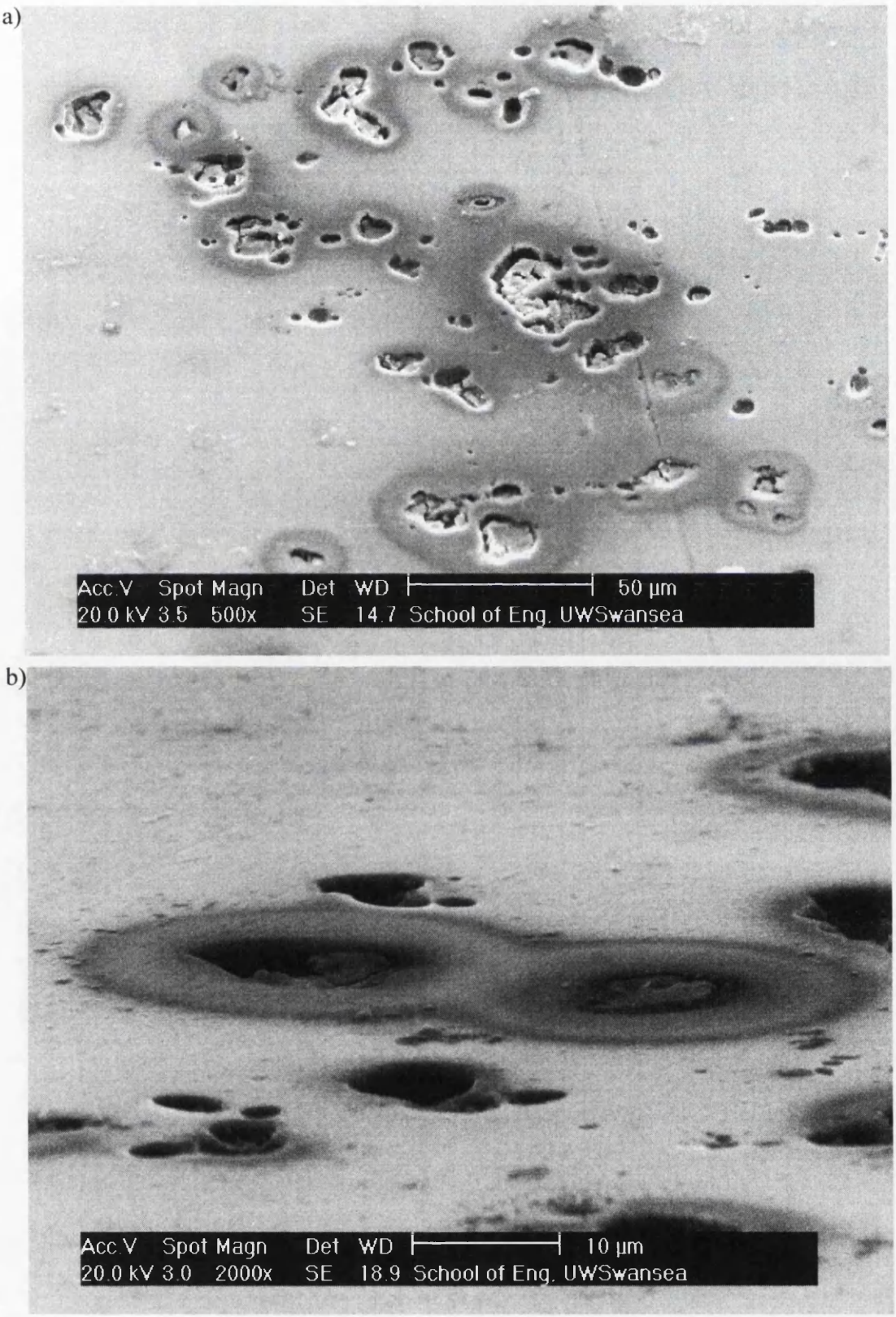

Figure 6.6: SEM images of cathodic pitting on AA2024-T3 substrates following 24 hour immersion in 0.86 M NaCl. EDTA concentration key: (a) and (b) 10^{-3} M, (c) and (d) 10^{-2} M.

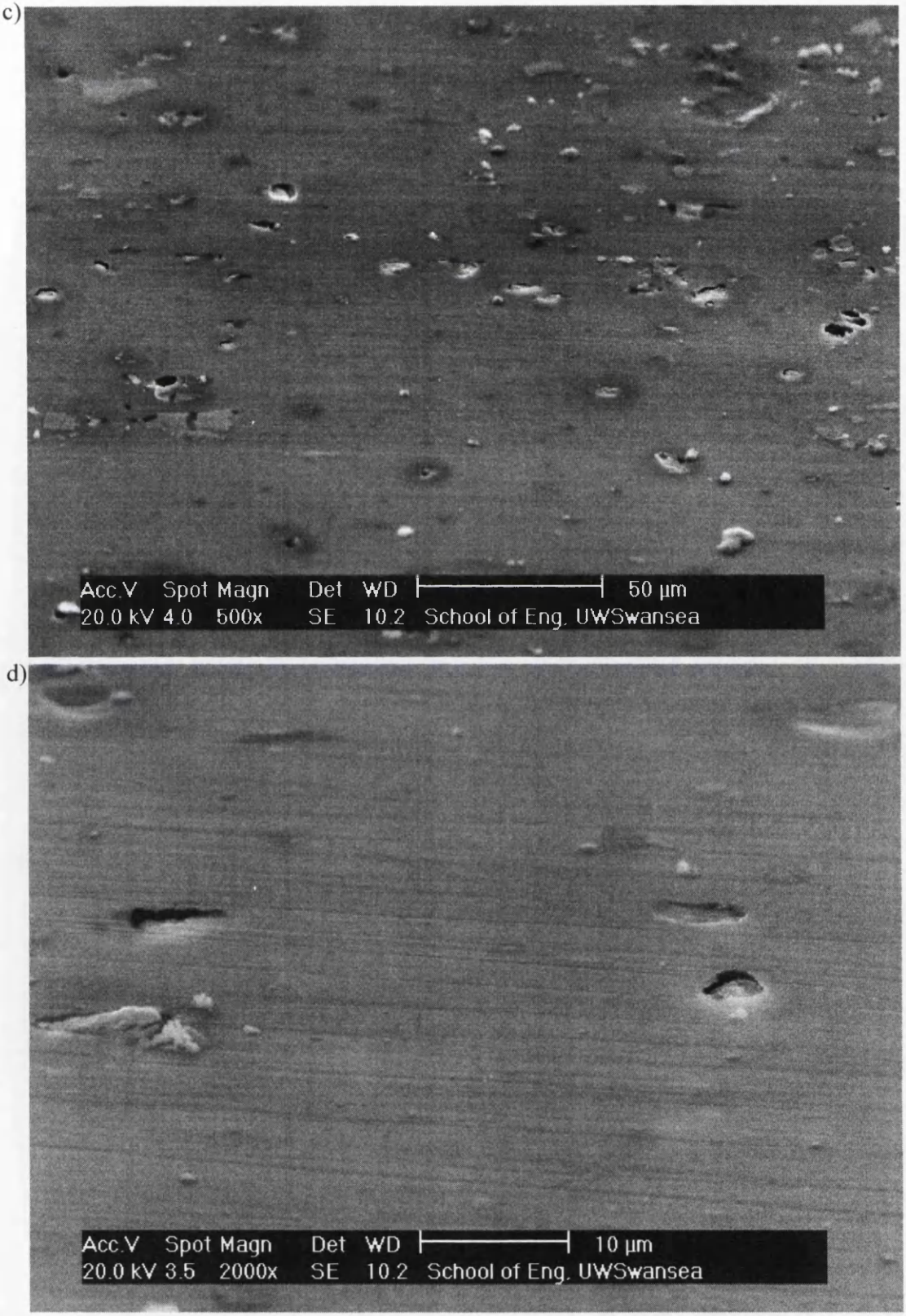

Figure 6.6(cont): SEM images of cathodic pitting on AA2024-T3 substrates following 24 hour immersion in 0.86 M NaCl. EDTA concentration key: (a) and (b) 10^{-3} M, (c) and (d) 10^{-2} M.

topographical SEM images shown are dependent on how many of the secondary electrons actually reach the detector.[12] Although an equivalent number of secondary electrons might be produced as a result of collisions between the primary electron beam and the specimen, secondary electrons that are prevented from reaching the detector will not contribute to the final image and these areas will appear as shadows or darker in contrast than those regions that have a clear electron path to the detector. This also has the important corollary that Region A and Region B appear to be the same material, which again is most likely aluminium hydr(oxide).

SEM images shown in Fig. 6.6c and Fig. 6.6d of an AA2024-T3 substrate corrosion tested in 10^{-2} M EDTA showed only minimal micro-crevices surrounding some IMPs and also only slight dark rings around most IMPs.

6.4 Discussion

Assuming that the deposits shown in the results above around cathodic IMPs on AA2024-T3 corroded in 10^{-3} M EDTA solution are aluminium (hydr)oxide, then there are three obvious questions regarding their origins:

1. Why do they only occur in the 10^{-3} M EDTA solution?

2. What is the transport mechanism?

3. Why do the deposits occur as a bi-phasic deposit?

An attempt will now be made in the following discussion to answer these questions and then subsequently to relate the implications of these results to the SVET data shown in Chapter 5.

6.4.1 Anomalous Aluminium (hydr)oxide Deposits Surrounding Cathodic IMPs

The basic mechanism of "cathodic corrosion" has been dealt with previously in Section 1.4.2.3 and in the introduction to this chapter, where it was shown that the term

is actually a misnomer as actually anodic dissolution of the Al-matrix occurs in regions of high local pH adjacent to local cathodes with the generation of AlO_2^- ions.

A question then arises as to how Region A and Region B, shown in Fig. 6.5, are formed as they are not readily explained simply by the generation of high local pH zones. Assuming that both Region A and Region B consist of aluminium hydr(oxide) deposits then a significant observation is that the deposits are only clearly visible in the 10^{-3} M EDTA electrolyte. Although, some deposits are visible on the substrate following immersion in 10^{-2} M EDTA electrolyte, as shown by dark rings surrounding some IMPs in Fig. 6.6c, the amount of deposit is minimal compared to the 10^{-3} M case and not detected by any AFM scans. If we assume that the cathodic current density is diffusion controlled[1,3,13] and hence more or less constant on both substrates and also that the geometry of IMPs is the same on both substrates then the level of deposition of aluminium hydroxide around IMPs for both concentrations of EDTA would be nominally the same, unless matrix dissolution was not occurring in the first place. This will be discussed again later on.

In terms of "cathodic corrosion", dissolution occurs due to an increase in local pH from the generation of OH^- ions from oxygen reduction on cathodic IMPs. Cathodic O_2 reduction normally occurs via one, or both, of two basic reaction mechanisms as described in Section 1.4.2.3. The first is a direct $4e^-$ pathway in which O_2 is completely reduced to OH^- ions as shown by Reaction (6.1). The second is a $2e^-$ reduction pathway through which O_2 is reduced to a mixture of H_2O_2 and OH^- as shown by Reaction (6.2). From the Pourbaix diagram shown in Fig. 6.1 it may be seen that at pH > ~8.6 dissolution of Al will occur and AlO_2^- anions will be generated from Reaction (6.3).

$$O_2 + 2H_2O + 4e^- \rightarrow 4OH^- \qquad (6.1)$$

$$O_2 + 2H_2O + 2e^- \rightarrow H_2O_2 + 2OH^- \qquad (6.2)$$

$$Al_{(s)} + 4OH^-_{(aq)} \rightarrow Al(OH)^-_{4(aq)} + 3e^- \qquad (6.3)$$

Under steady-state conditions the cathodic current density may be equated with the diffusional flux of dissolved O_2 to the metal surface and OH^- away from the metal surface using Equation(6.4),[14]

$$-j_c\delta / F = [O_2]_b \cdot nD_{O_2} = \left\{[OH^-]_s - [OH^-]_b\right\} \cdot D_{OH^-} \qquad (6.4)$$

where: j_c is the cathodic current density, F is Faraday's constant (96500 C/mol), D_{O2} is the diffusion coefficient for oxygen (2 x 10^{-5} cm^2 sec^{-1})[15] and D_{OH^-} is the diffusion coefficient for OH^- (5 x 10^{-2} cm^2 sec^{-1}), δ is the Nernst diffusion layer thickness, $[O_2]_b$ is the O_2 concentration in bulk electrolyte (2.8 x 10^{-4} mol dm^{-3} for air saturated water at 25°C)[16], $[OH^-]_b$ is the bulk hydroxyl ion concentration and $[OH^-]_s$ the surface hydroxyl ion concentration; n is the number of electrons involved in O_2 reduction *i.e.* 4 for Reaction (6.1) and 2 for Reaction (6.2). Under conditions where the Nernst diffusion layer thickness is determined hydrodynamically, and is therefore independent of the diffusion coefficient, the value of δ will be similar for both O_2 and OH^-. Furthermore, under near-neutral or acidic conditions the value of bulk electrolyte $[OH^-]_b$ is effectively zero. Therefore from Equation (6.4), a pH in the range 10.35 to 10.65 can be expected to be generated in electrolyte immediately adjacent to cathodic IMPs from the $4e^-$ and $2e^-$ oxygen reduction processes shown in Reaction (6.1) and Reaction (6.2). This is in good agreement with data shown elsewhere where a limiting cathodic current density for oxygen reduction on copper was measured as 40 μA/cm^2,[1] which, for a Nernst diffusion layer thickness of 100–200 μm, equates to a local OH^- concentration of 0.083 mM to 0.016 mM, or pH 9.9 to pH 10.2.[1] Therefore, the pH that can be generated immediately adjacent to a cathodic IMP is well above that needed (pH 8.6) for metal dissolution of the Al-matrix.

In an unbuffered electrolyte AlO_2^- ions and unreacted OH^- would diffuse away from the IMP with time and there would be a smooth monotonic decrease in pH without obvious deflection. A schematic diagram of the pH gradient in this scenario is shown in the upper portion of Fig. 6.7. From the solubility curves of aluminium (hydr)oxides[17] shown in Fig. 6.8 it may be seen that with decreasing pH, from pH 10, the solubility of

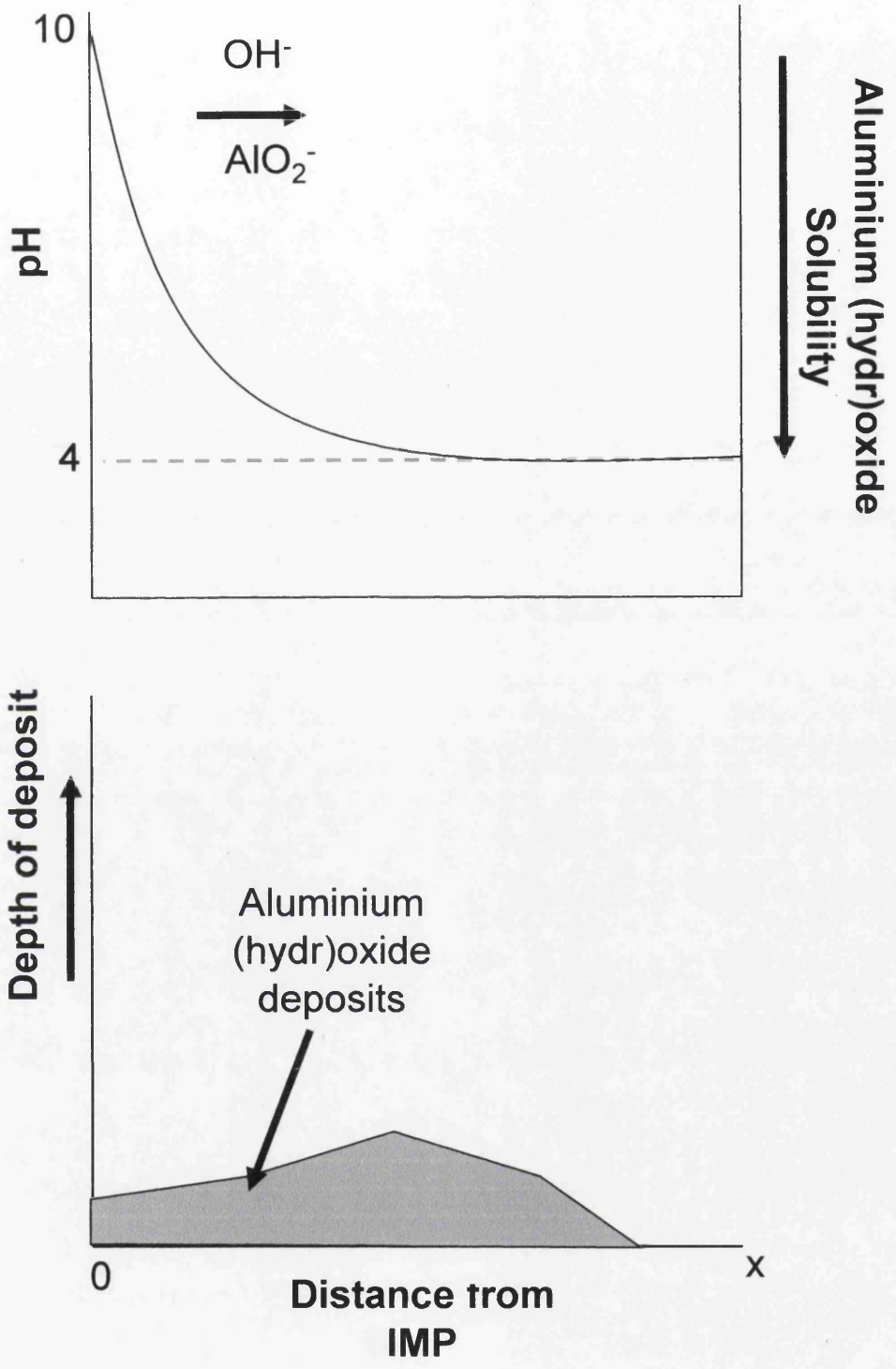

Figure 6.7: Schematic diagram showing the pH profile and aluminium (hydr)oxide deposits with increasing distance from a cathodic IMP on AA2024-T3 in unbuffered 0.86 M NaCl electrolyte.

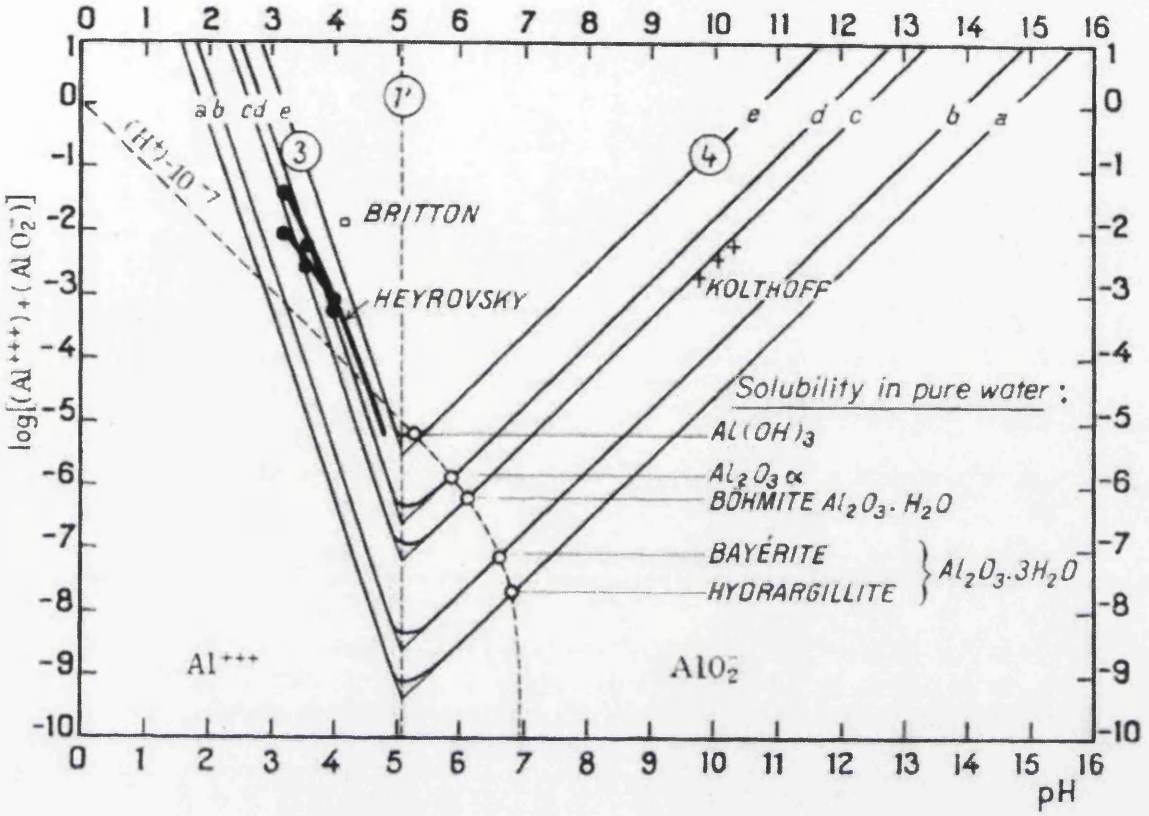

Figure 6.8: Influence of pH on the solubility of aluminium (hydr)oxides at 25°C.[17]

aluminium (hydr)oxides also decreases. Thus, AlO_2^- ions generated in zones of high local pH will tend to increasingly be removed from solution by the formation of insoluble aluminium (hydr)oxide as they move away from the cathodic IMP and down the pH gradient. This would produce a smooth curve of aluminium (hydr)oxides deposits as the distance from the cathodic IMP is increased, as shown by the plot in the lower half of Fig. 6.7. However, it would be difficult to detect these deposits in an unbuffered solution as there would be aluminium (hydr)oxide deposited from Al^{3+} cation hydrolysis and also redeposited copper on the surface.

It is self-evident from Fig. 6.5 that this smooth monotonic deposition does not occur in a 10^{-3} M EDTA buffered electrolyte but rather that two distinct areas (Region A and Region B in Fig 6.5) exist. Before a proposed mechanism for the formation of these regions is given it is important to understand what is meant by the term buffer solution, and how they function. In the introduction to this chapter EDTA is described as a tetraprotic acid with 4 pK_a values. The acidity constant K_a is determined from Reaction (6.5) which shows an acid reacting in water,[18]

$$HA_{(aq)} + H_2O_{(l)} \rightleftharpoons H_3O^+_{(aq)} + A^-_{(aq)} \qquad (6.5)$$

where H_3O^+, the hydrated proton, is called a hydronium ion and the proton acceptor, A^- is called the conjugate base of the acid HA. From this, the equilibrium constant for the proton transfer reaction in a weak acid can be defined in terms of the acidity constant, K_a, as follows.[18]

$$K_a \approx \frac{\left[H_3O^+\right]^2}{[HA]} \qquad (6.6)$$

The value pK_a is K_a reported in terms of its negative common logarithm as shown below,

$$pK_a = -\log K_a \qquad (6.7)$$

According to the Henderson-Hasselbalch[18,19] equation shown below in Equation (6.8), the pH of a buffer solution may be described in terms of pKa, [HA] and $[A^-]$ the molar concentration of the conjugate base.

$$pH = pK_a - \log \frac{[HA]}{[A^-]} \tag{6.8}$$

It follows that when molar concentrations of acid and conjugate base are equal, pH = pK_a. Furthermore, the buffering capacity, β, of a solution is given by Equation (6.9) below,[19]

$$\beta = 2.303\left(\frac{K_w}{[H^+]} + [H^+] + \frac{C_{buf}K_a[H^+]}{(K_a + [H^+])^2}\right) \tag{6.9}$$

where K_w is the autoprotolysis constant of water and C_{buf} is the total concentration of the buffer. From this equation it may be seen that the resistance to change in pH of a buffer solution is not only greatest at the pK_a values of the acid, but is also proportional to the concentration of the buffer solution.

In the case of a polyprotic acid (such as EDTA) a series of stepwise deprotonations of the acid occurs as the pH of the solution increases. This results in the acid having more than one pK_a value, and EDTA being a tetraprotic acid has 4 pK_a values, denoted $pK_{a1} = 0$, $pK_{a2} = 2.7$, $pK_{a3} = 6.2$ and $pK_{a4} = 10.3$.[2]

From Equation (6.9) it was shown that that ability of a buffer to resist changes in pH at its pKa values is proportional to the concentration of the buffer solution. This has important implications regarding the ability of the buffer solutions used in this chapter to prevent "cathodic corrosion". The oxygen reduction reactions occurring at a cathodic IMP would create OH^- ions. Initially in both the 10^{-2} and 10^{-3} M solutions OH^- ions would be generated in the ~pH 4 bulk solutions. However, as the concentration of OH^- ions increased, local pH would also increase approaching pK_{a3} for EDTA at pH = 6.2. As this point approaches the resistance to a change in pH would increase in both solutions. However, from Equation (6.9) it is evident that the 10^{-2} M solution would be 10 x more resilient to a change in pH than the 10^{-3} M solution. At this pH as shown by the Pourbaix diagram in Fig. 6.1, the alloy surface would be passive and thus matrix dissolution would be prevented. From the SEM images shown in Fig. 6.6c and 6.6d it

appears that the resistance to change in pH from the 10^{-2} M EDTA solution is enough to keep local pH in the passive region of the Pourbaix diagram throughout the duration of the corrosion experiment as there is minimal matrix dissolution visible around IMPs. This amount of matrix dissolution is consistent with observations made by other authors[10,11] on AA2024-T3 upon immersion in buffered electrolytes and is probably a result of anodic dissolution of S-phase particles. Similar observations were made in buffered electrolyte around Fe-rich IMPs on AA6061.[8]

This implies that the cathodic current generated by O_2 reduction at cathodic IMPs is not being consumed by a microgalvanically coupled anodic dissolution process in a region of high local pH. Thus the cathodic current is available for other preferred sites of anodic dissolution on the sample such as metastable or stable pitting events. This is supported by work carried out by Leclère and Newman,[1] described earlier, who found that immersion in a borate buffered solution increases the net cathodic current density that can be supplied to remote pitting sites, hence increasing the severity of pitting corrosion. The implications of this finding on SVET current density detection efficiency on corroding AA2024-T3 are discussed below in Section 6.4.2.

However, in a 10^{-3} M solution if diffusion–controlled O_2 reduction and associated OH^- production was faster than EDTA anion diffusion then OH^- would overwhelm the buffering capacity of EDTA and whilst resistance to an increase in pH would also occur at pK_{a4} a local pH value close to or in the range 10.35-10.65 (as determined from Equation (6.4)) would still be reached as in the unbuffered solution.

The resistance to change in pH encountered whilst pH is increasing will also be true in reverse. Therefore, if a pH of 10.35-10.65 is generated at a cathodic IMP the pH gradient away from the IMP will pass back through both pK_{a3} and pK_{a4} before the bulk solution value of ~pH 4, is reached. This will create a stepwise decrease in pH as shown by the pH curve in the schematic diagram in Fig. 6.9. It is noticeable that the stepwise curve shown here resembles the AFM line scan shown in Fig. 6.5 from the top of Region A, along and Region B to the bulk alloy. Thus it appears that as AlO_2^- solubility correspondingly decreases with increasing pH, aluminium (hydr)oxide is primarily deposited at the pH steps.

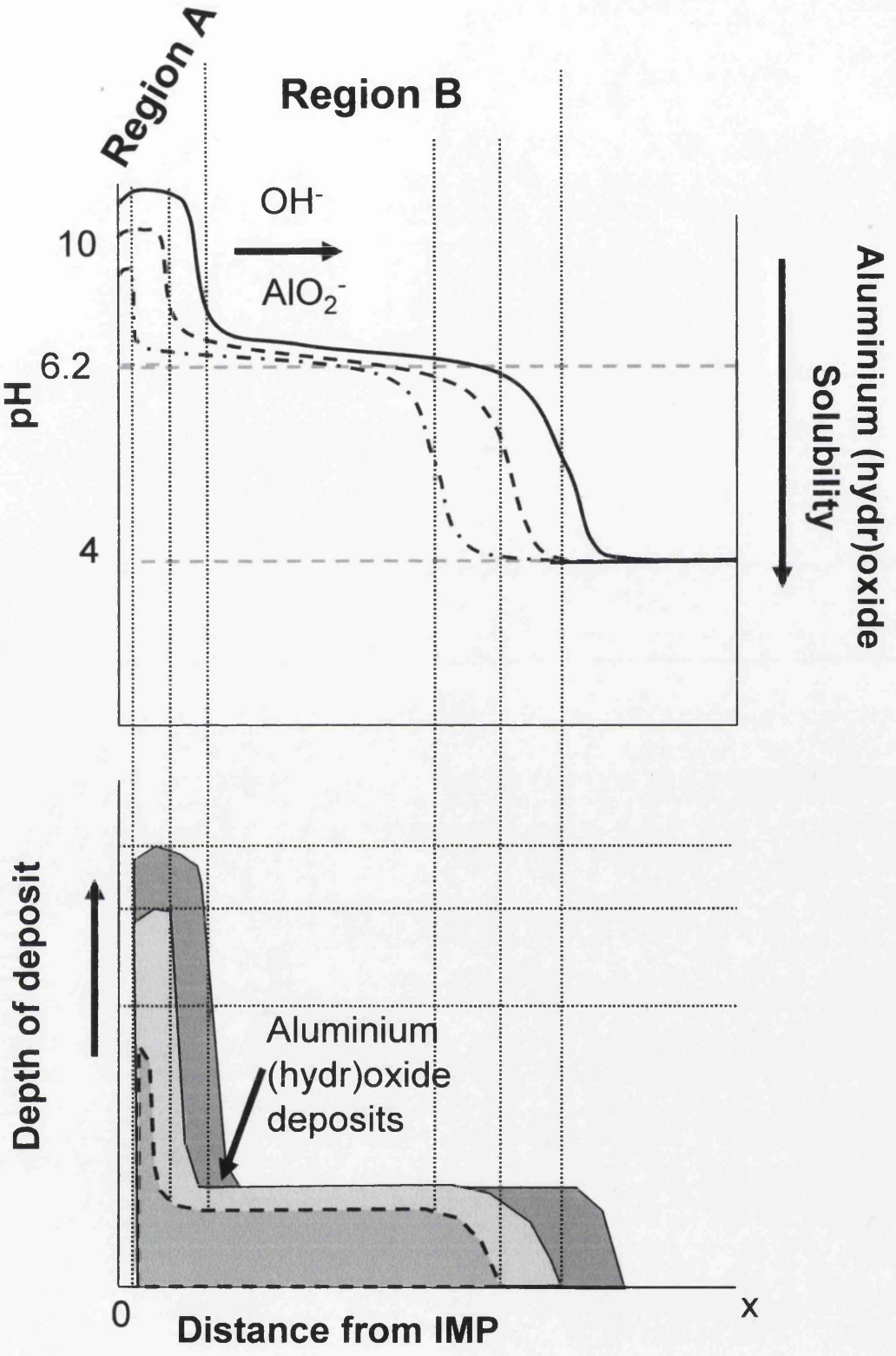

Figure 6.9: Schematic diagram showing the pH profile and aluminium (hydr)oxide deposits with increasing time and distance from a cathodic IMP on AA2024-T3 in 0.86 M NaCl electrolyte containing 10^{-3} M EDTA.

On the basis of the above information a possible mechanism for the creation of the bi-phasic Region A and Region B aluminium (hydr)oxide deposits occurring around cathodic IMPs in a 10^{-3} M EDTA solution is now proposed. Following the creation of a zone of high local pH (pH 10.35 – 10.65) generated by oxygen reduction at cathodic IMPs, aluminium matrix dissolution will occur in the immediatly adjacent area with the production of AlO_2^- anions. These will immediately enter a buffered zone of approximately constant pH, falling within the range of the fourth pK_a value for EDTA (pK_{a4} = 10.3). At this pH the rate of precipitation of insoluble aluminium (hydr)oxides would be very small, as shown by the solubility curves for aluminium hydr(oxides) in Fig. 6.8. For example, the solubility of $Al(OH)_3$ is very high and almost completely soluble at pH 10.3. However, as OH^- ions and AlO_2^- ions diffuse away from the IMP and move along the pH curve (shown in Fig. 6.9) they will reach the end of the buffering capacity of the $EDTA^{4-}$ anion. At this point there will be a sharp decrease in pH falling quickly towards pK_{a3} which is at pH 6.2. There will be a rapid decrease in the solubility of corrosion products and this will result in large deposits of aluminium hydr(oxides) on the substrate and result in the lip formation (Region A), as shown in Fig 6.5. Within the buffering zone of pK_{a3} there will be minimal deposition of corrosion products. However, again at the lower limit of the buffering range of pK_{a3} there will be a sharp decrease in pH to the bulk solution, (pH ~4.3) and a corresponding rapid deposition of corrosion products on the surface, resulting in the formation of Region B. As OH^- ions continuously diffuse through the same regions – gradually exceeding the buffering capacity of EDTA in each zone – the region of high local pH will increase. In this way the sharp decrease in pH and thus deposition of corrosion products will expand, resulting in the growth of Region A and Region B shown in Fig. 6.9.

Finally, as metal complexes are formed when metal cations (Cu^{2+} and Al^{3+}) are released into solution there is no replated copper or Al^{3+} corrosion products deposited on the surface. Thus we are allowed a unique look at only aluminium (hydr)oxide deposits from the hydrolysis of the AlO_2^- anion and the bi-phasic formations they produce around cathodic IMPs in 10^{-3} M EDTA electrolyte.

6.4.2 SVET Current Density Detection Implications

The results shown above have implications regarding the SVET data presented in Chapter 5, which was briefly outlined in the same chapter. However, before this is discussed it is first necessary to reiterate the limitations of SVET current density detection. Fig. 6.10 shows three different scenarios to highlight this. The first scenario, shown in Fig. 6.10a, is a schematic of a point anode where the cathodic reaction is diffusion controlled (*i.e.* the Nernst diffusion layer thickness is >> than cathodic IMP separation,[3,13] as described in Section 1.4.2.3) and so the whole surface may therefore act as a cathode. In this scenario the scan height, z, of the SVET microtip will cut through almost all paths of current and thus the detection efficiency will be excellent. In the second scenario shown in Fig. 10b the Nernst diffusion layer is < than cathodic IMP separation. In this scenario oxygen reduction will be ohmically controlled at cathodic IMPs and the majority of current will be contained within an area close to the anode. The line of planar scan at height z will not cut a large proportion of the lines of current flux and thus the detection efficiency of the SVET will be reduced.

However, whilst these scenarios are applicable to stable pitting events they do not apply to "cathodic corrosion". Corrosion currents are contained in this instance due to high localised pH and the local galvanic effect *per se* is irrelevant.[1] Therefore, in this scenario, shown in Fig. 6.10c, where pH is the limiting factor for current distribution, all of the current will be microgalvanically coupled between a cathodic IMP and the immediately adjacent surrounding anodic trench. Thus the line of planar scan of the SVET microtip at height *z* is unlikely to cut the lines of current flux between anode and cathode and so detection efficiency of the SVET will tend to 0.

This has the important corollary that a large proportion of the anodic current densities, occurring on AA2024-T3 freely corroding in conditions where "cathodic corrosion" is occurring, will remain undetected by the SVET. As discussed in the previous section, results from other authors have shown that in highly buffered solutions where "cathodic corrosion" is prevented from happening, the cathodic current available for stable pitting is increased. Combining these two results means that in fact, the plot of J_t for 10^{-2} M EDTA shown by curve (b) in Fig. 5.3, is probably a better reflection of the total anodic current density occurring on a AA2024-T3 substrate under immersion

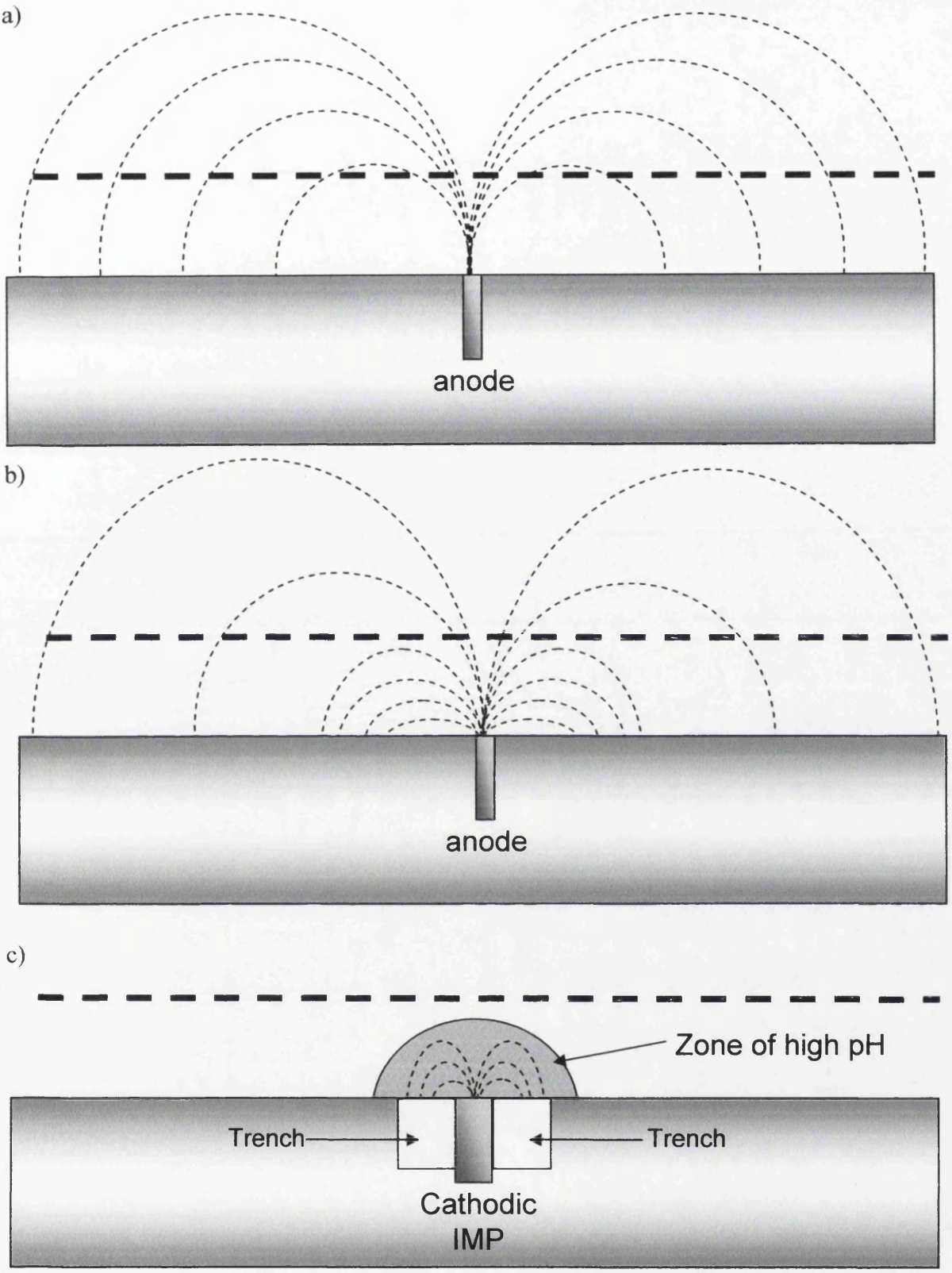

Figure 6.10: — — = scan height. Schematic diagrams showing detection efficiency of SVET under different conditions. a) O_2 reduction diffusion controlled. b) O_2 reduction ohmically controlled. c) "Cathodic corrosion" limited by zone of high pH

conditions in 0.86 M NaCl than the experimental data shown for AA2024-T3 in unbuffered electrolyte or indeed the 10^{-3} M EDTA electrolyte. The large values of J_t recorded when AA2024-T3 was immersed in electrolyte containing 10^{-2} M EDTA imply that the buffering ability of the solution, and thus elimination of "cathodic corrosion", means that cathodic current generated by O_2 reduction at cathodic IMPs is not being consumed by a microgalvanically coupled anodic dissolution process. Thus, the cathodic current is available for another preferred site of anodic dissolution increasing the net cathodic current density that can be supplied to remote pitting sites, hence increasing the severity of pitting corrosion events detectable by the SVET.

These findings do not mean that the SVET results presented in Chapter 5 are invalid but that the inhibitors tested are ranked in order of their effectiveness at preventing "pitting corrosion" as detectable by the SVET. That is to say, localised corrosion where the anode-cathode separation is >> z. Furthermore, these results highlight the danger of using SVET data quantitatively and reiterate the fact that it is a useful tool only for semi-quantitative analysis.

6.5 Conclusions

- AA2024-T3 has been shown to be susceptible to pitting corrosion following immersion in 0.86 M NaCl electrolyte. Analysis of the surface upon emersion showed significant deposits of corrosion products and redeposited copper.

- When corroded in electrolyte containing 10^{-3} M and 10^{-2} M EDTA the AA2024-T3 substrate surfaces remained relatively clean after immersion experiments. This was attributed to the complexing of metal cations preventing subsequent hydrolysis and the deposition of corrosion products. This allowed easy optical analysis of the substrates without the need for further processing.

- In 10^{-2} M EDTA buffered 0.86 M NaCl electrolyte there is no evidence of "cathodic corrosion" occurring on AA2024-T3. This is attributed to the

buffering capacity of EDTA preventing local zones of high pH being generated surrounding cathodic IMPs.

- However, in 10^{-3} M EDTA buffered 0.86 M NaCl electrolyte "cathodic corrosion" occurs as the concentration of buffer is not high enough to prevent zones of high local pH being generated at cathodic IMPs. This results in an anomalous bi-phasic feature occurring around some cathodic IMPs. AFM analysis shows that this is a topographically raised deposit. It is proposed that these deposits are aluminium (hydr)oxides formed from the hydrolysis of AlO_2^- anions released during matrix dissolution in local zones of high pH created at cathodic IMPs.

- A mechanism for the creation of the distinct bi-phasic topography is proposed whereby the deposition of aluminium (hydr)oxide occurs primarily in zones where there is a rapid decrease in pH. These rapid decreases in pH result from the resistance to pH change at pK_{a4} and pK_{a3} for EDTA. As each rapid decrease in pH occurs there is a corresponding rapid decrease in solubility of aluminium (hydr)oxide products and thus they are rapidly deposited on the AA2024-T3 surface.

- Even though "cathodic corrosion" is prevented in electrolyte containing 10^{-2} M EDTA oxygen reduction will still occur on cathodic IMPs. Thus the net cathodic current available for stable pitting is increased. This is shown by an increase in the detection efficiency of the SVET, indicating that microgalvanically coupled "cathodic corrosion" events occurring in zones of high local pH at cathodic IMPs are not detected by the SVET. This reiterates the fact that caution must be exercised when analysing SVET data. Furthermore, it clearly demonstrates that SVET results may only be interpreted semi-quantitatively.

6.6 References

1. T. J. R. Leclere and R. C. Newman, *J. Electrochem. Soc.*, **149**, B52 (2002).

2. R. M. C. Dawson, D. C. Elliott, W. H. Elliott and K. M. Jones, Data for Biochemical Research, Clarendon, Oxford (1959).

3. M. B. Vukmirovic, N. Dimitrov and K. Sieradzki, *J. Electrochem. Soc.*, **149**, B428 (2002).

4. K. Nisancioglu, K. Y. Davanger, O. Strandmyr and H. Holtan, *J. Electrochem. Soc.*, **128**, 1523 (1981).

5. P. Schmutz and G. S. Frankel, *J. Electrochem. Soc.*, **145**, 2295 (1998).

6. T. Suter and R. C. Alkire, *J. Electrochem. Soc.*, **148**, B36 (2001).

7. N. Dimitrov, J. A. Mann, M. Vukmirovic and K. Sieradzki, *J. Electrochem. Soc.*, **147**, 3283 (2000).

8. J. O. Park, C. H. Paik, Y. H. Huang and R. C. Alkire, *J. Electrochem. Soc.*, **146**, 517 (1999).

9. P. Hulser and F. Beck, *Aluminum*, **67**, 999 (1991).

10. J. C. Seegmiller, R. C. Bazito and D. A. Buttry, *Electrochem. Solid-State Lett.*, **7**, B1 (2004).

11. O. Schneider, G. O. Ilevbare, J. R. Scully and R. G. Kelly, *J. Electrochem. Soc.*, **151**, B465 (2004).

12. J. Goldstein, D. E. Newbury, D. C. Joy, C. L. Lyman, P. Ecglin, E. Lifschin, L. C. Sawyer and J. R. Michael, Scanning Electron Microscopy and X-ray Microanalysis Kluwer Academic, Plenum Publishers, New York (2003).

13. M. A. Jakab, D. A. Little and J. R. Scully, *J. Electrochem. Soc.*, **152**, B311 (2005).

14. H. Dafydd, D. A. Worsley and H. N. McMurray, *Corros. Sci.*, **47**, 3006 (2005).

15. R. E. Davis, G. L. Horvath and C. W. Tobias, *Electrochem. Acta*, **12**, 287 (1967).

16. G. W. C. Kaye and T. H. Laby, Tables of Physical and Chemical Constants, London (1986).

17. M. Pourbaix, Atlas of Electrochemical Equilibria in aqueous solutions, Pergamon Press, Oxford (1966).

18. P. W. Atkins and J. de Paula, Physical Chemistry, Oxford University Press (2002).

19. G. D. Christian, Analytical Chemistry, John Wiley & Sons, Inc., USA (1994).

Chapter 7

Time-lapse Investigation of FFC on Iron – Effects of Gas Composition

7.1 Introduction

Filiform Corrosion (FFC) was first accurately described by Sharman in 1944.[1] He used the term to describe filamentary ("worm-like") trails of corrosion products that formed on organically coated steel at high relative humidity in air. A detailed description of the current understanding of FFC on iron (steel) is given in Section 1.4.3. Briefly, filament heads are electrolyte filled, containing Fe^{2+} and Fe^{3+} cations and aggressive anions (typically Cl^-). A differential aeration cell is created and maintained in the head electrolyte due to the facile gaseous oxygen transport through the dry, porous filament tail.[2,3] This implies that the primary cathodic oxygen reduction site is at the back of the filament head. The pH towards the leading head of the filament head electrolyte is typically low as a result of cation (Fe^{3+}) hydrolysis with values of *ca.* pH 1 recorded,.[2,4] This in turn, implies that anodic metal dissolution, as shown in Reaction (7.1), will occur at the leading edge of a filament.

$$Fe_{(s)} \rightarrow Fe^{2+}_{(aq)} + 2e^- \qquad (7.1)$$

There are also three reactions occurring mainly in the tail. They are the homogeneous oxidation of Fe^{2+} by atmospheric O_2,

$$2H_2O + 4Fe^{2+}_{(aq)} + O_2 \rightarrow 4Fe^{3+}_{(aq)} + 4OH^-_{(aq)} \qquad (7.2)$$

cathodic O_2 reduction,

$$O_2 + 2H_2O + 4e^- \rightarrow 4OH^-_{(aq)} \qquad (7.3)$$

and corrosion product precipitation.

$$Fe^{3+}_{(aq)} + 3OH^-_{(aq)} \rightarrow FeOOH_{(s)} + H_2O \qquad (7.4)$$

The Fe^{2+} product of Reaction (7.1) can react further with O_2 diffusing through the defect and up the filiform tail via reaction (7.2) to produce Fe^{3+}. Reaction (7.3) is the principal cathodic reaction and occurs primarily at the filament head / tail junction due to facile O_2 diffusion through the porous tail. Inter diffusion of Fe^{3+} and OH^- then produces the dark coloured $Fe(OH)_3$ or Fe_2O_3 precipitate in the tail. However, it has also been reported that a cathodic anterior ring of corrosion products may form at the leading edge of a filament. The mechanism of this ring formation is similar to that seen in an 'Evans water drop' experiment.[5] That is to say O_2 diffusing vertically down through the PVB coating in to FFC head droplet does so most rapidly where the head droplet is thinnest *i.e.* at the edge (or limb) of the droplet. Reaction (7.3) then occurs at a secondary annular cathode at the droplet edge. It has further been reported that this cathodic anterior ring facilitates FFC propagation by the production of OH^- ions and a zone of high local pH, *i.e.* by a cathodic disbondment mechanism.[6-9]

However, there are two mechanisms other than cathodic disbondment that have been suggested as controlling the rate of FFC propagation on iron (steel). These are anodic undermining[10] whereby metal dissolution at the coating / metal interface leads to disbondment, and mechanical disbondment due to a build-up of pressure in the filament head by an (electro)osmotic mechanism.[2,11] Despite the amount of research carried out on FFC the primary mechanism of coating disbondment still remains unclear. However, it is obviously important to determine this primary mechanism of coating disbondment in order to design rational corrosion inhibitor and pre-treatment systems for organic-coated iron and carbon steel exposed to aggressive environments.

It is the intention of this chapter to probe the kinetics and mechanism of FFC on organically coated iron by systematically varying gas composition (pO_2). This was facilitated by the design of a new experimental cell that allowed the gas supplied to the head electrolyte through the tail to be controlled separately from the environment surrounding the head outside of the organic coating. There were two primary aims behind this investigation. Firstly, to ascertain the accuracy of the assumption that O_2 transport (in tail) occurs from the defect and not through the coating. Secondly, to determine whether cathodic disbondment (as a result of through coating cathodic O_2 reduction) at the preceding edge of a filament is an important factor in FFC kinetics. It

has previously been reported that the ring of corrosion products formed in this region is suggestive of a cathodic disbondment mechanism.[7-9]

7.2 Experimental

Iron foil (99.9% Fe) of 1.5mm thickness was supplied by Goodfellow materials Ltd. All other chemicals were supplied by Sigma Aldrich Ltd. A detailed description of the FFC initiation method and the experimental technique can be found in Section 2.10. All FFC experiments were initiated with 2μl of 2.5 x 10^{-3}M aqueous solution $FeCl_2$. This initiating electrolyte was used due to the problem of a preceding coating disbondment phase when using a group (I) chloride electrolyte as described in Section 1.4.3.5.

A dual compartment cell (Watson-Coleman device)[12] described in detail in Section 2.10, was used in these experiments allowing the filament head and penetrative coating defect to be exposed to differing atmospheres. In subsequent discussions the 'coating compartment' refers to the cell compartment containing the filiform head and a portion of the tail nearest to the head. The 'defect compartment' refers to the compartment containing the coating defect and the remaining portion of the filiform tail, as described in Section 2.10.2.

Images were taken *in-situ* of the filiform head at 10 minute intervals using a Nikon Coolpix 4500 digital camera in conjunction with a Meiji optical microscope operated in reflectance mode. Spatial analysis of the images was carried out using commercially available image analysis software as described in Section 2.10.3

7.3 Results and Discussion

7.3.1 Basic Kinetics of FFC

Time-lapse photography allows a convenient study of the propagation of FFC on iron and is used in conjunction with the dual-compartment cell for this purpose. Fig. 7.1 shows a typical series of optical micrographs of a filament where both the coating and defect compartments are exposed to humidified (93% r.h.) N_2/O_2 atmosphere containing

a)

b)

c)

d)

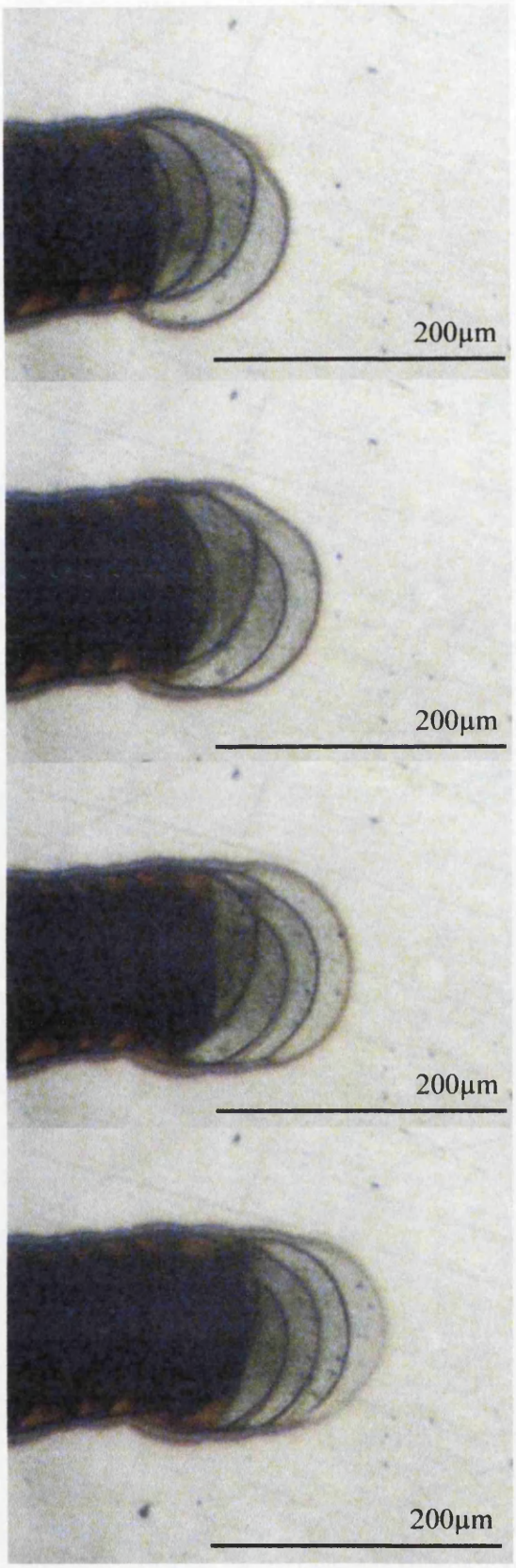

Figure 7.1: Reflective light optical micrographs of chloride induced FFC on iron in an air (pO_2 = 0.2 atm) atmosphere and 93% r.h. Time key: t = (a) 0 min (b) 105 min (c) 180 min (d) 255 min.

pO_2 = 0.2 atm (*i.e.* air). Time key for images: (a) t = 0, (b) t = 105, (c) t = 180 and (d) t = 255 mins. It must be noted that the value t_0 is not the time of FFC initiation but is the time that time-lapse imagery of the sample in the dual-compartment cell was started. When viewed as an animation, it may be seen that filament propagation appears to be saltatory [OED def: "pertaining to, characterised by, or adapted for leaping through a succession of forward jumps"], that is to say advancement occurs in a step-wise or discrete manner and not through a smooth continuous movement. Fig. 7.2 shows this propagation mechanism schematically as the formation of successive rings, observed as rings of dark precipitate (corrosion product) on the optical micrographs. A dark ring exists at the leading edge of the filament at t = 0 mins. Advancement occurs when electrolyte breaks through this ring (t = 30 mins) and edges forward, spreading until at t = 120 mins a new ring of corrosion products forms, halting further advancement of electrolyte. In turn this ring will be breached and so the cycle of ring formation and filament propagation continues. The saltationary propagation of the filament rings can also be seen on a plot of filament extension *vs.* time, as shown by curve (a) in Fig. 7.3. Conversely, the border between the filament tail and the filament head moves in a constant fashion as shown by curve (b) in Fig. 7.3.

At this point it is worthwhile defining some features from this plot that will be used to describe filament advancement throughout this chapter. Fig. 7.4 shows the filament extension data from Fig. 7.3 again, but with the important features marked. Firstly the period, T, is determined as the time from the formation of a new anterior ring to the formation of the next anterior ring and is ~150 mins for the filament shown. Although T remains relatively constant during experiments, a further value, σ, defined as the average frequency of saltation, is used to describe filament frequency. This value is determined by the number of T within time t_f, divided by t_f. The value of σ in for this filament is 5.4 x 10^{-3} min^{-1}. The velocity, v, of the filament equals F x A where A is defined as the as the distance that the filament moves between successive anterior rings.

From Fig. 7.3 it can be seen that the rate of filament propagation remains constant at 0.27 μm/min for the duration of the experiment. Indeed, the propagation velocity of all filaments exposed to conditions of pO_2 = 0.2 atm in both the coating and defect compartments during this work, remained constant over the experimental period.

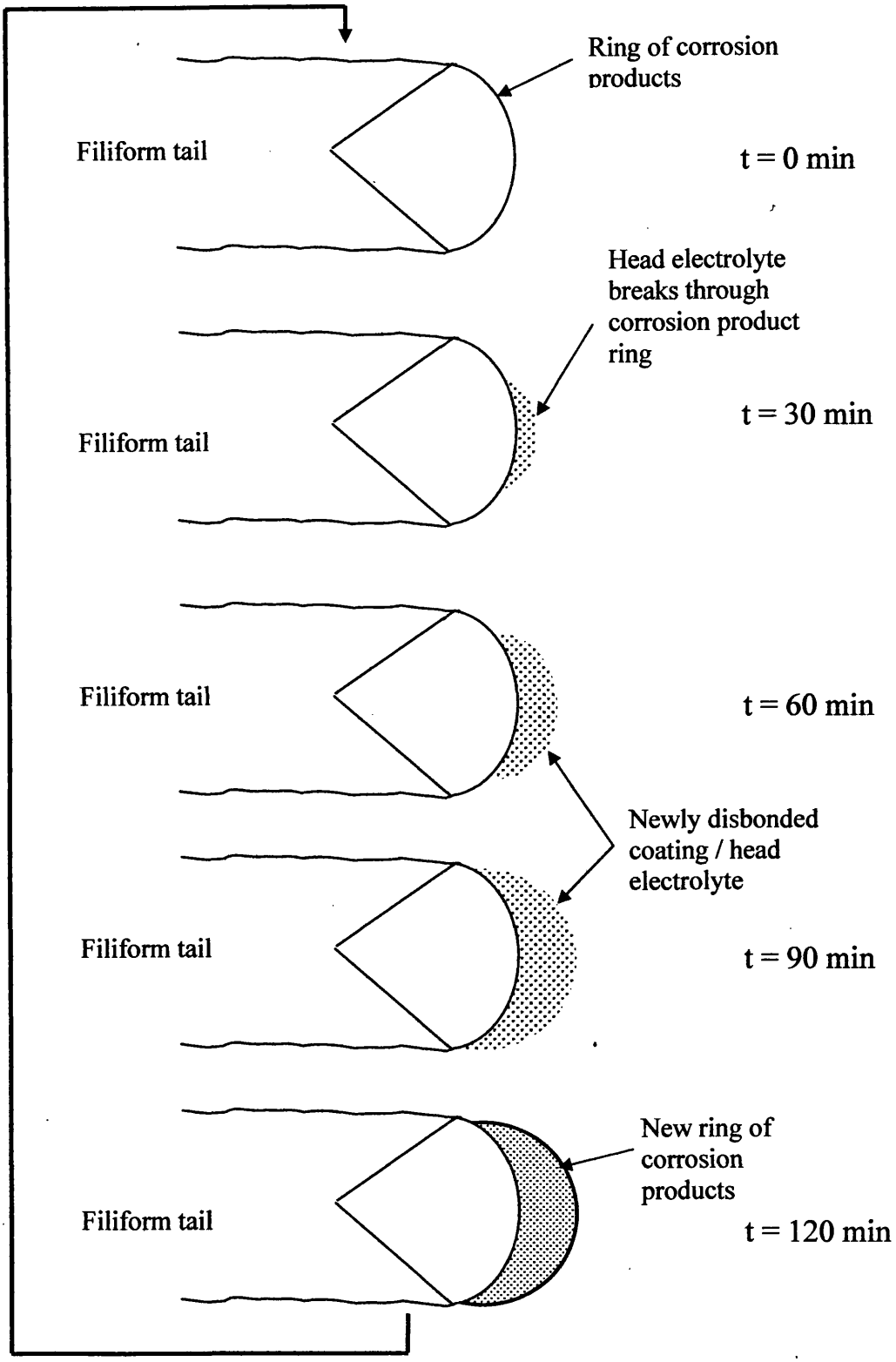

Figure 7.2: Schematic diagram of the saltatory propagation mechanism of FFC on iron. At the cathodic anterior ring, corrosion products are deposited which periodically inhibit filament progress.

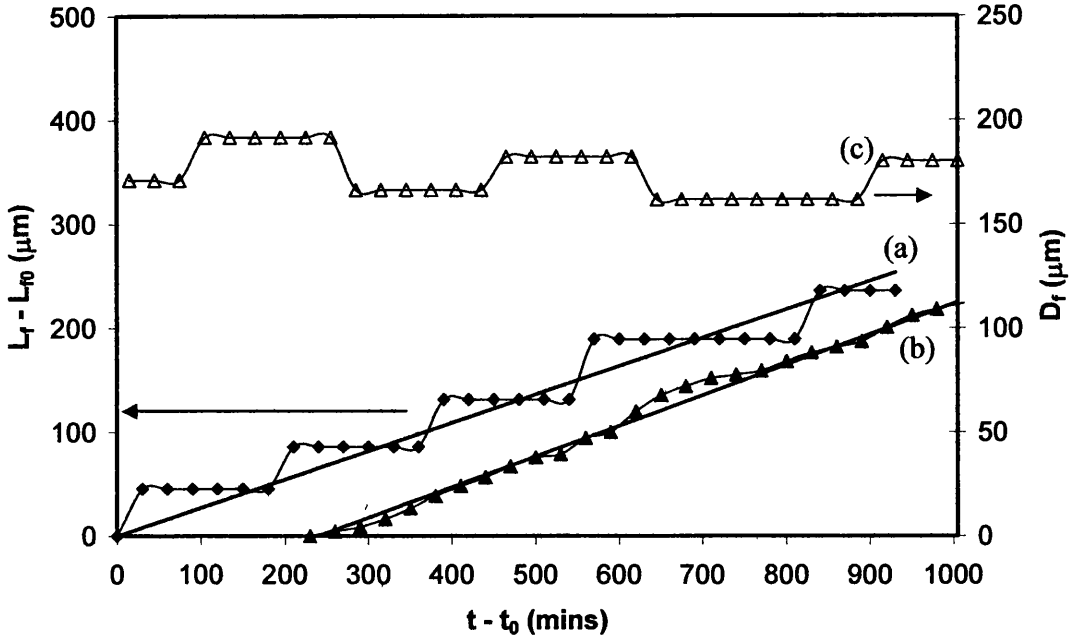

Figure 7.3: Plot of filament length (L_f) *vs.* time (t) and filament width (D_f) *vs.* t since FFC initiation on PVB coated iron for the filament shown in Fig. 7.1. Curve (a) filament ring and (b) head/tail junction are filament extension plots. Curve (c) is a plot of filament width. The quantity L_0 is the value of L_f in the first time-lapse image, acquired at time t_0.

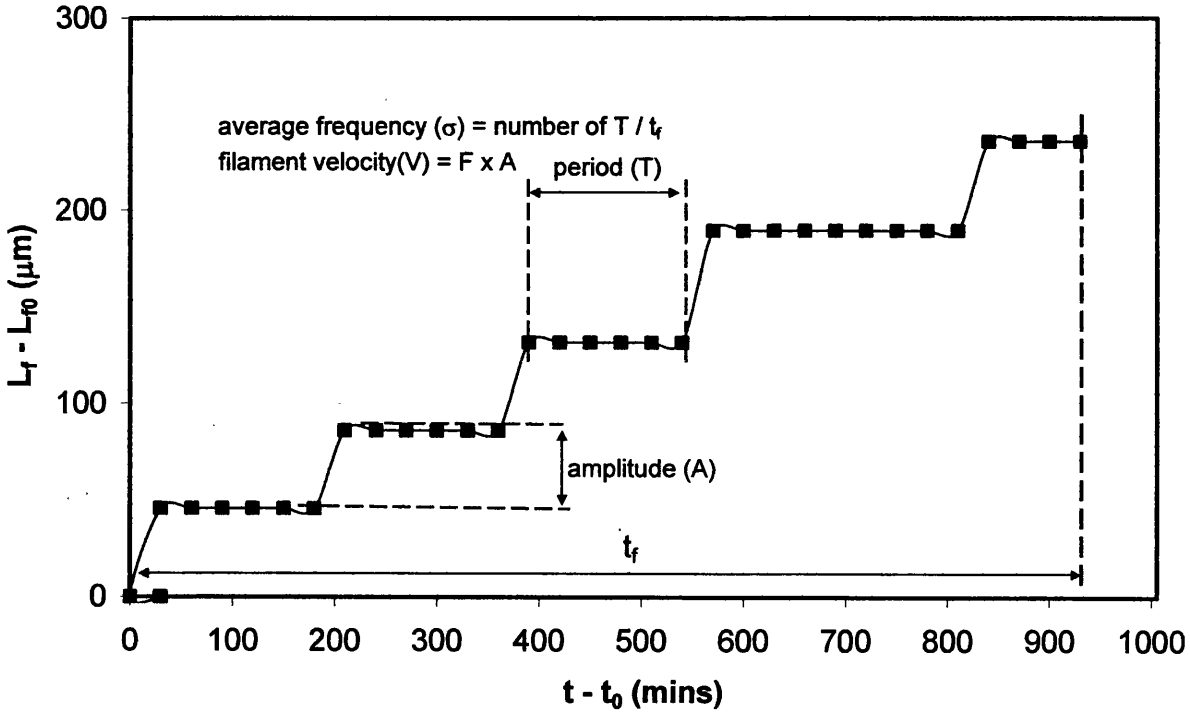

Figure 7.4: Plot of filament length (L_f) *vs.* time (t) taken from Fig. 7.3. The values of period, T, average frequency, σ, and filament amplitude, A, are shown.

This indicates that there is no mass transport control of filament propagation, from O_2 diffusion along the filament tail, as the filament extends. The constant velocity is consistent with electrolyte being pumped forward into the head by (electro)osmosis to build-up pressure in the head as has previously been suggested by other autohors.[2] The possible mechanism of (electro)osmosis by which this pressure build-up may occur will be discussed further in Chapter 8. Finally, it may also be seen in Fig. 7.3 that the filament diameter, D_f, shown by curve (c) stays constant throughout the duration of the experiment, indicating that the volume of free electrolyte in the filiform head also remains constant.

7.3.2 Effect of Defect pO_2

As discussed in Section 1.4.3 it is now generally accepted that the primary mode of water and oxygen transport takes place through the tail[2,13,14] and not by diffusion through the coating for FFC as has also been suggested.[15] Upon drying, the corrosion products found in the tail become porous allowing the transport of O_2 and water through the medium. Ruggeri and Beck[2] calculated that the transport of O_2 through the coating would be ten times slower than that through the defect and porous tail. They estimated that for tails shorter than 150 mm, diffusion through the coating break is preferred. This directional supply of oxygen from the tail causes a differential aeration cell to be set up in the head with the majority of the cathodic reaction (oxygen reduction) occurring at the back of the head and the majority of the anodic reaction (metal dissolution) occurring at the front of the head in the relatively deaerated region.[2,3,9,11,16] Despite this, the roles played by oxygen transport through the defect and through the coating are not fully understood. FFC has been shown to occur under metal plate strips with no oxygen permeability, when placed over filiforms occurring under organic coatings[9] suggesting that the primary source of oxygen is indeed from the defect. FFC has also been shown to be completely inhibited in the total absence of oxygen[2,3]. However, the dual-compartment cell allows an in-depth study to be made into the roles of oxygen diffusion through the defect and oxygen diffusion through the coating in terms of FFC propagation.

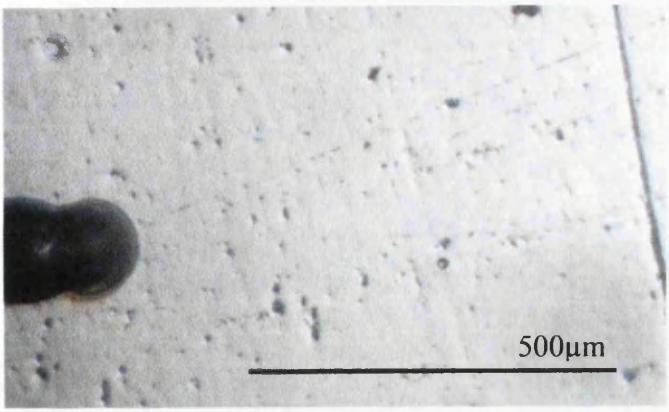

(a) t = 0 min
Coating compartment atmosphere is air
Defect compartment atmosphere is air

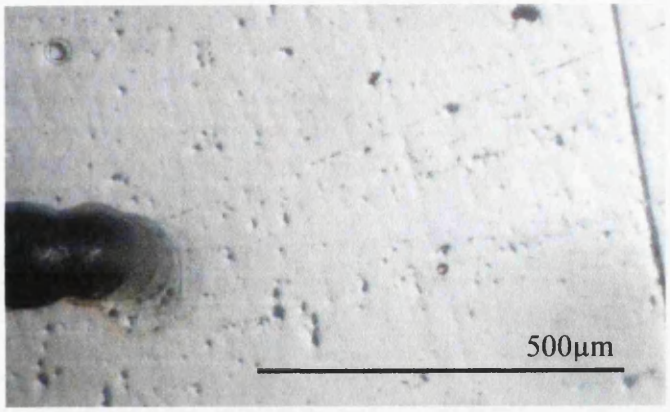

(b) t = 240 min
Coating compartment atmosphere is air
Defect compartment atmosphere is air

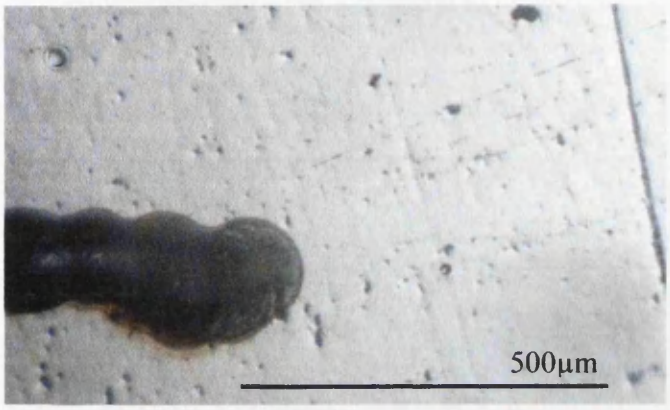

(c) t = 760 min
Coating compartment atmosphere is air
Defect compartment atmosphere is argon

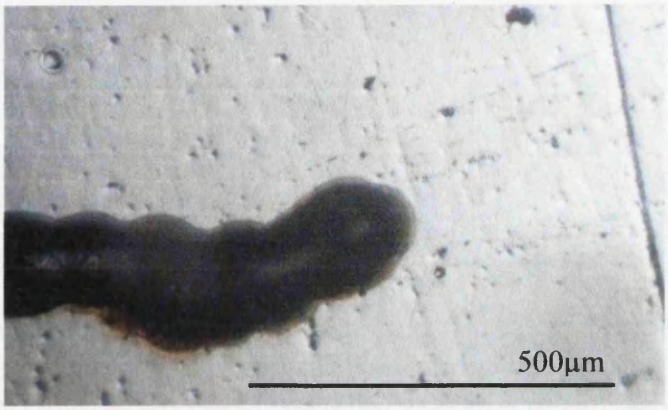

(d) t = 2520 min
Coating compartment atmosphere is air
Defect compartment atmosphere is argon

(e) t = 3000 min
Coating compartment atmosphere is air
Defect compartment atmosphere is air

(f) t = 3500 min
Coating compartment atmosphere is air
Defect compartment atmosphere is air

Figure 7.5: Visual summary of time-dependent FFC initiated using 2 µl of aqueous 0.0025 M $FeCl_2$. Defect and coating compartment atmospheres are indicated.

Figure 7.5(a-f) shows photographic images from an experiment where pO_2 is maintained at 0.2 atm throughout the duration of the experiment in the coating compartment but varied in the defect compartment. Fig. 7.6 is a summary plot of the data from this experiment. In Fig.7.5a and b pO_2 is maintained at 0.2 atm in the defect compartment and the rate of filiform propagation (shown in part A of Fig. 7.6) is 0.38 μm/min. When pO_2 is reduced to zero in the defect compartment by displacement through the introduction of argon, the filament still advances. This is presumably because O_2 is still being supplied by through coating O_2 diffusion into the portion of the tail exposed in the coating compartment. However, the rate of filiform propagation, although still constant, is significantly reduced (by ~63%) to 0.14 μm/min as shown in part B of Fig. 7.6. This indicates that the propagation rate is controlled by the pO_2 of oxygen in the tail of the filament. Upon the re-introduction of oxygen into the defect compartment (pO_2 = 0.2 atm) the rate of filiform increases to 0.42 μm/min as shown in part C of Fig. 7.6. This is entirely comparable to the initial rate of the filament when pO_2 = 0.2 atm in the defect compartment at the start of the experiment. A summary of the rates of propagation are shown below in Table 7.1.

Table 7.1: Rate of filiform progression different coating compartment environments

Coating atmosphere	Defect atmosphere	Rate (μm/min)
Air	Air	0.38
Air	Argon	0.14
Air	Air	0.42

From Fig. 7.6 it may also be seen that σ is proportional to defect pO_2 and is reduced from ~9.8 $x10^{-3}$ min^{-1} to 4.7 x 10^{-3} min^{-1} when O_2 is reduced from 0.2 atm to zero in the defect compartment. That is to say, when pO_2 is reduced in the tail it takes longer for the pressure in the head to be produced, hence a reduction in frequency. Conversely, once the required pressure to disbond the coating has been reached in the filament head, the filament amplitude, A, appears to remain constant (at ~30 μm for the filament shown in Fig. 7.6) when pO_2 is varied between 0.2 and zero in the defect

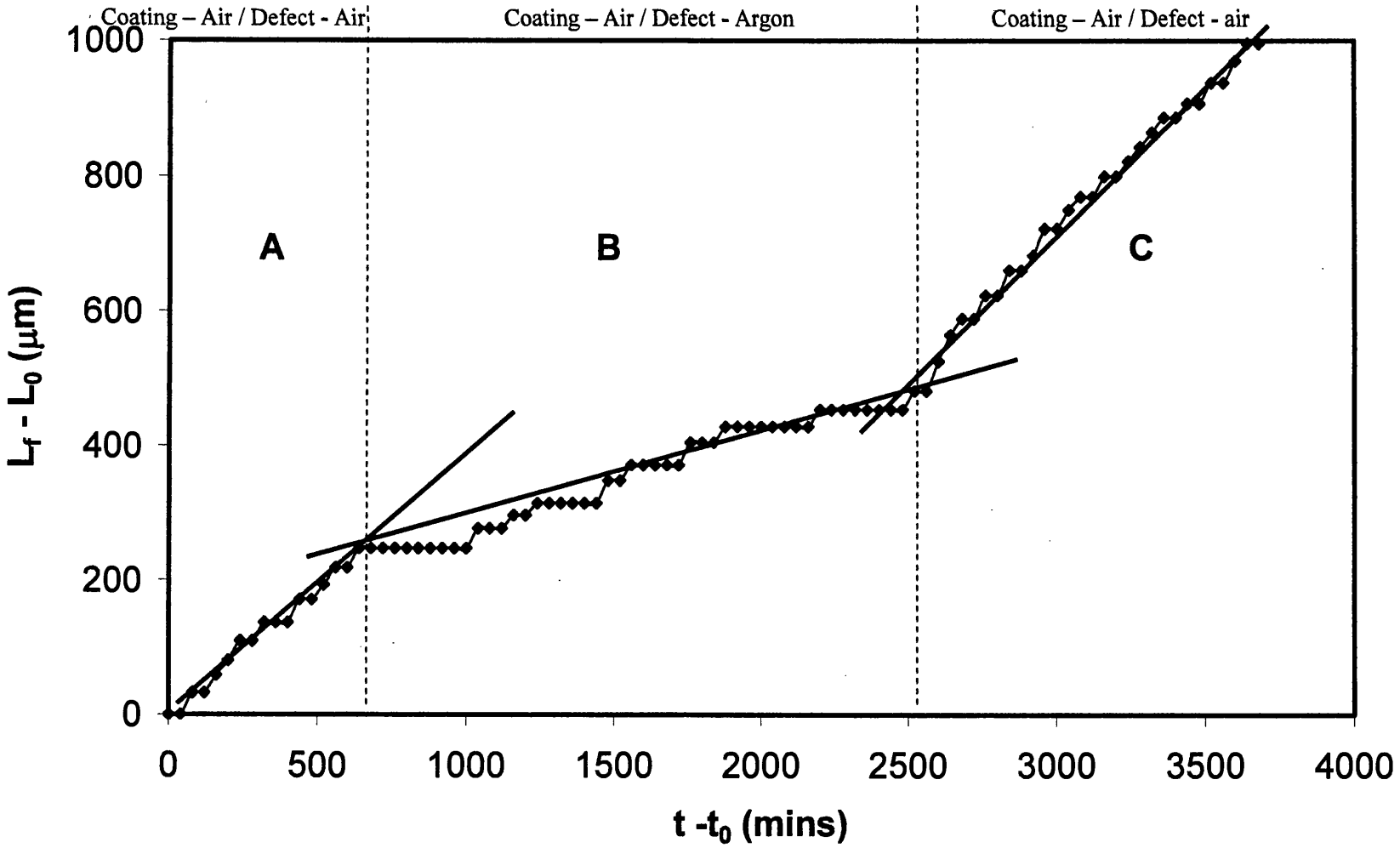

Figure 7.6: Plot of filament length (L_f) *vs.* time (t) since FFC initiation on PVB coated iron for the filament shown in Fig. 7.5. Gas conditions maintained in each compartment of the dual-compartment cell are shown on the plot. The quantity L_0 is the value of L_f in the first time-lapse image, acquired at time t_0.

compartment. Both of these observations are consistent with an O_2 reduction controlled electroosmotic pump mechanism (which will be described in detail in Chapter 8) determining the pressure build-up in the filiform head

The results in this section have shown that oxygen mass transport through the tail from the defect is indeed the primary mode of oxygen transport to the filiform head (shown schematically in Fig. 7.7a). However, FFC occurring under an oxygen permeable coating may still be maintained by O_2 diffusion through the coating into the porous tail region of the filament, even when the O_2 supply directly from the defect itself is cut off. A possible mechanism for continued propagation in the absence of defect O_2 is shown schematically in Fig. 7.7b. In this instance O_2 diffuses vertically through the PVB into the porous tail. This then rapidly diffuses (horizontally) to the tail / head junction. More O_2 will be supplied to the filament head this way than directly through the coating into the head electrolyte. Thus sufficient differential aeration is maintained in the head electrolyte for continued FFC propagation. However, due to the reduction of pO_2 in the filament tail in this case the rate of filiform propagation is significantly reduced.

The results above have shown that some oxygen diffusion through the coating into the tail occurs along the filament length. However the magnitude of this effect would be dependant on the thickness and oxygen permeability of the coating as observed by Leblanc and Frankel,[8] and discussed in Section 1.4.3. On initial analysis it may also be thought that filament length (surface area) may be important in determining the rate of propagation during this through coating O_2 diffusion mechanism of FFC. However, as only a small proportion of the total filament length is recorded during this experiment, no change in filament propagation rate was observed.

7.3.3 Effect of Coating pO_2

7.3.3.1 $pO_2 = 0.2$ atm

In Fig. 7.1 successive dark rings are clearly visible preceding the filament tail when $pO_2 = 0.2$ atm in both the coating and defect compartment. Characterisation of these rings using image analysis of a typical filament showing these rings is shown in

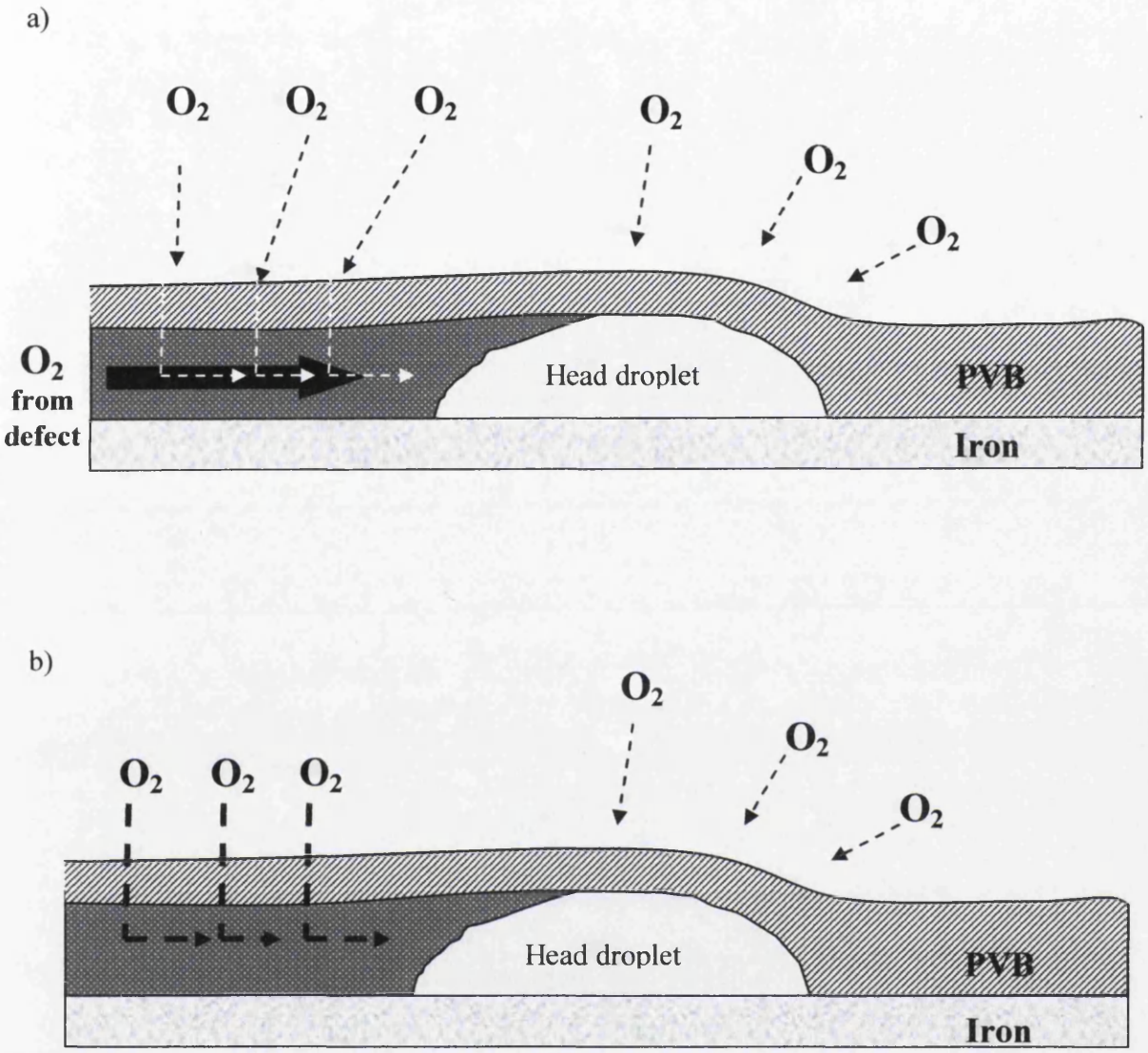

Figure 7.7: Schematic diagrams of FFC. (a) Sources of oxygen when defect oxygen is present. (b) Sources of oxygen when defect oxygen is not present. In diagram (b) sufficient differential aeration is still maintained by through coating O_2 diffusion into the tail for continued FCC propagation, albeit at a slower rate.

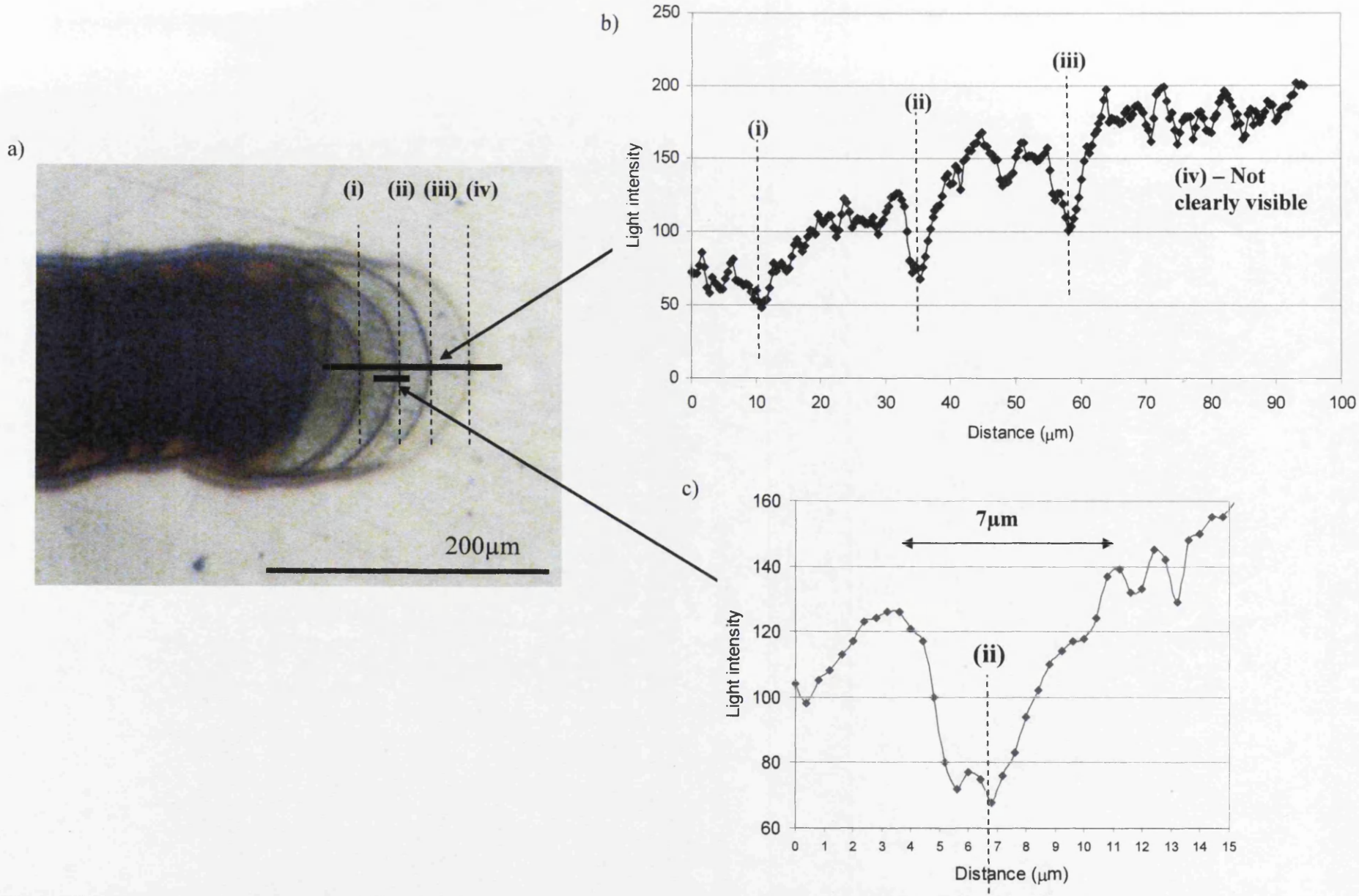

Figure 7.8: Intensity measurement of filament rings: (a) Optical micrograph of filiform corrosion in an air atmosphere and 93% r.h, (b) Light intensity of the four rings indicated in (a) and, (c) Light intensity of ring (ii)

Fig. 7.8. This was done in order to ascertain whether the rings were of comparable dimensionality to anterior cathodic rings reported elsewhere for FFC occurring on epoxy coated steel.[8] It was suggested that these corrosion products form by O_2 mass transport through the coating leading to a cathodic alkalisation and in turn disbondment of the coating. It was on this basis that a mechanism of cathodic disbondment was proposed whereby an anterior cathode produces ions sufficient to disbond the coating.

A line of colour intensity to is measured from the image, allowing the determination of step-size (distance between dark rings) and ring thickness. By converting the colour image to grey-scale, image pixel values proportional to light intensity (between 0 and 255) may be plotted. Fig. 7.8b shows that the distance between rings is *ca.* 25μm with succeeding rings appearing darker whilst Fig. 7.8c shows that the thickness of a ring of corrosion products is *ca.* 7μm. This later value has similar dimensionality to a previously identified cathodic area at the preceding periphery of a FFC head on steel.[8] Therefore, it seems probable that the annular head material shown in Fig. 7.1 and Fig. 7.8 forms as a result of through coating O_2 reduction, as shown in Reaction (7.3), and cation hydrolysis, shown in Fig. (7.2), acting to increase local pH at the perimeter of the head. This and the subsequent precipitation of hydrated ferric oxide corrosion products are shown schematically in Fig. 7.9. However, the importance of this anterior ring to the mechanism of FFC and whether it facilitates or hinders the propagation rate of FFC remains unclear.

7.3.3.2 $pO_2 = 0$ atm

In an attempt to establish the importance of the anterior cathodic ring a filament was allowed to propagate until t = 945 mins, with $pO_2 = 0.2$ atm in both the defect and coating compartments and an image of the filament is shown in Fig. 7.10a. A brown anterior ring may be seen preceding the filament at this point. Oxygen was then removed from the coating department ($pO_2 = 0$ atm) by pumping argon gas into the chamber (note: relative humidity was maintained at 93% throughout the experiment). Fig. 7.10b shows the same filament 350 mins after the removal of O_2 from the coating compartment at t = 1305 mins. In this image the anterior ring has disappeared but the

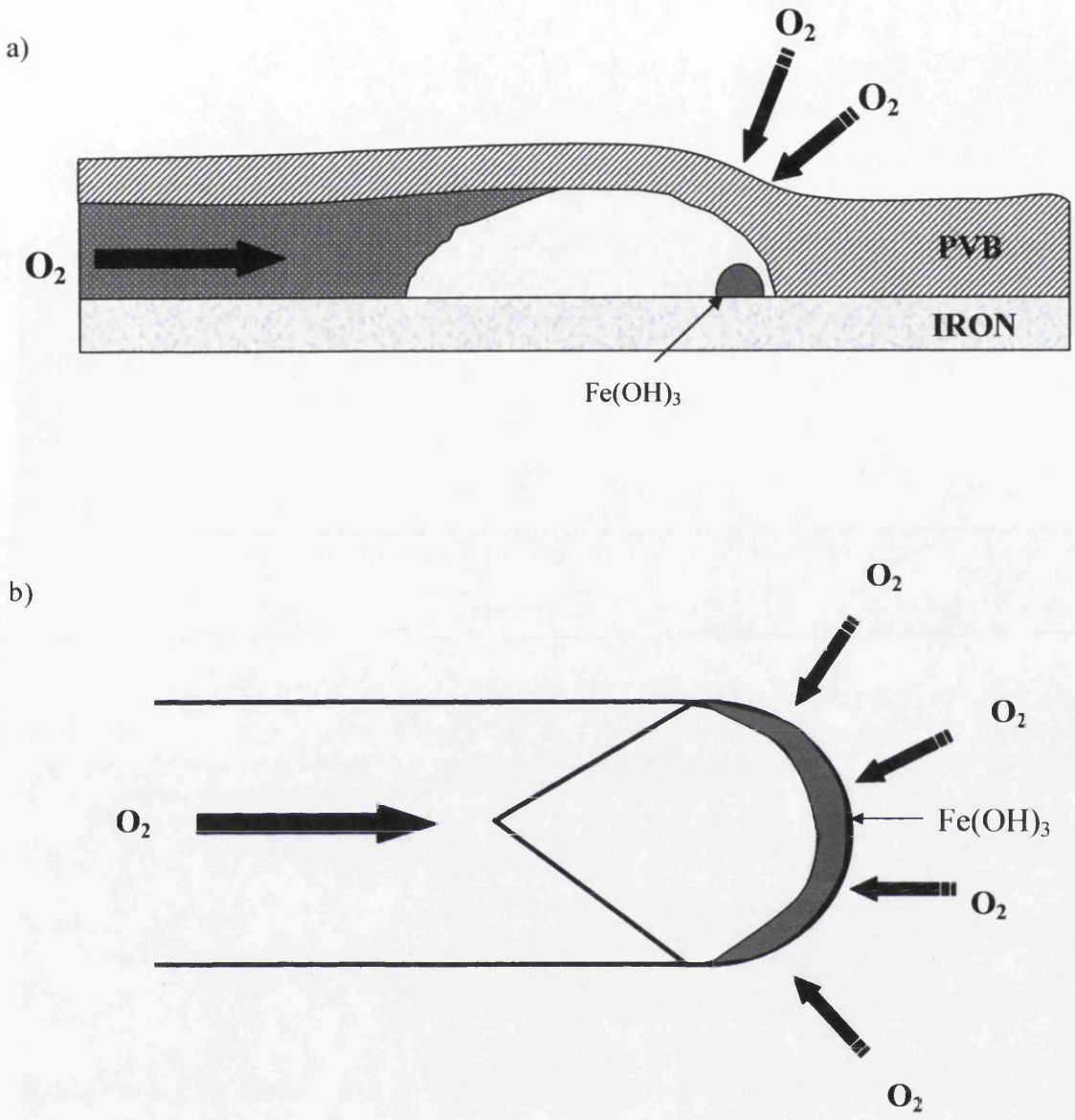

Figure 7.9: Schematic diagrams, (a) side-view and (b) top-view of FFC illustrating the mechanism of anterior ring formation. O_2 diffusing through the PVB coating and FFC head droplet does so most rapidly where the head droplet is thinnest, *i.e.* at the edge (periphery) of the droplet.

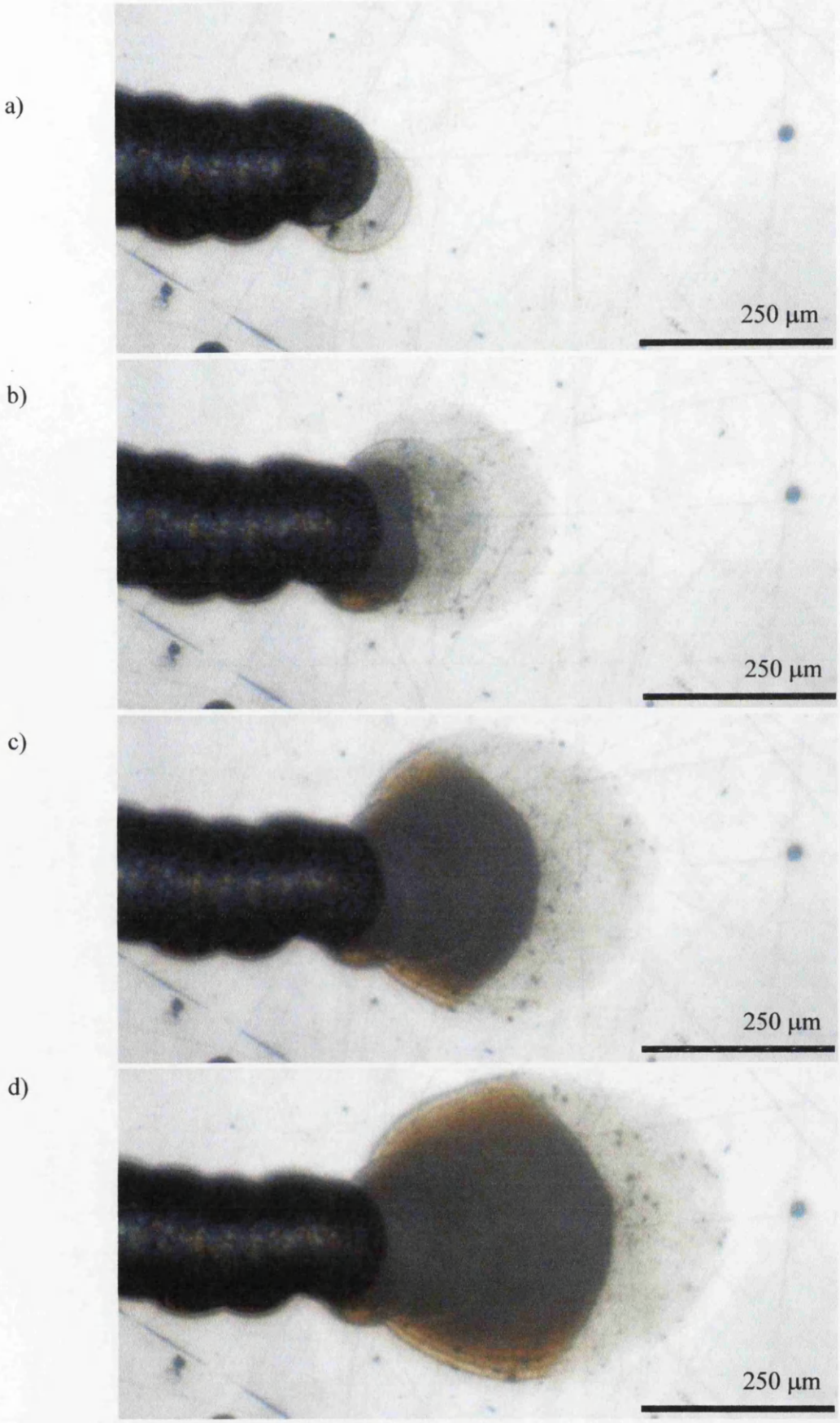

Figure 7.10: Reflective light optical micrographs of an advancing filament head in 93% r.h with defect pO_2 = 0.2 atm. Coating compartment pO_2 key: (a) 0.2 atm, and (b), (c) and (d) 0 atm. Time key: (a) 945, (b) 1305, (c) 1755 and (d) 2025 mins.

filament has still advanced. It is also immediately obvious from the image that D_f has increased dramatically upon the disappearance of the anterior ring of corrosion products. Fig. 7.10c and d show the filament at t = 1755 mins and t = 2025 mins respectively. In both cases it can be seen that there is no anterior cathodic ring visible at the leading edge of the filament. However, the filament has clearly advanced; whilst D_f has approximately doubled.

The images in Fig. 7.11 show the response of the same filament when oxygen was re-introduced into the coating compartment by pumping pure O_2 into the coating chamber (pO_2 = 1 atm). Fig. 7.11a is an image immediately before pO_2 is increased from zero to 1 at t = 2010 mins, whilst Fig. 7.11b is an image taken 60 mins after O_2 was introduced to the coating chamber (t = 2070 mins). In Fig. 7.11b an anterior ring of corrosion products can already be seen to be forming at the leading edge of the filament whilst 30 mins later, as shown in Fig. 7.11c, the anterior ring of corrosion products has fully formed. The disappearance of the anterior ring when O_2 is removed form the coating compartment and its subsequent re-appearance when O_2 is re-introduced into the coating chamber confirms that the anterior ring is the result of cathodic activity at the leading edge of the filament.

The experiment shown in Fig. 7.10 and Fig. 7.11 is summarised by the plot in Fig. 7.12. As described above, D_f increased upon the removal of O_2 from the coating compartment by ~120% from *ca.* 180 μm to a constant value of *ca.* 400 μm. From the time-dependent extension of FFC, shown on the same plot, it may be seen that filament propagation is saltatory with step sizes of *ca.* 40 μm when both the coating and defect compartment contain an air atmosphere (pO_2 = 0.2 atm). However, when O_2 is removed from the coating chamber (t = 885 mins) and hence the anterior ring disappears, saltatory propagation ceases and is replaced by a smooth continuous filament propagation. This shows that cathodic activity at the leading edge of the filament does influence disbondment but by hindering it rather than facilitating it as has previously been suggested.[8] However, it does appear that the cathodic anterior ring limits the lateral spread of the filament head.

From Fig. 7.12 it may be seen that although the saltatory propagation disappears when pO_2 = 0 atm in the coating compartment, the velocity of the filament remains

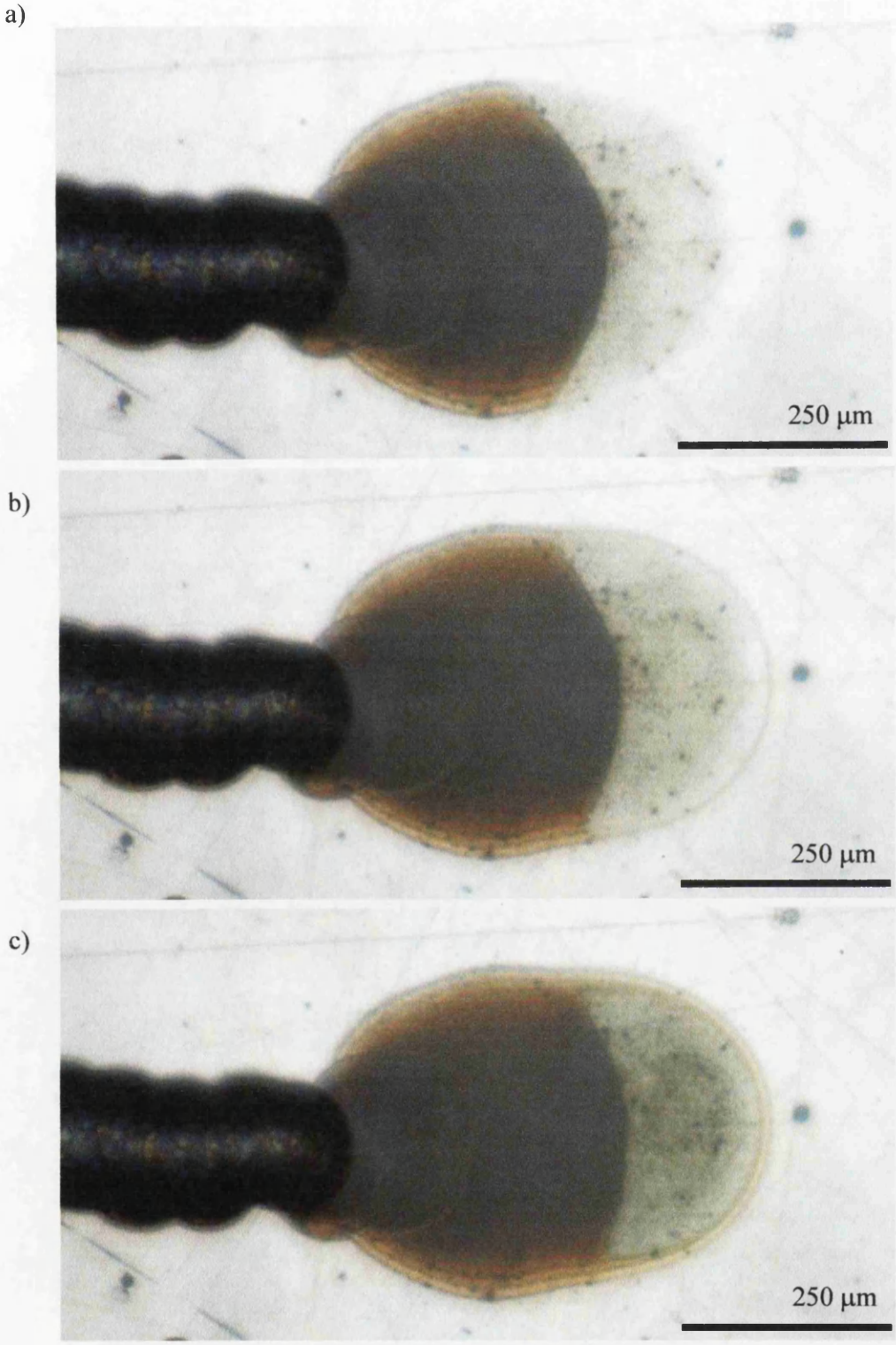

Figure 7.11: Reflective light optical micrographs of an advancing filament head in 93% r.h with defect compartment pO_2 = 0.2 atm. Coating compartment pO_2 key: (a) 0 atm, (b) and (c) are 1 atm. Time key: (a) 2010, (b) 2070, and (c) 2100 mins.

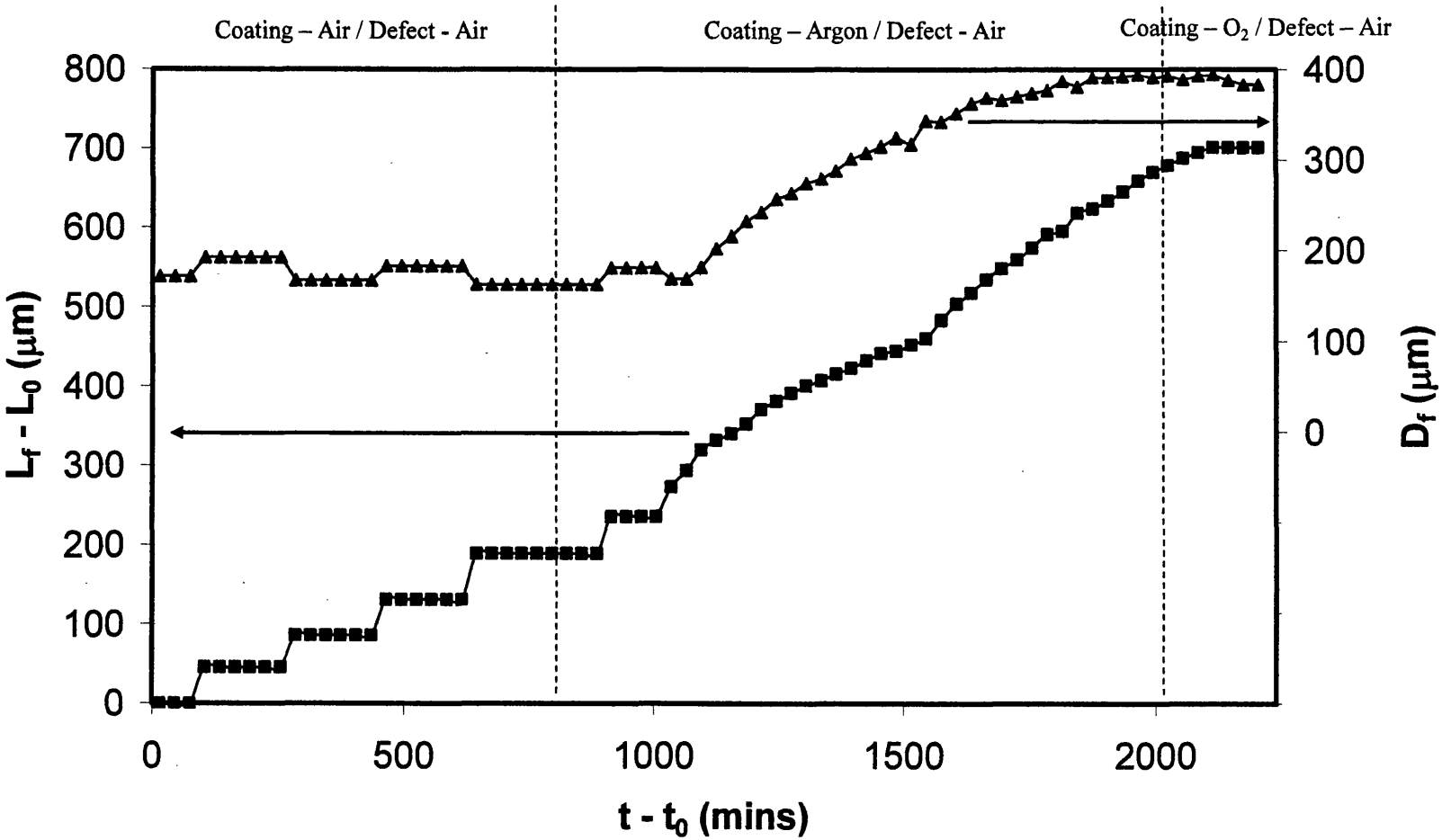

Figure 7.12: Plot of filament length (L_f) *vs.* time (t) and filament width (D_f) *vs.* t since FFC initiation on PVB coated iron for the filament shown in Fig. 7.10 and Fig. 7.11. Gas conditions maintained in each compartment of the dual-compartment cell are shown on the plot. The quantity L_0 is the value of L_f in the first time-lapse image, acquired at time t_0.

constant. This has the important corollary that the through-coating cathodic activity in the filament head does not influence the rate of electrolytic pumping and again, will be discussed further in Chapter 8.

It has already been shown in this section that when O_2 is removed from the coating chamber the filiform head spreads laterally. However, although the filament width appears to have reached a constant value of *ca.* 400 μm it is not entirely apparent whether, without the re-introduction of O_2 into the coating compartment, the removal of the anterior ring would eventually result in the lateral spread continuing to form a fully circular head. In this scenario an asymmetric differential aeration cell may no longer be maintained in the filament head and as a consequence would lead to the possible cessation of FFC and possibly blistering. Therefore, the experiment shown in Fig. 7.10 was repeated but without the re-introduction of oxygen to the coating compartment so that pO_2 remained at zero for the remainder of the experiment. A visual summary of the experiment may be seen in Fig. 7.13. Images (c) to (f) show that the filament continued to propagate for 1750 mins after the removal of oxygen from the coating chamber (at t = 425 mins) before the experiment was stopped to t = 2175 mins. There was no indication of blister formation. After the initial lateral spread of the filament head upon the removal of O_2 from the coating chamber, D_f stabilises and the filament continues to propagate without a visible anterior ring. Fig. 7.14 shows a summary plot of the time dependent extension of the filament and D_f for the same experiment. It may be seen that as with the filament shown in Fig. 7.10, D_f increase by ~100% over the first 500 mins following the removal of oxygen from the coating chamber, from *ca.* 200 μm to *ca.* 400 μm. However, the lateral spread then stabilises and remains relatively constant for the duration of the experiment (1250 mins). Table 7.2 shows that the rates of propagation as determined from Fig. 7.14 are very similar whether O_2 is present in the coating chamber or not. If anything, it appears that the presence of O_2 in the coating chamber, and hence an anterior cathodic ring, slightly reduces the velocity of the filament. However, there is certainly no indication that the cathodic anterior ring increases the velocity of the FFC on iron.

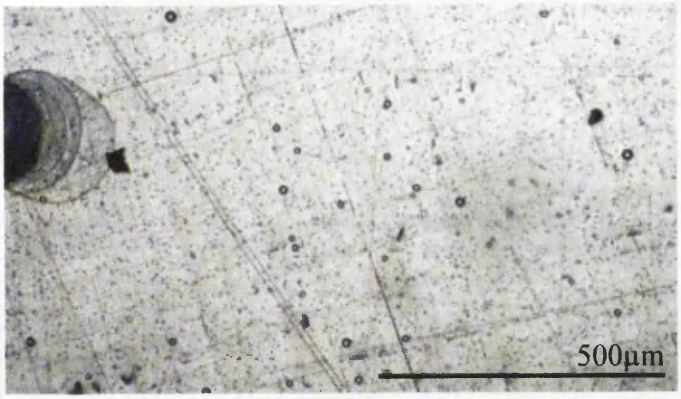

(a) t = 0 min
Coating compartment atmosphere is air
Defect compartment atmosphere is air

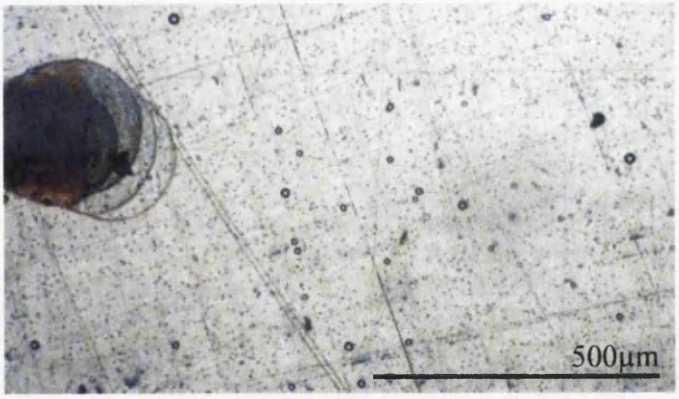

(b) t = 255 min
Coating compartment atmosphere is air
Defect compartment atmosphere is air

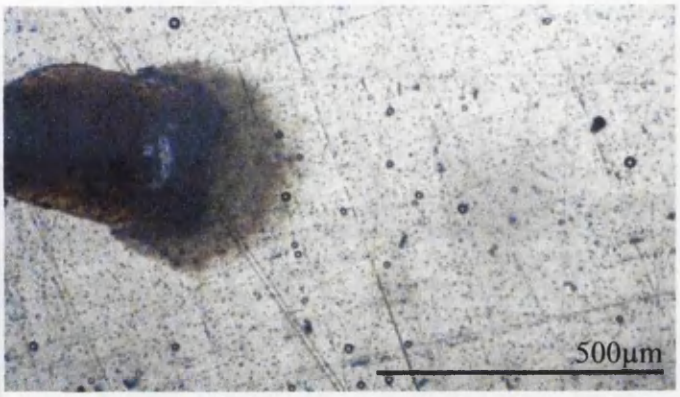

(c) t = 750 min
Coating compartment atmosphere is argon
Defect compartment atmosphere is air

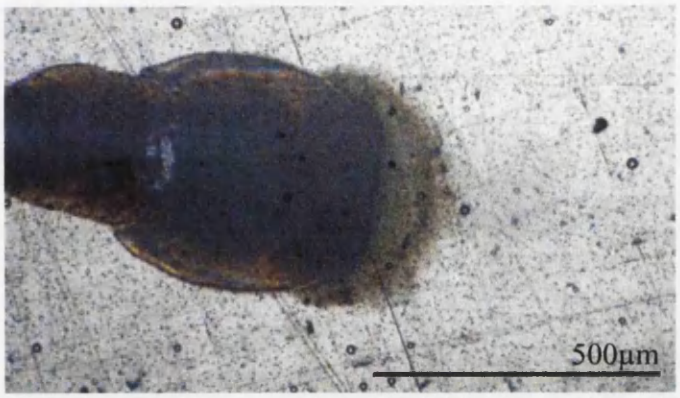

(d) t = 1380 min
Coating compartment atmosphere is argon
Defect compartment atmosphere is air

(e) t = 1800 min
Coating compartment atmosphere is argon
Defect compartment atmosphere is air

(f) t = 2175 min
Coating compartment atmosphere is argon
Defect compartment atmosphere is air

Figure 7.13: Visual summary of time-dependent FFC initiated using 2 µl of aqueous 0.0025 M $FeCl_2$. Defect and coating compartment atmospheres are indicated.

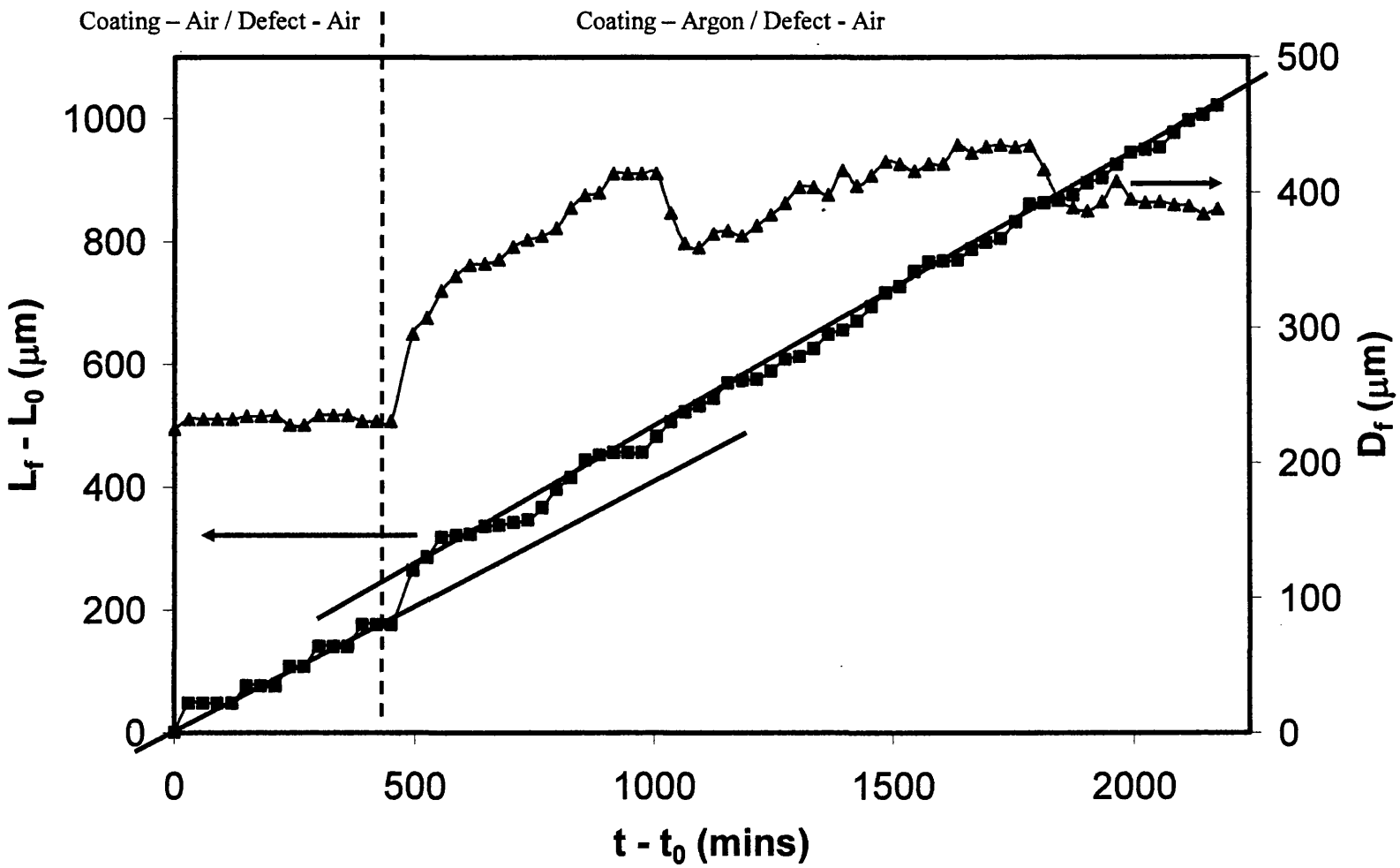

Figure 7.14: Plot of filament length (L_f) *vs.* time (t) and filament width (D_f) *vs.* t since FFC initiation on PVB coated iron for the filament shown in Fig. 7.13. Gas conditions maintained in each compartment of the dual-compartment cell are shown on the plot. The quantity L_0 is the value of L_f in the first time-lapse image, acquired at time t_0.

Table 7.2: Rate of filiform propagation under different coating compartment environments

Coating atmosphere	Defect atmosphere	Rate (μm/min)
Air	Air	0.38
Argon	Air	0.44

7.3.3.3 $pO_2 = 1$ atm

To further investigate the dependence of the propagation rate of FFC on pO_2 in the coating compartment a new experiment was carried out. Fig. 7.15 shows a series of time-lapse images of a filament as pO_2 in the coating department was increased from an initial value of 0.2 atm to 1 atm after 500 mins, whilst pO_2 in the defect compartment was kept at 0.2 atm for the duration of the experiment. It may be seen in Fig. 7.15d that when pO_2 is increased from 0.2 to 1 atm in the coating compartment D_f decreases by a small amount and also that a void appears to form in the centre of the filament. This appearance of the void will be discussed in more detail in the next section. Fig. 7.16 shows a summary plot of the time-dependent extension of a filament and also D_f for the same experiment. The rates of propagation for the filament are shown in Table 7.3.

Table 7.3: Rate of filiform progression different coating compartment environments

Coating atmosphere	Defect atmosphere	Rate (μm/min)
Air	Air	0.39
Oxygen	Air	0.63

It may be seen from Fig. 7.16 that the rate of filiform propagation increases from 0.39 μm/min to 0.63 μm/min when pO_2 is increased to from 0.2 atm to 1 atm in the coating compartment. A decrease in D_f is also observed when pO_2 is increased in the coating compartment. Initially D_f is maintained at *ca.* 200 μm when pO_2 is equal to 0.2 atm in both compartments. However, when pO_2 is increased to 1 atm in the coating chamber D_f is reduced to *ca.* 175 μm. This is consistent with O_2 diffusion through the coating becoming easier and the formation of corrosion products at the filiform edge occurring faster, constraining the lateral spread. An increase of D_f to *ca.* 200 μm does occur

a)

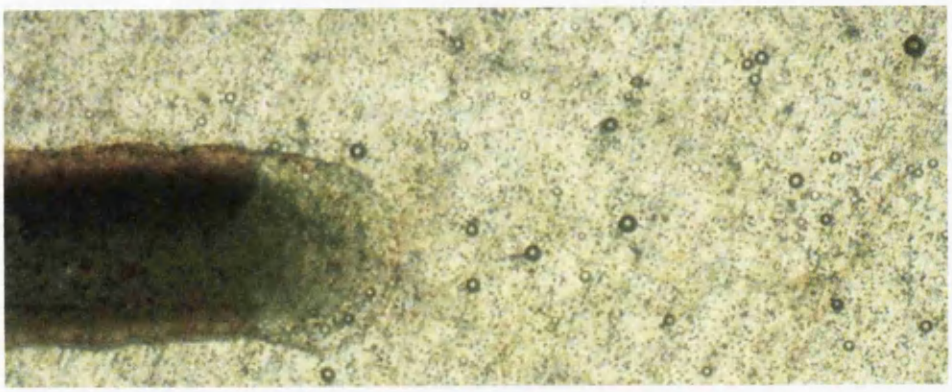

(a) t = 420 min
Coating compartment atmosphere is air
Defect compartment atmosphere is air

b)

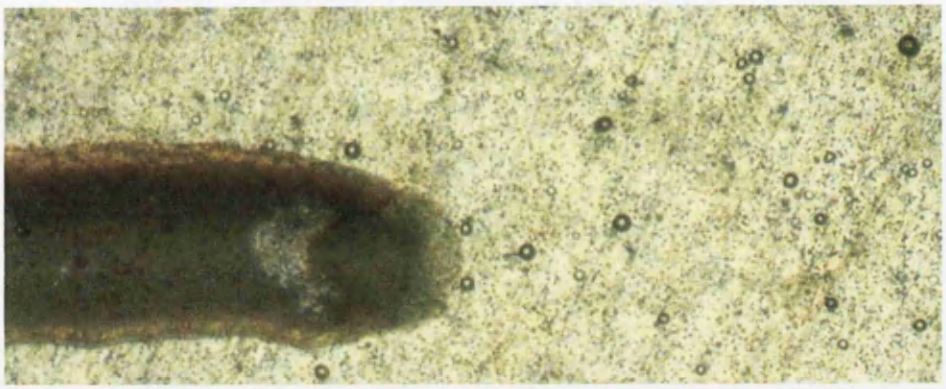

(b) t = 600 min
Coating compartment atmosphere is oxygen
Defect compartment atmosphere is air

c)

(c) t = 1020 min
Coating compartment atmosphere is oxygen
Defect compartment atmosphere is air

Figure 7.15: Visual summary of time-dependent FFC initiated using 2 μl of aqueous 0.0025 M $FeCl_2$. Defect and coating compartment atmospheres are indicated.

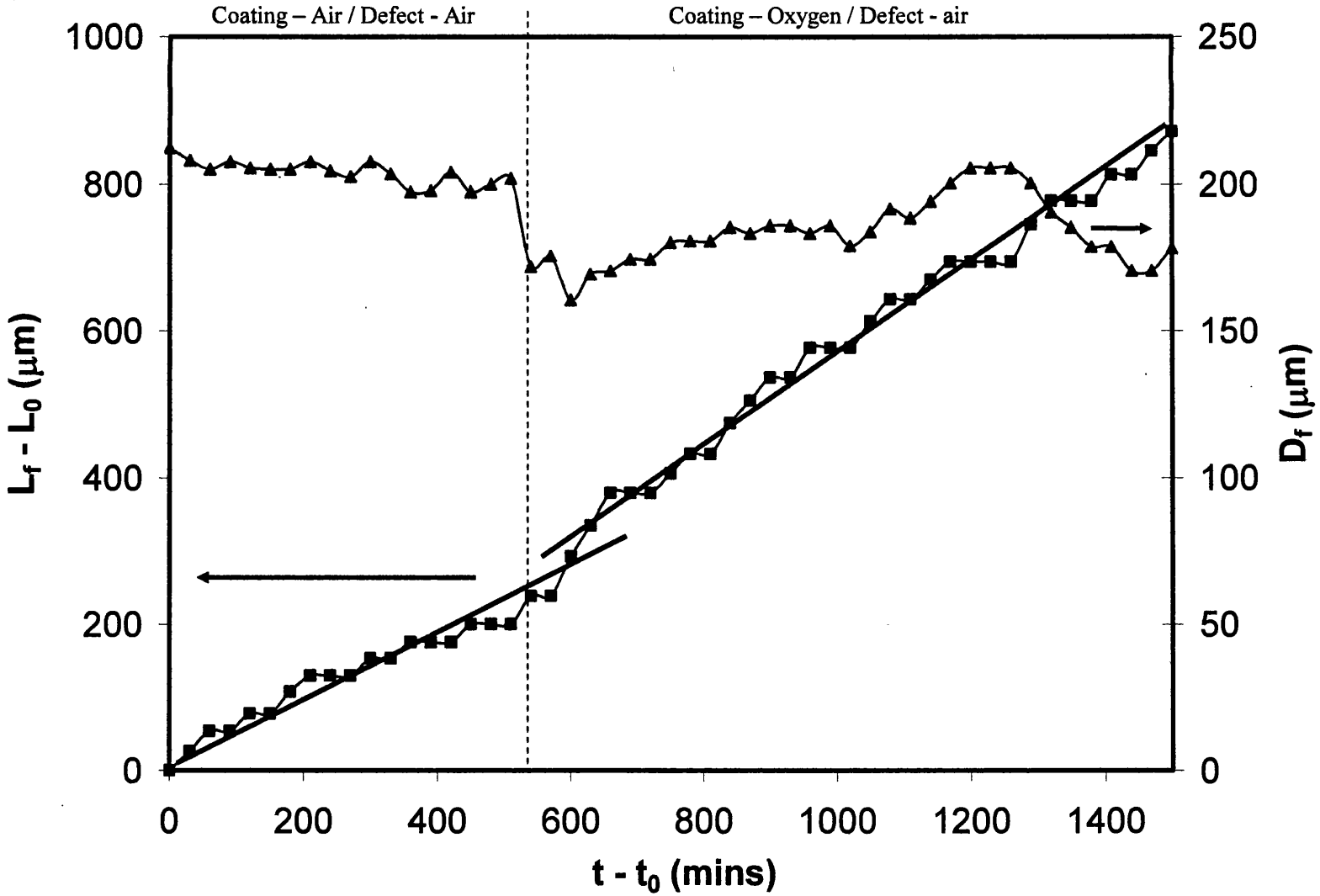

Figure 7.16: Plot of filament length (L_f) *vs.* time (t) and filament width (D_f) *vs.* t since FFC initiation on PVB coated iron for the filament shown in Fig. 7.15. Gas conditions maintained in each compartment of the dual-compartment cell are shown on the plot. The quantity L_0 is the value of L_f in the first time-lapse image, acquired at time t_0

briefly at *ca.* 1200 mins before returning the narrower filiform. It may be that this increase occurred due to a portion of weakly adhered coating. However, typically D_f is less when pO_2 is increased in the coating compartment.

Fig. 7.16 shows that A is proportional to pO_2 in the coating compartment increasing from ~30 μm to 80±30 μm, whilst σ appears to remain independent of pO_2 in the coating compartment, at a value of ~1.15×10^{-2} min^{-1}. This is consistent with more O_2 diffusion occurring at the leading edge of the filament when pO_2 in the coating compartment is increased, and thus faster production of corrosion products. Thus the barrier to filament propagation is greater and so it takes longer for sufficient filament head pressure to develop to breach the ring of corrosion products. Once the ring of corrosion products has been broken the pressure in the head is sufficiently great to disbond more of the coating than when pO_2 = 0.2 atm in the coating compartment, and thus the filament advances in bigger steps.

This experiment has also shown that when pO_2 coating compartment > pO_2 defect compartment the influence that this secondary source can exert will be increased. This may be seen in Fig. 7.16 as an increase in rate. It is possible that this increase in rate is simply a result of decreasing D_f, *i.e.* the anode area in the head is smaller and thus the current density at the anode increases.

7.3.4 Filament Tail Corrosion Products

An interesting observation from the images shown in Fig. 7.15 is the generation of a visible void in the centre of the filament during the experiment. The area where the void is present is shown in close-up in Fig. 7.17. The void develops during the experiment when the atmosphere in the defect compartment is argon, (*i.e.* pO_2 = 0 atm) and pO_2 = 0.2 atm in the coating compartment. That is to say when O_2 is prevented from migrating through the defect along the tail to the head, and is only available from the coating compartment by diffusing directly into the tail or directly into the cathodic area at the back of the head. The filament in Fig. 7.15 also shows a void forms when pO_2 = 1 atm in the coating compartment and pO_2 = 0.2 atm in the defect compartment. The v-shaped boundary at the back of the head is also more pronounced in these images.

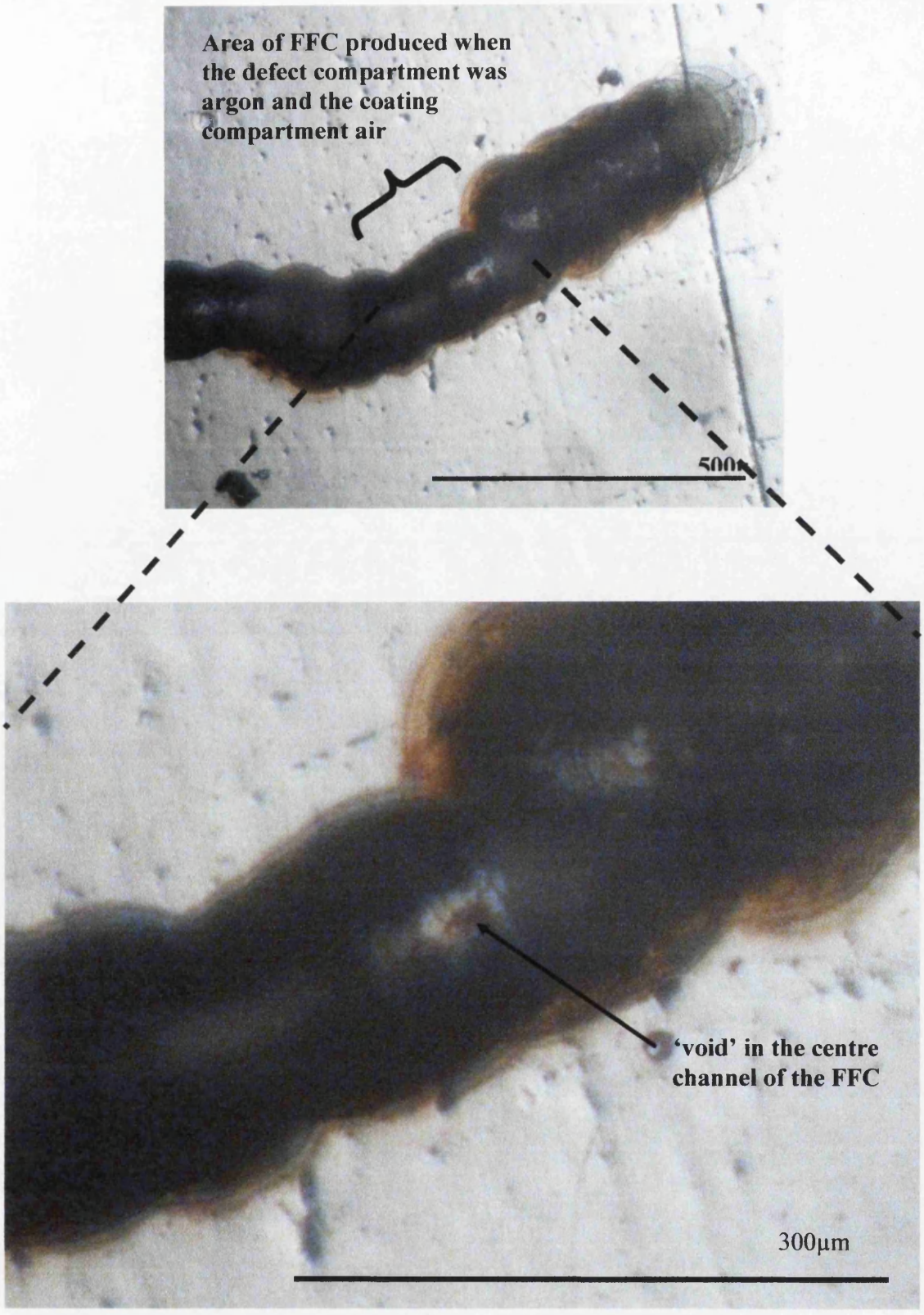

Figure 7.17: Magnified image of FFC. The image shown represents the section of filament tail produced when the defect compartment contained argon (pO_2 = 0 atm) and the coating compartment air (pO_2 = 0.2 atm). A void in the centre of the filiform tail is labeled.

Interestingly though a pattern has emerged where when through coating O_2 diffusion into the tail becomes the dominant (or indeed only in the case of Fig. 7.11) O_2 source a void in the tail representing a porous channel occurs. Clearly from Fig. 7.15 significant visual differences exist between the time that the filament spent with air in the coating compartment and the area where the coating compartment contained oxygen.

Fig. 7.18a shows a close-up image of a portion of the tail when both head and tail sections contained an air atmosphere. Fig. 7.18b is an identically sized portion of the tail but in this instance when this portion was created the coating compartment atmosphere was O_2. The key difference in these images is the apparent concentration of corrosion products seen along the centre of the tail. In Fig. 7.18a, the area has almost full coverage of Fe_2O_3. Based on the progression of the filament this apparently low level of porosity is certainly sufficient to allow oxygen transport. However when considering Fig. 7.18b where the pO_2 level in the head section is raised from 0.2 to 1 the narrow channel along the centre of the filament has visibly increased porosity. In fact the dry corrosion products appear to be of greater concentration at the sides of the filament. This is confirmed by the image analysis shown in Fig. 7.19 where a line of colour intensity is drawn directly through the filament tail sections shown in Fig. 7.18.

Slabaugh[11] suggests that the V-shape boundary that occurs in FFC on iron represents the boundary between ferrous and ferric ions, and forms due to the shape of the roof of the corrosion cell, as illustrated in Fig. 7.20. He proposed that diffusion of equal quantities of atmospheric oxygen through various portions of the film meant that higher oxygen concentrations would be present in the shallow periphery region of the head than at the centre. He further proposed that the conversion of Fe^{2+} to Fe^{3+} would occur more rapidly at the sides of the filament than at the centre leading to a lag in oxidation manifesting itself in a v-shape formation. This is consistent with observation that the v-shape is not observed in coatings under 300 nm thick where the influence of coating thickness would be less.[8] When an increase in pO_2 occurs over the filament tail but not at the break in the coating then the oxidation of Fe^{2+} to Fe^{3+} is going to be more rapid at the edges of the filament. Due to the continual progressive nature of FFC a finite amount of dissolved Fe^{2+} from the anodic reaction for any section of surface area will be produced. Therefore, it is probable that due to the efficiency with which

a)

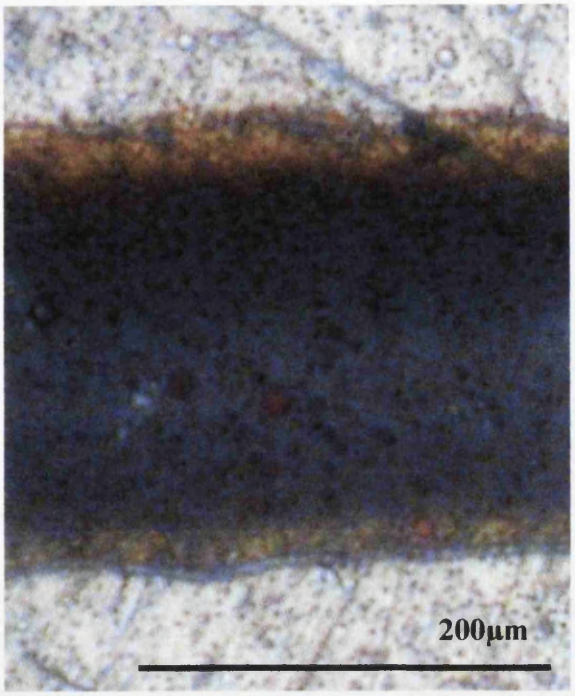

b)

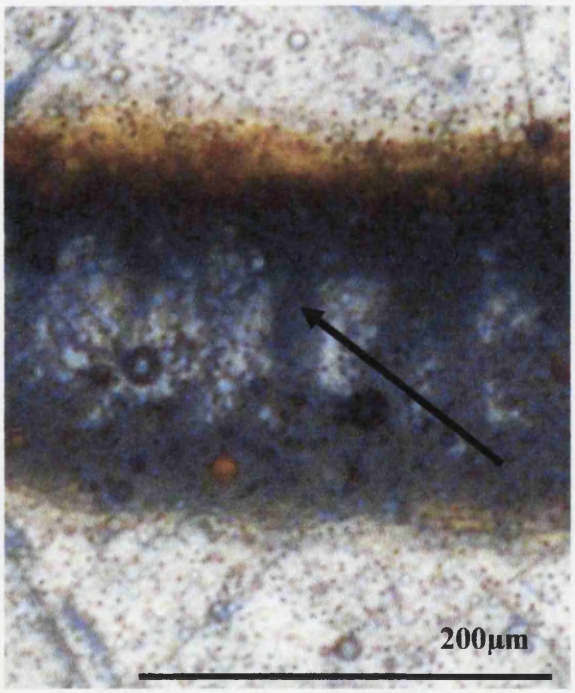

Figure 7.18: Reflective light optical micrographs of two separate sections of a FFC tail. Section (a) produced when the coating and defect sections both contained air and (b) when the coating compartment contained oxygen and the defect compartment contained air

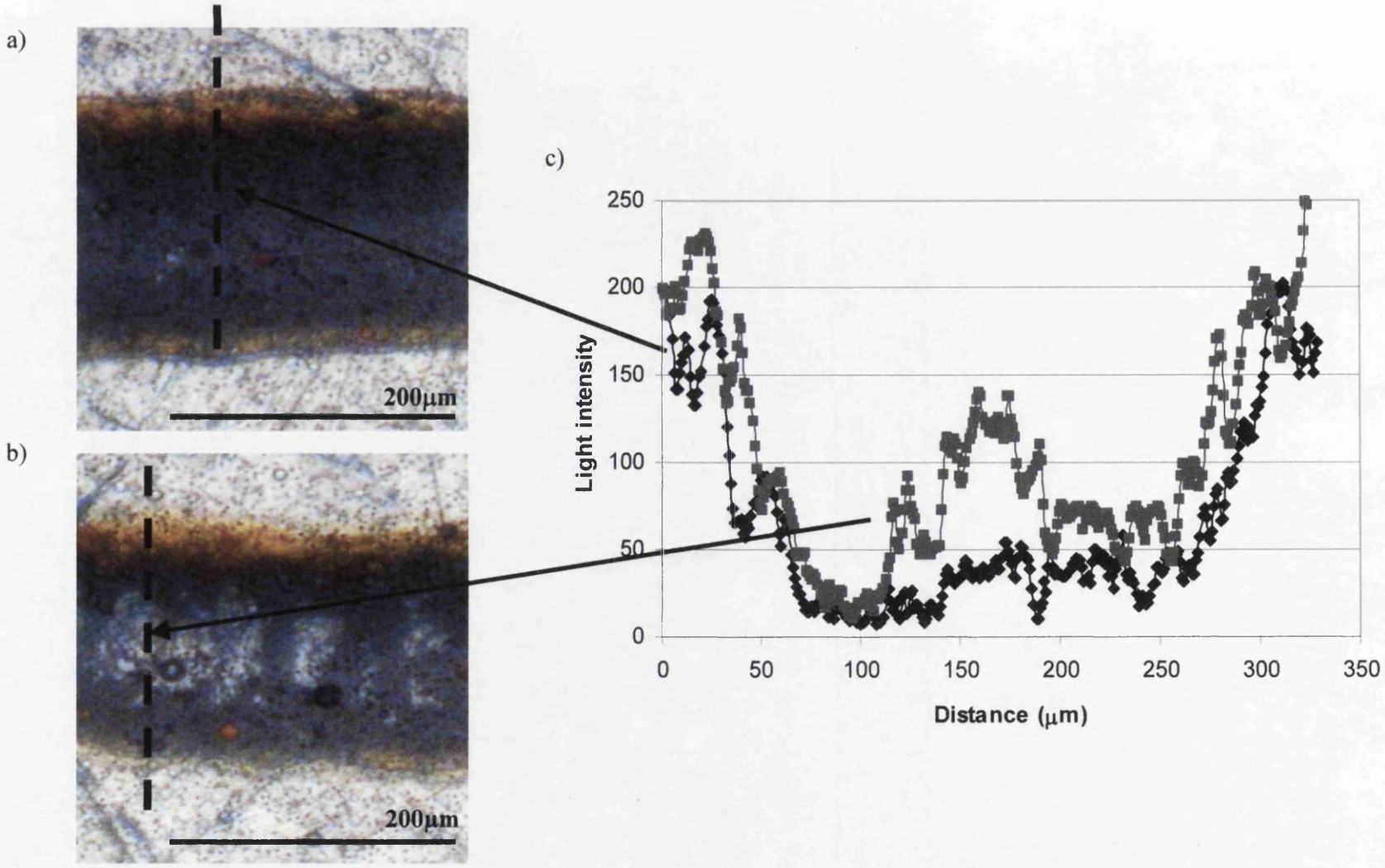

Figure 7.19: Images a) and b) are as shown in Fig. 7.17. The plot shown in c) is light intensity measurements taken across the filament tail sections. Image (b) shows an area of higher light intensity at the centre of the line. This indicates a 'lighter' region and infers the absence of corrosion products.

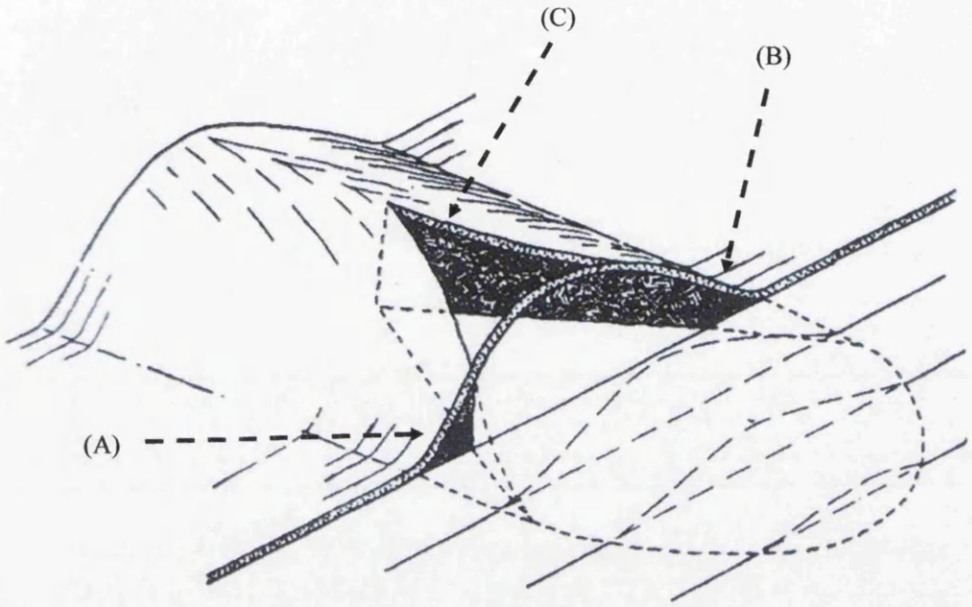

Figure 7.20: Roof of a filiform corrosion cell as proposed by Slabaugh *et* al.[17] Diffusion of equal quantities of atmospheric oxygen through various portions of the film mean that higher oxygen concentrations would be present in the shallow periphery regions of the head (A and B) than at the centre (C).

oxidation of Fe^{2+} to Fe^{3+} occurs at the periphery of the filament at increased atmospheric pO_2, Fe^{2+} will become quickly depleted (at the periphery) leading to a visibly porous central channel.

7.4 Conclusions

- A novel experimental (Watson-Coleman) dual-compartment cell has been developed enabling the separation of head and tail sections of FFC. The cell was successfully used to expose each section of the filament to different pO_2. Combined with *in-situ* time-lapse photography a study of the effect of gas composition on FFC propagation has been made.

- By varying gas composition in the coating compartment FFC was shown to propagate in a saltatory manner when $pO_2 \geq 0.2$ atm. The saltatory progression of FFC appears to occur due to the formation of a cathodic anterior ring of corrosion products formed by through coating O_2 diffusion at the leading edge of the filament head. The anterior ring temporarily halts filament progression and creates a step-wise growth of the filament. This is suggestive of a mechanism whereby filament advancement is due to a build-up of pressure in the filament head. It was also shown that the amplitude (step-size), A, of filament advancement was proportional to pO_2 in the coating compartment with increasing pO_2 increasing A. Conversely, the frequency of saltation was found to remain constant.

- When O_2 is removed from the coating compartment the cathodic anterior ring disappears resulting in a lateral increase in filament width. However, there is no corresponding decrease in the rate of propagation – indicating that cathodic disbondment of the organic coating by the anterior ring is not rate determining for filament growth. Conversely, filament width is dependent on pO_2 in the

coating department which indicates that cathodic O_2 reduction is important in limiting the lateral spread of the electrolyte droplet.

- Oxygen transport from the initiating defect and along the filament tail was found to be the primary mode of oxygen supply to the filament head. However, it was also shown that when FFC is occurring under an oxygen permeable coating FFC propagation may still be maintained by through coating O_2 diffusion into the filament tail. However, the rate of propagation was significantly reduced when oxygen supply from the initiating defect was completely removed.

7.5 Further Work

In the introduction to this Chapter three possible mechanisms for the advancement of FFC on iron were given. It has been shown that the rate limiting process for FFC propagation on iron is not cathodic disbondment by an cathodic anterior ring. The saltatory propagation mechanism shown by the filiform indicate that anodic dissolution is also not the primary mechanism of filament advancement. However, the visual evidence shown in Fig. 7.2 of the saltatory propagation of FFC indicates that filiform head pressure may have a strong influence on disbondment. To investigate this phenomenon further it is proposed that the dual-compartment cell is modified to allow the pressure in the coating compartment to be controlled and hence the pressure in the filiform head directly measured. This is examined in more detail in Chapter 8.

7.6 References

1. C. F. Sharman, *Nature*, **153**, 621 (1944).
2. R. T. Ruggeri and T. R. Beck, *Corrosion-NACE*, **39**, 452 (1983).
3. A. Bautista, *Prog. Org. Coat.*, **28**, 49 (1996).
4. G. M. Hoch, *NACE*, 134 (1974).
5. K. R. Trethewey and J. Chamberlain, Corrosion for Science and Engineering, (1988).
6. W. Funke, *Ind. Eng. Chem. Prod. Res. Dev*, **24**, 343 (1985).
7. W. Funke, *Prog. Org. Coat.*, **9**, 29 (1981).
8. P. P. Leblanc and G. S. Frankel, *J. Electrochem. Soc.*, **151**, B105 (2004).
9. H. J. W. Lenderink, *PhD. Thesis* (1995).
10. M. Van Loo, D. D. Laiderman and R. R. Bruhn, *Corrosion*, **9**, 277 (1953).
11. W. H. Slabaugh, W. Dejager, S. E. Hoover and J. Hutchinson, *Paint Tech.*, **44**, 76 (1972).
12. T. Watson, EngD. Thesis, University of Wales - Swansea, 2006
13. H. Kaeshe, *Werks. Korros.*, **10**, 668 (1959).
14. Morita J and Y. M, *Corrosion*, **50** (1994).
15. W. H. Slabaugh and M. Grotheer, *Ind. Eng. Chem.*, **46**, 1014 (1954).
16. N. LeBozec, D. Persson, A. Nazarov and D. Thierry, *J. Electrochem. Soc.*, **149**, B403 (2002).

Chapter 8

Time-lapse Investigation of FFC on Iron – Effects of Gas Pressure

8.1 Introduction

In Chapter 7 a specially designed dual-compartment (Watson-Coleman) cell was used to investigate filiform corrosion (FFC) occurring on organically coated iron. Experiments carried out using the cell showed that the gas supplied to the FFC head electrolyte through the tail (defect compartment) could be controlled separately from the gas in the environment surrounding the head (coating compartment) outside of the organic coating. Time-lapse microphotography was used to show that FFC on iron occurs in a saltatory fashion when the coating compartment is exposed to an environment containing O_2. A postulation was made whereby through coating O_2 diffusion from the coating compartment and subsequent reduction precipitated an anterior ring of corrosion products. Furthermore, the anterior ring periodically contained the filament head electrolyte until sufficient pressure was produced in the head electrolyte to breech the anterior ring of corrosion products and allow the filament to propagate forwards. These notions necessarily give rise to a question as to the mechanism(s) by which filament head pressure may be produced.

Ruggeri and Beck[1] have previously suggested that filiform head pressures may be produced from osmotic or electroosmotic (EO) processes occurring in the filament. They noted a number of problems with the osmotic model on iron, primarily with the composition of the necessary semi-permeable membrane for which there is no obvious candidate iron compound. However, they were unable to examine the EO model due to the lack of available quantitative data or mathematical models at the time. Such data and such models have recently become available as a result of interest in EO pumps for microfluidic applications.[2-9]

EO pumps are suitable for microfluidic applications because they can be made very compact and deliver high pressures.[3,4] Moreover, they can produce a pulse-free flow without containing any moving parts. EO micropumps have been shown to generate pressures > 550 bar[7] or flow rates > 1 μl/min.[9] This has enabled the miniaturization of High Performance Liquid Chromatography (HPLC) systems,[7] cooling of microelectronics,[5] and actuation of microscale mechanical components.[6] Electroosmotic flow (EOF) in porous matrices has been used in a variety of applications, including

capillary electrochromatography,[8] and microfluidic pumping.[3,4,7,9] Perhaps most importantly regarding FFC, EO pumps based on porous structures have been shown to produce very high pressures with simple geometries.[3,9]

With the developments in EO pumps the time seems ripe for a reappraisal of FFC mechanisms in light of EO pump theory. It also seems appropriate to design experiments by means of which EO theory may be tested in the context of FFC.

In this chapter the Watson-Coleman cell is used in a modified form to apply a differential gas pressure between the coating and defect cell compartments, in such a way as to oppose FFC coating delamination. The characteristics, dimensions and propagation kinetics of FFC filaments are followed as a function of differing gas pressure using *in-situ* time-lapse microphotography. The initial aim of this work was to ascertain whether iron FFC exhibited a pressure dependence which was explicable in terms of pressure – flow rate relationships derived by researchers in the field of electroosmotic pumping. However, it became a further aim to measure or predict the maximum pressure developed by iron FFC – with a view to determining the likely importance of mechanical coating disbondment in FFC.

8.2 Experimental

Iron foil (99.9% Fe) of 1.5mm thickness was supplied by Goodfellow Cambridge Ltd. All other chemicals were supplied by Sigma Aldrich Ltd. All experiments were initiated with 2µl of $FeCl_2$ aqueous solution (0.0025 M and 0.025 M). A detailed description of the FFC initiation method and the experimental technique can be found in Section 2.10. Once FFC was initiated a glass dome was placed over the top and sealed to separate a "head" and a "tail" section of the filament as described in Section 2.10. This is shown photographically in Fig. 8.1 where several exposed filiform "heads" can be seen on the left side of the image.

The dual compartment (Watson-Coleman) cell (shown in Fig. 8.2) employed in these experiments was the same as that described in Section 2.10 but with a modified setup being used. This is shown schematically in Figure 8.3. For the experiments in this Chapter the exit line of the coating compartment is connected to a manometer (SPER

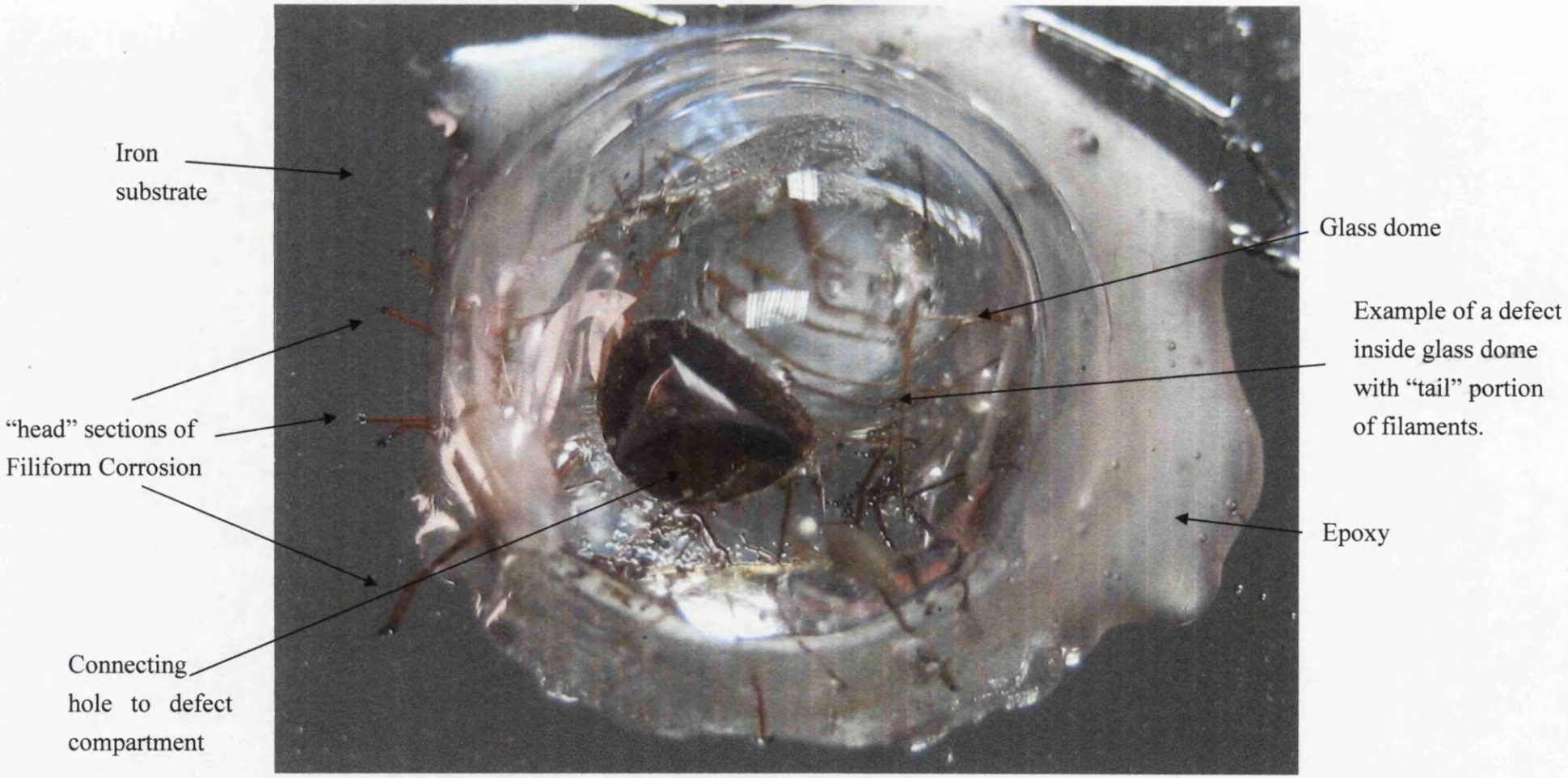

Figure 8.1: Photographic image the iron substrate with overlying glass dome. Exposed filiforms may be seen on the left of the image and the connecting hole to the lower (defect) compartment is visible in the centre of the dome.

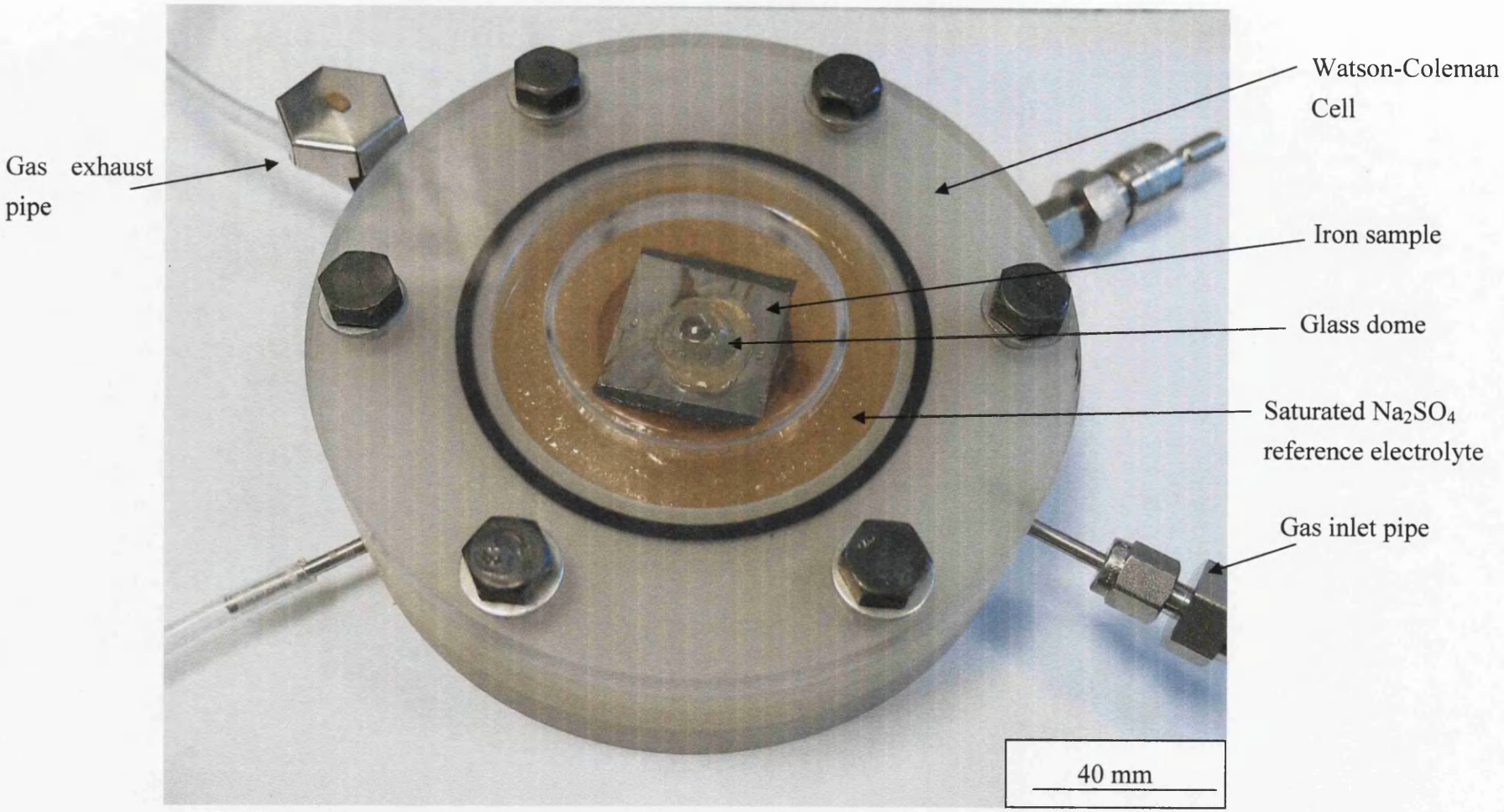

Figure 8.2: Photographic image of the Watson-Coleman cell set-up during an experiment. The iron sample and glass dome shown in Fig. 8.1 may be seen in the centre of the cell.

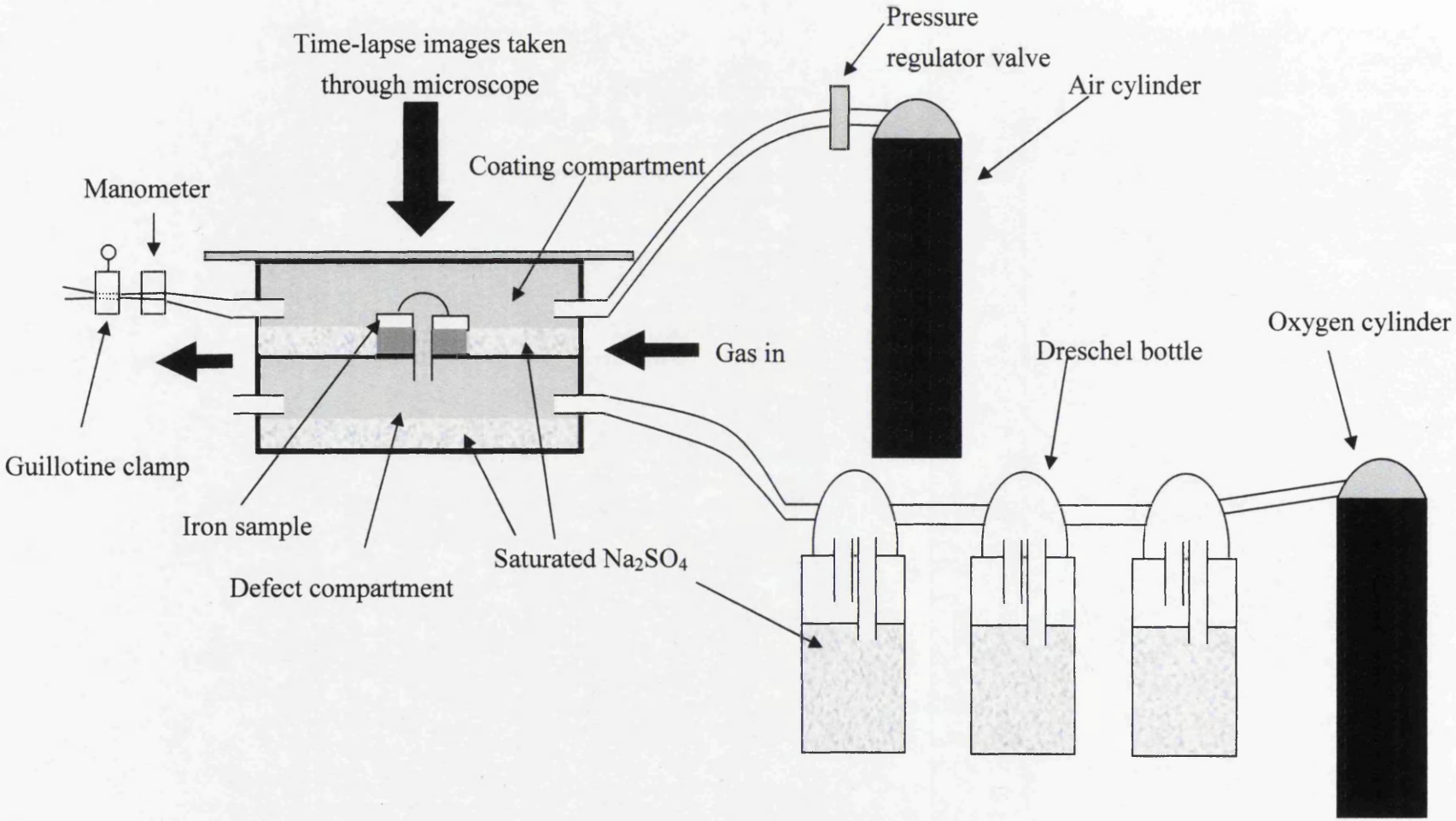

Figure 8.3: Schematic diagram of the experimental setup for FFC pressure experiments using the Watson-Coleman cell. A pressure regulator is used to control pressure in the coating compartment and is measured on the exit pipe using a manometer.

Scientific 100 PSi) before being almost completely shut-off using a guillotine clamp, allowing only a minimal gas flow. Due to the need to produce pressures in the coating compartment the dreschel bottles previously used were removed and the cell was connected directly to the gas cylinder. This could be done as there was a minimal flow of gas and thus maintaining humidity in the coating compartment could be achieved by just the saturated well of Na_2SO_4 reference electrolyte in the coating compartment. In this setup a pressure valve on the gas cylinder was used to incrementally increase the pressure in the coating compartment which was accurately determined using the manometer. The Watson-Coleman cell was designed to be able to function over a pressure range of 0-6 bar (0-87 psi) and constant pressures were accurately maintained (± 0.1 bar) at any pressure value in this range. The cell was rigorously and consistently checked for leaks throughout the duration of the experiment and thus it was ensured that the saturated Na_2SO_4 reference electrolyte in the top chamber remained hydrated so that a constant relative humidity (r.h.) of 93% was maintained throughout the duration of the experiment.

Throughout the experiment humidified oxygen (93% r.h.) was supplied to the defect compartment. Oxygen was used rather than air for the defect compartment as filaments were found to be more robust during the experimental setup when O_2 was used.

Images of the filiform head were taken *in-situ* at 15 minute intervals using a Nikon Coolpix 4500 digital camera adapted for use with a Meiji light microscope. The visual images produced were subjected to computerised digital image analysis as described in Section 2.10.3.

8.3 Results

Typical time-lapse images of a filament during a pressure experiment, where FFC was initiated with 0.025M $FeCl_2$, are shown in Fig. 8.4a and b. The maximum backpressure applied to the filament was 4 bar, where backpressure ΔP = pressure in the coating compartment – pressure in the defect compartment. Fig. 8.4b shows the filament at t= 810 mins, after ΔP was increased rapidly from 0 to 4 bar at t = 330 mins. The filament width, D_f (determination of filament width is shown in Section 2.10.3) is shown to sharply decrease with the increase in ΔP. Fig. 8.5b is a summary plot of filament

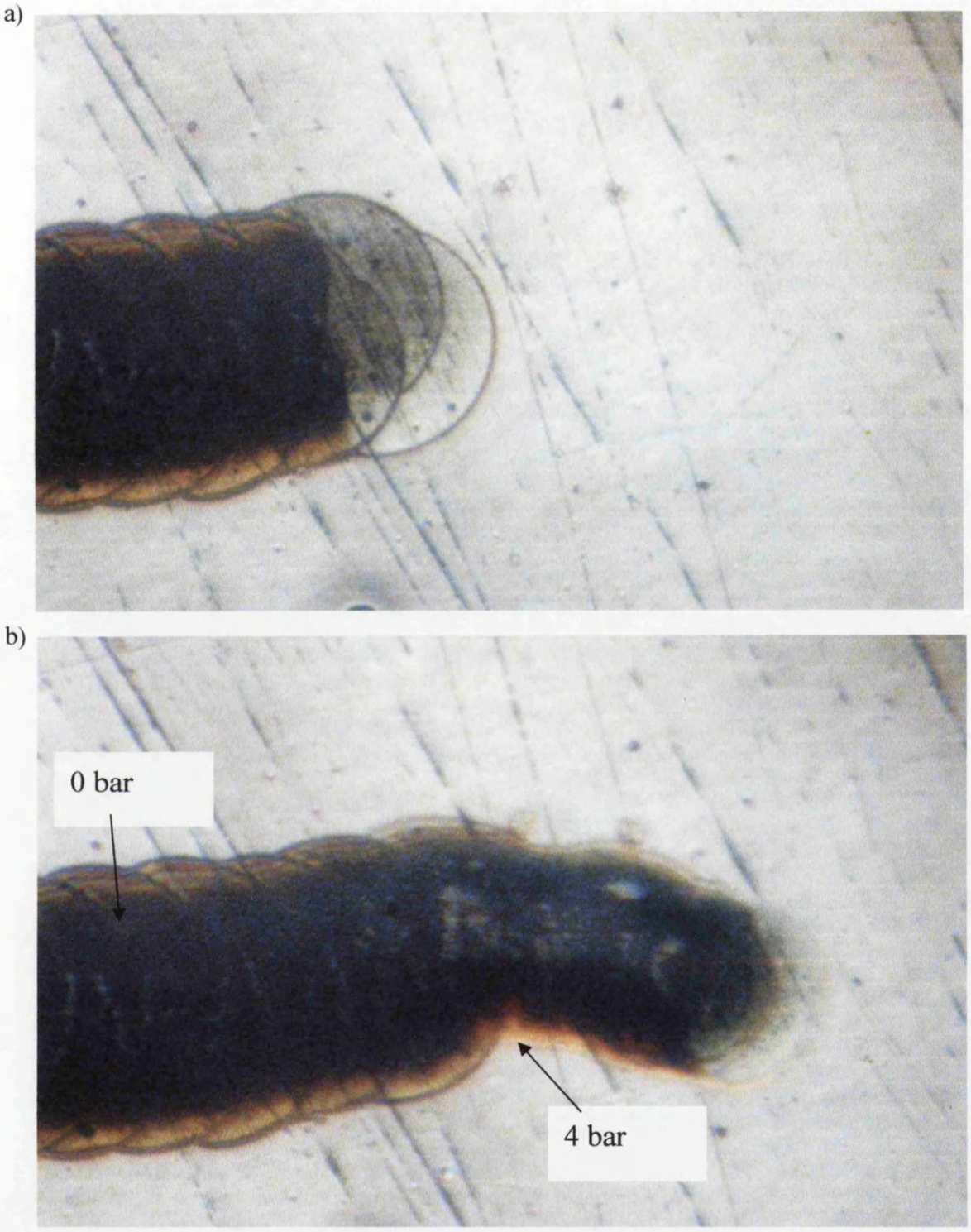

Figure 8.4: Visual summary of time-dependent filiform propagation with an incremental pressure increase in the coating compartment from 0 Bar – 4 Bar where there is a rapid decrease in filament width, D_f. Time / Pressure key: a) 300 min / 0 bar, and b) 810 min / 4 bar.

a)

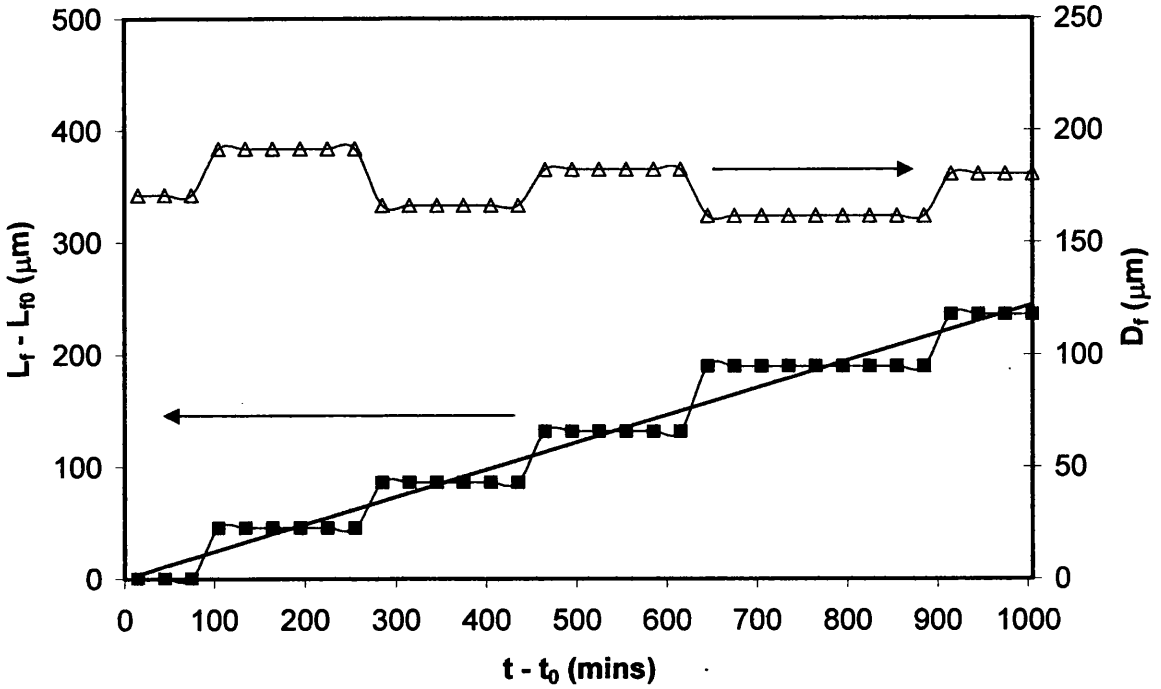

b)

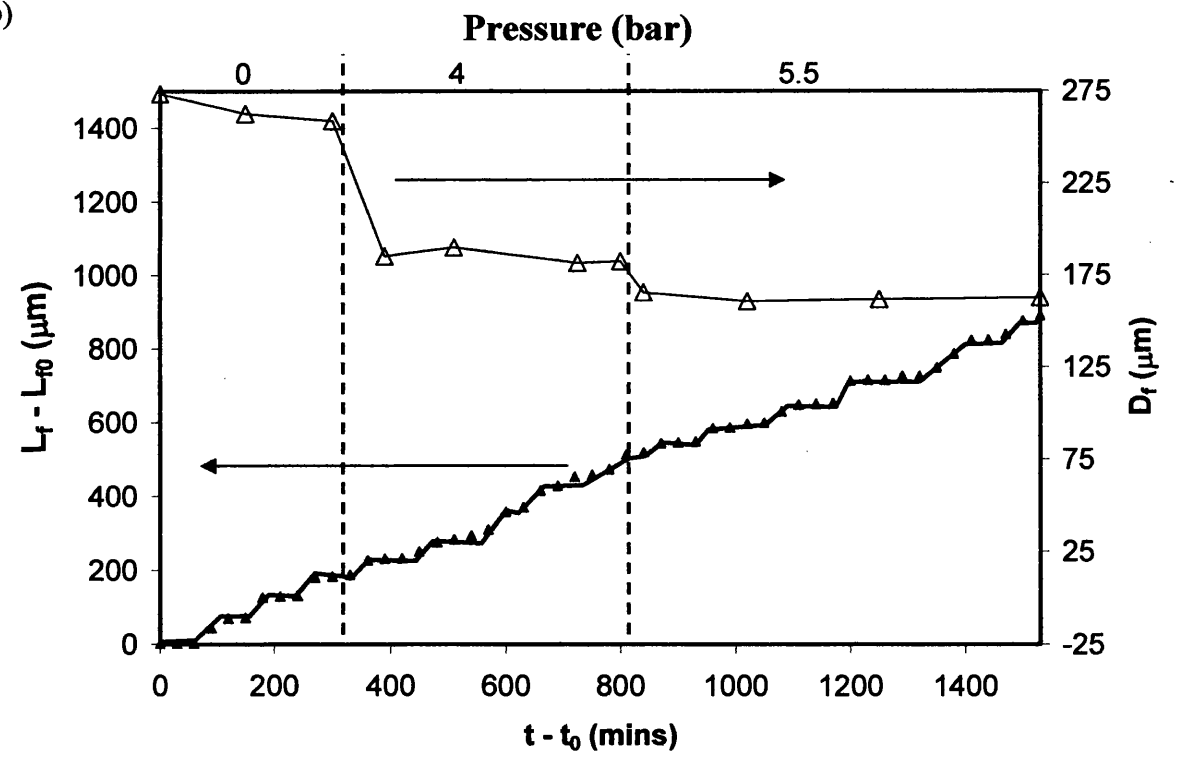

Figure 8.5: Plot of filament length (L_f) *vs.* time (t) and filament width (D_f) vs. t since FFC initiation on PVB coated iron a) FFC initiated with 0.0025 M $FeCl_2$, no backpressure and b) from Fig. 8.7 (a-c) where FFC was initiated with 0.025 M $FeCl_2$, backpressure applied indicated on plot. The quantity L_0 is the value of L_f in the first time-lapse image, acquired at time t_0.

extension, L_f, plotted *vs.* time, t, and also D_f plotted *vs.* t. In Fig. 8.5a, a typical filament from Chapter 7 is shown. This plot is shown as a reminder of the saltatory propagation mechanism, the constant rate of propagation and the constant value of D_f for FFC on iron. It should be noted that the propagation rate of this filament is slower because it was initiated with a less concentrated (0.0025 M) $FeCl_2$ electrolyte and also because gas conditions of pO_2 = 0.2 atm were present in both the coating and defect compartments. In both (a) and (b) the quantity L_{f0} is the value of L_f in the first time-lapse image, acquired at time t_0.

In Fig. 8.5b ΔP in the coating compartment at t is also indicated on the plot. From this plot it is clear that with each increase in ΔP there is a corresponding decrease in D_f. It must be remembered that as ΔP increases in the coating compartment so the pO_2 of oxygen will increase in the coating compartment and at 5 bar will be, pO_2 = 1 atm. Chapter 7, Fig. 7.16 shows that a small decrease (~25 μm) in D_f occurs when pO_2 was increased from 0.2 to 1 in the coating compartment; probably as a result of the faster production of the cathodic anterior ring of corrosion products. However, the decrease in D_f observed with increasing backpressure ΔP is much greater (~75 μm) when ΔP is increased from 0 to 4 bar (pO_2 increased form 0.2 to 0.8 atm). Therefore, as ΔP is increased in the coating compartment, although a contribution to the reduction in D_f is probably due to the increase in pO_2, the larger proportion appears to be as a direct result of the backpressure ΔP applied to the filament.

It is also evident from Fig. 8.5b that there is no change in the rate of propagation, dL/dt, (which is constant at 0.72 μm/min), period, T, amplitude, A, or the frequency of saltation, σ, of the filament as ΔP is increased. [note: the variables A, T and σ are defined in Chapter 7, Fig. 4]

As ΔP is increased the volume of free electrolyte that exists in the filament head appears to decrease. This is shown in Fig. 8.6(a-c) which shows a series of images of a filament head as pressure is increased. Pressure key: (a) 0 bar, (b) 4 bar and (c) 5.5 bar. Here, the tail separation between the front ring and the corrosion products in the tail of the filament can be seen to decrease with increasing ΔP, i.e. the volume of free electrolyte in the filament head is decreasing.

a)

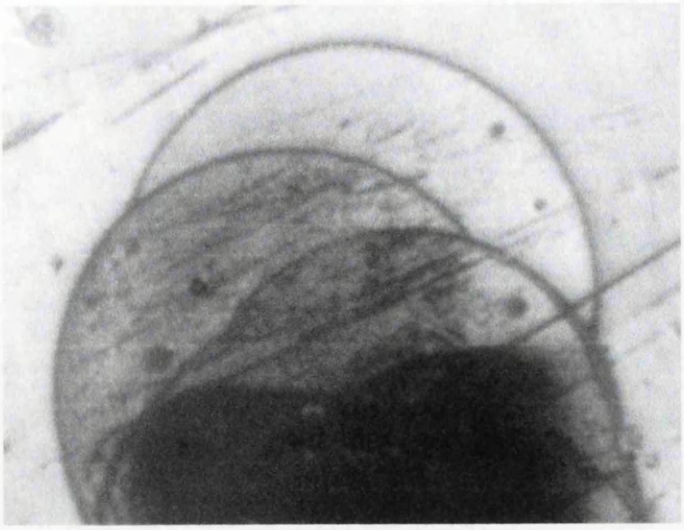

b

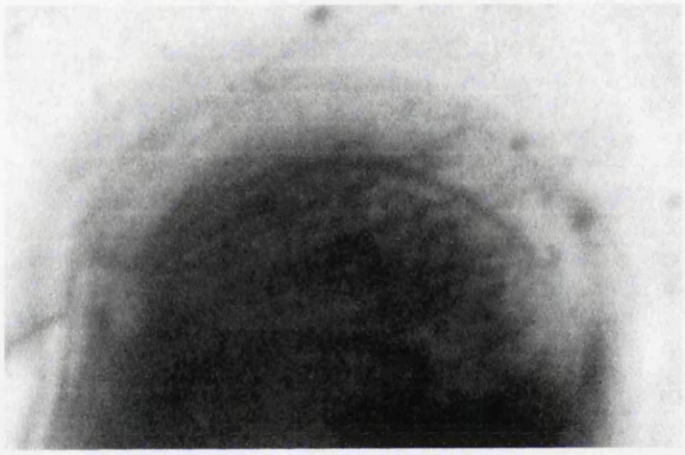

c)

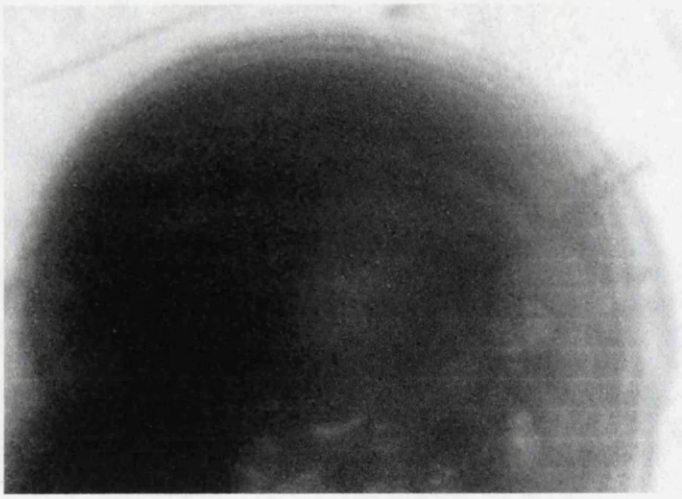

Figure 8.6: Filament head close-up images. Backpressure key: a) 0 bar, b) 4 bar and c) 5.5 bar.

8.4 Discussion

As discussed in the introduction a number of models have been suggested as the propagation mechanism for FFC on iron. In Chapter 7 cathodic disbondment was shown not to be the rate determining step but rather that an anterior ring of corrosion products appeared to periodically constrain the head electrolyte producing a saltatory filament propagation mechanism. The only viable reason for this saltatory propagation was that a pressure build-up was occurring in the head electrolyte until sufficient pressure had been achieved to breach the anterior cathodic ring of corrosion products. Once breached the pressure in the head would immediately decrease in the head and the process would repeat itself. The results described in the above section show that FFC on iron can continue to propagate even when backpressure of $\Delta P = 5.5$ bar is applied to the filament head in the coating compartment. In the sections below two possible mechanisms that have previously been suggested by Ruggeri and Beck[1] are considered that could provide filiform head pressure and their relative merits considered.

8.4.1 Osmotic Pressure Model

A schematic diagram of a filament where the head electrolyte pressure is controlled by osmosis is shown in Fig. 8.7. In this scenario a semi-permeable membrane is implicit and would separate the anode and cathode of the electrochemical cell. The semi-permeable membrane must allow the passage of water whilst preventing the passage of iron(II) chloride (*i.e.* the head electrolyte) into the tail section. The cathode where oxygen reduction would occur would exist immediately behind the semi-permeable membrane in a hydrated portion of the tail and thus in electrical contact with the head.

In this scenario and at equilibrium the filament-head electrolyte and reference solutions are isopiestic, *i.e.* their concentrations will be such that they exhibit an equal vapour pressure (of water)[10-14] and hence water activity a_w[10] so that,

$$\text{Head } a_w = a_w \text{ Ref} \tag{8.1}$$

whilst osmolality in both the head electrolyte and reference electrolyte will be

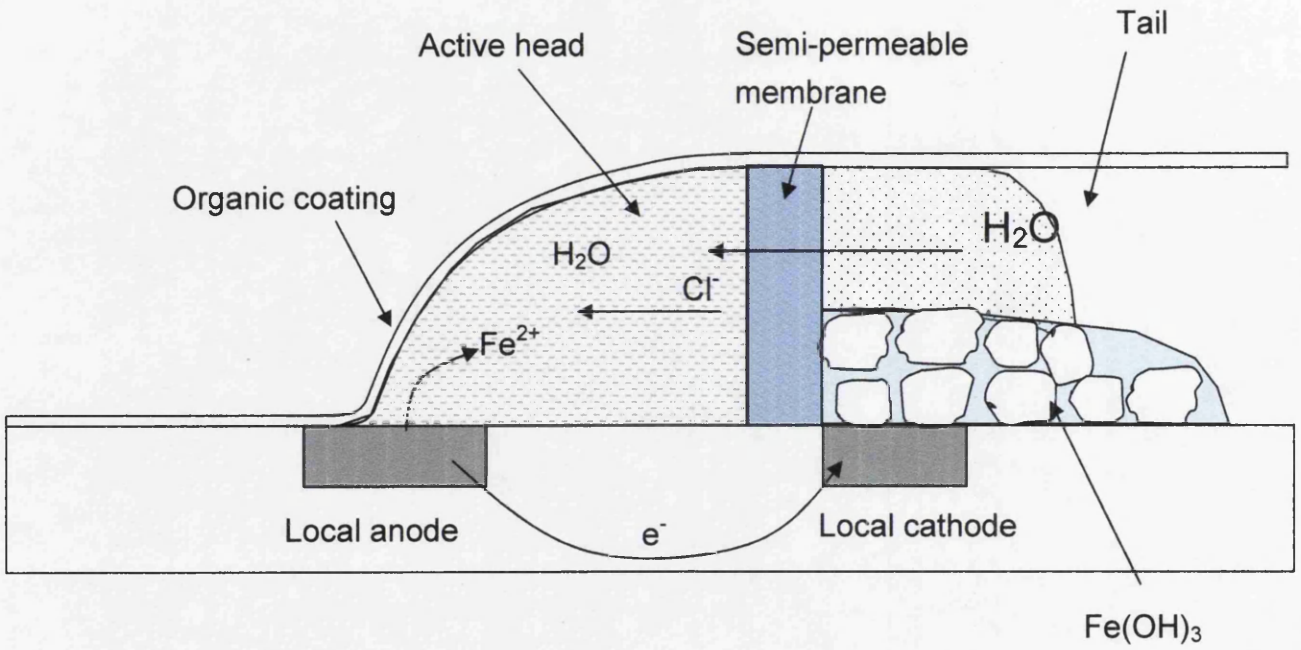

Figure 8.7: Schematic diagram of filiform corrosion occurring on organically coated iron where filament head pressure is controlled by osmosis.

approximately equal.,

$$\text{Head osmolality} \approx \text{Ref osmolality} \tag{8.2}$$

Under these equilibrium conditions it is possible to make an estimate of the osmotic pressure Π that would be attainable in a filiform head if the pressure in the head was maintained by an osmotic process. Osmotic pressure may be determined using the van't Hoff equation[15]

$$\Pi V = n_B RT \tag{8.3}$$

where V is the volume of electrolyte and n_B is the amount solute, R is the gas constant in terms of pressure = 8.31 x 10^{-2} l atm/K, and T is the absolute temperature. However, this may be rearranged using $n_B/V = [B]$, where [B] is the molar concentration of the solute, to give a simpler form of Equation (8.3),

$$\Pi = [B]RT \tag{8.4}$$

As at equilibrium filament-head electrolyte and reference solutions are isopiestic, the concentration of Na_2SO_4 in the reference electrolyte will be equal to the solute concentration in the head. The solubility of Na_2SO_4 in water at 20°C is 280g/l which equates to 2.6 mols/l.[16] Na_2SO_4 is a colligative compound so its osmalality when fully disassociated into its ions of, two Na^+ cations and one SO_4^- anion, will be 3 osmoles. Therefore for the 2.6 mols/l of Na_2SO_4 present there will effectively be 7.8 osmoles of ions affecting the osmotic pressure. From Equation (8.4) the osmotic pressure that could be produced in a filament head at 20°C would be,

$$\begin{aligned} \Pi &= 7.8 \times \left(8.31 \times 10^{-2}\right) \times 293 \\ \Pi &= 189 \text{ bar} \end{aligned} \tag{8.5}$$

Therefore, in principal, the osmotic model is sufficient to explain the result shown in Fig. 8.4 and Fig. 8.5 where a filament is shown to still propagate even with backpressure ΔP = 5.5 bar.

However, there is a fundamental problem with this model, *i.e.* what is the semi-permeable membrane and where exactly would it be positioned? Iron hydroxide seems to be the only possible material that could be considered for use as a semi-permeable membrane. However, as Ruggeri and Beck[1] state, "the membrane would have to be impermeable to iron(II) chloride (*i.e.* the head electrolyte) and it is difficult to see how this would be so when iron(III) chloride and hydroxychloride products are known." The authors also suggest an alternative semi-permeable membrane as air, where water may pass as vapour but organic salts may not. Again, they discard this idea due to the low mobility of chloride ions in the nearly dry solution immediately adjacent to the membrane (air).

Therefore, without a suitable semi-permeable membrane the osmotic model is not capable of producing the high pressure that has been shown to exist in a fialment head. However, Ruggeri and Beck[1] suggest another mechanism where the problem of a semi-permeable membrane may be overcome and that is a mechanism whereby head pressure is produced by electroosmosis (EO). This postulate will be discussed in the following section.

8.4.2 Electroosmotic Pressure Model

Ruggeri and Beck[1] suggest that filament head pressure may be produced by EO pressure. However, at the time of their review there was little quantitative data available on EO. As described in the introduction recent developments in the design of EO pumps has meant that there is now the necessary quantitative and also mathematical model data available. Therefore, in this section, the mechanism by which FFC head pressure is produced is compared to the mechanism by which pressure is produced in EO pumps. However, firstly a brief description of EO pumps and their governing principles is given.

In EO pumps an electrolyte is pumped by applying an electric field to the charged electrical double layer (EDL).[2-4,7,9] When a charged solid surface and a polar medium are

in contact, the surface charge influences the distribution of the ions within the liquid near the solid surface. The counterions in the liquid are attracted toward the surface and coions are repelled from the surface. The EDL is the region formed by the excess counterions in the liquid.[2,3,5] The EDL consists of two regions: the Stern layer and diffuse (or Gouy–Chapman) layer[2,5] as shown schematically in Fig. 8.8. The Stern layer is a thin region in which counterions are adsorbed onto the charged surface. Although ions in the Stern layer are fixed in place, ions in the diffuse layer are free to migrate. The plane between the Stern layer and diffuse layer is called the Shear plane. The potential at this plane is called the zeta potential, ζ, and the distance over which significant charge separation can occur is called the debeye length λ_D. The lower portion of Fig. 8.8 shows that as the distance from the surface increases the potential drops off roughly linearly in the Stern layer and then exponentially through the diffuse layer, approaching zero at the imaginary boundary of the double layer. The potential curve is useful because it indicates the strength of the electrical force between particles and the distance at which this force comes into play. Fig. 8.9 is a plot of normalised potential drop and normalised electroosmotic speed, u, plotted against distance from a charged wall.[5] It may be seen that as the potential drops with distance, electroosmotic speed rapidly increases. For the schematic shown in Fig. 8.8 and under an applied electric field, the diffuse layer negative ions would move in the direction of the field, causing ion drag on the surrounding liquid. The liquid motion in the diffuse layer is translated to the rest of the channel via viscous forces.

An EO pump similar to the possible mechanism occurring in FFC is perhaps best described by considering a structure with a large number of nanochannels, a so-called "nanoporous frit". To a first approximation the geometry of the porous structure may be modelled as a large number of parallel coupled capillaries with length L and radius a.[3] The cross sectional area and thickness of the frit is denoted A and L, respectively. The porosity is defined as $\psi = v_e/v$ where v_e is the void volume of the frit, *i.e.*, the volume available to an electrolyte solution and v is the total volume defined as $v = A \cdot L$.

The surface charge generates a potential distribution within the capillaries. In a cylindrical capillary this can be solved analytically for a symmetric electrolyte by invoking the Debye–Hückel approximation in the Poisson–Boltzmann equation.[3] The

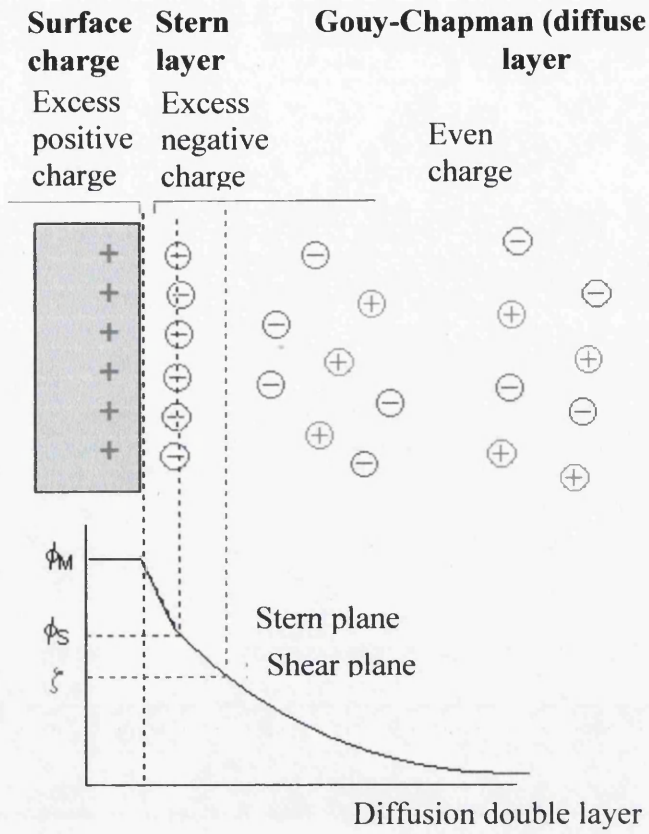

Figure 8.8: Schematic diagram of the electrical double layer (EDL).

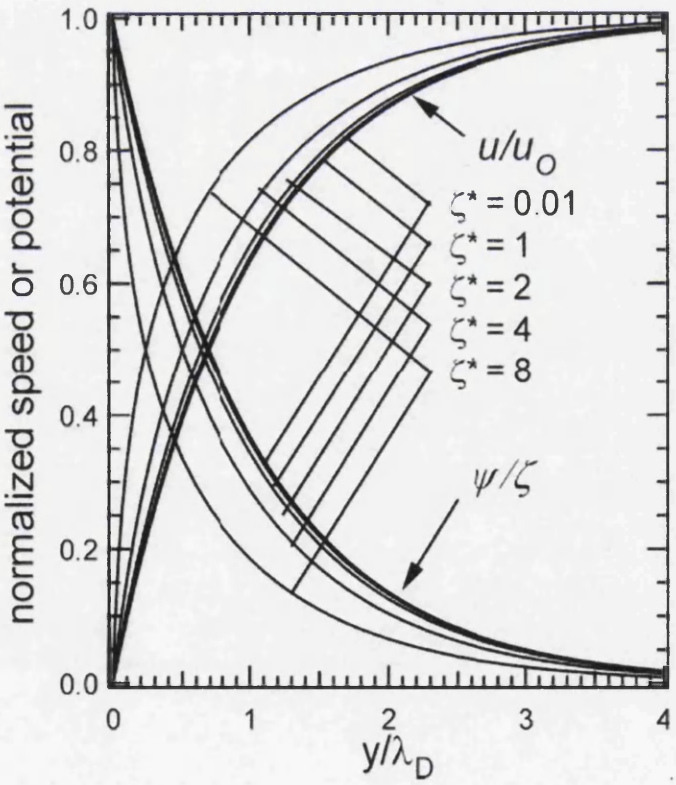

Figure 8.9: Calculated potential distribution and electroosmotic speed; u, where u_0 is the value at infinity; ψ, potential; ζ, potential at shear plane; ζ^*, normalized ζ.[12]

principal governing equations for the theoretical flow rate, Q, and pressure, P, performance of a frit based EO pump are as follows:[3,9]

$$Q = -\frac{\psi \Delta P A a^2}{8\mu L\tau} - \frac{\psi \varepsilon \varsigma V A}{\mu L\tau}\left(1 - \frac{2\lambda I_1(a/\lambda)}{a I_0(a/\lambda)}\right) \tag{8.6}$$

$$Q_m = \alpha_{eo}\psi \frac{A}{L}\left[1 - \frac{2\lambda I_1(a/\lambda_D)}{a I_0(a/\lambda_D)}\right]\Delta V \tag{8.7}$$

$$\Delta P_m = \alpha_{eo} \frac{8\mu}{a^2}\left[1 - \frac{2\lambda I_1(a/\lambda_D)}{a I_0(a/\lambda_D)}\right]\Delta V \tag{8.8}$$

$$\lambda_D = \left(\frac{\varepsilon kT}{e^2 \sum_i c_i z_i^2}\right)^{1/2} \tag{8.9}$$

$$Q = Q_m\left(1 - \frac{\Delta P}{\Delta P_m}\right) \tag{8.10}$$

where, τ is tortuosity, ζ is the zeta potential of the particles which make up the "walls" of the frit, α_{eo} is the electro-osmotic mobility, μ the dynamic viscosity, ε the dielectric constant of the electrolyte, ΔV the applied voltage, e is the elementary charge, c_i and z_i the concentration and valence of the *i-th* species, respectively, Q_m the maximum flow rate, and ΔP_m is the maximum backpressure generated across the porous structure. I_k is the *k'th*-order modified Bessel function of the first kind.[3,9]

The term in the square brackets in Equations (8.7) and (8.8) is denoted the correction factor.[3] In the case of $a/\lambda_D >> 1$ the correction factor equals unity. If the channel radius a and the Debye length λ_D become comparable, the flow Q_m is reduced due to an effect termed Debye layer overlap, *e.g.*, for $a/\lambda_D = 1$ the correction factor is 0.11. Starting from large values of a/λ_D the electroosmotic pressure increases with decreasing a/λ_D until $a/\lambda_D \approx 1$ hereafter it does not change considerably. The relationship

between these equations and FFC on iron will be examined in more detail later on.

EO pumps typically use nanoporous silica frits with a negative surface charge. These produce high flow rates where, $Q_m \propto A$, and also high pressure capacity, where $P_m \propto a^{-2}$, as determined from Equations (8.7) and (8.8). However, in the case of a FFC filament on iron it is self-evident that the frit material will not be nanoporous silica. It is also apparent that the surface charge of the frit must be positive in order to create the necessary directional (forward) movement of ions (Cl^-) in the EDL to produce filiform head pressure. It is well known that at the front of the filament head metal dissolution would occur at the anode with the production of Fe^{2+} cations, as described in Section 7.1. The Fe^{2+} cations are further oxidised to Fe^{3+} upon contact with oxygen in the head electrolyte and in turn Fe^{3+} ions are hydrolysed due to their high affinity for the OH ligand, creating the strongly acidic, hydrated Fe^{3+} cation. The resulting iron hydroxides have a low solubility at pH > 3. Therefore, it may be assumed that anywhere there is water in the head electrolyte the pH will be acidic (pH < 7). It has also been shown elsewhere that the surface charge of hydrated Fe(III) oxide follows pH in a Nernstian fashion with a point of zero charge (pH_{pzc}) and inner layer capacitance of pH 7.5 and 177 μFcm^{-2}.[17] Below pH_{pzc} the acidic water donates protons and so the adsorbent surface is positively charged attracting anions. Thus hydrated Fe(III) oxide has the required positive surface charge (below pH 7) and is therefore a suitable material for the porous frit structure required to form an EO pump within a filiform tail. An "electric screen" of negatively charged Cl^- ions will form on the hydrated Fe(III) oxide surface, producing a higher concentration of Cl^- ions in this region. The existence of an electric field, due to the presence of a local anode and cathode (see Section 7.1) within the FFC electrolyte, means that Cl^- ions will migrate towards the anode at the front of the filament head. Diffuse layer Cl^- ions would move in the direction of the field, causing ion drag on the surrounding liquid. The liquid motion in the diffuse layer is translated to the rest of the channel via viscous forces, opposing backpressure.

With the above information it is now possible to propose a possible model for an "EO pump" mechanism which can produce filament head pressure in FFC occurring on iron. A schematic of the model is shown in Fig. 8.10. At the anode, positioned towards the front of the filament head, metal (iron) dissolution would occur with the release of

Fe^{2+} cations. Most Fe^{2+} ions would migrate towards the back of the head and be oxidised to Fe^{3+} which in turn will eventually precipitate hydrated iron(III) oxide corrosion products as described in Section 7.1. However, some Fe^{2+} would immediately be further oxidised with atmospheric O_2 that had diffused through the coating and thus an anterior cathodic ring would be formed at the leading edge of the filament by the hydrolysis and subsequent precipitation of hydrated iron(III) oxide. The anterior ring of hydrated iron(III) oxide would temporarily prevent the advancement of the filament whilst at the back of the head/start of the filament tail hydrated iron(III) oxide corrosion products would form the necessary positively charged porous frit material for an EO pump. Chloride (Cl^-) ions will form a negatively charged screen on the positively charged frit surface as shown in Fig. 8.10. Behind this will be the primary cathodic region where O_2 reduction and the formation of OH^- ions will occur. As diffuse layer Cl^- ions move in the direction of the field they will cause ion drag on the surrounding liquid. The liquid motion in the diffuse layer is translated to the rest of the channel via viscous forces, thus opposing backpressure ΔP. As ΔP is increases there will be a decrease in the volume of free electrolyte in the filiform head as more electrolyte will be forced backwards into contact with hydrated iron(III) oxide. This is consistent with the observations shown in Fig. 8.6 that shown the volume of free electrolyte in the filament head decreased with increasing ΔP.

8.4.3 Comparison of Experimental Data with EO Model

The EO model described above suggests a possible mechanism whereby EO could produce pressure within a filiform head. However, in the above section a number of equations (Equations (8.7) to(8.10)) were described that govern the theoretical flow rate and pressure performance of EO pumps. Thus a necessary attempt to validate the model by checking that experimental data is consistent with EO pump theory is now made. However, to do this some simplifying assumptions are made during the analysis and these will be discussed when relevant. However, the first assumption that is made is that, V, the potential difference existing between the local anode and cathode within a filament, will remain constant. This assumption is made as in EO pump analysis the potential

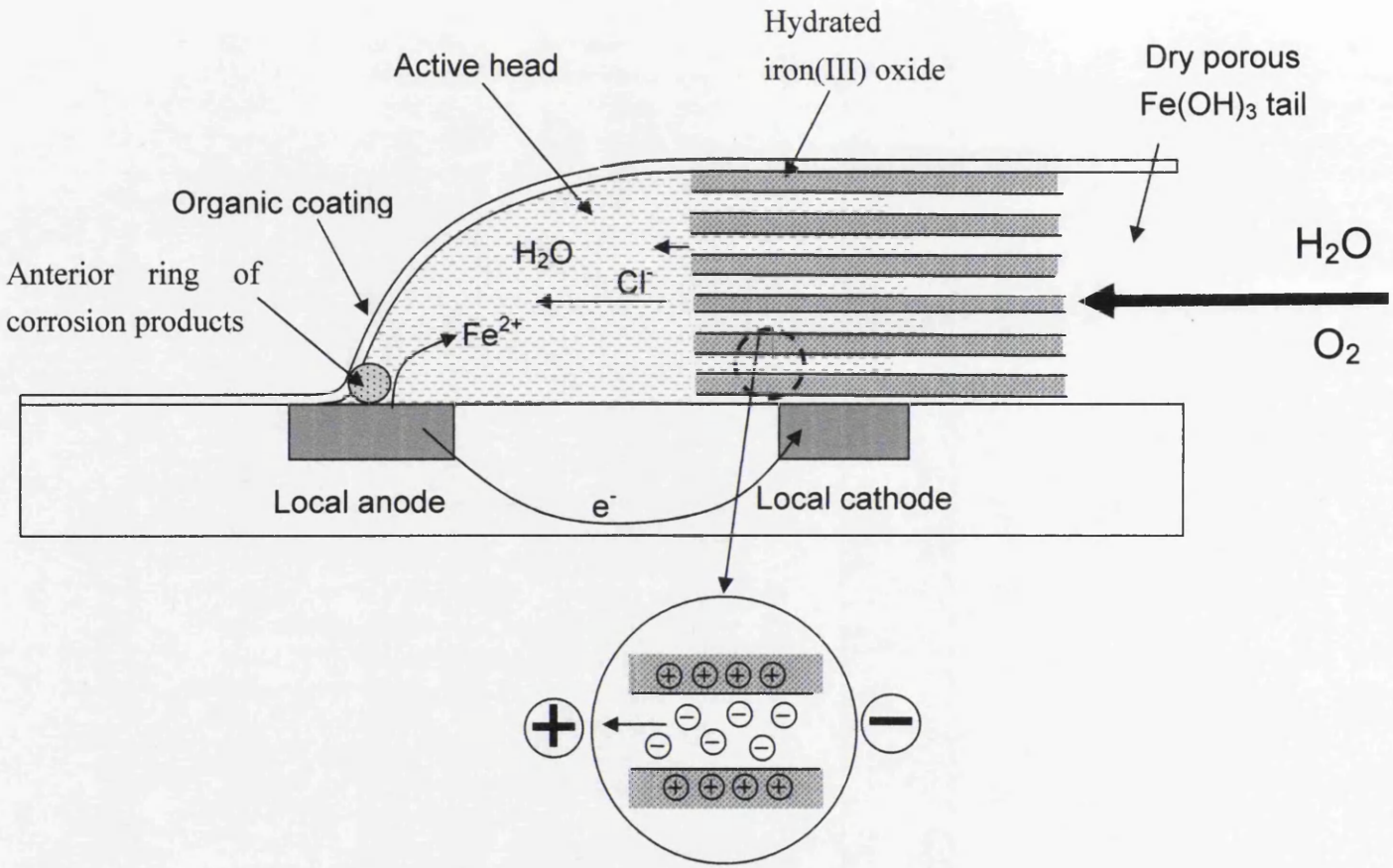

Figure 8.10: Schematic diagram of filiform corrosion occurring on organically coated iron where filament head pressure is controlled by electroosmosis.

gradient, $E = V/L$ and thus V is independent of length. In Fig. 8.6 images of a filament head are shown with increasing pressure. From these it seems reasonable to assume that anode cathode separation will not increase and thus V between them will remain constant. For a given V, frit material and working fluid it is implicit that ε the dielectric constant of the electrolyte, ζ the zeta potential of the particles which make up the "walls" of the frit, and μ the dynamic viscosity will also be fixed.[9] Therefore, only the relationship between flow rate and backpressure ΔP will be discussed.

Equation (8.10) shows that as backpressure ΔP increases the volume flow rate, Q, will decrease, *i.e.*

$$Q = 0, \text{ when } \Delta P = \Delta P_m \tag{8.11}$$

However, from the experimental data shown in Fig. 8.3 it can be seen that,

$$\frac{dL}{dt} \neq f(\Delta P) \tag{8.12}$$

where $\frac{dL}{dt}$ is filament velocity. This is not immediately consistent with Equation (8.10). However, filament width D_f decreases with increasing ΔP, so for FFC the volume flow rate may be determined as,

$$Q = f\left(\frac{dL}{dt}, D_f\right) \tag{8.13}$$

which is consistent with Equation (8.10). To determine the effect of ΔP and D_f (and thus filament head dimensionality) on flow rate it is possible to consider two scenarios. In scenario 1 a constant aspect ratio between filament width D_f and filament height h_f is maintained, whilst in scenario 2, h_f remains constant. These two scenarios are shown in Fig. 8.11. Considering scenario 1 (see Fig. 8.11a) where the assumption is made that a constant aspect ratio between D_f and h_f is maintained with increasing ΔP, then volume

flow rate. Q will be given by,

$$Q = const.\left(D_f\right)^2 \frac{dL}{dt} \tag{8.14}$$

By rearranging Equation (8.10) to give,

$$\frac{Q}{Q_m} = 1 - \frac{1}{\Delta P_m}\Delta P \tag{8.15}$$

a plot of normalised flow rate *vs.* ΔP may be plotted. Such a plot is shown in Fig. 8.12 for two typical filiform pressure experiments. The data shown on the plot has a poor fit to the predicted linear relationship, as was the case for all the pressure experiments carried out during this work and therefore it is unlikely that a constant aspect ratio is maintained in a filament head with increasing ΔP.

In scenario 2 (see Fig. 8.11b) the assumption is made that the height of the filament, h_f, remains constant but filament diameter D_f changes with increasing ΔP and so the volume flow rate Q will be given by,

$$Q = const.\left(D_f\right)\frac{dL}{dt} \tag{8.16}$$

Thus a new plot of normalised flow rate *vs.* ΔP may be made, as shown in Fig. 8.13. In this scenario there is a much better linear relationship between Q and ΔP, and therefore it seems probable that filament height is not changing even with increasing ΔP.

However, in both the scenarios shown here the cross-sectional area of a filament is given by, in scenario 1,

$$A_1 = const\left(D_f\right)^2 \tag{8.17}$$

whilst in scenario 2 cross sectional area is given by,

a)

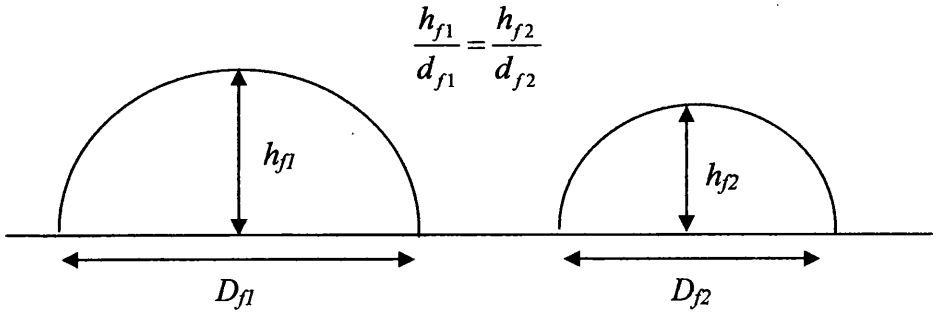

b)

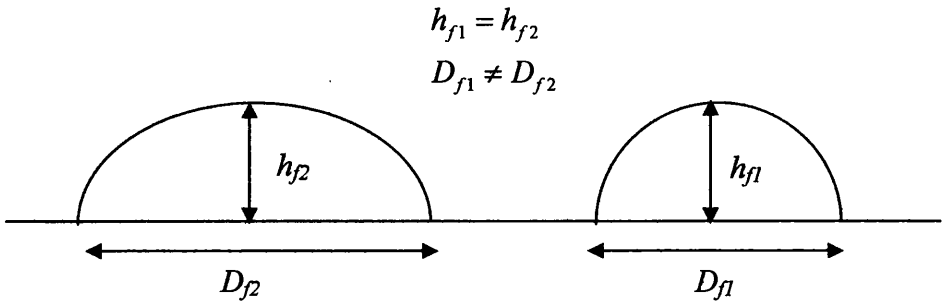

Figure 8.11: Schematic diagrams of filament head dimensions(height, h_f and width, D_f) changing with increasing backpressure. (a) Constant aspect ratio and (b) constant height.

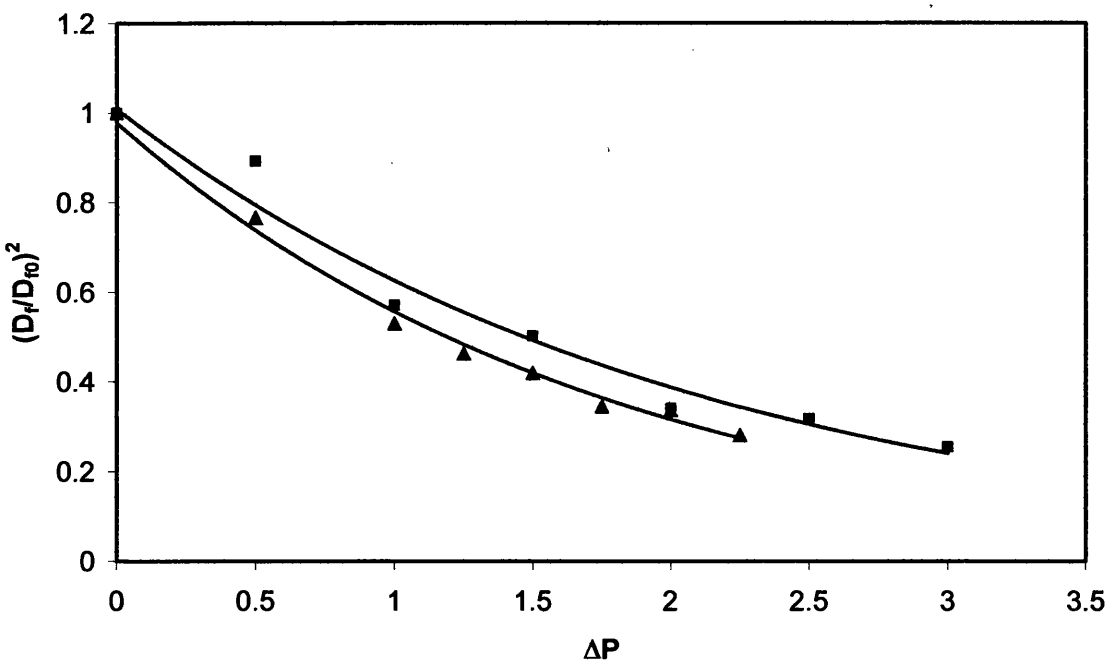

Figure 8.12: Plot of normalised flow rate vs. backpressure ΔP for two FFC pressure experiments where $Q_m \propto f(D_f)^2$, *i.e.* the aspect ratio of filament height and width remains constant. Lines of best fit are shown for each data set.

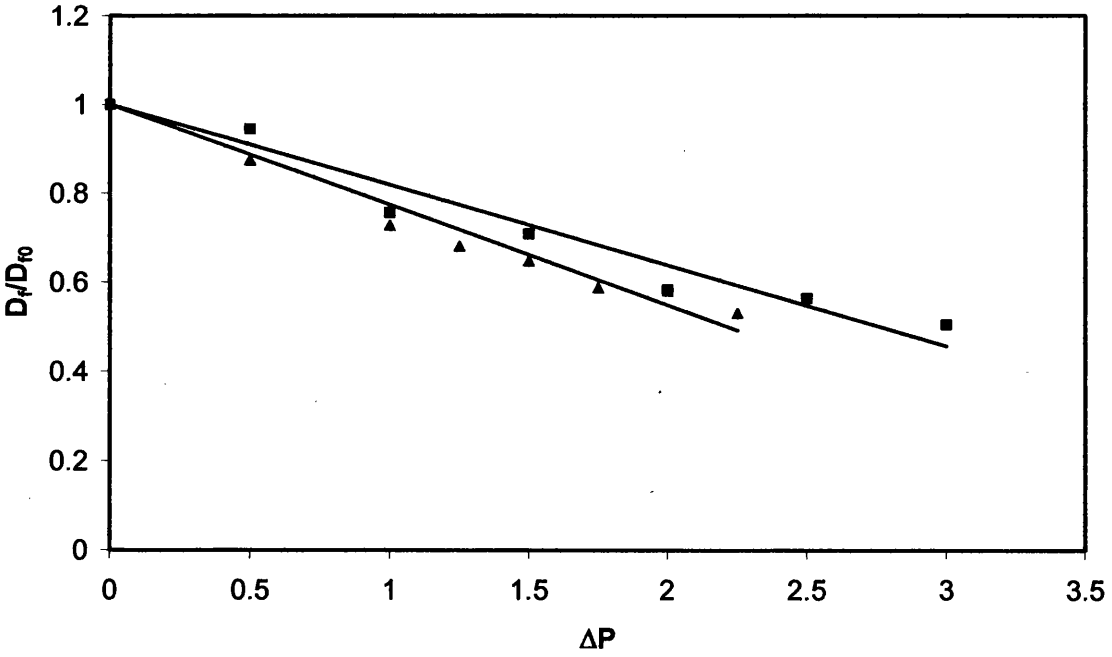

Figure 8.13: Plot of normalised flow rate vs. backpressure ΔP for two FFC pressure experiments where $Q_m \propto f(D_f)$, *i.e.* filament height remains constant. Linear lines of best fit are shown for each data set.

$$A_2 = const(D_f) \tag{8.18}$$

The change in cross-sectional area with increasing ΔP is shown schematically in Fig. 8.14. For the two scenarios shown, there are immediately apparent inconsistencies with Equation (8.7) which shows that $Q_m \propto A$. The transition from A_1 to A_2 in an EO pump frit should produce a time-dependent change in Q_m and therefore Q which was not observed experimentally (as shown in Fig. 8.5b), where a step-wise (instantaneous) response in D_f and hence Q is shown to occur when ΔP is incrementally increased. However, Leblanc and Frankel[18] have previously shown, using scanning Kelvin probe force microscopy (SKPFM), that a "void" exists along the edges of filament tails on epoxy-coated 1045 carbon steel. They showed this by scanning over a filament tail both in the presence and absence of the epoxy coating. Therefore only the centre portion of a filiform tail is occupied by corrosion products and on either side of this there was an empty space (void) between the substrate and the overlying organic coating. With this in mind Fig. 8.16 again shows a typical image of a filament responding to increasing ΔP under experimental conditions. In this image the "core" of corrosion products occupying the filament tail is indicated by the white dotted line. From Fig. 8.16 it is apparent that the change in this core portion of the filament tail with increasing ΔP is much smaller (~12% decrease from ~205 μm to 180 μm) when compared to the large change in D_f (~41% decrease) observed with increasing ΔP. The changes in D_f and the core cross-section of corrosion products is shown schematically in Fig. 8.17. This shows that the void area, outside of the core corrosion products making up the tail, can be decreased with increasing ΔP and so a large decrease in D_f would be observed. However, the cross-sectional area of the core corrosion products making up the filament tail remains relatively unchanged. Therefore, if the cross-sectional area of the frit or EO pump is not changing (or only changing by a small amount) with increasing backpressure ΔP then it is reasonable to assume that there will be no detected change in filament velocity $\frac{dL}{dt}$ and that scenario 2 can be true. If the core cross-sectional area of the filament tail is not

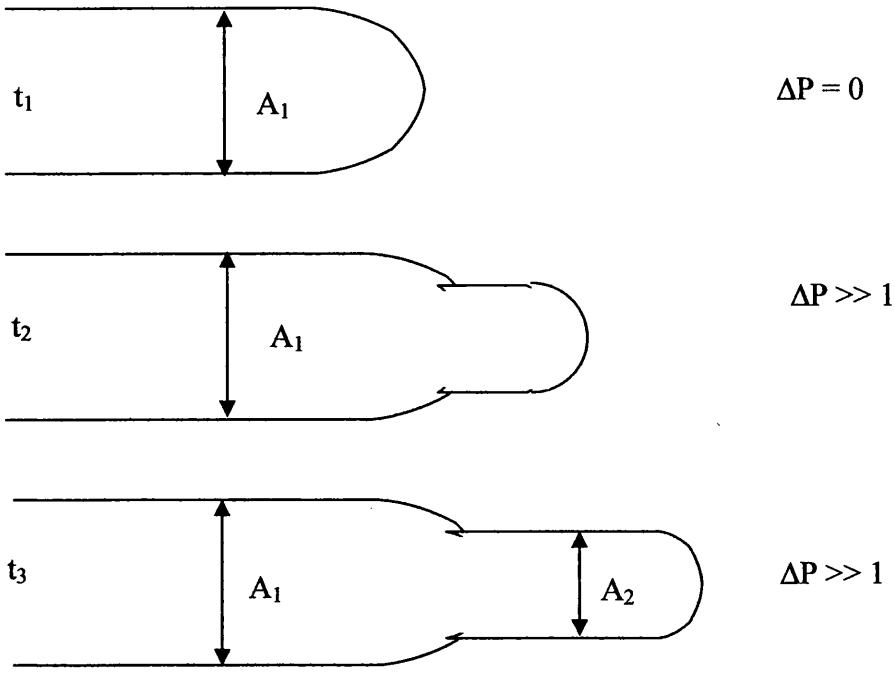

Figure 8.14: Schematic diagram of the change in filament width, D_f, with increasing backpressure, ΔP.

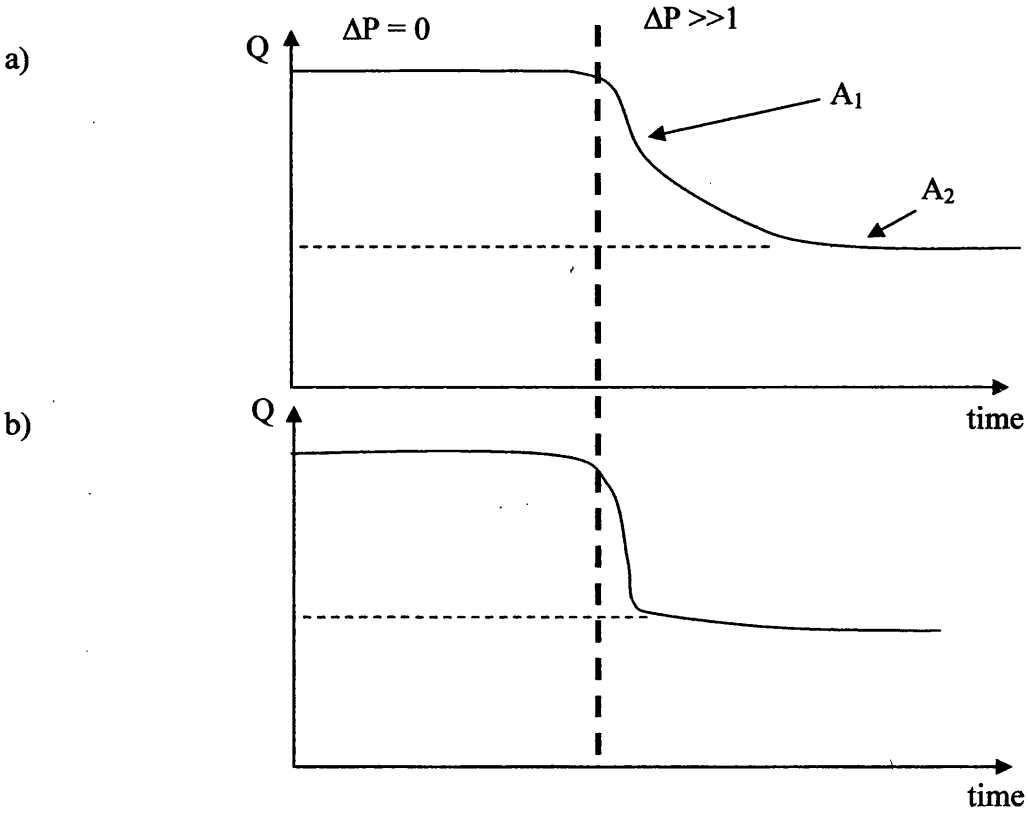

Figure 8.15: Schematic representation of volume flow rate, Q, response to increasing ΔP and decreasing filament width (shown schematically in Fig. 8.14). (a) theoretical and (b) experimentally observed.

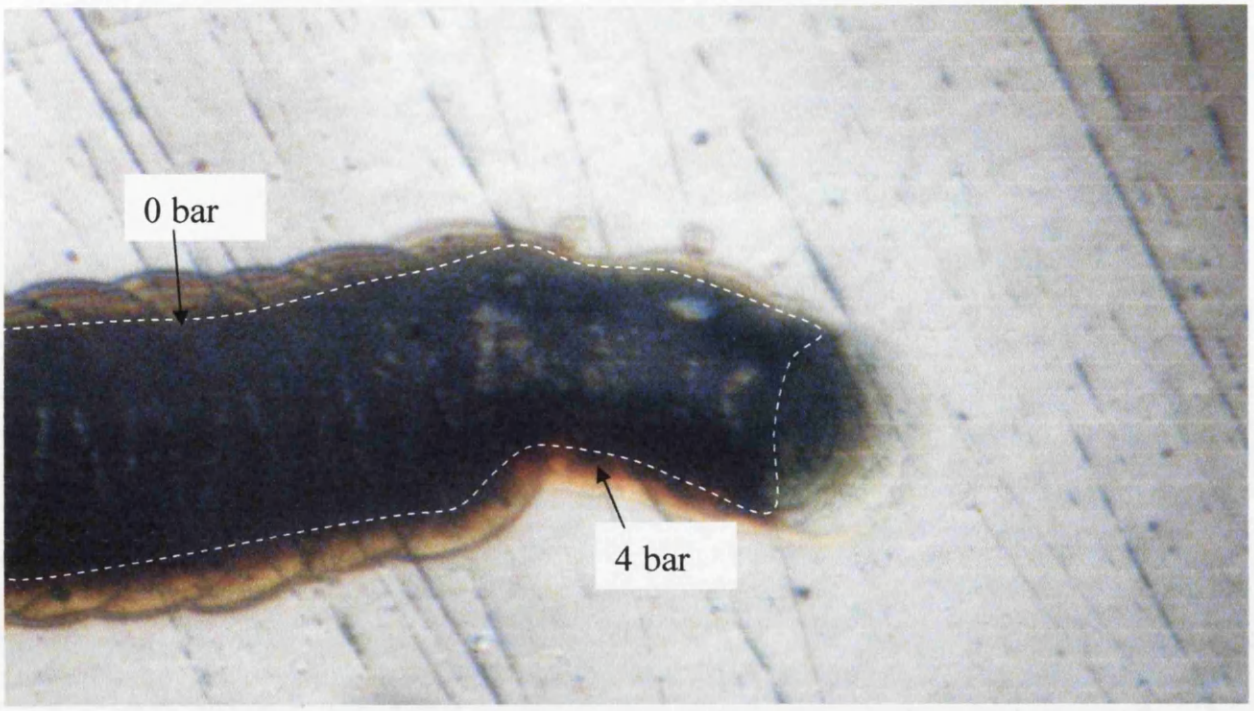

Figure 8.16: Optical micrograph of a filiform after backpressure ΔP has been increased from 0 to 4 bar. The white dotted line indicates the "core" corrosion products making up the filament tail.

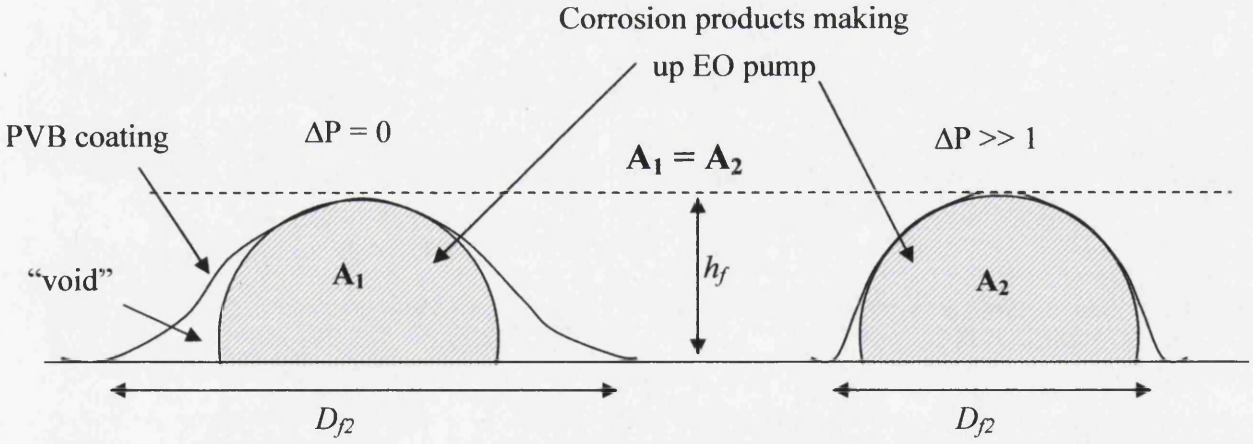

Figure 8.17: Schematic diagram showing how the cross-sectional of corrosion products in a filament tail remains largely unaffected with increasing pressure, ΔP. Diagrams show that only the void area between the core corrosion products and the overlying PVB coating changes with increasing ΔP.

changing (or only changing by a small amount), as shown in Fig. 8.17, then it also follows that the assumption made in scenario 2 - that filament head height remains constant with decreasing filament width D_f - also has more validity.

By using scenario 2 described above and Equation (8.15) it is possible make an estimate of the maximum pressure ΔP_m that may exist within a filament head. Fig. 8.18 is a plot of normalised flow rate *vs.* ΔP for six filiform pressure experiments. The filaments shown in Fig. 8.18(a-c) were initiated with 0.0025 M $FeCl_2$ whilst the filaments in Fig. 8.18(d-f) were initiated with 0.025 M $FeCl_2$. By plotting linear lines of best fit (obtained using least squares analysis) and extrapolating to find the *x*-axis intercept, it is possible to determine ΔP_m. For the filaments initiated with the lower concentration (0.0025 M) $FeCl_2$ it is shown that ΔP_m is predicted to fall in the range 4.4 – 5.8 bar, whilst when $FeCl_2$ concentration is increased by an order of magnitude this significantly increases to 12.1 – 15.5 bar. These are significant maximum attainable pressure values within a filament head and certainly suggest that filiform head pressure could make a contribution to a mechanical disbondment mechanism during FFC propagation.

A number of simplifying assumptions are made during this analysis but it is felt that the EO pump mechanism of filament coating disbondment propagation can help to explain the characteristic saltatory mechanism of FFC on iron. However, there are also a number of questions raised by this analysis. In particular it would be of great interest to determine the actual height of the filament head and tail *in-situ* during FFC propagation with increasing pressure to assess if the assumptions made regarding constant height being maintained in the filament head with increasing ΔP is valid. *In-situ* filament tail cross-sectional area measurement would also help to establish the role that the "voids" at filament tail edges play in FFC propagation. Leblanc and Frankel suggest that the voids may provide facile O_2 transport to the filament head. However results in this work show that with decreasing void width filament velocity remains constant. This was consistent with a constant cross-sectional area of the "core" corrosion product filled tail. However, as ΔP is increased in the coating compartment pO_2 will also increase. As through coating O_2 diffusion can make a contribution to filament propagation, as shown in Chapter 7, it is therefore not possible to eliminate the possibility that the voids provide a facile O_2 transport pathway along the filament tail.

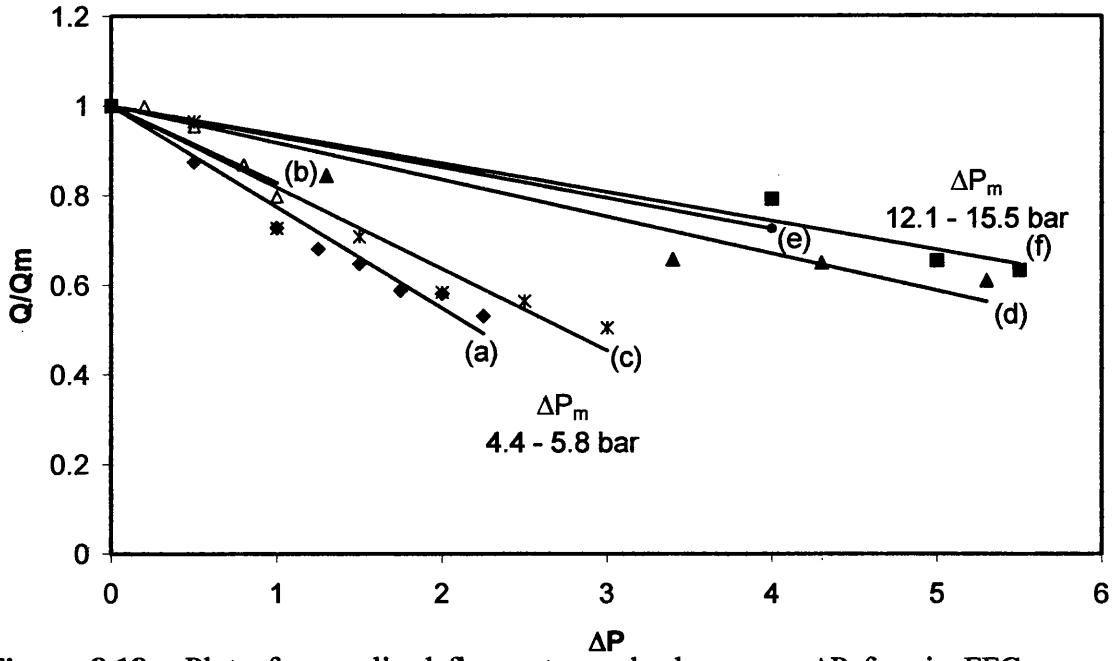

Figure 8.18: Plot of normalised flow rate vs. backpressure ΔP for six FFC pressure experiments where $Q_m \propto f(D_f)$, *i.e.* filament height remains constant. Linear lines of best fit are shown for each data set. FFC initiating salt key: (a-c) 0.0025 M $FeCl_2$, (d-e) 0.025 M $FeCl_2$.

8.5 Conclusions

- The novel experimental (Watson-Coleman) dual compartment cell used in Chapter 7 has been modified to allow the pressure in the coating compartment to be controlled separately from that in the defect compartment. This was done in combination with *in-situ* time-lapse microphotography to successfully study the effect of backpressure ΔP (in the range 0 to 5.5 bar) on the characteristics, dimensions and propagation kinetics of FFC filiform corrosion (FFC) on iron.

- A number of pressure experiments were carried out (FFC initiated with 0.0025 M and 0.025 M $FeCl_2$) where the defect compartment was under conditions of pO_2 = 1 atm and in the coating compartment initially when $\Delta P = 0$, $pO_2 = 0.2$ atm. However, pO_2 in the coating compartment increased with increasing ΔP. In all cases filaments were shown to propagate at a constant velocity and with constant amplitude, A, as ΔP was increased. However, the filament head width, D_f was shown to decrease with increasing ΔP. Filaments imitated with 0.025 M FeCl2 were shown to propagate, even when ΔP was 5.5 bar.

- The previously postulated electro(osmotic) models for filament head pressure were examined. Whilst osmosis was shown to be capable of producing large filament head pressures, the lack of any suitable material for the necessary semi-permeable membrane required by this mechanism, makes the model implausible.[1]

- An electroosmotic (EO) pump mechanism to produce filiform head pressure is proposed, whereby hydrated iron(III) oxide makes up the positively charged "nanoporous frit" that produces EO pumping of electrolyte under an electric field.

- Recent developments in the field of EO pumps were used to determine the relationship between ΔP and volume flow rate, Q. This was used to show that, for

FFC occurring on iron, Q is proportional to both filament velocity and D_f. This decrease in D_f is attributed to the shrinking of "voids" that have been shown to exist along the filament edge between the underlying substrate and the organic coating.[18] However, the "core" corrosion products making up the filament tail remain relatively unchanged with increasing ΔP and thus there is no change in the linear velocity of FFC.

- Further analysis predicts that for filaments initiated with 0.0025 M $FeCl_2$ the maximum filament head pressure will be in the range 4.4 – 5.8 bar, whilst when $FeCl_2$ concentration is increased by an order of magnitude this significantly increases to 12.1 – 15.5 bar. This result certainly suggests that mechanical coating disbondment by filament head pressure is a viable mechanism for FFC propagation on iron.

8.6 References

1. R. T. Ruggeri and T. R. Beck, *Corrosion-NACE*, **39**, 452 (1983).
2. T. Bayraktar and S. B. Pidugu, *International Journal of Heat and Mass Transfer*, **49**, 815 (2006).
3. A. Brask, J. P. Kutter and H. Bruus, *The Royal Society of Chemistry: Lab. Chip.*, **5**, 730 (2005).
4. C. H. Chen and J. G. Santiago, *Journal of Microelectromechanical Systems*, **11**, 672 (2002).
5. B. J. Kirby and E. F. Hasslebrink Jr., *Electrophoresis*, **25**, 187 (2004).
6. J. H. Knox and I. H. Grant, *Chromatographia*, **32**, 317 (1991).
7. D. S. Reichmuth, G. S. Chirica and B. J. Kirby, *Sensors and Actuators*, **B**, 37 (2003).
8. D. J. Throckmorton, T. J. Shepodd and A. K. Singh, *Analytical Chemistry*, **74**, 784 (2002).
9. S. Zeng, C. H. Chen, J. C. Mikkelsen Jr. and J. G. Santiago, *Sensors and Actuators*, **B**, 107 (2001).
10. C. B. Monk, Electrolytic Dissociation, Academic Press, London (1961).
11. R. A. Robinson, Electrolyte Solutions, Butterworths, London (1955).
12. H. S. Harned and B. B. Owen, The Physical Chemistry of Electrolyte Solutions, Reinhold Publishing Corporation ACS monograph series, NY (1943).
13. K. S. Pitzer, Activity Coefficeints in Electrolyte Solutions, CRC Press, Boca Raton, FL (1991).
14. D. A. Sinclair, *J. Phys. Chem.*, **37**, 495 (1933).
15. P. W. Atkins and J. de Paula, Physical Chemistry, Oxford University Press (2002).
16. R. A. Weast, Editor, CRC Handbook of Chemistry and Physics, Boca Raton, FL (1987).
17. I. Larson and P. Attard, *Journal of Colloid and Interface Science*, **227**, 152 (2000).
18. P. P. Leblanc and G. S. Frankel, *J. Electrochem. Soc.*, **151**, B105 (2004).

Chapter 9

Conclusions and Future Work

9.1 Introduction

This thesis has contributed to the mechanistic understanding of filiform corrosion (FFC) both on organically coated automotive aluminium alloys and iron. Along the way a novel corrosion-inhibited organic coating has been identified and shown to profoundly inhibit surface active FFC. Copper complexing reagents have also been identified for potential use as in-coating inhibitor pigments for the prevention of successive pitting FFC on high copper containing alloys. It is also believed that the findings in this thesis provide a better understanding of the coating disbondment mechanism of FFC on iron. Each of these areas is now discussed in more detail below with possible future work suggested in each case.

9.2 Automotive Aluminium Alloys

In Chapter 3 the scanning Kelvin probe (SKP) was used to quantify localised free corrosion potentials (E_{corr}) on abraded and polyvinylbutyral (PVB) overcoated AA6016-T4 aluminium alloy. The kinetics of atmospheric corrosion, initiated by HCl exposure, were quantified by following the subsequent evolution of E_{corr} patterns. When caustic-etched to remove any deformed surface layer, AA6016-T4 is effectively corrosion resistant. However, when the abraded damaged surface layer is present the same material exhibits a rapid, superficial, surface-active FFC, in which metal loss is limited to the thickness of the (abrasion-induced) deformed layer (*i.e.* < *ca.* 2 μm). Post-abrasion heat-treatment at temperatures in the range 180°C to 350°C was found to increase FFC propagation rates. Potentials (E_{intact}) measured over the intact, uncorroded, PVB coated surface were shown to be *ca.* 0.2 V lower for abraded AA6016-T4 than for the bulk alloy, a difference which increases to 0.4 – 0.5 V following heat-treatment at 180 - 350°C respectively. These findings are consistent with a thermally enhanced anodic activation in the abrasion-induced deformed layer and this notion was confirmed by potentiodynamic polarisation measurements in near-neutral 0.5% aqueous NaCl. A mechanism was therefore proposed in which anodic activation causes the deformed layer to react sacrificially with respect to bulk AA6016-T4 and contribute substantially to the driving force for surface-active FFC.

Samples of AA6016-T4 subject to post-abrasion heat-treatment between 180°C and 350°C are also subject to a slower, more deeply penetrating, successive-pitting type of FFC in which the bulk alloy is penetrated to a depth of 10 – 50 μm. Successive-pitting FFC only occurs in the absence of a sacrificial deformed layer, *i.e.* either as a secondary process following surface-active FFC or on samples which have been caustic etched. In both surface-active and successive-pitting FFC the appearance of the corroded surface under SEM is consistent with intergranular corrosion (IGC). In successive-pitting FFC the apparent grain size is typical of the bulk alloy, *i.e. ca.* 20 μm. In surface-active FFC the apparent grain size is reduced to *ca.* 1 μm, as would be expected for a "micro-grained" surface layer.

The exact mechanism whereby AA6016-T4 becomes sensitized to IGC remains unclear and future work should focus on determining this. However, given the low copper content (0.06%) of the samples used in our studies, it seems likely that sensitisation involves precipitation of anodically active Mg_2Si at grain boundaries. The greater anodic activation of the abrasion-induced surface deformed layer is therefore explicable on the basis of the greater density of grain boundaries in this layer. Further work should also focus on electrochemically characterising other automotive aluminium alloys such as AA6111-T4. Increased understanding of the electrochemical and microstructural properties of mechanically induced surface layers will contribute further to the understanding of FFC and will be applicable to a wider range of surface sensitive rolled aluminium alloys.

Chapter 4 showed that "self-anodising" coatings consisting of Polyaniline dispersed in a PVB primer were ineffective as a corrosion inhibition mechanism. In fact the PAni coating itself increased the rate of surface active FFC by providing a facile cathodic reaction through the reduction of PAni-ES. However, FFC corrosion on an abraded AA6111-T4 surface was successfully inhibited by applying an inhibitor coating consisting of phenylphosphonic acid (H_2PP) dissolved in a PVB primer. In-coating H_2PP was found to suppress E_{intact} and filament E_{corr} values by up to 0.35 V – an observation which has tentatively been attributed to the adsorption of HPP^- or PP^{2-} anions on the oxide-covered aluminium surface, although metal/H_2PP salt formation may also contribute in the filament region.

The efficiency of in-coating H_2PP as an inhibitor of FFC on AA6111-T4 is such that the exact mechanism(s) of inhibition and the determination of optimum inhibitor concentration is worthy of further investigation, with a possible view to developing new coating and/or pre-treatment systems. Current electrophoretic bath coating systems used in the automotive industry would render the soluble acid unusable without a microencapsulating delivery mechanism. However, there certainly seems to be promising application as a primer during in-service automotive repairs. Future work should also look at the applicability of this coating system to other areas of the aluminium industry where FFC is a problem, *i.e.* structural and aerospace.

9.3 Successive pitting FFC Inhibition

In Chapter 5 the scanning vibrating electrode technique (SVET) was used to perform a systematic and comparative study of a series of copper complexing reagents that are known to (or were identified as likely to) stifle oxygen reduction on Cu-rich intermetallic particles (IMPs). This was done to determine their relative efficiencies as inhibitors of pitting corrosion under immersion conditions with a view to then incorporating them into a coating system to prevent successive pitting FFC. Unpolarised AA2024-T3 which is known to pit under free corrosion conditions when immersed in near-neutral aerated 0.86 M NaCl aqueous electrolyte, was used for this study. The most effective inhibitors of AA2024-T3 pitting were Cu specific chelators which form Cu^{2+} complexes of limited aqueous solubility and appear to adsorb strongly onto Cu-rich IMPs. It was shown by inhibiting Cu replating using ethylenediaminetetraacetic acid (EDTA), that replated Cu is not necessary for stable pit maintenance and that sufficient cathodic activity can be sustained on Cu-rich intermetallic particles (IMPs).

It was proposed that the apparent critical factor in pitting inhibition is not the prevention of copper redistribution, but rather the stifling of cathodic oxygen reduction on Cu-rich IMPs. This work demonstrates that an effective method of so doing appears to be by incorporating species which either adsorb strongly onto, or form, insoluble films on the surface of copper containing intermetallics.

It therefore seems probable that the copper specific chelators will also profoundly inhibit successive pitting FFC when dispersed in a primer pigment and it is hoped that

further work will be carried out to demonstrate this. It is proposed that both bulk AA6111-T4 and AA2024-T3 would be suitable alloys to use for this study.

The dual properties of EDTA as a metal cation complexant and pH buffer were further used to characterise cathodic corrosion on AA2024-T3 under specific conditions in Chapter 6. A bi-phasic aluminium (hydr)oxide was identified around cathodic IMPs when a 10^{-3} M EDTA addition is made to 0.86 M NaCl aqueous electrolyte. It was also shown that when cathodic corrosion is inhibited by a 10^{-2} M EDTA addition that the net cathodic current available for stable pitting is increased. This was shown by an increase in the detection efficiency of the SVET, indicating that microgalvanically coupled "cathodic corrosion" events occurring in zones of high local pH at cathodic IMPs are not detected by the SVET. This reiterated the fact that caution must be exercised when analysing SVET data. Furthermore, it clearly demonstrated that SVET results may only be interpreted semi-quantitatively.

9.4 Mechanistic Understanding of FFC on Iron

A novel experimental (Watson-Coleman) cell was developed in Chapters 7 and 8 enabling the separation of head and tail sections of FFC. It was successfully demonstrated that this cell can be used to expose each section of the filament to different pO_2 and pressure. Combined with *in-situ* time-lapse photography a study of the effect of gas composition on FFC propagation was made. Using the cell oxygen transport from the initiating defect and along the filament tail was shown to be the primary mode of oxygen supply to the filament head. However, it was also shown that when FFC is occurring under an oxygen permeable coating, FFC propagation may still be maintained by through coating O_2 diffusion into the porous filament tail. However, the rate of propagation was significantly reduced when oxygen supply from the initiating defect was completely removed.

It was further shown that when $pO_2 \geq 0.2$ atm in the coating compartment, FFC propagates in a saltatory (step-wise) manner. The saltatory progression of FFC appears to occur due to the formation of a cathodic anterior ring of corrosion products formed by through coating O_2 diffusion at the leading edge of the filament head. The anterior ring

temporarily halts filament progression and creates a step-wise growth of the filament. It was also shown that when O_2 is removed from the coating compartment the cathodic anterior ring disappeared resulting in a lateral increase in filament width. However, there was no corresponding decrease in the rate of propagation – indicating that cathodic disbondment of the organic coating by the anterior ring is also not rate determining for filament growth. Filament width was shown to be dependent on pO_2 in the coating department which indicated that cathodic O_2 reduction is important in limiting the lateral spread of the electrolyte droplet.

The results indicated that filiform advancement is controlled by an electroosmotic (EO) pump mechanism which acts to build up pressure in the filament head and a subsequent mechanical disbondment of the organic coating. It was shown, by applying an incrementally increased pressure applied to a filament head, that the maximum achievable pressures are significant (> 4 bar). This is comparable to pressures produced by EO pumps designed for microfluidic applications and thus it is entirely feasible that the filament head pressures observed could be produced by an EO pump mechanism.

It is hoped that the Watson-Coleman cell will be adapted for use with a phase-contrast microscope so that a similar systematic study of the effect of gas composition and pressure may be made on FFC occurring on aluminium alloys. In particular it would be interesting to study surface active FFC.

Appendix A

Appendix A

A.1 Theoretical Surface Charge

The theoretical surface charge contained within the damaged surface area exposed during the anodic polarization curves shown in Chapter 3 is determined below. If we assume that the maximum thickness of the surface layer is 1μm and a unit area of 1 cm^2 is defined, then

$$\begin{aligned} V &= 1\times10^{-5}\,cm^2 \\ m &= \frac{V}{\rho} \\ &= \frac{1\times10^{-5}}{2.7} \\ &= 3.7\times10^{-6}\,g \end{aligned} \tag{A.1}$$

where, V = volume of surface layer (per unit area), m = mass and ρ = density of Al. The molar mass M of Al is 26.96gmol^{-1}, and assuming that all Al is consumed through

$$Al \rightarrow Al^{3+} + 3e^- \tag{A.2}$$

then the total electric charge produced by the dissolution of this surface layer, (Coulombs per unit area), C is given by,

$$\begin{aligned} C &= n\times \text{no. of moles}\times F = n\times\frac{m}{M}\times F \\ &= 3\times\frac{3.70\times10^{-6}}{26.96}\times 96487 \\ &= 0.039\ Ccm^{-2} \end{aligned} \tag{A.3}$$

A.2 Experimental Measurements

The values of C determined from experimental data were determined for samples subject to post-abrasion heat treatment at: T_{HT} = 25°C and T_{HT} = 350°C. A value C_{Eb} was determined as the surface charge produced between the open circuit potential OCP and

the breakdown potential E_b which is determined from anodic polarization curves when j_{an} = 2 x 10^{-5} A cm^{-2}.

To determine C_{Eb} the anodic polarisation data was replotted as current *vs.* time, t, using the scan rate of 0.005 Vs^{-1}. Values of C were determined using a numerical estimation (trapezium rule) of the area under the resulting curve using the following integral,

$$\int_a^b f(t)dt \tag{A.4}$$

where a = OCP and $b = E_b$.

In the table below are given two values of C_{Eb} for an abraded only surface, and an abraded and heat treated (T_{HT} = 350°C) surface.

Surface preparation	C_{Eb} **(Ccm^{-2})**
180 grit	**0.000491215**
180 grit, H_T = 350°C	**0.000871333**

Therefore, from these results it is apparent that the information that has been obtained (*i.e.* j_{an} and E_b) from anodic polarization curves is entirely valid for describing the activity (response) of the surface deformed layer. However, caution must be exercised when measuring j_{an} after E_b as the rapid increase in current density beyond E_b will result in accelerated metal dissolution (removal of the surface deformed layer), thus the determined values will be reflective of the bulk alloy rather than the surface layer.

Appendix B

The area of PAni-EB coating that may be protonated through the inoculation of FFC can be calculated. The absolute number of moles of HCl added is 2 x 10^6 moles and this is the maximum number of moles available to react with the EB. The molecular weight, M_w, of the double aniline residue (shown below in Figure A.1) is 181 g/mol.

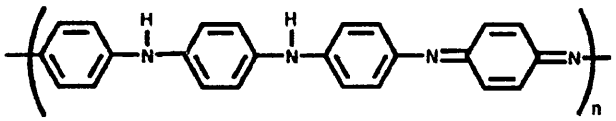

Figure A.1: Molecular structure of Polyaniline Emeraldine base showing 4 aniline residues

Therefore, the mass *m*, of Polyaniline required to fully react with the HCl is given by,

$$\begin{aligned} m &= \text{no. of mols} \times M_w \\ &= 2 \times 10^6 \times 181 \\ &= 3.62 \times 10^{-4} g \end{aligned} \qquad \text{(B.1)}$$

The density, ρ, of PAni-EB is given as 1.25 g cm^{-3} [1], and thus the volume *V*, occupied by 3.62 x 10^{-4} g of PAni-EB is,

$$\begin{aligned} V &= \frac{m}{\rho} \\ &= \frac{3.62 \times 10^{-4}}{1.25} \\ &= 2.90 \times 10^{-4} cm^3 \end{aligned} \qquad \text{(B.2)}$$

However, as the pigment volume fraction, ϕ = 0.2, the real physical volume occupied by the coating is 5x greater, that is 1.45 x 10^{-3} cm^3. Therefore, for a coating with a thickness *t*, of 30 μm coating this equates to a total area of,

$$A = \frac{V}{t}$$
$$= \frac{1.45 \times 10^{-3}}{3 \times 10^{-3}} \qquad \text{(B.3)}$$
$$= 0.47 cm^2$$

Therefore, an area of 0.47cm^2 of Pani-EB around the defect could be protonated by the introduction of 1μl of 2M HCl into the defect.

References

[1] J. Stejskal, R. G. Gilbert, Pure Applied Chemistry 74 (2002) 857 - 867.